Transient Melt Pool Response in Additive Manufacturing of Ti-6Al-4V

Submitted in partial fulfillment of the requirements for

the degree of

Doctor of Philosophy

in

Mechanical Engineering

Jason Cho Fox

B.S., Integrated Science and Technology, James Madison University
M.S., Mechanical Engineering, Carnegie Mellon University

Carnegie Mellon University
Pittsburgh, PA

May 2015

Dedication

To my son, Jameson

and

my wife, Chloe

Acknowledgements

This thesis could not be completed without a vast amount of support. I would like to thank my advisor and mentor, Professor Jack Beuth (committee chair) for his guidance through my dissertation research. I am also grateful to the other members of my committee, Professor Fred Higgs, Professor Anthony Rollett, and Professor Kaushik Dayal for their advice and insight. I also would like to acknowledge the contribution of all the staff at the department of Mechanical Engineering and those I have been lucky enough to work with from the department of Material Science and Engineering.

The financial support for this research is provided by the National Science foundation under grant CMMI-1131579 and Carnegie Mellon University's Institute for Complex Engineered Systems under the Northrop Grumman Fellowship.

I would like to give a special thanks to Joy Gockel, a friend and colleague whose guidance and help as a discussion partner has been irreplaceable. I would like to thank Sneha Narra for her help designing and carrying out experiments for analysis of the powder bed electron beam based systems. I would also like to thank all of the students in Professor Beuth's group who have been present during my time at Carnegie Mellon: Colt Montgomery, Zachary Francis, Daniel Christiansen, Luke Scime, Brian Fisher, Greg LeMon, Piyapong Reeseewat, Rui Yang, Haipeng Qiao, and Amin Anvari. All of these students have helped my research by discussing ideas, helping cut and polish some of the 100+ experiment samples, and reviewing papers and presentations. You have made my experience at Carnegie Mellon a wonderful one. Additionally, I would like Ross Cunningham from the department of Material Science and Engineering for all of his suggestions and help in preparing samples for analysis.

I must also acknowledge the collaborators at NASA Langley Research Center, Karen Taminger and Robert Hafley, who have provided helpful insight and guidance through their assistance with the design and execution of experiments.

I would like to thank my parents, Rick and Heisun, for providing me with a strong foundation as a student and as a person. I would like to thank my brother and best friend, Chris, for all of his guidance and support over the years. I would also like to thank my "in-laws" in Pittsburgh, Dan Bekavac Sr., Patti Bekavac, and Dan Bekavac Jr. for all their support in this endeavor and being family… not just "in-laws".

I would like to thank my son Jameson, who has given me drive and purpose while reminding me of what is truly important. Know that while you were not the reason I started this PhD, you have become the reason for finishing.

Lastly, I would like to thank my wife Chloe who has put up with late nights working, driven me to and from campus on her way to and from work, and gone above and beyond to care for Jameson and me without hesitation. This thesis could not be accomplished without her love, strength, and support.

Abstract

Additive manufacturing (AM) processes are candidates for manufacturing and repair in the aerospace industry. For process stability, control of melt pool dimensions is imperative. This can be achieved via feedback and/or feedforward control approaches; however, the time needed for a change in process variables (beam power and travel velocity) to translate into changes in melt pool dimensions is a critical concern. Prior works have determined the relationship between process variables and melt pool geometry, which can be monitored in situ for feedback control. In the current work, Ti-6Al-4V is studied as it is commonly used in aerospace applications due to its desirable properties. Melt pool depth response is determined in terms of response distance rather than response time in order to develop a relationship that is not dependent on the position or path taken in the Power-Velocity (P-V) Process Map, but instead on the initial and final melt pool geometry.

Research is performed through finite element simulations run in the ABAQUS™ software package and validated by experiments performed at the NASA Langley Research Center on their Electron Beam Free Form Fabrication system and at Carnegie Mellon University on their Arcam system. The work presented investigates the transient melt pool response due to changes in process variables in steady state build geometries, as well as extending relationships to transient build geometries and other AM systems yielding a comprehensive understanding of melt pool response across all direct metal AM processes. These relationships will allow for the development of effective feedback and feedforward control systems.

Table of Contents

Dedication i

Acknowledgements ii

Abstract iv

List of Tables ix

List of Figures and Illustrations xi

Nomenclature xxv

Chapter 1 Introduction 1

1.1 Additive Manufacturing 1

1.1.1 Direct Metal Additive Manufacturing 2

1.2 Motivation 2

1.3 Background 4

1.4 Organization 11

Chapter 2 Transient Response in Single Beads 13

2.1 Process Map Approach 13

2.2 Single Bead Finite Element Analysis 15

2.2.1 Material Added Finite Element Models: 15

2.2.2 Simulation Results 17

2.3 Experiments 20

2.3.1 No Material Added Experiments 20

2.3.2 Material Added Experiments 26

2.4 Effect of Added Material Size 38

2.5 Fitting of Transient Melt Pool Response 43

2.5.1 Rule of Thumb Estimate 43

2.5.2 Fitting of Transient Response Behavior 45

2.5.3 Suggested Application to Feedback Control Systems 47

2.6 Discussion 52
Chapter 3 Effect of Geometry on Transient Response 55
3.1 Thin Wall Finite Element Analysis 55
3.1.1 Thin Wall Finite Element Models 55
3.1.2 Thin Wall Process Maps 57
3.1.3 Thin Wall Simulations 57
3.2 Thin Wall Experiments 63
3.3 Fitting of Transient Melt Pool Response for Thin Walls 69
3.3.1 Rule of Thumb Estimate 69
3.3.2 Fitting of Transient Response Behavior 71
3.3.3 Suggested Application to Feedback Control Systems 73
3.4 Corner Geometry FEM 77
3.4.1 Corner Geometry Finite Element Analysis 77
3.4.2 Suggested Application to Feedback Control Systems 86
3.5 Discussion 87
Chapter 4 Extension to Additional Systems 93
4.1 Electron Beam Powder Bed Finite Element Analysis 94
4.2 Fitting of Transient Response Behavior 98
4.2.1 Rule of Thumb Estimate 98
4.2.2 Fitting of Transient Response Behavior 100
4.2.3 Suggested Application to Feedback Control Systems 102
4.3 Electron Beam Powder Bed Experiments 105
4.4 Discussion 112
Chapter 5 Effect of Modeling Parameters and Assumptions 114
5.1 Effect of Preheating in Thin Walls 114
5.2 Effect of Preheating in Thin Walls on Melt Pool Response Prediction 119
5.2.1 Rule of Thumb Estimate 119

5.2.1 Suggested Application to Feedback Control Systems 120
5.3 Additional Parameters and Their Effect on Modeling 123
5.3.1 Square Bead Assumption 123
5.3.2 2D vs 3D for Thin Walls 125
5.3.3 Melt Pool Convection and Surface Radiation 127
5.4 Discussion 129
Chapter 6 Conclusions and Future Work 131
6.1 Conclusions 131
6.2 Implications of the Research 132
6.3 Future Work 134
References 136
Appendix A Measurement of Single Bead Samples 144
No Added Material 144
Added Material 146
Experiment Line 1 146
Experiment Line 2 147
Experiment Line 3 150
Experiment Line 4 152
Experiment Line 5 154
Experiment Line 6 157
Experiment Line 7 159
Experiment Line 8 161
Experiment Line 9 164
Experiment Line 10 165
Experiment Line 11 165
Experiment Line 12 168
Appendix B Measurement of Thin Wall Samples 169

Experiment Line 1 169
Experiment Line 2 171
Experiment Line 3 173
Experiment Line 4 175
Experiment Line 2R 177
Experiment Line 4R 179
Appendix C Measurement of Single Bead Electron Beam Powder Bed Samples. 182
Surface Width Measurements 182
Area Measurements 186

List of Tables

Table 1. Analysis plan for transient response to step changes in power or velocity. Power presented is absorbed power. 18

Table 2. Response times and response distances from 3D finite element simulations. 19

Table 3. Experimental results based on surface width for Cool Down and Rapid plates. 23

Table 4. Experiment process variables for single bead tests. 29

Table 5. Comparisons of steady state melt pool areas from simulations to experimental measurements. 34

Table 6. Parameters and results for new simulations. 41

Table 7. Comparison of Rule-of-Thumb estimates to simulation data. 45

Table 8. Parameters for prediction of melt pool behavior. 46

Table 9. Comparison of response distance and response time via rule of thumb. 51

Table 10. Analysis plan for the thin wall geometry. 59

Table 11. Response times and distances for thin wall step changes. 60

Table 12. Analysis plan for thin wall experiments. 65

Table 13. Comparison of Rule-of-Thumb estimates to simulation data. 71

Table 14. Parameters for prediction of melt pool behavior. 72

Table 15. Comparison of response distance and response time via rule of thumb. 76

Table 16. Parameters for step changes in power plan for electron beam powder bed system. 97

Table 17. Response times and response distances for step changes. 97

Table 18. Comparison of rule of thumb estimates to simulation data. 100

Table 19. Parameters for prediction of melt pool behavior. 101

Table 20. Comparison of response distance and response time via rule of thumb. 104

Table 21. Parameters for Arcam experiments.....105

Table 22. Melt pool area measurements. 111

Table 23. Red and Green curve of constant area parameters for 373 K and 773 K preheat.....116

Table 24. Blue and Red curve of constant area parameters for 373 K and 773 K preheat.....116

Table 25. Response time and distance for a thin wall with 373K and 773K preheat.....117

Table 26. Rule of thumb estimate for response distance in thin walls (373K and 773K preheat).....120

Table 27. Determination of response time via response distance and $\boldsymbol{L'}$ for 373 K preheat.....122

Table 28. Determination of response time via response distance and $\boldsymbol{L'}$ for 773 K preheat.....122

Table 29. Comparison of round bead to square bead simulations. 124

Table 30. Comparison of 2D and 3D thin wall simulation results.....126

Table 31. Review of melt pool convection and surface radiation.....128

List of Figures and Illustrations

Figure 1. A schematic of wire fed electron beam based AM components [1]..... 1

Figure 2. An example of a part built through AM prior to removing excess material (left) and after removing excess material (right). 2

Figure 3. Power-Velocity (P-V) process space for additive manufacturing. 5

Figure 4. The maximum area of the melt pool as seen from a cut view of the model (left) and the melt pool length (right). 13

Figure 5. P-V Process Map for a single bead of added material in wire feed electron beam based processes..... 14

Figure 6. A representative 3D model for finite element simulation using ABAQUS software. 16

Figure 7. Analysis plan for transient response to step changes in power or velocity..... 18

Figure 8. Response behavior for step changes in beam power or travel velocity. 20

Figure 9. Experiments performed at NASA Langley Research Center. 21

Figure 10. Comparison of melt pool widths seen in simulations versus experiments. 22

Figure 11. Sectioned and polished images from Rapid experiment run 2. Each black/white scale bar section measures 7.87E-2in (2mm). 24

Figure 12. Comparison of results from experiment line #1 to simulation results..... 25

Figure 13. Comparison of results from experiment line #2 to simulation results..... 26

Figure 14. Comparison of results from experiment line #4 and #8 to simulation results. 26

Figure 15. Experiment plates for single bead deposition. 29
Figure 16. Comparison of surface width for experiment lines 1 and 3 to the effective depth from simulations. 30
Figure 17. Comparison of surface width for experiment lines 5, 7, and 9 to the effective depth from simulations. 31
Figure 18. Comparison of surface width for experiment lines 2, 4, and 6 to the effective depth from simulations. 31
Figure 19. Comparison of surface width for experiment lines 8, 10, and 11 to the effective depth from simulations. 32
Figure 20. Example cross section from analysis of steady state values (Experiment 1, Initial Steady State). Green scale bar is 0.25 in. 33
Figure 21. Example cross sections to view melt pool depth (Experiment 1, Transient Section). Green scale bar is 0.25 in. 35
Figure 22. Comparison of simulation and experiment results for Green to Red transitions. 36
Figure 23. Comparison of simulation and experiment results for Blue to Red transitions. 36
Figure 24. Comparison of simulation and experiment for center cut samples. 37
Figure 25. Comparison of simulation and experiment for center cut samples. 37
Figure 26. Effect of φ on curves of constant area. 39
Figure 27. P-V Process Map for single bead deposition. 40
Figure 28. New simulations for determining response behavior. 41
Figure 29. Response behavior for step changes in beam power or travel velocity. 42

Figure 30. Response behavior for step changes in beam power or travel velocity. 43
Figure 31. Response distance predicted using rule of thumb versus measured in simulations. 44
Figure 32. Comparison of predicted behavior to simulation results. 47
Figure 33. Schematic of response distance calculation versus response time calculation. 49
Figure 34. Predicted response time versus measured response time from simulation results. 50
Figure 35. 2D Finite Element Model for deposition on a thin wall. 56
Figure 36. PV Process Map for 2D Thin Wall Finite Element Model. 57
Figure 37. Analysis plan for the thin wall geometry. 58
Figure 38. Response behavior for thin wall step changes. 61
Figure 39. Response behavior averages with absolute deviation from averages. 62
Figure 40. Comparison of Single Bead and Thin Wall Response Behavior. 63
Figure 41. Thin wall experiment setup. 64
Figure 42. Analysis plan for thin wall experiments. 65
Figure 43. Example thin wall experiments post deposition. 66
Figure 44. Close up of transitions in thin wall deposition. Left column from top to bottom: experiment 1, 2, 3. Right column from top to bottom: experiment 4, 2R, 4R. Travel velocity is from left to right. 66
Figure 45. Polished cross-section (left) and the measurement of the heat affected zone (middle) and melted portion of the wall (right) for the initial steady state of experiment line 1. Green scale bar is 0.25 in. 67

Figure 46. Comparison of thin wall experimental results and simulations for increases in area. 68
Figure 47. Comparison of thin wall experimental results and simulations for decreases in area. 68
Figure 48. Predicted response distance versus measured response distance from simulation results. 70
Figure 49. Comparison of predicted behavior to simulation results. 73
Figure 50. Predicted response time versus measured response time from simulation results. 75
Figure 51. Example of an external corner geometry. 77
Figure 52. Melt pool depth through the corner. 78
Figure 53. Example model for corner geometry. 79
Figure 54. P-V Process Map for maximum depth in an external corner geometry. 80
Figure 55. Normalized maximum melt pool depth from decreasing power as a control scheme. 81
Figure 56. Control approaches based on increase in melt pool depth. 82
Figure 57. Normalized maximum melt pool depth based on control approaches from Figure 56. 83
Figure 58. Normalized maximum melt pool depth for control approaches. 84
Figure 59. Normalized maximum melt pool depth for control approaches. 85
Figure 60. Control approaches for maintaining consistent melt pool depth in an exterior corner geometry. 85
Figure 61. Results from control approaches in Figure 60. 86

Figure 62. P-V process space for all Direct Metal AM. 94
Figure 63. Example model for electron beam powder bed simulations. 95
Figure 64. P-V Process Map for no material added electron beam powder bed (Ti-6Al-4V). 96
Figure 65. Analysis plan for electron beam powder bed system. 96
Figure 66. Response behavior for the electron beam powder bed system. 98
Figure 67. Predicted response distance versus measured response distance from simulation results. 99
Figure 68. Comparison of predicted behavior to simulation results. 102
Figure 69. Predicted response time versus measured response time from simulation results. 103
Figure 70. Example experiment plate. 106
Figure 71. Example image of bead surface and surface width measurement (Experiment 1-1). Green scale bar is 2 mm (7.87E-2 in)..... 107
Figure 72. Surface width measurements for experiment lines 1-1, 2-1, 1-9, and 2-9..... 108
Figure 73. Surface width measurements for experiment lines 1-11, 2-11, 1-13, and 2-13. 108
Figure 74. Surface width measurements for experiment lines 1-2, 2-2, 1-10, and 2-10..... 109
Figure 75. Surface width measurements for experiment lines 1-12, 2-12, 1-14, and 2-14. 109

Figure 76. Measurement of melt pool area (experiment line 1 initial steady state). Green scale bar is 1 mm (3.94E-2 in). 110
Figure 77. Comparisons of P-V Process Maps for different levels of preheat in a thin wall geometry. 115
Figure 78. Response behaviors for a thin wall with 373 K preheat. 118
Figure 79. Response behaviors for a thin wall with 773 K preheat. 118
Figure 80. Example of a round bead used in simulations. 124
Figure 81. 3D Thin Wall Finite Element Model. 125
Figure 82. Response behaviors for 3D thin wall simulations with 373 K preheat. 126
Figure 83. Sectioned and polished images of Cool Down experiment run 2. Black / white scale bars are 1 mm (3.94E-2 in). 144
Figure 84. Sectioned and polished images of Cool Down experiment run 8. Black/white scale bar measures 7.87E-2 in (2 mm). 144
Figure 85. Sectioned and polished images of Rapid experiment run 1. Black/white scale bar measures 7.87E-2 in (2 mm). 145
Figure 86. Sectioned and polished images from Rapid experiment run 2: initial steady state (top left), final steady state (top right), transient region (bottom). Each black/white scale bar section measures 7.87E-2 in (2 mm). 145
Figure 87. Sample 1A. Experiment line 1, initial steady state. 146
Figure 88. Example cross section to view melt pool depth (Experiment 1, Transient Section). 146
Figure 89. Sample 1B. Experiment line 1, final steady state. 146
Figure 90. Sample 2A. Experiment line 2, initial steady state. 147

Figure 91. Sample 2-1. Experiment line 2, first section in transient region. 147

Figure 92. Sample 2-2. Experiment line 2, second section in transient region. 147

Figure 93. Sample 2-3. Experiment line 2, third section in transient region. 147

Figure 94. Sample 2-4. Experiment line 2, fourth section in transient region. 148

Figure 95. Sample 2-5. Experiment line 2, fifth section in transient region. 148

Figure 96. Sample 2-6. Experiment line 2, sixth section in transient region. 148

Figure 97. Sample 2-7. Experiment line 2, seventh section in transient region. 148

Figure 98. Sample 2-8. Experiment line 2, eighth section in transient region. 149

Figure 99. Sample 2-9. Experiment line 2, ninth section in transient region. 149

Figure 100. Sample 2-10. Experiment line 2, tenth section in transient region. 149

Figure 101. Sample 2B. Experiment line 2, final steady state. 149

Figure 102. Sample 3A. Experiment line 3, initial steady state. 150

Figure 103. Sample 3-1. Experiment line 3, first section in transient region. 150

Figure 104. Sample 3-2. Experiment line 3, second section in transient region. 150

Figure 105. Sample 3-3. Experiment line 3, third section in transient region. 150

Figure 106. Sample 3-4. Experiment line 3, fourth section in transient region. 151

Figure 107. Sample 3-5. Experiment line 3, fifth section in transient region. 151

Figure 108. Sample 3-6. Experiment line 3, sixth section in transient region. 151

Figure 109. Sample 3-7. Experiment line 3, seventh section in transient region. 151

Figure 110. Sample 3B. Experiment line 3, final steady state. 152

Figure 111. Sample 4A. Experiment line 4, initial steady state. 152

Figure 112. Sample 4-2. Experiment line 4, second section in transient region. 152

Figure 113. Sample 4-3. Experiment line 4, third section in transient region. 152

Figure 114. Sample 4-4. Experiment line 4, fourth section in transient region. 153
Figure 115. Sample 4-5. Experiment line 4, fifth section in transient region. 153
Figure 116. Sample 4-6. Experiment line 4, sixth section in transient region. 153
Figure 117. Sample 4-7. Experiment line 4, seventh section in transient region. 153
Figure 118. Sample 4-8. Experiment line 4, eighth section in transient region. 154
Figure 119. Sample 4B. Experiment line 4, final steady state. 154
Figure 120. Sample 5A. Experiment line 5, initial steady state. 154
Figure 121. Sample 5-1. Experiment line 5, first section in transient region. 154
Figure 122. Sample 5-2. Experiment line 5, second section in transient region. 155
Figure 123. Sample 5-3. Experiment line 5, third section in transient region. 155
Figure 124. Sample 5-4. Experiment line 5, fourth section in transient region. 155
Figure 125. Sample 5-5. Experiment line 5, fifth section in transient region. 155
Figure 126. Sample 5-6. Experiment line 5, sixth section in transient region. 156
Figure 127. Sample 5-7. Experiment line 5, seventh section in transient region. 156
Figure 128. Sample 5-8. Experiment line 5, eighth section in transient region. 156
Figure 129. Sample 5B. Experiment line 5, final steady state. 156
Figure 130. Sample 6A. Experiment line 6, initial steady state. 157
Figure 131. Sample 6-2. Experiment line 6, second section in transient region. 157
Figure 132. Sample 6-3. Experiment line 6, third section in transient region. 157
Figure 133. Sample 6-4. Experiment line 6, fourth section in transient region. 157
Figure 134. Sample 6-5. Experiment line 6, fifth section in transient region. 158
Figure 135. Sample 6-6. Experiment line 6, sixth section in transient region. 158
Figure 136. Sample 6-7. Experiment line 6, seventh section in transient region. 158

Figure 137. Sample 6-8. Experiment line 6, eighth section in transient region. 158
Figure 138. Sample 6B. Experiment line 6, final steady state. 159
Figure 139. Sample 7A. Experiment line 7, initial steady state. 159
Figure 140. Sample 7-1. Experiment line 7, first section in transient region. 159
Figure 141. Sample 7-2. Experiment line 7, second section in transient region. 159
Figure 142. Sample 7-3. Experiment line 7, third section in transient region. 160
Figure 143. Sample 7-4. Experiment line 7, fourth section in transient region. 160
Figure 144. Sample 7-5. Experiment line 7, fifth section in transient region. 160
Figure 145. Sample 7-6. Experiment line 7, sixth section in transient region. 160
Figure 146. Sample 7-7. Experiment line 7, seventh section in transient region. 161
Figure 147. Sample 7-8. Experiment line 7, eighth section in transient region. 161
Figure 148. Sample 7B. Experiment line 7, final steady state. 161
Figure 149. Sample 8A. Experiment line 8, initial steady state. 161
Figure 150. Sample 8-3. Experiment line 8, third section in transient region. 162
Figure 151. Sample 8-4. Experiment line 8, fourth section in transient region. 162
Figure 152. Sample 8-5. Experiment line 8, fifth section in transient region. 162
Figure 153. Sample 8-6. Experiment line 8, sixth section in transient region. 162
Figure 154. Sample 8-7. Experiment line 8, seventh section in transient region. 163
Figure 155. Sample 8-8. Experiment line 8, eighth section in transient region. 163
Figure 156. Sample 8-9. Experiment line 8, ninth section in transient region. 163
Figure 157. Sample 8-10. Experiment line 8, tenth section in transient region. 163
Figure 158. Sample 8B. Experiment line 8, final steady state. 164
Figure 159. Sample 9A. Experiment line 9, initial steady state. 164

Figure 160. Experiment line 9, transient section. 164
Figure 161. Sample 9B. Experiment line 9, final steady state. 164
Figure 162. Sample 10A. Experiment line 10, initial steady state. 165
Figure 163. Experiment line 10, transient section. 165
Figure 164. Sample 10B. Experiment line 10, final steady state. 165
Figure 165. Sample 11A. Experiment line 11, initial steady state. 165
Figure 166. Sample 11-2. Experiment line 11, second section in transient region. 166
Figure 167. Sample 11-3. Experiment line 11, third section in transient region. 166
Figure 168. Sample 11-4. Experiment line 11, fourth section in transient region. 166
Figure 169. Sample 11-5. Experiment line 11, fifth section in transient region. 166
Figure 170. Sample 11-6. Experiment line 11, sixth section in transient region. 167
Figure 171. Sample 11-7. Experiment line 11, seventh section in transient region. 167
Figure 172. Sample 11-8. Experiment line 11, eighth section in transient region. 167
Figure 173. Sample 11B. Experiment line 11, final steady state. 167
Figure 174. Sample 12A. Experiment line 12, initial steady state. 168
Figure 175. Sample 12B. Experiment line 12, final steady state. 168
Figure 176. Sample 1A. Experiment line 1, initial steady state. 169
Figure 177. Sample 1-1. Experiment line 1, first section in transient region 169
Figure 178. Sample 1-2. Experiment line 1, second section in transient region 170
Figure 179. Sample 1-3. Experiment line 1, third section in transient region. 170
Figure 180. Sample 1-4. Experiment line 1, fourth section in transient region. 170
Figure 181. Sample 1-5. Experiment line 1, fifth section in transient region. 170
Figure 182. Sample 1-6. Experiment line 1, sixth section in transient region. 171

Figure 183. Sample 1B. Experiment line 1, final steady state. 171
Figure 184. Sample 2A. Experiment line 2, initial steady state. 171
Figure 185. Sample 2-1. Experiment line 2, first section in transient region. 171
Figure 186. Sample 2-2. Experiment line 2, second section in transient region. 172
Figure 187. Sample 2-3. Experiment line 2, third section in transient region. 172
Figure 188. Sample 2-4. Experiment line 2, fourth section in transient region. 172
Figure 189. Sample 2-5. Experiment line 2, fifth section in transient region. 172
Figure 190. Sample 2-6. Experiment line 2, sixth section in transient region. 173
Figure 191. Sample 2B. Experiment line 2, final steady state. 173
Figure 192. Sample 3A. Experiment line 3, initial steady state. 173
Figure 193. Sample 3-1. Experiment line 3, first section in transient region. 173
Figure 194. Sample 3-2. Experiment line 3, second section in transient region. 174
Figure 195. Sample 3-3. Experiment line 3, third section in transient region. 174
Figure 196. Sample 3-4. Experiment line 3, fourth section in transient region. 174
Figure 197. Sample 3-5. Experiment line 3, fifth section in transient region. 174
Figure 198. Sample 3-6. Experiment line 3, sixth section in transient region. 175
Figure 199. Sample 3A. Experiment line 3, final steady state. 175
Figure 200. Sample 4A. Experiment line 4, initial steady state. 175
Figure 201. Sample 4-1. Experiment line 4, first section in transient region. 175
Figure 202. Sample 4-2. Experiment line 4, second section in transient region. 176
Figure 203. Sample 4-3. Experiment line 4, third section in transient region. 176
Figure 204. Sample 4-4. Experiment line 4, fourth section in transient region. 176
Figure 205. Sample 4-5. Experiment line 4, fifth section in transient region. 176

Figure 206. Sample 4-6. Experiment line 4, sixth section in transient region. 177
Figure 207. Sample 4B. Experiment line 4, final steady state. 177
Figure 208. Sample 2RA. Experiment line 2R, initial steady state. 177
Figure 209. Sample 2R-1. Experiment line 2R, first section in transient region. 177
Figure 210. Sample 2R-2. Experiment line 2R, second section in transient region. 178
Figure 211. Sample 2R-3. Experiment line 2R, third section in transient region. 178
Figure 212. Sample 2R-4. Experiment line 2R, fourth section in transient region. 178
Figure 213. Sample 2R-5. Experiment line 2R, fifth section in transient region. 178
Figure 214. Sample 2R-6. Experiment line 2R, sixth section in transient region. 179
Figure 215. Sample 2RB. Experiment line 2R, final steady state. 179
Figure 216. Sample 4RA. Experiment line 4R, initial steady state. 179
Figure 217. Sample 4R-1. Experiment line 4R, first section in transient region. 179
Figure 218. Sample 4R-2. Experiment line 4R, second section in transient region. 180
Figure 219. Sample 4R-3. Experiment line 4R, third section in transient region. 180
Figure 220. Sample 4R-4. Experiment line 4R, fourth section in transient region. 180
Figure 221. Sample 4R-5. Experiment line 4R, fifth section in transient region. 180
Figure 222. Sample 4R-6. Experiment line 4R, sixth section in transient region. 181
Figure 223. Sample 4RB. Experiment line 4R, final steady state. 181
Figure 224. Experiment 1-1. Surface width measurement of line 1 on plate 1. 182
Figure 225. Experiment 1-2. Surface width measurement of line 1 on plate 1. 182
Figure 226. Experiment 1-9. Surface width measurement of line 9 on plate 1. 182
Figure 227. Experiment 1-10. Surface width measurement of line 10 on plate 1. 183
Figure 228. Experiment 1-11. Surface width measurement of line 11 on plate 1. 183

Figure 229. Experiment 1-12. Surface width measurement of line 12 on plate 1. 183
Figure 230. Experiment 1-13. Surface width measurement of line 13 on plate 1. 183
Figure 231. Experiment 1-14. Surface width measurement of line 14 on plate 1. 184
Figure 232. Experiment 2-1. Surface width measurement of line 1 on plate 2. 184
Figure 233. Experiment 2-2. Surface width measurement of line 1 on plate 2. 184
Figure 234. Experiment 2-9. Surface width measurement of line 9 on plate 2. 184
Figure 235. Experiment 2-10. Surface width measurement of line 10 on plate 2. 185
Figure 236. Experiment 2-11. Surface width measurement of line 11 on plate 2. 185
Figure 237. Experiment 2-12. Surface width measurement of line 12 on plate 2. 185
Figure 238. Experiment 2-13. Surface width measurement of line 13 on plate 2. 185
Figure 239. Experiment 2-14. Surface width measurement of line 14 on plate 2. 186
Figure 240. Sample 1-1A. Melt pool area measurement of plate 1, experiment line 1, initial steady state..... 186
Figure 241. Sample 1-1B. Melt pool area measurement of plate 1, experiment line 1, final steady state..... 186
Figure 242. Sample 1-2A. Melt pool area measurement of plate 1, experiment line 2, initial steady state..... 186
Figure 243. Sample 1-2B. Melt pool area measurement of plate 1, experiment line 2, final steady state..... 187
Figure 244. Sample 1-9A. Melt pool area measurement of plate 1, experiment line 9, initial steady state..... 187
Figure 245. Sample 1-9B. Melt pool area measurement of plate 1, experiment line 9, final steady state..... 187

Figure 246. Sample 1-10A. Melt pool area measurement of plate 1, experiment line 10, initial steady state..... 187
Figure 247. Sample 1-10B. Melt pool area measurement of plate 1, experiment line 10, final steady state..... 188
Figure 248. Sample 1-11A. Melt pool area measurement of plate 1, experiment line 11, initial steady state..... 188
Figure 249. Sample 1-11B. Melt pool area measurement of plate 1, experiment line 11, final steady state..... 188
Figure 250. Sample 1-12A. Melt pool area measurement of plate 1, experiment line 12, initial steady state..... 188
Figure 251. Sample 1-12B. Melt pool area measurement of plate 1, experiment line 12, final steady state..... 189
Figure 252. Sample 1-13A. Melt pool area measurement of plate 1, experiment line 13, initial steady state..... 189
Figure 253. Sample 1-13B. Melt pool area measurement of plate 1, experiment line 13, final steady state..... 189
Figure 254. Sample 1-14A. Melt pool area measurement of plate 1, experiment line 14, initial steady state..... 189
Figure 255. Sample 1-14B. Melt pool area measurement of plate 1, experiment line 14, final steady state..... 190

Nomenclature

A	≡	Maximum Melt Pool Area (measured perpendicular to travel velocity)
d	≡	Effective Depth (Depth determined by assuming a semicircular melt pool area)
d_1	≡	Initial steady state melt pool effective depth
d_2	≡	Final steady state melt pool effective depth
D	≡	Penetration depth
L	≡	Melt pool length (measured from the point of maximum area to the tail end of the melt pool)
L/d	≡	Length to depth ratio
L'	≡	Length of the melt pool measured from the heat source to the point of maximum area
t	≡	Wall thickness
t/d	≡	Ratio of wall thickness to effective depth
t/D	≡	Ratio of wall thickness to penetration depth

Chapter 1 Introduction

1.1 Additive Manufacturing

Additive Manufacturing (AM) is a layer additive process. In this process, a computer aided drawing (CAD) model of the part to be built is sliced into layers. Those layers are used by equipment as build instructions to add new material on a base substrate or previously added material. Metals, polymers, and ceramics can be used with an electron or laser beam as the heat source. For either case, the heat source creates a pool of melted material (the melt pool) that travels along the part to be built based on the movement of a positioning system and solidifies into a cross-section of the model. Added material can be in wire or powder form that is added directly to the melt pool, or powder can be spread across the build platform as a bed of material that is selectively melted. A schematic of a wire fed electron beam based system can be seen in Figure 1.

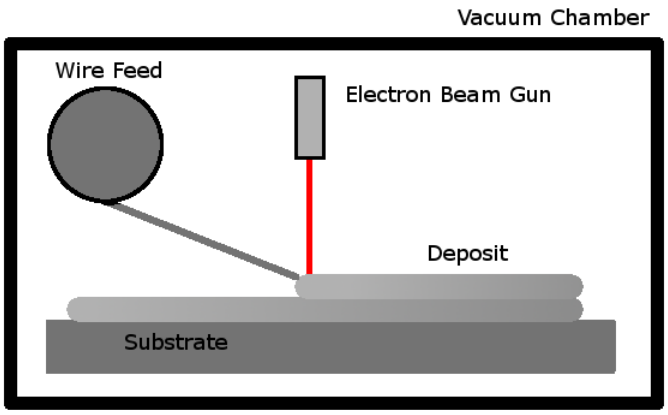

Figure 1. A schematic of wire fed electron beam based AM components [1].

Once a part has been built by successive layers, the part can be machined to remove excess material and smooth edges, as seen in Figure 2.

Figure 2. An example of a part built through AM prior to removing excess material (left) and after removing excess material (right).

1.1.1 Direct Metal Additive Manufacturing

AM or 3D printing are blanket terms that can apply to many systems that use metals, polymers, or ceramics and a more specific term for the metal portion of AM is Direct Metal Deposition or Direct Metal Additive Manufacturing. Under Direct Metal Additive Manufacturing, several systems exist, but they are divided by two main variables (power source and feedstock). Either an electron beam or a laser is used for the power source and feedstock can be in the form of powder or wire. This has led to four main categories: Electron Beam Wire Feed, which include NASA's Electron Beam Free Form Fabrication (EBF^3) and Sciaky; Electron Beam Powder Bed, which includes Arcam; Laser Powder Feed, which includes the LENS system; and Laser Powder Bed, which includes EOS and Renishaw, among others.

1.2 Motivation

AM processes have developed a great demand in the aerospace industry for both repair and production applications as well as in the medical and dental industry for custom implants. Reduced production and material costs (reduced waste), reduced development and lead time, and increased design flexibility make these very attractive

processes [1]. To help ensure process efficiency, accurate control of the process is required at high deposition rates (high beam power and travel velocity), when depositing fine geometries and features (low beam power and travel velocity), and transitions in between. As such, an understanding of the transient melt pool response and behavior across these extremes is of critical importance.

In this work, the response of melt pool dimensions to step changes in beam power and travel velocity is explored for single beads and thin walls as well as response due to changes in feature geometry (corner geometries). In an important development of this research, melt pool response is determined in terms of response distance rather than response time, allowing for the development of relationships that are not dependent on position or path taken in the Power-Velocity (P-V) Process Map but on initial and final steady state melt pool geometry.

Several factors were considered in choosing a focus for this research. Ti-6Al-4V is a desirable material in the aerospace industry due to its strength and corrosion resistance in high temperature applications [2]. There are also several advantages to electron beam systems over laser based systems including transfer efficiencies that are not a function of substrate reflectivity and the ability to deposit a wider range of material systems [3]. Wire feed systems are also less complex than powder systems as the powder adds additional variables that may need to be taken into account (powder density, distribution, and usage efficiency) [4]. Finally, and most importantly, in these processes anecdotal experimental observations of melt pool behavior have suggested a noticeable lag in the response of the melt pool to abrupt changes in thermal conditions. For these reasons, this work focuses

on Ti-6Al-4V deposition within a wire feed electron beam system. Knowledge gained from this system is then applied to the electron beam powder bed system.

1.3 Background

There are several advantages to the use of AM of metals over subtractive or formative methods. AM has the ability to manufacture more complex geometries (such as internal lattice structures or highly complex internal channels). It has reduced waste, lead time, and cost to manufacture, which is ideal for small batch part production and functional prototyping. Damaged parts can be repaired using AM and returned to service, lengthening part life cycles [5]. It is ideal for medical implants as custom implants can be made patient specific and can be built into a porous medium, which is better for bone growth [6–8].

Despite the advantages there exist areas of concern that inhibit the success and adoption of AM. The major areas of concern include residual stress, microstructure, geometric and melt pool size/shape control, evaporation of alloy components, and the relationship between build time and accuracy. While AM can reduce build time, it still can be difficult for it to compete with the speed of more traditional methods in large batch production [5]. Process mapping is a way to increase the speed of a build by extending the range of powers and velocities available for use [9]. Metal AM is often based on trial and error or has highly limited access to control machine parameters [5]. In many cases, machine operators find a combination of process variables that can build a part to their specifications and do not stray far from those variables. AM processes, however, span a large quantity of process variables, as seen in Figure 3 below. Process mapping allows for the increase of material feed rates when large quantities of material

can be deposited and decrease when fine features are being deposited, all while maintaining control of the process. This is accomplished through an understanding of output variables, such as melt pool size and shape, in terms of process variables that can be controlled directly by machine operators (beam power, travel velocity, preheat temperature, etc.) [9]. Work by Soylemez et al. [3] has created a process map for curves of constant melt pool cross sectional area and length-to-depth (L/d) ratios in a process space of 1-5 kW and 0-100 in/min for Ti-6Al-4V in EBAM processes. The process mapping approach has also been applied to multiple materials beyond Ti-6Al-4V including Stainless Steel [10], In718 [11], In625 [12], CoCr [9], and Aluminum Alloys [13]. Additionally, multiple patent filings [14,15] and the work by Beuth et al. [9] describe the process map approach and its use in multiple forms of AM.

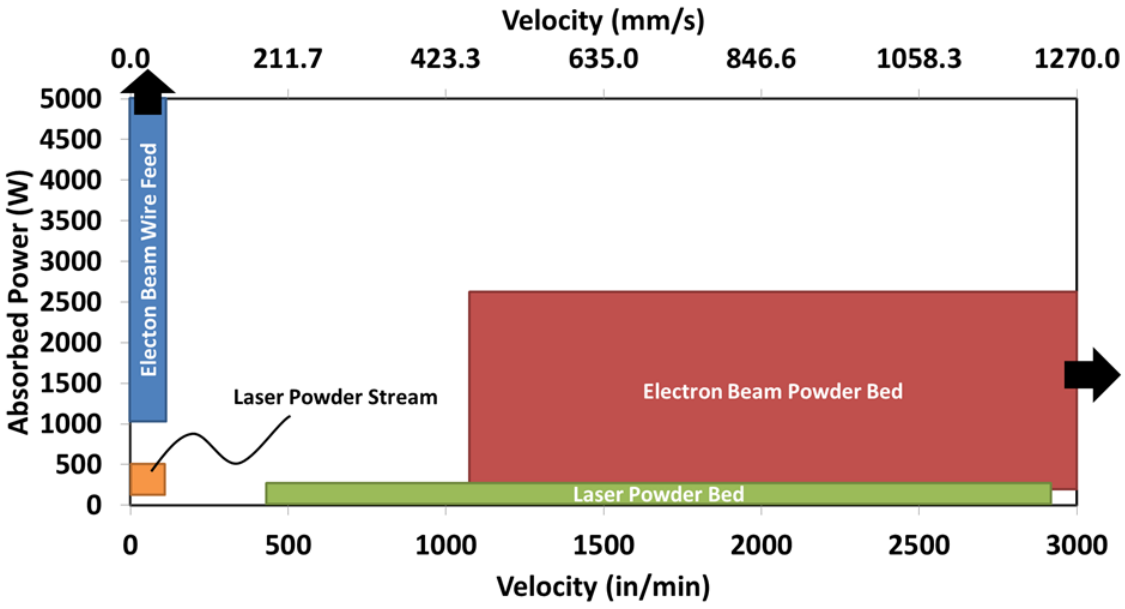

Figure 3. Power-Velocity (P-V) process space for additive manufacturing.

Modeling in additive manufacturing stems from analytical approaches originally developed by Rosenthal for welding applications in 1946 [16]. Dobranich and Dykhuizen

have detailed its use in the LENS system [17]. However, this approach has its limitations as it is unable to model complex geometries, temperature dependent properties, distributed heat sources, or other variables commonly seen in AM processes. Siegle and Goldstein discussed an analytical method for steady state heat transfer in 2D porous media [18], and in the mid 1980's, Goldak et al. adjusted the approach used by Rosenthal to include distributed power sources and investigated the use of FEA for modeling the moving heat source in welds [19,20]. Mundra et al. discussed the numerical prediction of fluid flow and heat transfer when welding with a moving heat source [21]. Westerberg et al. analyzed evaporation in electron beam melting of titanium and Ti-6Al-4V [22] and Barclay used parameter optimization to control the loss of aluminum in laser powder stream systems [23]. Nguyen et al. explores an analytical temperature solution for semi-infinite body with moving heat source [24]. Lee et al. investigated the influence of convection on weld pool formation in laser cladding [25]. Rai et al. investigated fluid flow during keyhole mode [26,27]. Mahrle and Schmidt investigated the influence of fluid flow in the fusion zone and the local temperature distribution [28]. In addition to these developments, Zacharia [29] and Lindgren [30] have summarized the advancement of modeling in the welding community.

The approaches developed for welding, however, lack the ability to model the scale, complexity, and thermal history associated with AM. In response to this, modeling based research in AM has also been accomplished. Han et al. used a three dimensional, physics based model to predict fluid flow and free surface effects in the LENS system [31]. Neela and De used three dimensional finite element simulations to investigate the influence of process parameters on melt pool dimensions, peak temperatures, and thermal cycles in

the LENS system [32]. Roberts et al. used three dimensional finite element models to simulate successive layers of deposition in laser powder bed based systems [33]. Shen et al. used finite element based thermal models to study the effect of preheating, powder porosity and beam spot size on the size of the melt pool in Electron Beam based AM [34,35]. Fachinotti et al. used finite element simulations to predict heat transfer and deposition shape in building thin walls with wire feed electron beam based AM [36]. Raghavan et al. investigated heat transfer and fluid flow in AM and suggested that closed loop control can benefit from mathematical modeling [37]. Hodge et al. developed thermo-mechanical models for investigation of the laser powder bed process [38]. Martukanitz et al. worked to integrate process modeling, coupled thermal-mechanical modeling, and microstructural modeling to describe key attributes of additive manufacturing [39] as well as developing physics based models to understand both heat and fluid flow within the melt pool [40,41].

Residual stress is a concern for AM as it can lead to part warping. While this can be taken care of through post process stress relief treatments, it remains an issue during the build process if not accounted for and can lead to failed builds. This is not a major concern for the Arcam process as the elevated temperatures facilitate controlled cooling and low thermal gradients to prevent residual stress. In the other processes, common practice is to include additional supports to prevent warping during the build, which can be removed once post process stress relief is complete [5]. While this may work for many scenarios, there are still situations where additional supports may be unwanted. The addition of supports increases material usage as well as post processing efforts to remove them. Various forms of process maps to understand laser based AM systems were

developed by Vasinonta et al. [42–44], by Beuth and Klingbeil [45], and by Vasinonta [46] for controlling steady state melt pool size and residual stress in thin-walled and bulky parts. Modeling of residual stress in metal and polymer deposition has also been studied in the work of Klingbeil et al. [47–49], Ong et al. [50], Mercelis and Kruth [51], and van Belle et al. [52].

Microstructure in laser and electron beam based processes has been studied in several works and is critical for determining part quality. Miller et al. and Mishra et al. have developed Monte Carlo simulations to determine grain growth and microstructure in welding and the LENS system respectively [53,54]. Microstructure evolution in laser based AM has been explored by Kobryn and Semiatin [55], who introduced solidification maps for use in AM, as well as Kelly and Kampe [56] and Zheng et al. [57]. Microstructure evolution has also been studied in electron beam based AM by Hrabe and Quinn [58,59]. Brandl and Greitemeier examined the effect of heat treatment on the microstructure and hardness of Ti-6Al-4V parts built in AM processes [60]. Vrancken et al. examined the effect of heat treatment on the relationship between microstructure and mechanical properties of Selective Laser Melted Ti-6Al-4V [61]. The microstructure and properties of Ti-6Al-4V in AM is detailed extensively by Alphons [62]. Bontha et al. [63,64] and Klingbeil et al. [65] developed process maps of cooling rates and thermal gradients to predict microstructure. Davis et al. [66] investigated the effect of free edges and process variables (beam power and travel velocity) on melt pool geometry and solidification microstructure (grain size and morphology). Doak investigated the microstructure evolution in Ti-6Al-4V below melting temperatures in electron beam based AM [67]. Gockel et al. identified links between melt pool geometry and

microstructure for single beads [68] as well as thin walls [69]. These links have also been extended to the electron beam powder bed (Arcam) system for single beads [70].

The link between melt pool size and microstructure has given added importance to the control of melt pool dimensions and it was also shown by Wang et al. that there is a strong dependence of melt pool size and cooling rate on beam power and velocity in LENS™ systems [71]. Thus, the reason for controlling melt pool size and shape is to allow a part to be built while maintaining consistent melt pool geometry, even as thermal conditions change. Control approaches have been developed for welding applications using imaging of the melt pool (thermal [72] and spectroscopic [73]), however, most control applications are governed by viewing the shape of the weld surface [74–77].

Extensive research covering thermal imaging and control in AM has been accomplished. Control schemes even go as far back as 1994 where the key control element is the powder temperature and the focal point of the beam in the laser powder bed system [78]. Hu et al. used infrared imaging in conjunction with powder delivery tracking to verify thermal finite element simulations of the LENS system and ensure build accuracy [79–81]. Wang et al. employed infrared imaging of the melt pool to validate thermal models of the LENS system [82]. Kruth et al. developed a feedback control system for the laser powder bed system based on a high speed CMOS camera and photodiode system calibrated experimentally to determine melt isotherms in the recorded image [83]. Tang et al. used thermal imaging in conjunction with displacement sensors for tracking build height to ensure a geometrically accurate build in the LENS system [84]. Song et al. investigated feedback control in laser powder feed systems [85], as well as feedback control of melt pool temperature and deposition height [86]. Rodriguez et al.

used infrared thermal images after each layer had been deposited in the electron beam powder bed (Arcam) system for layer by layer feedback to prevent defects, such as porosity [87]. Craeghs et al. used optical imaging of the melt pool to detect failures due to deformation and over-melting [88]. Rieder et al. used ultrasonic monitoring of the build platform to detect residual stress and porosity [89]. Zalameda et al. used near infrared thermal imaging to ensure weld quality in NASA's EBF^3 system [90]. Dinwiddie et al. created a system to use infrared thermal imaging in the Arcam system to capture data while the beam is running, not just between layers [91]. Krauss et al. used infrared thermal imaging to detect pores and other irregularities in the EOS M270 [92]. The National Institute of Standards and Technology are in the process of developing an infrared thermography system for laser based powder bed processes [93].

Given all of the advancements in thermal imaging and control, little research has been accomplished to quantify the transient response of the melt pool. The process map approach to controlling melt pool size and shape has been extended to consider transient conditions by Birnbaum et al. [94]. Work by Aggarangsi [95] characterized the transient response of melt pool size for AISI 304 Stainless Steel for small scale (<500W) Laser Engineered Net Shaping (LENS™) systems (laser powder feed). In this work, Aggarangsi found that for that process melt pool size response could be characterized by distance related to a combination of initial and final steady state melt pool area sizes. Additionally, Aggarangsi et al. explored the transient geometry of approaching and leaving a free edge in a thin wall [96]. Reeseewatt and Beuth explored the control of melt pool dimensions during the build of a thin wall [97]. Through a recent patent by Beuth and Fox, the process mapping approach has been generalized to determine transient

response in the building of 3-D shapes across all direct metal AM processes and related processes [98].

1.4 Organization

This thesis is divided into six chapters. The first chapter introduces additive manufacturing, the process mapping approach, and the benefits/concerns related to the technology. A literature review of research related to this topic is presented, as is the motivation behind the work carried out by this dissertation.

The second chapter introduces the process mapping approach for maintaining constant melt pool geometry of single beads in electron beam wire feed deposition of Ti-6Al-4V and how it is used to aid in the analysis of transient response. Three dimensional finite element models are developed and run in the ABAQUS software package and results are compared to no added material experiments (beam on plate only) as well as single bead of added material experiments. This chapter also explores the ratio of added material to total material melted (φ) and its effect on steady state melt pool geometry control.

The third chapter explores the effect of geometry on transient response. To accomplish this, two dimensional and three dimensional finite element simulations are developed and run in the ABAQUS software package. Results from these simulations are compared to thin wall added material experiments. Analysis of transient response is then extended to transient geometries by investigating how the size of the melt pool changes as the beam passes around an interior corner. This analysis is performed using three

dimensional finite element simulations, and a method for maintaining maximum melt pool depth through the corner is developed.

The fourth chapter extends the knowledge gained from the analysis of transient response in single bead deposition in an electron beam wire feed system to that of an electron beam powder bed system. Analysis is performed through three dimensional finite element simulations and those results are compared to no added material (beam on plate only) experiments.

The fifth chapter reviews preheat temperature, to determine their effect on transient response in thin walls. Assumptions made throughout the dissertation are explored to determine the extent of their effect on the results. 3D finite element simulations of a thin wall attached to a bulky substrate are compared to the 2D thin wall simulations presented. Single bead simulations with a rounded bead instead of the square bead used in the wire feed electron beam system are also analyzed to determine its effect on the results. Also, convection within the melt pool and surface radiation is explored.

Finally, the sixth chapter summarizes conclusions based on the contributions of this work and recommendations for future work are discussed.

Chapter 2 Transient Response in Single Beads

2.1 Process Map Approach

This analysis is rooted in the P-V Process Map for single bead geometry previously explored by Soylemez *et al.* [3], which spans beam powers of 1-5 kW and travel velocities of 0-100 in/min. In this work, melt pool area (*A*) was determined on the plane whose normal is the beam travel direction (the x-direction) at the point of maximum area, seen in Figure 4 (left). Melt pool length (*L*) was measured from the point of maximum area to the tail end of the melt pool, seen in Figure 4 (right). The depth measurements (*d*) presented in this work are effective depths, determined by assuming the maximum cross sectional area to be semicircular with a radius equal to depth. This is not to be confused with penetration depth (*D*), which is used in later analysis and is the maximum vertical distance (in the y-direction) measured from the top of the added material (or plate when no material is added) that the melt pool penetrates into the existing substrate material.

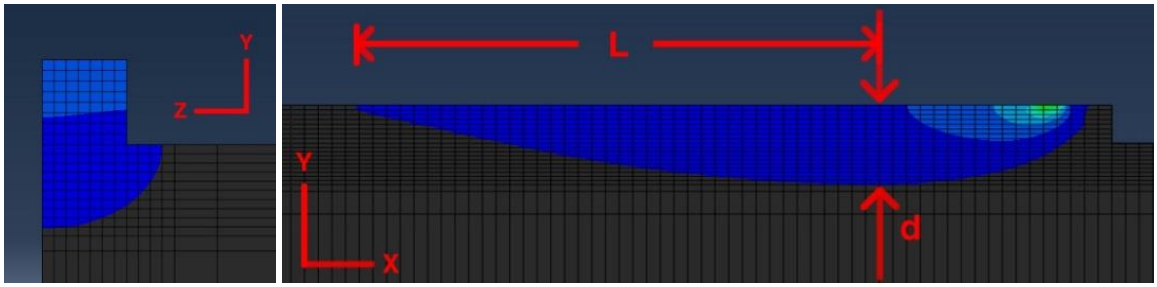

Figure 4. The maximum area of the melt pool as seen from a cut view of the model (left) and the melt pool length (right).

The P-V Process Map containing curves of constant area and length to depth ratio (*L/d*) determined by Soylemez et al. [3] is presented in Figure 5, below. Curves of constant area are represented by solid curves of green, red, and blue (0.063 in^2, 0.031 in^2,

and 0.016 in^2 respectively). Curves of constant *L/d* are represented by dashed curves of dark blue, light blue, and orange (4, 6, and 8 respectively).

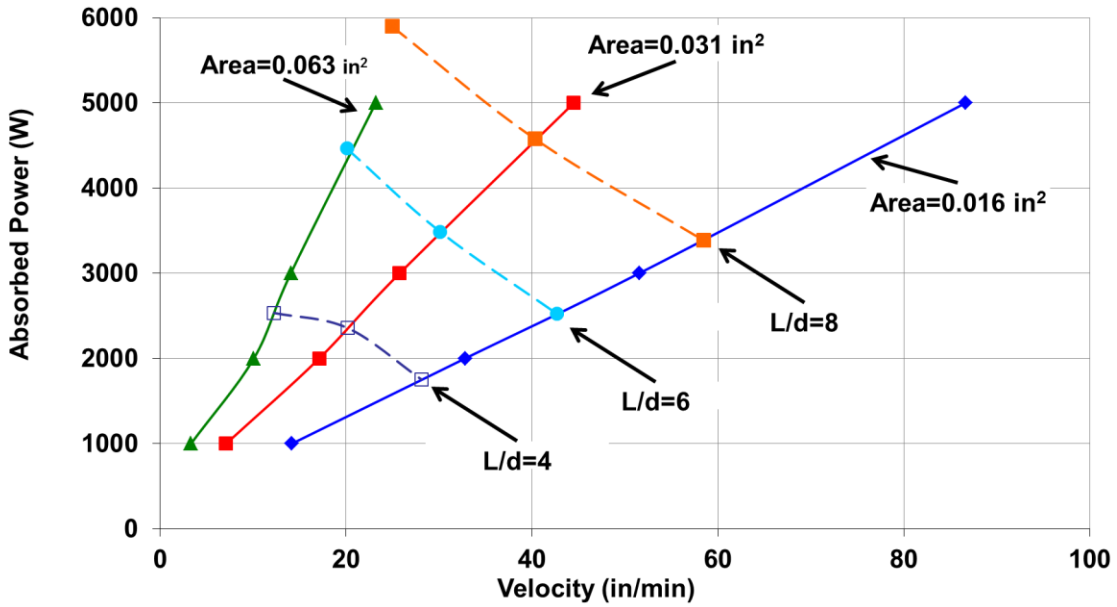

Figure 5. P-V Process Map for a single bead of added material in wire feed electron beam based processes.

The transient melt pool response can be analyzed by selecting multiple step changes in P-V process parameters. Instead of selecting arbitrary changes in power or velocity, the P-V process map can be used to make intelligent parameter selections such that the steady state melt pool areas remain constant. This will enable the dependence of transient melt pool response on the initial and final steady state melt pool geometry to be determined, and is analogous to the work of Aggarangsi [95]. The work presented here will extend theories of Aggarangsi [95] into the process space defined by Soylemez *et al.* [3] for Ti-6Al-4V through 3D added material finite element simulations and experiments of step changes in beam power or beam travel velocity.

In this work, response time refers to as the time immediately following the process parameter step change for the melt pool to reach 90% of the difference between

the initial and final steady state depth values. Response distance refers to the distance from the initial steady state point of melt pool depth to 90% of the difference between the initial and final steady state depth values.

2.2 Single Bead Finite Element Analysis

2.2.1 Material Added Finite Element Models:

The numerical models presented in this chapter were developed to be run in the ABAQUS™ software package. Three-dimensional finite element simulations have been performed with these models to replicate single bead deposition. The simulations begin with all elements of the model defined and elements representing added material are deactivated. At each step, bead material is reactivated three elements ahead of the heat source. This allows for modeling of the material being added and some heat conduction into the wire being fed into the system. The models have an initial temperature throughout and a constant base temperature that are dependent on the preheating of the system (room temperature for the wire fed electron beam based process). The models include latent heat as well as temperature dependent properties (density, specific heat, and thermal conductivity). Since the electron beam based processes are performed in a vacuum, the simulations do not model convection of heat from the outer surfaces. Simulations also do not include convection within the melted region of the model or losses due to radiation. Prior work by Sandia National Laboratories has performed thermal calculations to determine what phenomena may be of interest in the laser powder bed system. Surface radiation, forced convection, evaporative cooling, powder heating, powder flux particle melting, superheat at the center of the melt pool surface, and marangoni flow within the melt pool were included in this work. Findings from this

research determined that these effects are negligible when compared to conduction through the substrate [17]. Additionally, a review of surface radiation and convection within the melt pool is presented in Chapter 5.

The models are symmetric along the X-Y face pointing in the positive Z-direction, as seen in Figure 6. They are biased toward the region where material is being added as well as toward the center of the model in the X direction (region of interest) to reduce computation time. The biased region is sufficiently long to allow the melt pool to reach an initial steady state, induce a step change in beam power or travel velocity, and then reach a new steady state. The models are sufficiently tall, wide, and long to ensure no edge effects are seen in the melt pool. A distributed heat flux is applied to the top surface of the added material to represent the electron beam and mimic rapid oscillation of the beam across the melt pool. The direction of beam travel is in the positive X-direction.

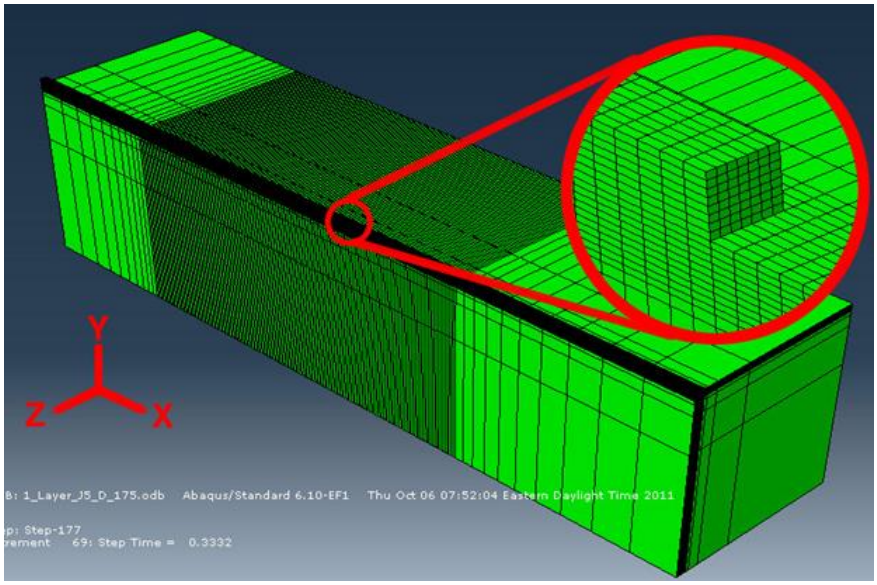

Figure 6. A representative 3D model for finite element simulation using ABAQUS software.

Consistent with prior analysis, melt pool area is determined at the point of maximum area perpendicular to the beam travel velocity, depth is the effective depth assuming a semicircular melt pool area, and length is the distance between the point of maximum area and the tail end of the melt pool (see section 2.1 and Figure 4).

2.2.2 Simulation Results

The analysis plan is detailed in Figure 7 and Table 1. Step changes in power at constant velocity are represented by vertical dashed lines and step changes in velocity at constant power are represented by horizontal solid yellow and purple lines. These step changes were chosen to cover the full process space (range of beam powers and travel speeds used in the process) and move only between the curves of constant melt pool area. All step changes end on points on the red constant area curve. Lines numbered 1, 3, 5, and 7 are step changes that start on the green curve of constant area and decrease in area through decreases in power or increases in velocity to a point on the red curve of constant area (Green to Red step changes). Lines numbered 2, 4, 6, and 8 are step changes that start on the blue curve of constant area and increase in area through increases in power or decreases in velocity to a point on the red curve of constant area (Blue to Red step changes). Lines numbered 1 through 6 are step changes in power at constant velocity and lines numbered 7 and 8 are step changes in velocity at constant power.

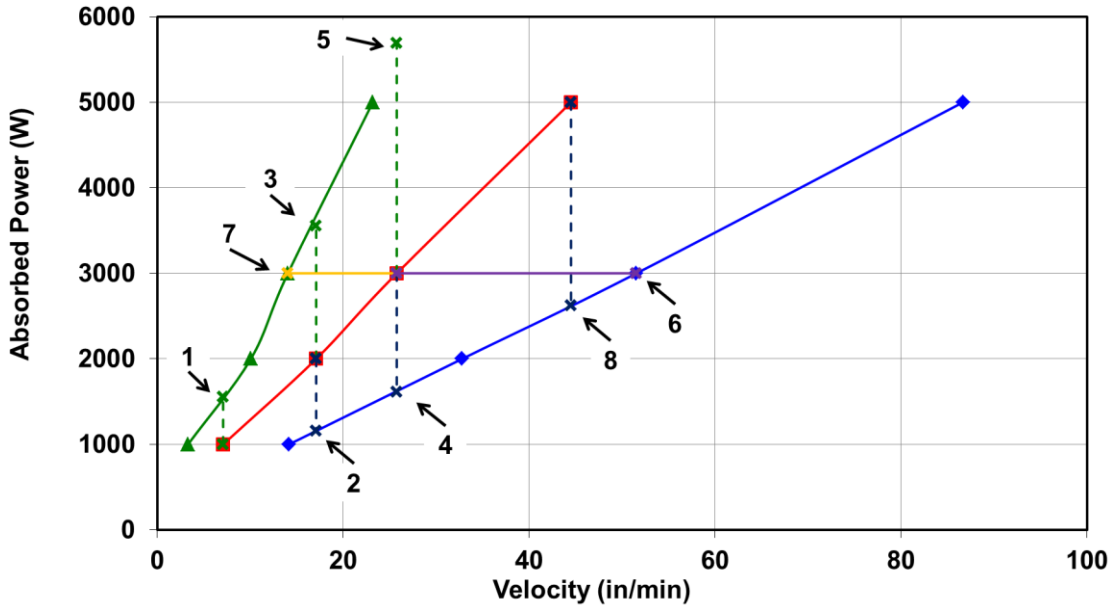

Figure 7. Analysis plan for transient response to step changes in power or velocity.

Table 1. Analysis plan for transient response to step changes in power or velocity. Power presented is absorbed power.

Run #	Starting Power (W)	Final Power (W)	Starting Velocity (in/min)	Final Velocity (in/min)
1	1559	1000	7.1	7.1
2	1157	2000	17.1	17.1
3	3555	2000	17.1	17.1
4	1614	3000	25.8	25.8
5	5693	3000	25.8	25.8
6	2625	5000	44.5	44.5
7	3000	3000	14.0	25.8
8	3000	3000	51.5	25.8

Response times and distances are listed in Table 2. For the response times, there is no clear trend in the values and the times are on the order of seconds. This would represent the limiting factor in a feedback control system as the response times are orders of magnitude longer than the time required for a control system to perform a change in process variables. Response distances, however, group together closely for step changes

with matching initial and final steady state melt pool effective depths. Also, the response distances for the Blue to Red step changes are much shorter than the response distances for Green to Red step changes.

Table 2. Response times and response distances from 3D finite element simulations.

	Run #	Initial Width (in)	Final Width (in)	Response Time (s)	Response Distance (in)
Green to Red	1	0.38	0.30	4.0	0.57
	3	0.40	0.30	2.1	0.63
	5	0.41	0.29	1.7	0.64
	7	0.41	0.29	2.0	0.66
Blue to Red	2	0.21	0.28	1.6	0.40
	4	0.21	0.29	1.1	0.43
	6	0.21	0.29	0.75	0.38
	8	0.21	0.29	1.2	0.45

The correlation seen in response distances can also be seen in Figure 8, which shows the melt pool effective depths as they transition from an initial steady state to a final steady state. The data presented in this figure are representative of the maximum melt pool area achieved at each value of *x*. This is equivalent to sectioning an experiment plate perpendicular to the travel velocity to view the extent to which the plate was melted. In Figure 8, some variation from the expected initial and final steady state melt pool depths can be seen and is due to the size of the added material. This effect will be discussed in detail later in this chapter. Regardless of this variation, it is apparent that step changes with matching initial and final steady state melt pool effective depths respond similarly as they transition. The explanation for this behavior is that the melt pool must move a certain *distance* after an abrupt change in beam power or beam velocity to achieve a new steady-state depth and that distance is largely governed by the

initial and final melt pool sizes (melt pool depths or cross sectional areas), regardless of the initial and final power and velocity values.

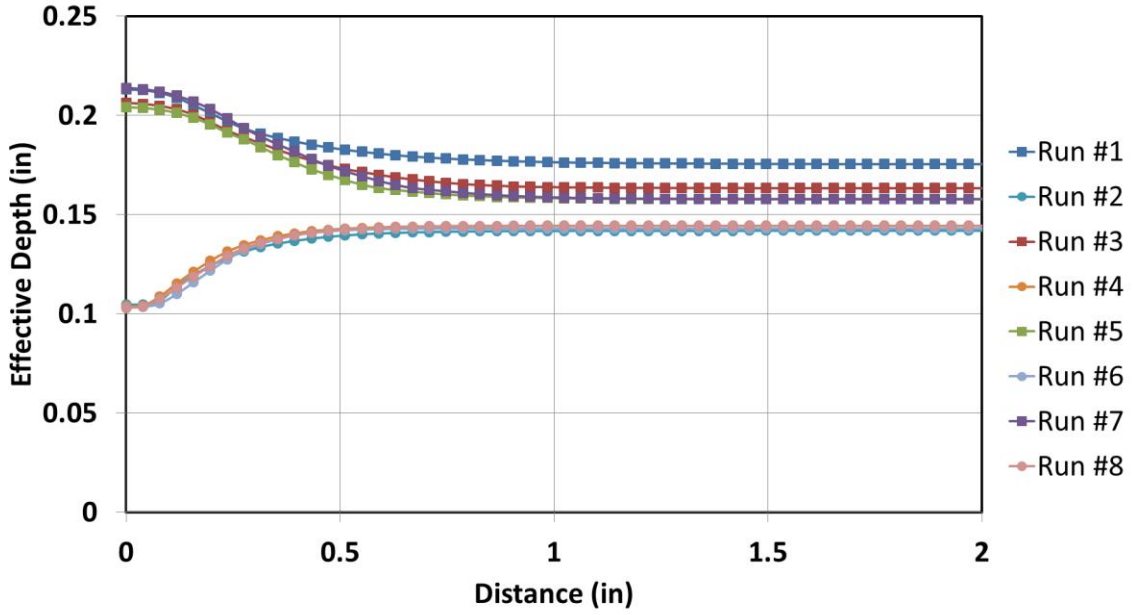

Figure 8. Response behavior for step changes in beam power or travel velocity.

2.3 Experiments

2.3.1 No Material Added Experiments

Initial experiments presented were performed at the NASA Langley Research Center. The equipment used was the EBF^3 process developed at NASA Langley. The experiments did not add material (beam on plate only) and used the power and velocity combinations presented for Green to Red and Blue to Red transitions simulations. Tests were performed on a 6 in × 12 in × 0.25 in plate with a distance of approximately 0.75 in from each edge and 0.65 in between each experiment line. Tests ran for 5.25 in at the initial power and velocity and 5.25 in at the final power and velocity to ensure the melt pool had an adequate distance to reach steady state prior to and following the step change in power or velocity.

Two sets of experiments were performed and the result is presented in Figure 9, below. The left plate in Figure 9 contains experiments in which the plate was allowed to return to room temperature between each of the eight experiment lines (Cool Down experiments). The right plate in Figure 9 contains experiments that were run in rapid succession (Rapid experiments).

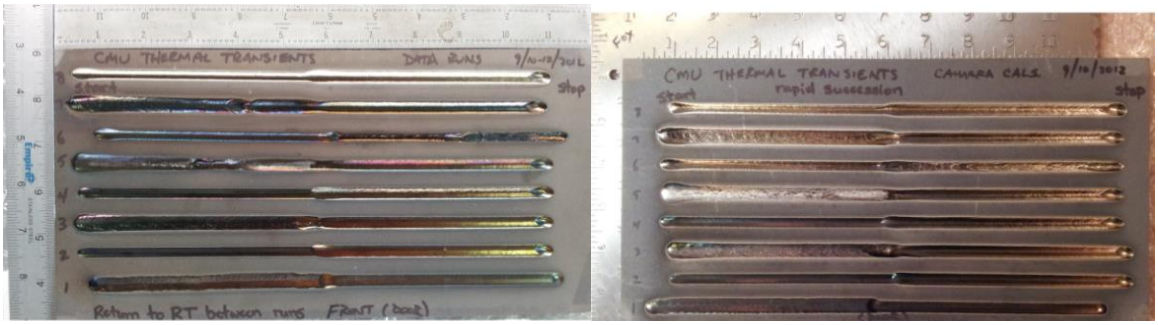

Figure 9. Experiments performed at NASA Langley Research Center.

An initial, qualitative comparison of the expected bead width based from simulation results and some of the experiments can be seen in Figure 10. Images a) through d) correspond to experiment runs 1, 2, 4, and 8 on the plate for Cool Down experiments and images e) and f) correspond to runs 1 and 2 on the plate for Rapid experiments. Other experiment lines (3, 5, 6, and 7 on the Cool Down plate and 3 through 8 on the Rapid plate) are not included in the continued analysis because the beam was able to fully penetrate the titanium plate. This penetration was due to several factors. Analysis of successful experiment lines later in this chapter shows the presence of keyholing, which would contribute to the penetration of the experiment plate if present in the unsuccessful passes. In addition to this, thermocouples placed under the plate that insulated it from the stainless steel protection plate and table (simulations assume that the table acts as a heat sink) as well as insufficient plate thickness contributed to the

penetration of the plates. However, from the review of successful passes, it is clear that the predicted melt pool width and the response distance match well with the experiment results in Figure 10, below.

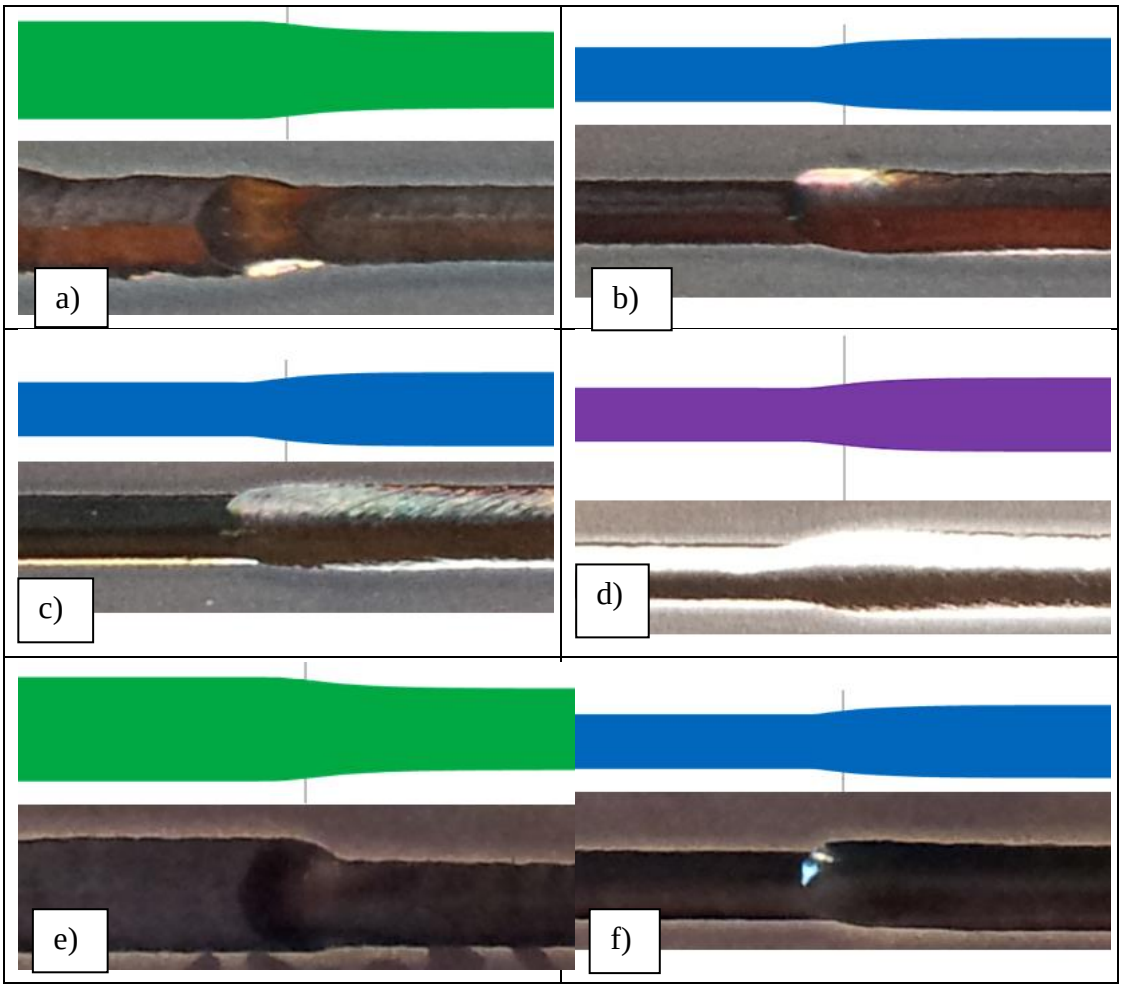

Figure 10. Comparison of melt pool widths seen in simulations versus experiments.

In addition to the qualitative analysis, quantitative review of surface widths can be seen in Table 3 below. Note that experiment runs 5 and 6 fully penetrated the plate leaving the response distance unmeasurable from surface widths. Initial and final steady state width show good agreement with previously determined results [3] as well as expected results from simulations, however, response distances are much shorter than expected in several cases. Because the response distance is determined from surface

width, the measured response distance can be affected by the movement of material on the surface of the plate. From images b), c), d), and f) in Figure 10, it is apparent that some of the material is pushed back and is on top of the previously solidified bead near the transition. Therefore sectioning of the experiment lines for a more detailed examination of the experiments was required to confirm the results.

Table 3. Experimental results based on surface width for Cool Down and Rapid plates.

		Cool Down Experiments			Rapid Experiments		
	Run #	Initial Width (in)	Final Width (in)	Response Distance (in)	Initial Width (in)	Final Width (in)	Response Distance (in)
Green to Red	1	0.32	0.25	0.44	0.36	0.27	0.23
Blue to Red	2	0.21	0.25	0.13	0.23	0.29	0.18
	4	0.22	0.26	0.13	*	*	*
	8	0.19	0.25	0.14	*	*	*

In addition to surface width measurements, the experiment plates were sectioned, polished, and etched to measure melt pool area through the transition region. Experiment lines can either be sectioned perpendicular to travel velocity to determine the melt pool area or sectioned down the center of the experiment line to determine melt pool depth. Experiment lines 2 and 8 from the Cool Down plate and line 1 from the Rapid plate were sectioned perpendicular to travel velocity to measure melt pool area. Experiment line 2 from the rapid plate was sectioned parallel to travel velocity to measure melt pool depth. Unfortunately, samples from experiment line 1 and 4 on the Cool Down plate were improperly cut, making it impossible to prepare the sample for melt pool measurements and so those experiment lines are excluded from the following analysis.

Examples of both of sectioning methods are shown in Figure 11 below, which is an analysis of Experiment run 2 on the Rapid plate. The top two images in Figure 11 are sections perpendicular to the direction of beam travel for the initial (left) and final (right) steady state melt pool and the bottom image is the top and side view of a section parallel to the direction of beam travel down the experiment line. ImageJ image processing software was used to measure melt pool widths on the surface of the plate, melt pool areas of sectioned samples, and actual (not effective) melt pool depth in the case of Rapid experiment run 2. It should be noted that it can be difficult to determine the melt pool boundary from looking at the microstructure in polished samples. This is because the beta transus temperature is much lower than the melting temperature and therefore microstructural transformation also occurring in the Heat Affected Zone (HAZ). The HAZ is the first guide for determining melt pool boundary, as it is the outer clear line seen in Figure 11. Additionally, the point where the surface begins to deform can be seen in most cases. From this a line is drawn that is qualitatively perpendicular to grain growth in order to determine the boundary of the melt pool. All images used for measurements can be found in Appendix A.

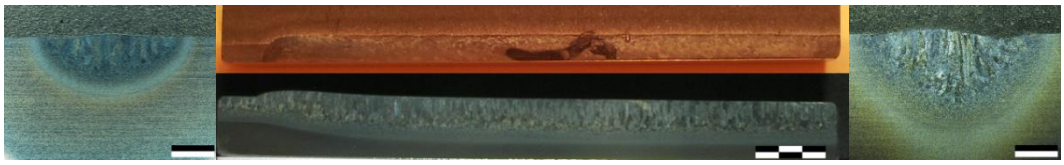

Figure 11. Sectioned and polished images from Rapid experiment run 2. Each black/white scale bar section measures 7.87E-2in (2mm).

Figure 12 through Figure 14 show the comparison of the measured results of the experiments to the results of 3D finite element simulations for both the Rapid and Cool Down plates. Slight variability in measurements from experimental data is due to the

limited resolution of the images and difficulty discerning the exact boundary of the melt pool. In the case of experiment line 8 from the Cool Down plate, the effective depth measurements are much higher than expected. It is suspected that the keyhole effect seen in the polished experiment samples, insufficient plate thickness, insulation due to thermocouples being placed under the plate, or a combination of these effects is responsible for this increase in effective depth. Regardless of these issues, it is apparent from the graphs presented in Figure 12 through Figure 14 that the expected melt pool effective depth as well as the melt pool response behavior in the experiments closely matches that seen in the simulations. These findings help validate the results of the finite element simulations and the premise that melt pool depth response distance is dependent on initial and final melt pool depth and not on position or path taken through the P-V Process Space.

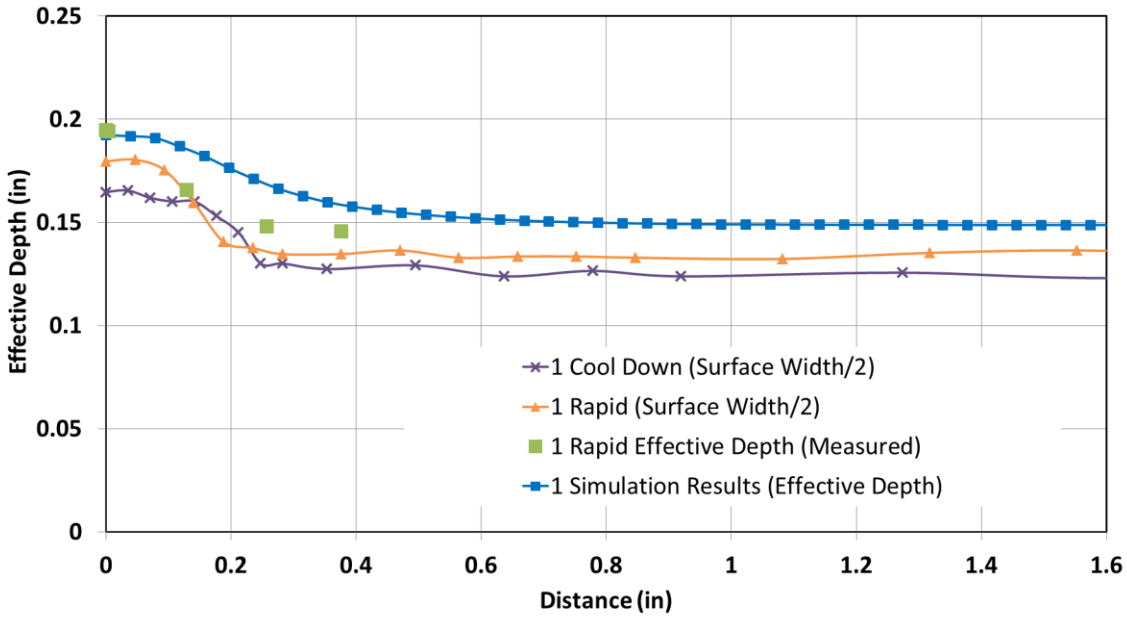

Figure 12. Comparison of results from experiment line #1 to simulation results.

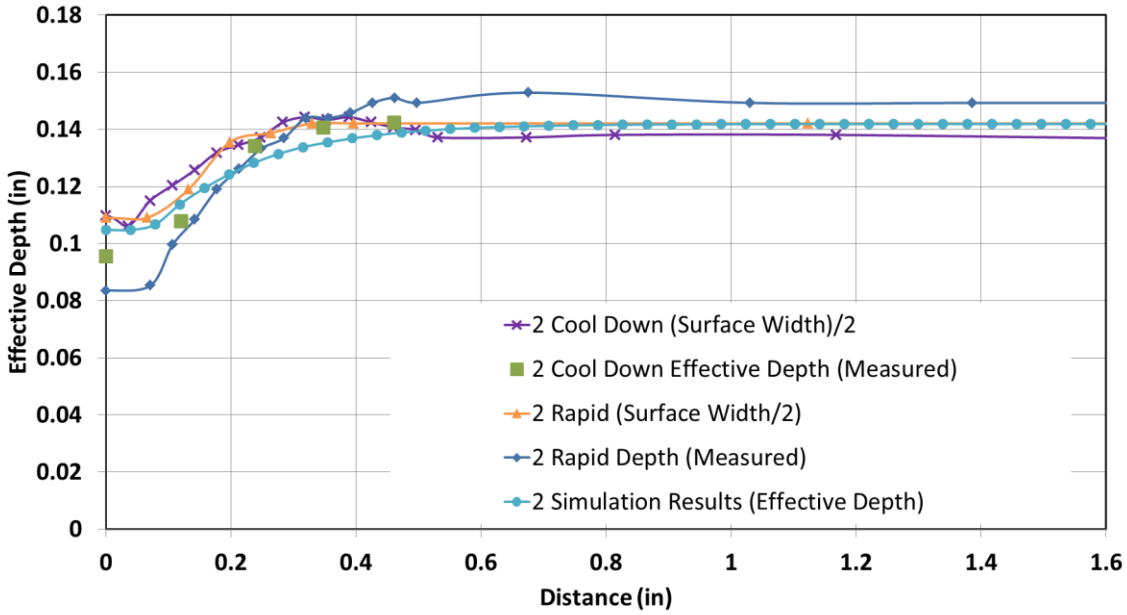

Figure 13. Comparison of results from experiment line #2 to simulation results.

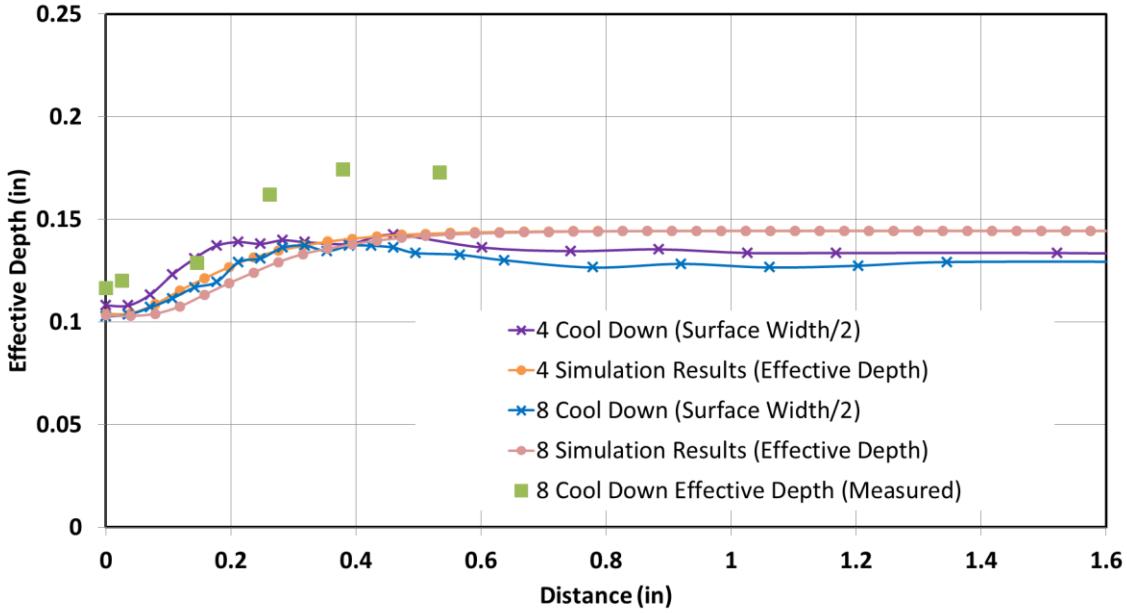

Figure 14. Comparison of results from experiment line #4 and #8 to simulation results.

2.3.2 Material Added Experiments

In addition to the experiments with no added material (beam on plate only) presented in the previous subsection, experiments with added material were also performed. These single bead experiments are an extension of the previous "No Added Material"

simulations (see Figure 7). Again, all step changes start on a point on the blue or green curves of constant area and end on a point on the red curve of constant area. Vertical green and blue lines represent power decreases and increases with constant velocity, respectively. Horizontal purple and yellow lines represent velocity decreases and increases with constant power, respectively.

Experiments were performed on three 7 in × 12 in × 0.5 in plates (the increased size of the plate is due to lessons learned from the no material added experiments in the previous section). Each experiment line ran for 5.25 in at the initial power and velocity and 5.25 in at the final power and velocity settings. Details of process variables for the single bead experiments are listed in Table 4. Beam power settings in the table assume an absorptivity of the substrate of 0.9 (chosen based on discussions with researchers at NASA Langley), so they are equal to absorbed powers in the plot of Figure 7 divided by 0.9. Wire feed rates are also included and assume a 0.063 in diameter wire and beam widths (perpendicular to travel direction) are included for determining beam oscillation. For both step changes that increase and decrease melt pool area, the wire feed rate is chosen to ensure a bead size that is properly melted throughout the experiment. Note that the wire feed rate is held constant during each pass to avoid complications in the experiments. For constant velocity experiments (Run #1 through #6), the wire feed rate is held constant at the smaller of the two bead sizes to ensure proper melting at both initial and final power settings. For constant power experiments (Run #7 and #8), the wire feed rate is chosen to give a bead size appropriate for the Red curve of constant area at the final velocity. Although the wire feed rate is held constant, the initial velocity

setting in each case will change the size of the bead, but still allow the bead and substrate to be properly melted.

In addition to the eight planned experiment lines, four additional experiments were run based on the initial analysis (also included in Table 4). Experiments 9 through 12 are a repeat of 1 but with material feed rate that changes at the step change in process parameters, a repeat of 2, a repeat of 4 with changing material feed rate, and a repeat of 8. The reason 1 and 4 were repeated with a changing material feed rate was because initial discussions led the thought that changing the material feed rate would cause added and unnecessary variables to the analysis. Since experiment lines 1 and 4 were well behaved, the repeat was an attempt to determine if changing material feed rate would create unexpected results. Experiment lines 2 and 8 were repeated because the surface was not well behaved and large quantities of material were ejected while the experiment ran. Thus, the repeat was to determine if the behavior was simply a fluke error in the build or if that should be expected from the chosen parameter sets. Results of the experiments can be seen in Figure 15.

Table 4. Experiment process variables for single bead tests.

Run #	Starting Power Setting (W)	Final Power Setting (W)	Starting Velocity (in/min)	Final Velocity (in/min)	Wire Feed Rate (in/min)	Beam Width (in)
1	1732	1111	7.1	7.1	55	0.22
2	1286	2222	17.1	17.1	67	0.16
3	3950	2222	17.1	17.1	132	0.22
4	1793	3333	25.8	25.8	101	0.16
5	6326	3333	25.8	25.8	200	0.22
6	2917	5556	44.5	44.5	174	0.16
7	3333	3333	14.1	25.8	200	0.22
8	3333	3333	51.5	25.8	200	0.16
9	1732	1111	7.1	7.1	110 to 55	0.22
10	1286	2222	17.1	17.1	67	0.16
11	1793	3333	25.8	25.8	101 to 202	0.16
12	3333	3333	51.5	25.8	200	0.16

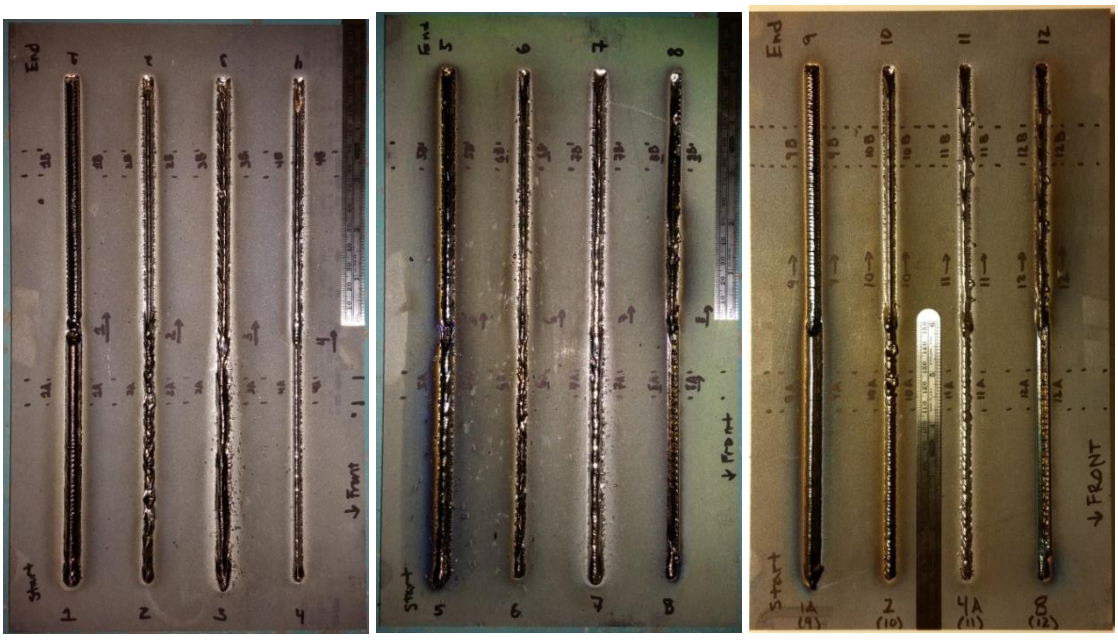

Figure 15. Experiment plates for single bead deposition.

Analysis of surface widths has been performed and is presented in Figure 16 through Figure 19. In these figures, the average melt pool effective depth is compared to half of

the surface width. Although there are variations in the surface width (due to splattering at the edge of the added material) the values are close to expected. This is an important finding as many of the samples show extensive keyholing, which will be seen in later analysis. This confirms that while keyholing has a large effect on penetration depth, it has little effect on the melt pool surface width. An effect that has been expected, but not yet verified by experimental results for the wire feed electron beam based systems.

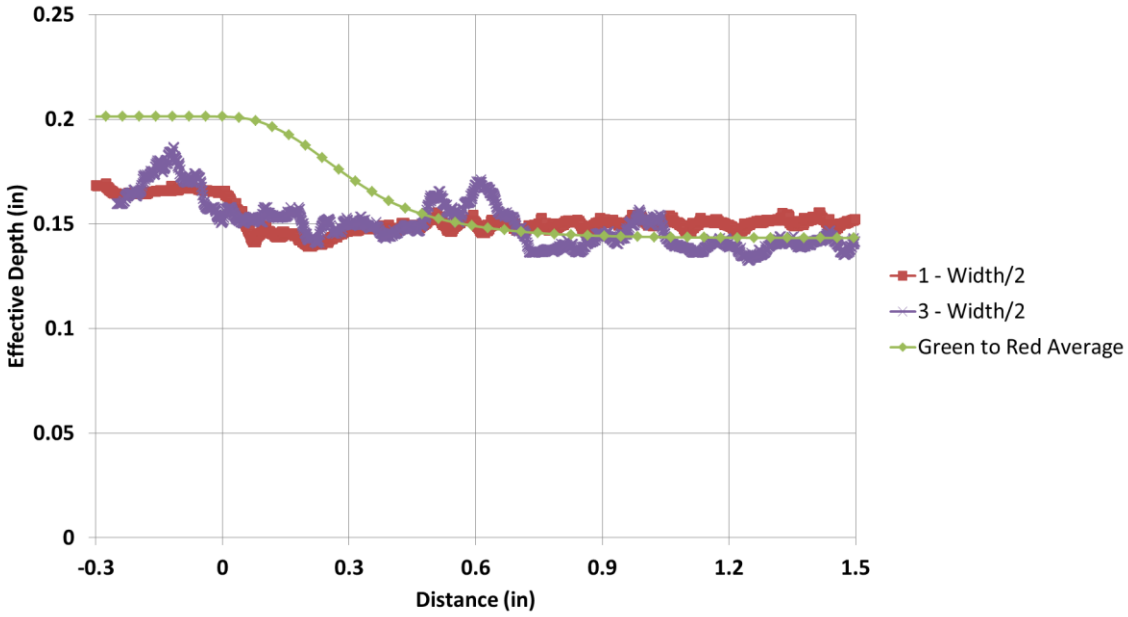

Figure 16. Comparison of surface width for experiment lines 1 and 3 to the effective depth from simulations.

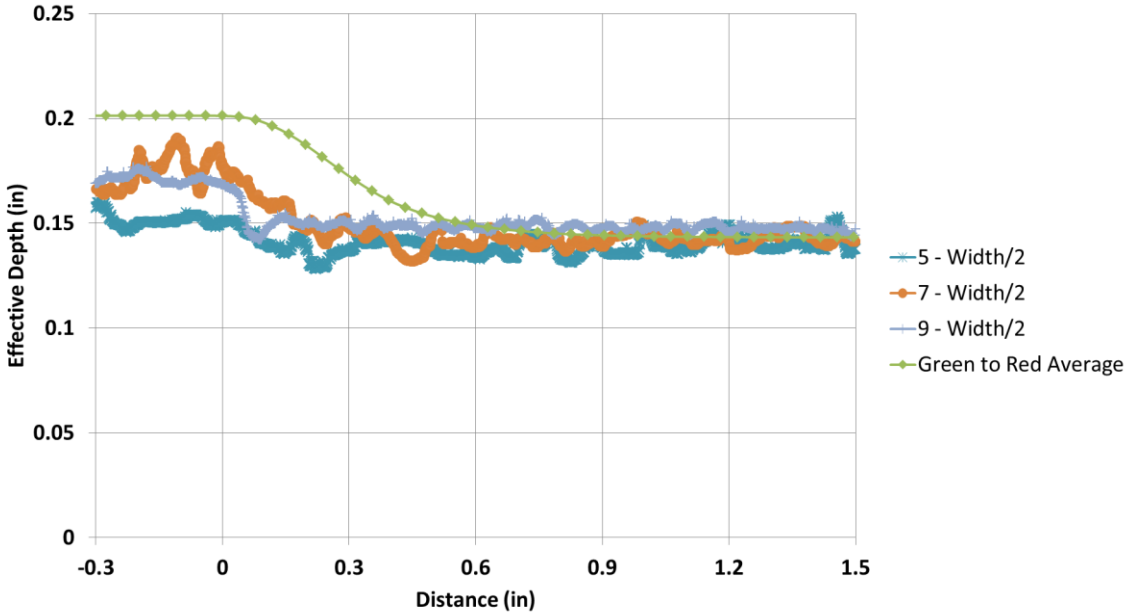

Figure 17. Comparison of surface width for experiment lines 5, 7, and 9 to the effective depth from simulations.

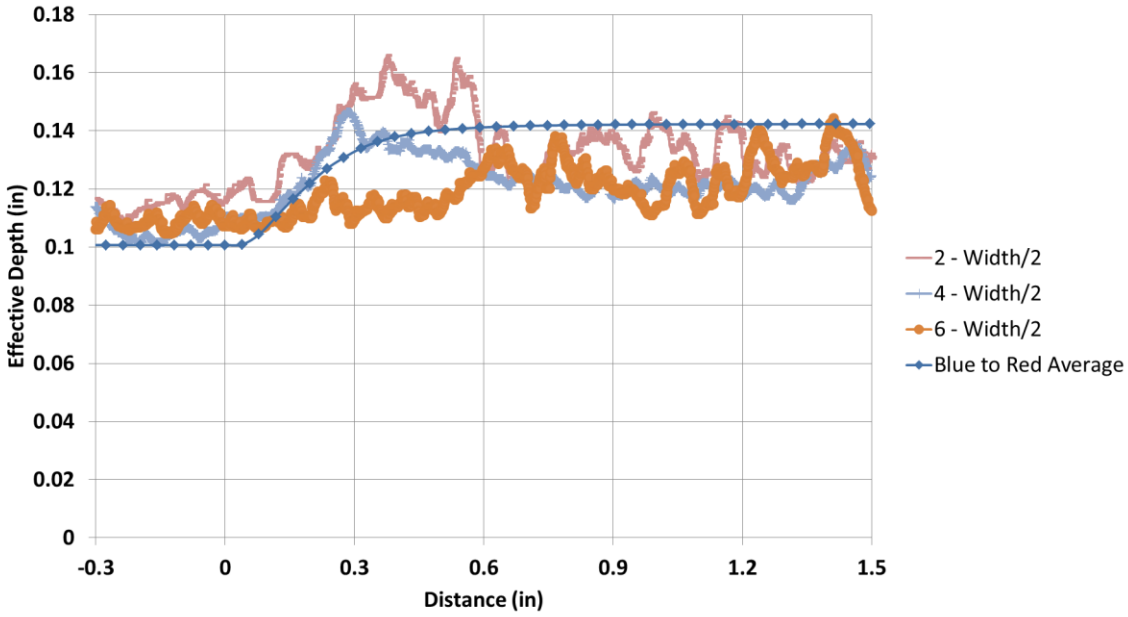

Figure 18. Comparison of surface width for experiment lines 2, 4, and 6 to the effective depth from simulations.

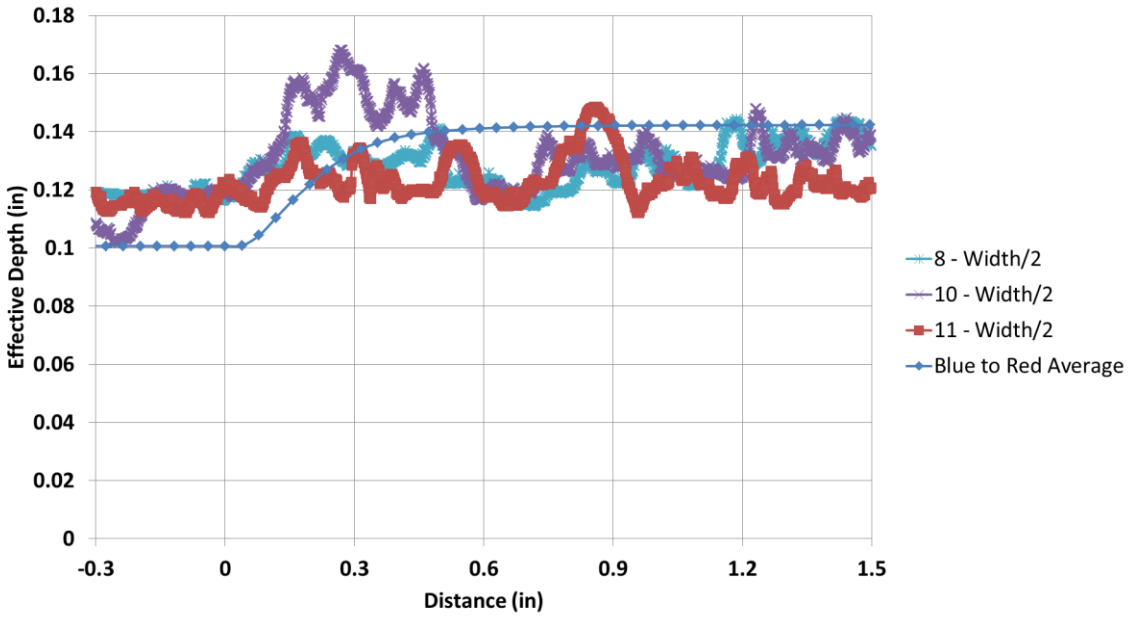

Figure 19. Comparison of surface width for experiment lines 8, 10, and 11 to the effective depth from simulations.

Determination of response distances through analysis of the surface has proven difficult, therefore, experiment plates have been sectioned and polished to determine the extent to which the melt pool penetrates the surface. From these polished sections, melt pool areas and the depth of penetration can be determined. Initial and final steady state values were analyzed first to determine the appropriate method for sectioning. All steady state portions were sectioned such that the surface perpendicular to beam travel could be polished and the melt pool area could be determined. An example of this method of sectioning can be seen in Figure 20, below. In this figure, the left most image is the polished section, the center image is the HAZ, and the right most image is the melt pool boundary. The same methods for determining the melt pool boundary in the no added material experiments was used in this analysis. Measurements, however, were made using Matlab's bwarea() function to measure area from the white pixels of binary images

similar to the center and right most images in Figure 20. All polished steady state samples from this analysis are included in Appendix A.

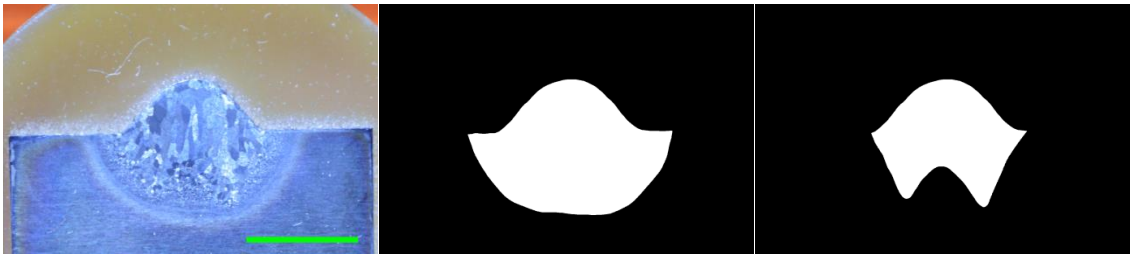

Figure 20. Example cross section from analysis of steady state values (Experiment 1, Initial Steady State). Green scale bar is 0.25 in.

The analysis of the steady state areas can be seen in Table 5 and the steady state melt pool areas presented are close to or slightly larger than the expected value. In the analysis of the steady state samples, keyholing was seen in several of the cross sections. While this this isn't always an indication that the melt poola area will be larger than expected, it appears that melt pools that are larger than expected are the ones that have two keyholes (left and right of the center of the melt pool). The rational for this is that with a single keyhole in the center of the melt pool, the high energy density required to create the keyhole causes large peak temperatures, deep beam penetration, and vaporization of material. With the two keyholes that are slightly separated, lower peak temperatures are expected, lower vaporization of material, and the substrate material is raised to the melting temperature in a more optimized fashion. This effect was also seen in work by Qiao and Beuth where they looked at the change in melt pool size in relation to distance from the free edge [99]. Since the free edge boundary is insulated, this would be equivalent to a line of symmetry where the free edge is actually the center of a large substrate and the heat sources are approaching from both sides of the line of symmetry. Although not discussed in the paper, increases in melt pool area were seen as the heat

source approached the free edge and then decreased to the expected value once on the free edge. This creates a very similar situation to the melt pools where two keyholes are seen in the melt pool and explains the larger melt pool areas seen in the experiments.

Table 5. Comparisons of steady state melt pool areas from simulations to experimental measurements.

	Initial Steady State		Final Steady State	
	Expected Area (in^2)	Melted (in^2)	Expected Area (in^2)	Melted (in^2)
1	0.058	0.059	0.035	0.034
2	0.017	0.020	0.032	0.043
3	0.064	0.076	0.034	0.039
4	0.017	0.020	0.033	0.033
5	0.065	0.078	0.034	0.038
6	0.017	0.021	0.032	0.041
7	0.067	0.075	0.034	0.041
8	0.017	0.021	0.033	0.036
9	0.058	0.066	0.035	0.036
10	0.017	0.022	0.032	0.037
11	0.017	0.022	0.033	0.038
12	0.017	0.021	0.033	0.043

Due to the keyholing present in many of the samples, it was decided that the best method to analyze the transient response would be to look at cross sections that are perpendicular to the travel velocity (the same style as the steady state cross sections) at several points through the transition. For experiment lines 1, 9, and 10, however, the steady state melt pool penetration into the substrate was much more circular. So for those experiments, the samples were cut down the center of the bead (parallel to travel velocity) to view the melt pool depth. Examples of this type of sectioning can be seen in Figure 21 and images of all polished samples from this analysis are included in Appendix A. In these images, beam travel direction is from left to right and each contain three red

lines. The top red line is the top of the bead, the middle red line is the melt boundary, and the bottom red line is the HAZ boundary.

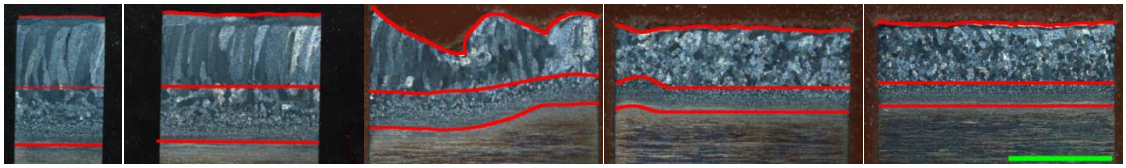

Figure 21. Example cross sections to view melt pool depth (Experiment 1, Transient Section). Green scale bar is 0.25 in.

Results of the measurements can be seen in Figure 22 through Figure 25. Some of the area values seen in Figure 22 and Figure 23 are larger than the simulations have predicted. This is likely due to the keyholing seen in the polished sections and described earlier in this section. Regardless of this issue, data presented in these figures show that the experiments correlate well with the simulations. While many of the area measurements are larger than the expected value from simulation, the expected behavior and thus the distance to reach the new steady state validate the data from simulation results.

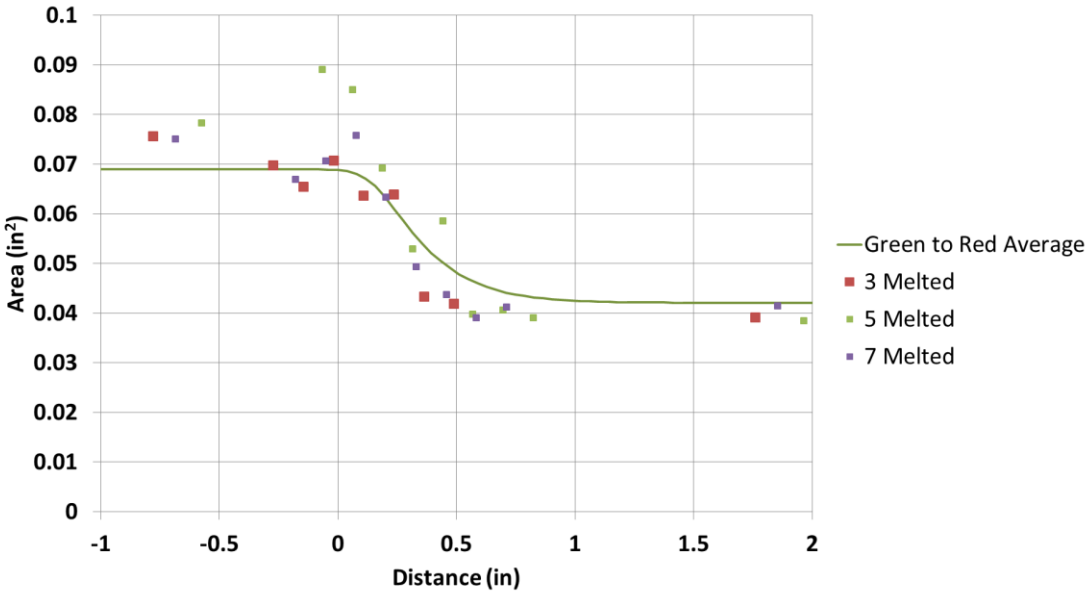

Figure 22. Comparison of simulation and experiment results for Green to Red transitions.

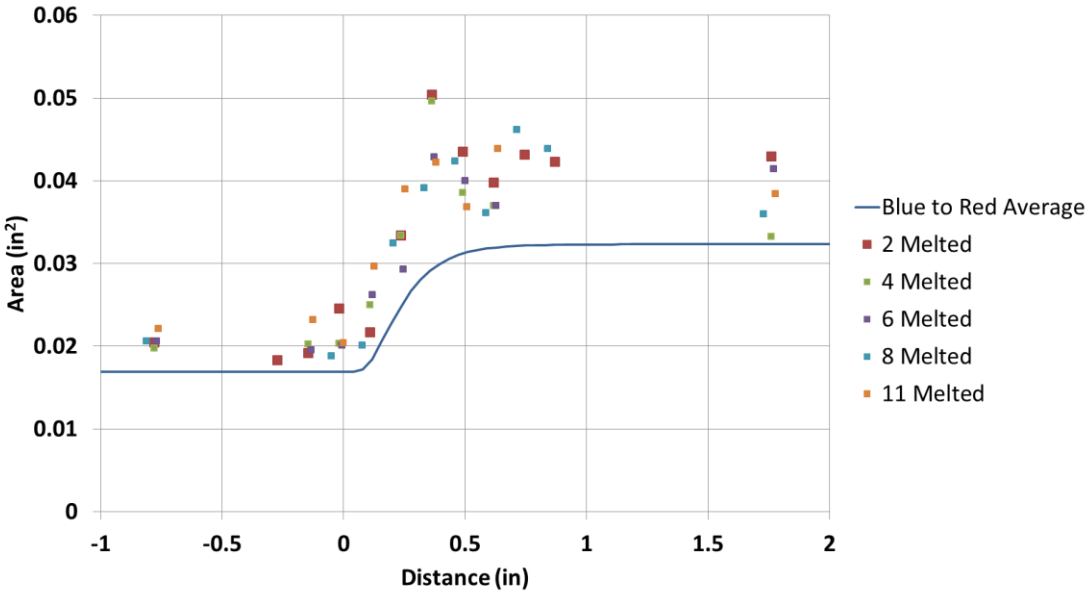

Figure 23. Comparison of simulation and experiment results for Blue to Red transitions.

In Figure 24 and Figure 25 the results from penetration depth measurements are compared to the effective depth from simulation results. Recall that penetration depth is defined as the vertical measurement from the top of the added material to the bottom of the melt pool. Figure 24 contains transitions from Green to Red melt pool areas (experiment lines 1 and 9) and Figure 25 contains transitions from Blue to Red melt pool areas (experiment line 10). In these figures, the general trend in response behavior predicted by the simulation results can also be seen in the experimental results.

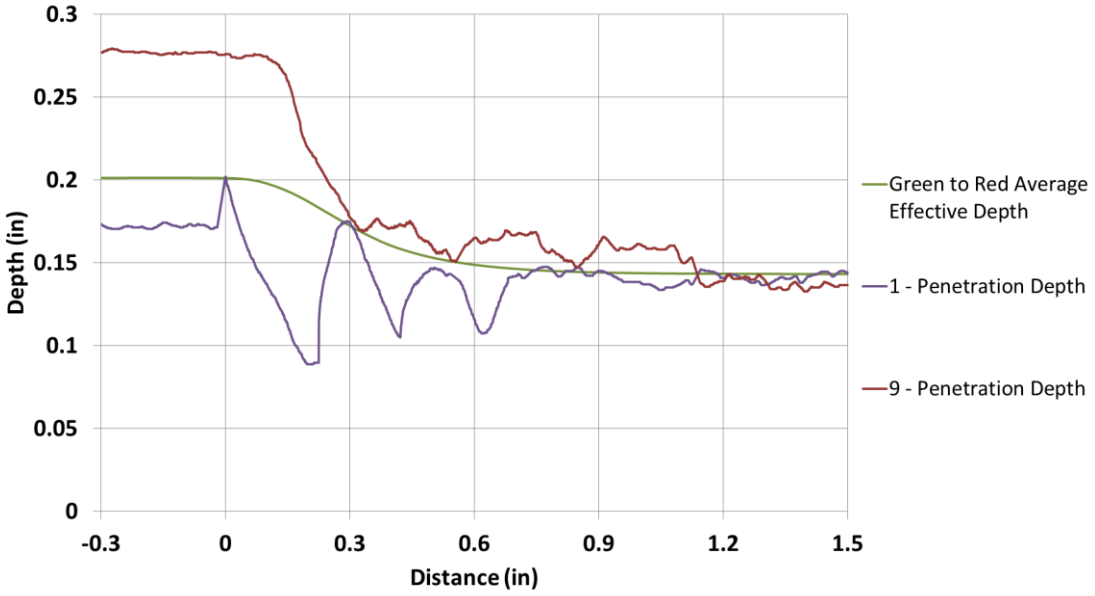

Figure 24. Comparison of simulation and experiment for center cut samples.

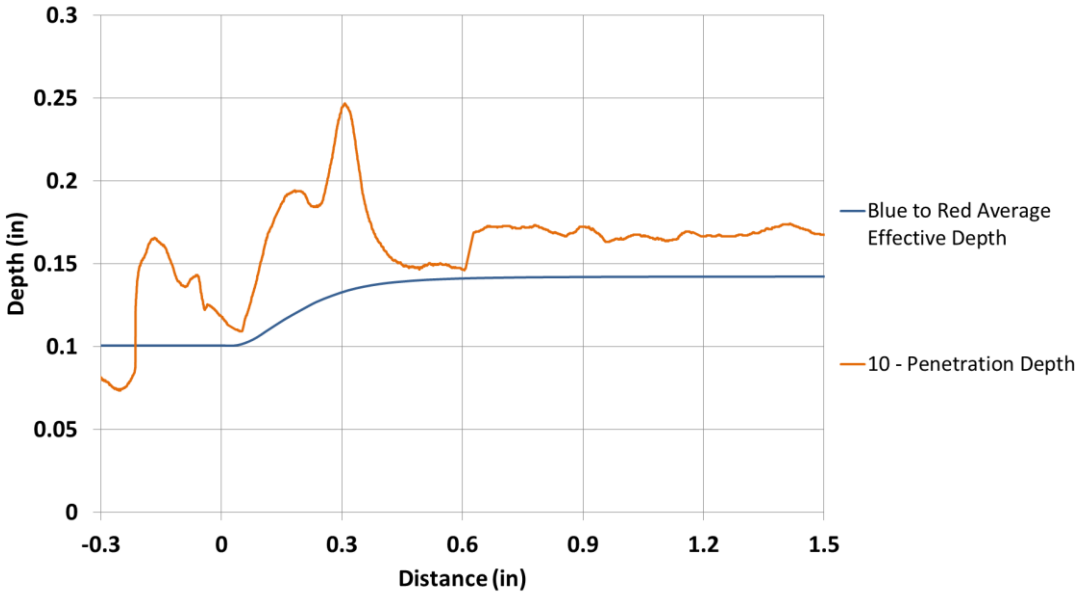

Figure 25. Comparison of simulation and experiment for center cut samples.

It should be noted that in Figure 24, the initial melt pool depth in experiment run 9 is much higher than the effective depth from simulations and then transitions to the expected value after the step change. This is due to the increased wire feed rate at the initial power/velocity setting that decreases to the setting used in other experiments and

simulations. As mentioned before, the wire feed rate for this experiment was set to a higher value during deposition at the initial power and velocity to test the step change in wire feed rate. While this increases the depth measurement, the steady state melt pool areas for this experiment are still close to the expected value (see Table 5) and the trend in response behavior is still clear and further validates the accuracy of the simulations performed.

2.4 Effect of Added Material Size

While presented simulations and experimental results show significant correlation, the initial and final steady state values differed from expected values. Analysis of the results has shown that this difference is due to the ratio of the cross sectional area of added material to the total cross-sectional area of melted material, defined as φ. When $\varphi = 1$, only the added material is melted. When $\varphi = 0$, there is no added material (beam on plate only). Ideally, a value of $\varphi \approx 0.75$ is desired to ensure enough substrate is being melted to create a good bond between added material and substrate without applying excessive amounts of heat and this was the basis for the P-V Process Map developed by Soylemez et al. [3]. However, by holding the size of the added material constant in simulations the value of φ changes through the transition from initial to final steady state. The effect of φ on the position of curves of constant area can be seen in Figure 26, below.

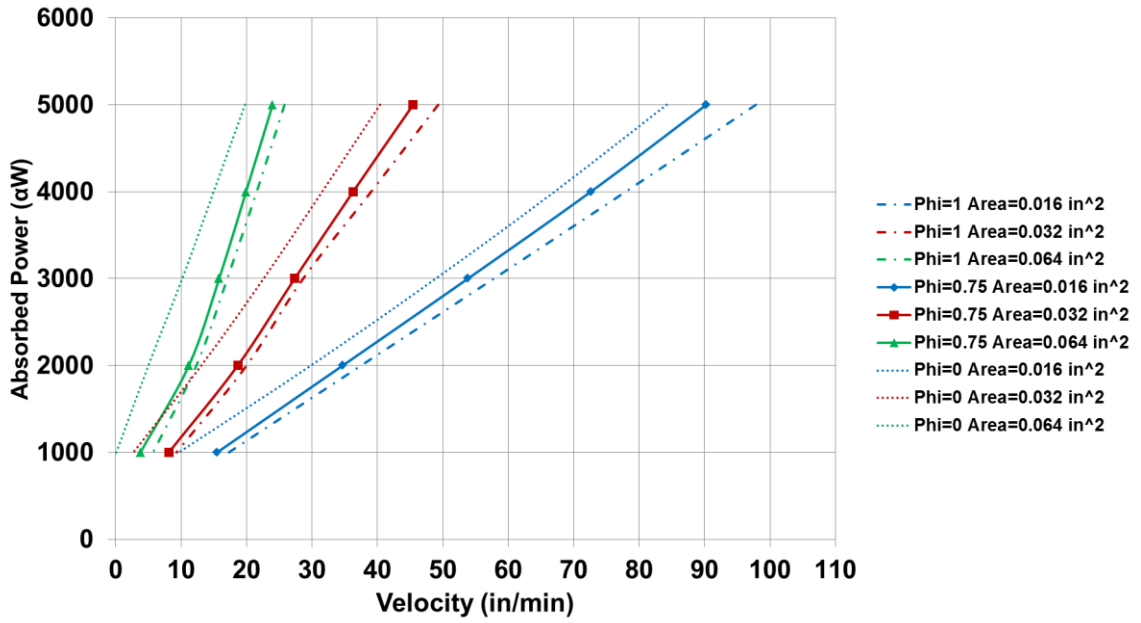

Figure 26. Effect of φ on curves of constant area.

Based on this, a new process map has been created to account for the effect of added material size as well as update the accuracy of the previous process map and is seen in Figure 27, below. In this figure, the solid curves represent the curves of constant area and *L/d* originally presented in Figure 5 and updated for accuracy. The dashed curves are new curves of constant area that have a different added material size. As a reminder, the simulations presented do not change the added material size through the transition. Thus power and/or velocity must be adjusted from the original curves of constant area to account for the change in the value of φ. So in this figure, for the curves of constant area, the color of the curve represents the area achieved (Green = 0.064 in^2, Red = 0.032 in^2, Blue = 0.016 in^2) and the color of the data point on the curve represent the size of added material (Green = 0.0484 in^2, Red = 0.0241 in^2, and Blue = 0.0122 in^2). Curves with data points of a matching color are for $\varphi \approx 0.75$, which was used in previous work by Soylemez et al. [3], and curves with data points of different colors represent the φ adjusted to hold added material size constant in transient simulations. Thus, there are two

red curves of constant area present in the figure: one for the added material size used in the Blue to Red and Red to Blue transitions, and one for the added material size used in the Red to Green and Green to Red transitions.

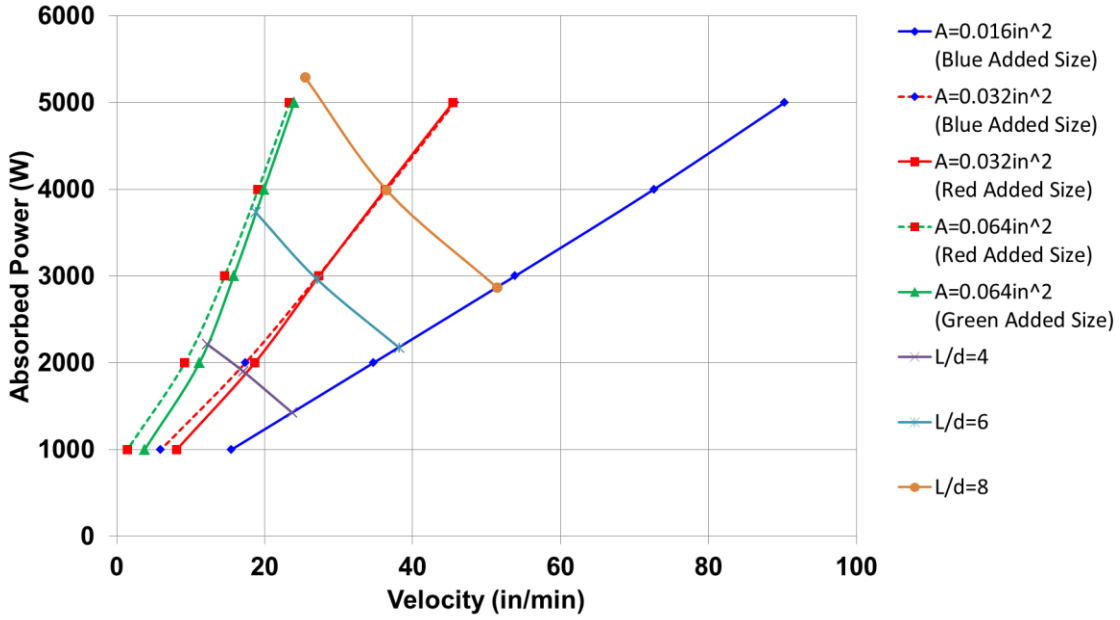

Figure 27. P-V Process Map for single bead deposition.

Using the knowledge of how the value of φ can affect the curves of constant area, new simulations are defined based on the Process Map presented in Figure 27. These simulations are detailed in Figure 28 and Table 6. Again, simulations start on the green and blue curves of constant area and end on the red curve of constant area (consistent with previous simulations). Power values listed in Table 6 are absorbed power. Also listed in Table 6 are response distances and times determined from the simulations.

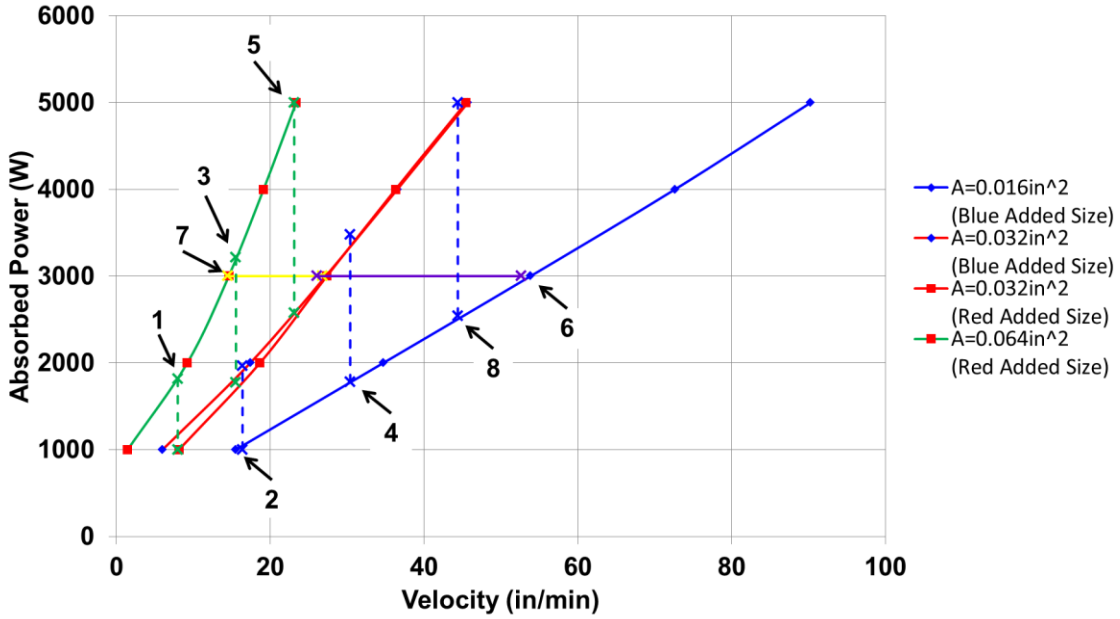

Figure 28. New simulations for determining response behavior.

Table 6. Parameters and results for new simulations.

Run #	Starting Power Setting (W)	Final Power Setting (W)	Starting Velocity (in/min)	Final Velocity (in/min)	Response Time (s)	Response Distance (in)
1	1817.6	1000	8.0	8.0	3.80	0.58
3	3217.2	1774.5	15.5	15.5	2.30	0.63
5	5000	2574.4	23.1	23.1	1.82	0.63
7	3000	3000	14.5	26.8	1.84	0.63
2	1000	1962.5	16.4	16.4	1.50	0.41
4	1777.5	3481	30.4	30.4	0.94	0.37
6	2544.1	5000	44.4	44.4	0.74	0.38
8	3000	3000	52.6	26.1	1.13	0.41

As shown in Table 6, response times are still on the order of seconds and show little correlation. Response distances, on the other hand, show a strong correlation. The values group together for Green to Red transitions (Run # 1, 3, 5, and 7) and Blue to Red transitions (Run #2, 4, 6, and 8), respectively. Additionally, response behaviors presented in Figure 29 show that the steady state values are much closer to the expected values and

response behaviors are similar for step changes between the same curves of constant area, regardless of position or path taken in the P-V Process Map.

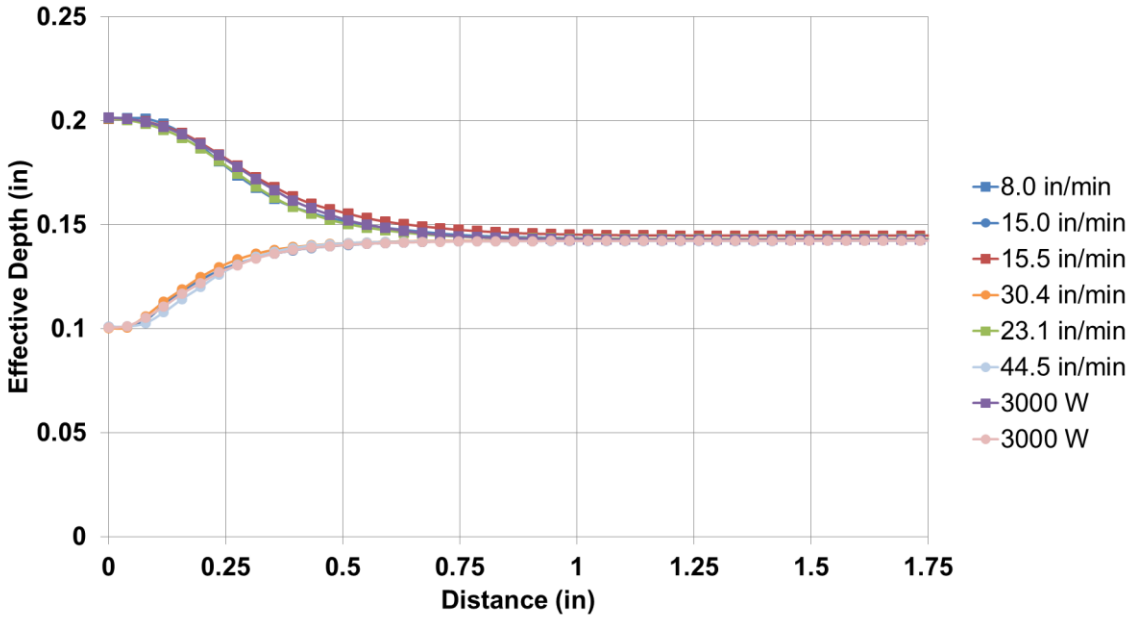

Figure 29. Response behavior for step changes in beam power or travel velocity.

In addition to these, simulations for the reverse transitions were also performed. These response behaviors in addition to the ones presented in Figure 29 are summarized in Figure 30. In this figure, solid lines are the average of all simulations performed. Error bars represent the maximum and minimum deviation from average for all the simulations performed. Additionally, response distances are highlighted in the figure.

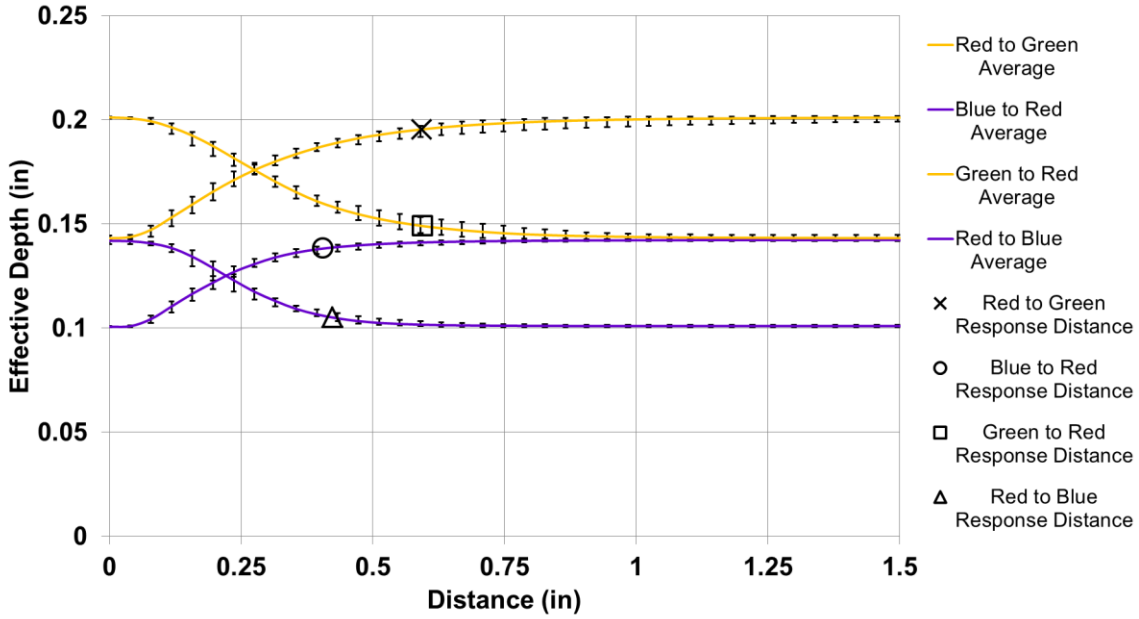

Figure 30. Response behavior for step changes in beam power or travel velocity.

From these results, the consistency in response behavior can be seen. This confirms that the value of φ accounts for the variation in steady state melt pool area from expected values discussed during the analysis of Figure 8.

2.5 Fitting of Transient Melt Pool Response

2.5.1 Rule of Thumb Estimate

Prior work by Aggarangsi determined a relationship between response distance and the initial and final melt pool areas for Stainless Steel in laser powder feed systems [95]. In that work, a "rule of thumb" generalization was developed for determining the response distance. The generalization was that a response distance can be approximated by one initial steady state depth plus two final steady state depth values ($d_1 + 2d_2$), where all length scales were normalized using velocity, specific heat, density, and thermal conductivity.

Similar rule of thumb generalizations can be made using the simulation data (non-normalized) presented in the previous section and the results can be seen in Figure 31 and Table 7, below. Unlike Aggarangsi's work, it was found that the rule of thumb equations were different for increases in area versus decreases in area. For single bead deposition in the electron beam wire feed system, it was found that increases in area can be estimated by $d_1 + 2d_2$ and decreases in area can be better estimated by $d_1 + 3d_2$. This is a key finding because it shows that the melt pool response distance can be determined across the entirety of the processing space for a given process and material after a minimal number of simulations or experiments have been performed.

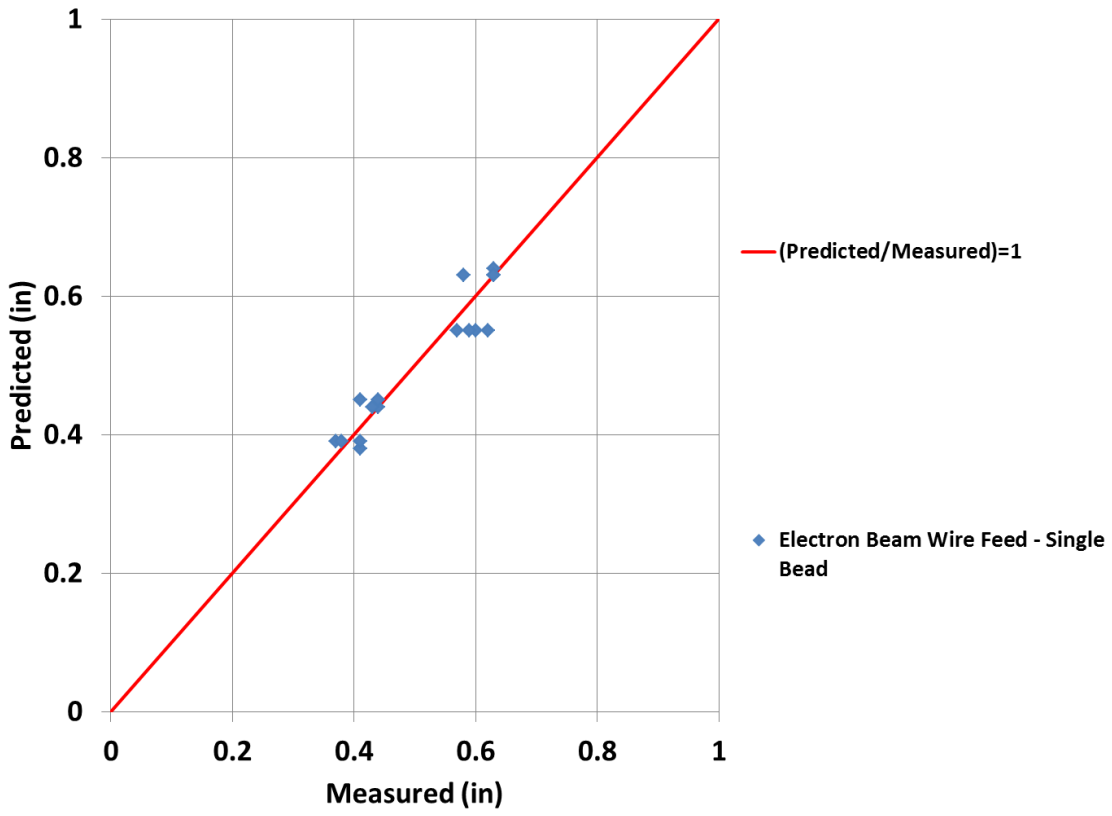

Figure 31. Response distance predicted using rule of thumb versus measured in simulations.

Table 7. Comparison of Rule-of-Thumb estimates to simulation data.

	Simulation Details	Initial Effective Depth (in)	Final Effective Depth (in)	Response Distance (in)	Rule-of-Thumb Estimate (in)	Percent Error (%)
Decrease in Area	Green to Red @ 8 in/min	0.20	0.14	0.58	0.63	8.1
	Green to Red @ 15.5 in/min	0.20	0.14	0.63	0.64	0.9
	Green to Red @ 23.1 in/min	0.20	0.14	0.63	0.63	0.6
	Green to Red @ 3000 W	0.20	0.14	0.63	0.63	0.6
	Red to Blue @ 16.4 in/min	0.14	0.10	0.44	0.44	-2.0
	Red to Blue @ 30.4 in/min	0.14	0.10	0.43	0.44	2.7
	Red to Blue @ 44.4 in/min	0.14	0.10	0.44	0.45	0.4
	Red to Blue @ 3000 W	0.14	0.10	0.41	0.45	7.5
Increase in Area	Blue to Red @ 16.4 in/min	0.10	0.14	0.41	0.38	-6.5
	Blue to Red @ 30.4 in/min	0.10	0.14	0.37	0.39	4.5
	Blue to Red @ 44.4 in/min	0.10	0.14	0.38	0.39	1.0
	Blue to Red @ 3000 W	0.10	0.14	0.41	0.39	-6.9
	Red to Green @ 8 in/min	0.14	0.20	0.57	0.55	-4.8
	Red to Green @ 15.5 in/min	0.14	0.20	0.60	0.55	-8.5
	Red to Green @ 23.1 in/min	0.14	0.20	0.59	0.55	-7.6
	Red to Green @ 3000 W	0.14	0.20	0.62	0.55	-11.7

2.5.2 Fitting of Transient Response Behavior

Also presented in Aggarangsi's work was an exponential function used to determine melt pool response behavior in length scales normalized by velocity, specific heat,

density, and thermal conductivity. This approach, however, does not capture the s-curve shape seen in the melt pool behavior in Figure 30. Thus as a starting point, the equation for a cumulative distribution function of a Gumbel distribution is selected, as seen in (1) below.

(1) $$\boldsymbol{F(x) = e^{-e^{-(x-\mu)/\beta}}}$$

This equation creates an s-shaped curve between zero and one. Therefore additional parameters are required: an offset, *C* to adjust the bounds of the s-curve and a multiplier, *A* to adjust the gap between the upper and lower bound. This creates a new equation, seen in (2) below.

(2) $$\mathbf{F(x) = Ae^{-e^{-(x-\mu)/\beta}} + C}$$

With the general form of the curve determined, Excel's solver tool can be used to fit parameters in the function to the average data curves from Figure 30 by minimizing the squared difference between the function and the average melt pool area data from simulations. The resulting parameters from this fitting are listed in Table 14 and the predicted curves are compared to simulation results in Figure 32.

Table 8. Parameters for prediction of melt pool behavior.

	A	**μ**	**β**	**C**	**Initial Area (in^2)**	**Final Area (in^2)**	**Difference in Area (in^2)**
Red to Green	0.03164	0.21103	0.16420	0.03185	0.0321	0.0637	0.0316
Green to Red	-0.03143	0.23341	0.14124	0.06371	0.0637	0.0322	-0.0314
Blue to Red	0.01594	0.16875	0.10733	0.01586	0.0159	0.0319	0.0159
Red to Blue	-0.01563	0.19800	0.09997	0.03163	0.0317	0.0160	-0.0156

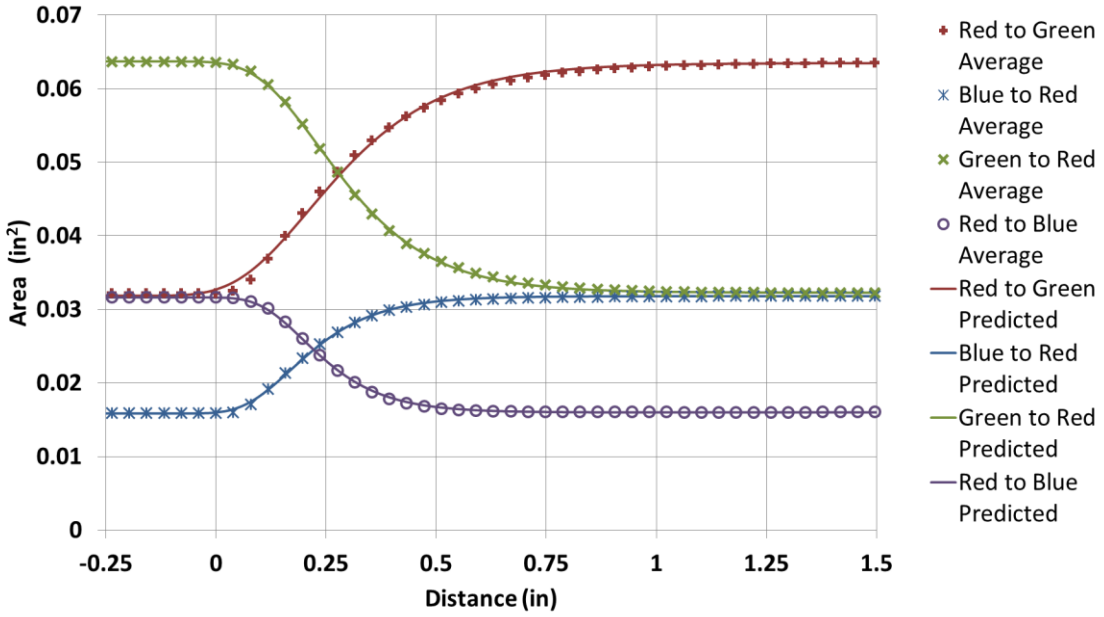

Figure 32. Comparison of predicted behavior to simulation results.

From Figure 32, it is clear that the parameters for the selected equation accurately predict behaviors. The accuracy of the fit can also be confirmed by the coefficient of determination, R^2, which did not go below a value of 0.96 for any curve. Table 14 shows that the multiplier, A is approximately equal to the difference in area and the offset, C is approximately equal to the difference in area. However, a correlation for μ and β has not yet been found and more combinations of initial and final area simulations would be required to determine if a correlation exists for these variables.

2.5.3 Suggested Application to Feedback Control Systems

The purpose of this section is to re-iterate the difference in calculation of the response time (no correlation) and response distance (correlation) to aid the use of data presented in this thesis toward development of feedback/feedforward control algorithms. Recall that the measurement of response time is the time it takes the melt pool depth to reach 90% of the difference between initial and final steady state melt pool, starting from the time the

step change is initiated (or the distance the beam travels divided by the velocity). This is a real time measurement that would be akin to in-process monitoring. The response distance, however, is the distance required for the melt pool to reach 90% of the difference between initial and final steady state melt pool depth, starting at the initial steady state. This distance is determined by measuring the maximum melt pool area that is achieved at a given location, regardless of the position of the heat source. This would be akin to sectioning an experiment line after it had solidified to determine the extent to which the part was melted at several locations along the travel direction. Because the start of the change in melt pool area does not necessarily correspond with the point at which the step change in process variables is initiated the calculation of response time is not as simple as dividing the response distance by the travel velocity. Additionally, it does not take into account the distance between the heat source and the point of maximum area, which is defined as L'. That value can differ between the initial and final steady states and can even change along the same curve of constant area. This makes it difficult to predict a response time from in-situ measurement of steady state parameters and knowledge of the response distance.

To determine a relationship between the response time and the response distance, the differences in their calculation must be examined. These differences are detailed in Figure 33, below. Response time is based on the distance that the beam travels from the initiation of the step change (Point 1) to the new steady state (Point 2) and response distance is based on the distance between initial steady state (Point 3) and final steady state (Point 4). The key differences are that the values of L' for the initial and final steady states come into play. The point where the melt pool begins to change is generally before

the point where the step change is initiated and this distance should be based on the initial L' value. Once the melt pool reaches the new steady state, there should be a new value of L' associated with the melt pool. Therefore, a "rule of thumb" equation can be developed based on the response distance, plus some fraction of the final L' value, and minus some fraction of the initial L' value. The reason a fraction of the initial L' value is subtracted from the distance is to account for the fact that the melt pool area responds to the step change prior to the position in the experiment line (x-direction) where the step change is initiated.

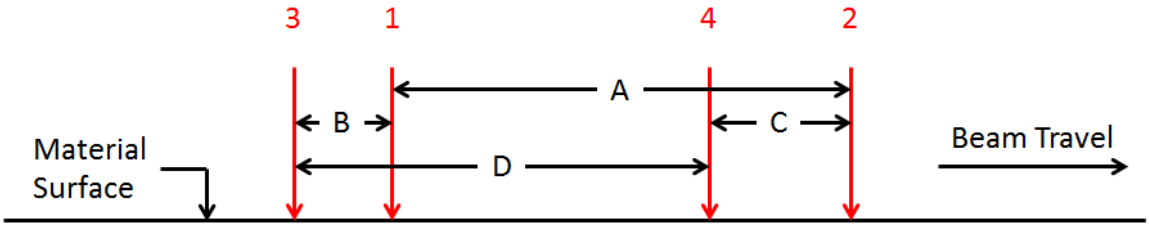

1 = Point where step change is initiated
2 = Position of beam when final steady state is achieved
3 = Point where the area deviates from the initial steady state
4 = Point of maximum area when final steady state is achieved

A = Distance beam travels from the point of step change and the final steady state (determines response time)
B = Distance behind the point of step change where the maximum area deviates from the initial steady state
C = Distance between the beam and point of maximum area for the final steady state
D = Response distance

Figure 33. Schematic of response distance calculation versus response time calculation.

Using this method and Excel's solver function to minimize the squared difference between the estimate and actual values, a rule of thumb can be determined. The results of this analysis can be seen in Figure 34 and Table 9, below. The equation used to determine the estimate was [Response Distance – (0.1 × Initial L') + (0.4 × Final L')] for increases

in area and [Response Distance – (0.1 × Initial L') + (0.6 × Final L')] for decreases in area. This distance divided by the final velocity will determine an estimate for response time. From the data presented in Figure 34 and Table 9, it is clear that the predicted values for response time are in good agreement with the measured values (especially for increases in area). This represents an important finding as, prior to this work, no methods for accurately determining the response time of the melt pool have been presented in the literature.

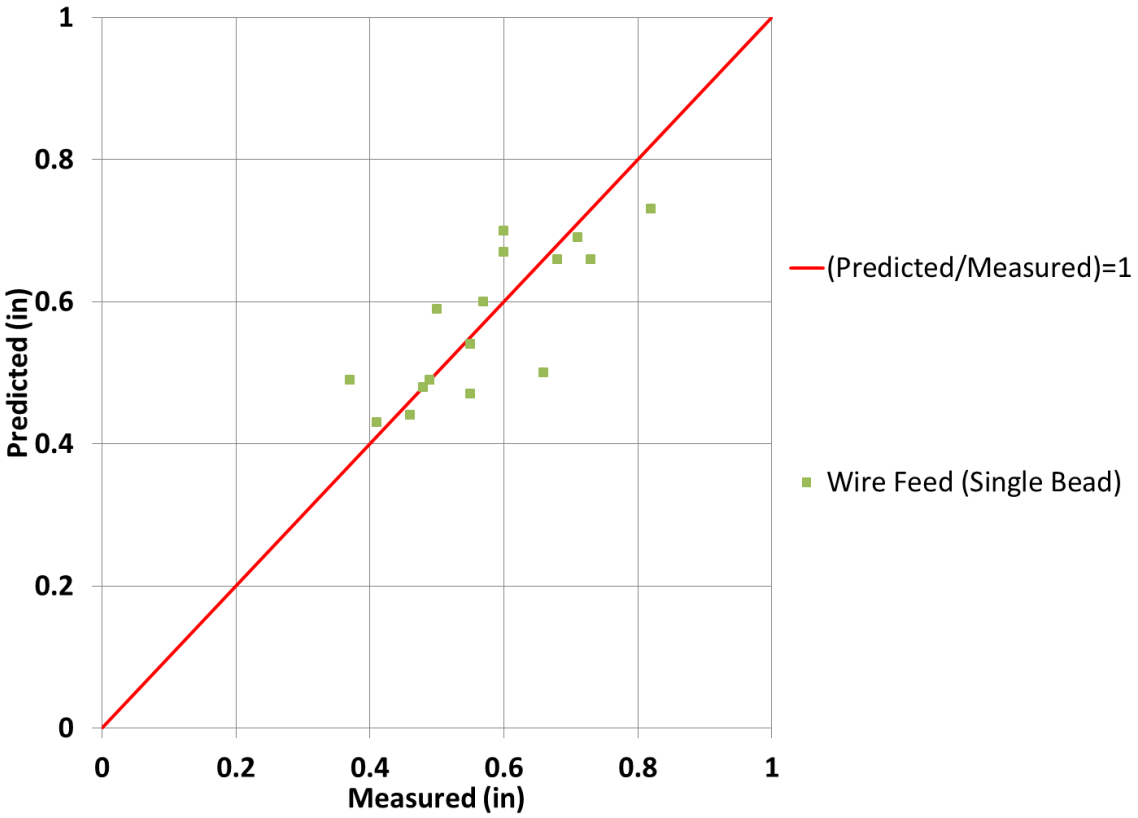

Figure 34. Predicted response time versus measured response time from simulation results.

Table 9. Comparison of response distance and response time via rule of thumb.

	Initial L'	**Final L'**	**Response Time × Velocity (in)**	**Response Distance (in)**	**Estimated Response Time × Velocity (in)**	**Percent Error (%)**
Blue to Red @ 16.4 in/min	0.10	0.14	0.41	0.38	0.43	4.7
Blue to Red @ 30.4 in/min	0.05	0.28	0.48	0.37	0.48	-0.4
Blue to Red @ 44.4 in/min	0.11	0.43	0.55	0.38	0.54	-0.6
Blue to Red @ 3000 W	0.19	0.24	0.49	0.41	0.49	-0.7
Red to Green @ 8 in/min	0.03	0.09	0.57	0.57	0.60	5.9
Red to Green @ 15.5 in/min	0.10	0.18	0.68	0.60	0.66	-2.9
Red to Green @ 23.1 in/min	0.17	0.29	0.71	0.59	0.69	-2.6
Red to Green @ 3000 W	0.21	0.17	0.73	0.62	0.66	-9.5
Red to Blue @ 16.4 in/min	0.14	0.10	0.37	0.44	0.49	33.6
Red to Blue @ 30.4 in/min	0.28	0.05	0.46	0.43	0.44	-6.3
Red to Blue @ 44.4 in/min	0.43	0.11	0.55	0.44	0.47	-14.7
Red to Blue @ 3000 W	0.24	0.19	0.66	0.41	0.50	-24.2
Green to Red @ 8 in/min	0.09	0.03	0.50	0.58	0.59	17.8
Green to Red @ 15.5 in/min	0.18	0.10	0.60	0.63	0.67	13.0
Green to Red @ 23.1 in/min	0.29	0.17	0.60	0.63	0.70	17.8
Green to Red @ 3000 W	0.17	0.21	0.82	0.63	0.73	-10.4

Regardless of the ability to predict melt pool response time from response distance for decreases in area, the response distance here can be used in feedback control systems. While the change in melt pool width will not be instantaneous, once the system senses the

change in melt pool width, the distance to the new steady state melt pool width is then known, regardless of the change in L' or the point in which the melt pool width begins to change.

2.6 Discussion

In this chapter the transient response of the melt pool effective depth to step changes in beam power and beam velocity for single bead deposition of Ti-6Al-4V in a wire feed electron beam based system is investigated through simulations and experiments. 3D finite element simulations were developed and run in the ABAQUS software package and initial simulation work was based on process maps previously developed by Soylemez et al. [3]. No added material and single bead of added material experiments were performed at the NASA Langley Research Center on their EBF^3 system.

Potential sources of error in the simulations presented include the neglecting of physical phenomena through which heat can be removed from the system (such as melt pool convection and radiation); however, prior work has found this to be minimal when compared to conduction through the substrate. Another source of error is the measurement of the melt pool area in the analysis of experiments. As described in section 2.3, it can be very difficult to determine the exact boundary of the melt pool because of microstructural development occurring at temperatures below the melt temperature in the HAZ. Regardless of these issues, the behavior seen in the experimental measurements closely match the expected results, which validates the simulations presented.

From this investigation, it was found that the response time of the melt pool is on the order of seconds and shows little correlation. This would be a limiting factor in the

development of a feedback control system as the response time is orders of magnitude larger than the time required to initiate a change in beam power or velocity. Response distances, however, show a strong correlation. When moving between the same curves of constant area, the response distance and response behavior is the same regardless of path or position taken in the P-V Process Space.

It was also found that the size of the added material plays a role in the position of the curves of constant area. As such, the variable φ was defined to capture the effect of added material size. Simulations were performed to update the accuracy of the P-V Process Map and define new simulations based on the effect of φ. With the new process map defined, simulations were performed to ensure the accuracy of the steady state melt pool areas in the transient response. These simulations further confirmed the relationship between response distance and the initial and final steady state melt pool areas or effective depths.

As with previous work, it was found that response distance can be determined through a combination of initial and final melt pool effective depths. Unlike previous work in the laser powder feed systems for stainless steel, it was found that the equation differed between increases and decreases. Also, it was shown that the response behavior can be predicted through a modified cumulative distribution function of a Gumble distribution. However, not enough information is available to derive physical meaning from certain parameters and analysis of additional step changes would be required to do so.

In addition to this, it was determined that response time can be estimated by the response distance and a combination of the initial and final L' values. This is an important

development as it gives machine operators and control system developers a method for predicting the distances and times required for a change in system variables to translate to changes in melt pool dimensions and will aid in the development of feedback or feedforward control systems.

It is apparent that step changes with matching initial and final steady state melt pool effective depths respond similarly as they transition. The explanation for this behavior is that the melt pool must move a certain ***distance*** after an abrupt change in beam power or beam velocity to achieve a new steady state depth and that distance is largely governed by the initial and final melt pool sizes (melt pool depths or cross sectional areas), regardless of the initial and final power and velocity combinations.

Based on these findings, the response distance and response time can be ***predicted*** for a new system and/or material by fitting the multiples of key features of the steady state melt pool geometry (d_1, d_2, L'_1, and L'_2) to a small set of simulations (or even a single simulation) and extrapolating to cover the entire process space.

Chapter 3 Effect of Geometry on Transient Response

For this chapter, two types of geometries are examined: a tall, thin wall geometry and a corner geometry. The tall, thin wall and single bead geometries represent fundamental quasi-steady state geometries. It is called quasi-steady state because, assuming the wall is long enough that melt pool does not see the effects of the start or end of the wall and all other variables are held constant, the size and shape of the melt pool does not change as it moves through the geometry. This is in contrast to the second geometry, an exterior corner, which is considered a transient geometry. In this geometry, there is an initial melt pool on the free edge of the material. As the beam approaches the corner the melt pool will increase in size and change shape as the conduction pathways through the substrate are reduced. Then the melt pool will return to the original free edge steady state as the beam continues away from the corner, down the adjacent free edge.

3.1 Thin Wall Finite Element Analysis

3.1.1 Thin Wall Finite Element Models

For this analysis, 2D finite element simulations that replicate a thin wall geometry (see Figure 35) have been set up and run in the ABAQUS software package. Wall thickness (t) is chosen such that the ratio of wall thickness to penetration depth (t/D) is equal to 1.95. Thus, for melt pool areas of 0.064 in^2, 0.032 in^2, and 0.016 in^2 the corresponding wall thicknesses are 0.35 in, 0.25 in, and 0.18 in, respectively. This ratio is consistent with experimental observations and prior work in thin wall geometry [70]. For these simulations no material was added (beam on wall only). The models include temperature dependent properties and latent heat, but do not include convection on the wall exterior as the process takes place in a vacuum. The models also do not include

radiation nor do they include convection within the melt pool, consistent with the single bead simulations. All simulations begin with all elements set to room temperature (293 K) and the base of the model is set and held at this temperature. The reason for starting the wall at room temperature rather than including the build-up of heat from previously deposited layers was to isolate the effect of geometry. The inclusion of the build-up of heat from previous layers would be an additional variable that could change based on manner in which the wall is deposited. Thus, to eliminate this variable, no residual heat from previously deposited layers was included. The effect of preheat in thin walls, however, is discussed in Chapter 5.

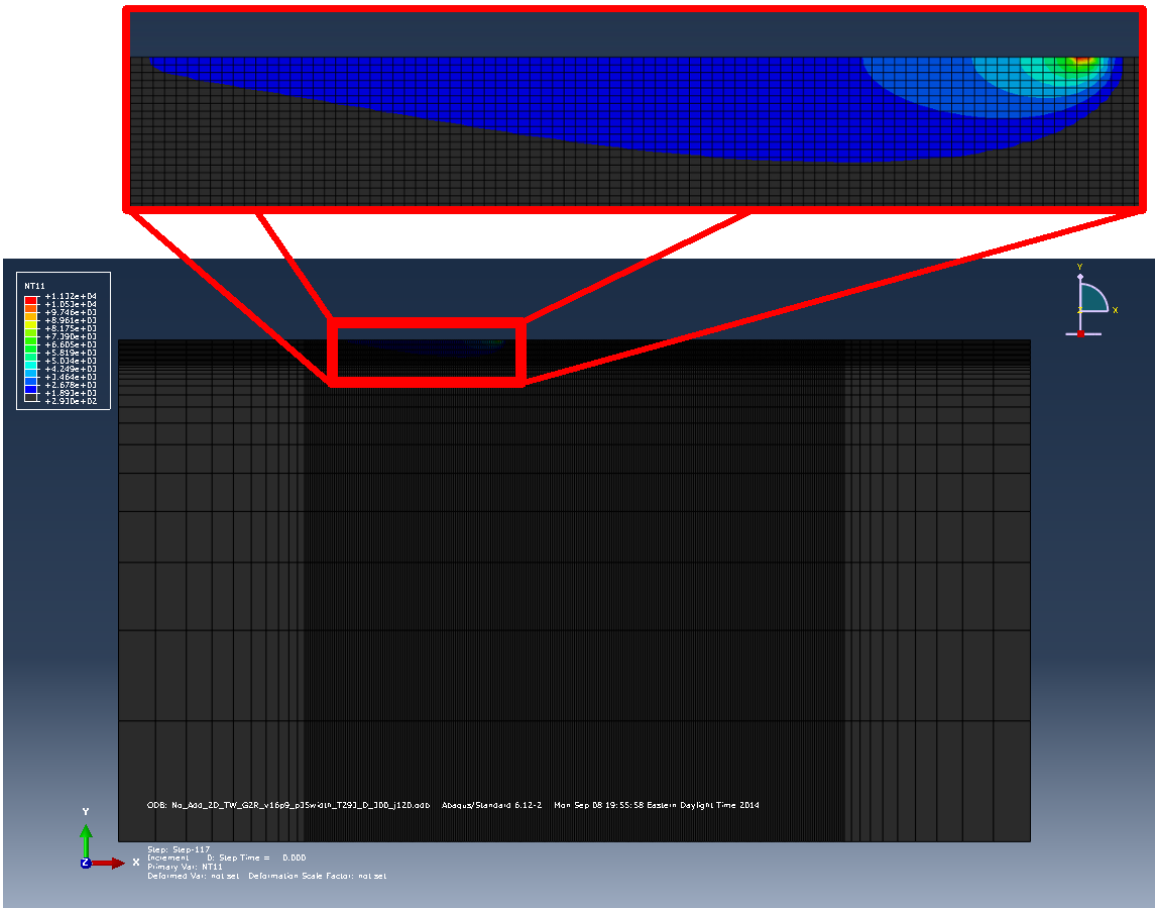

Figure 35. 2D Finite Element Model for deposition on a thin wall.

3.1.2 Thin Wall Process Maps

Prior to this work, no process maps have been developed for deposition of a tall, thin wall geometry. Thus, several 2D simulations were run at varying powers and velocities to determine curves of constant melt pool area and *L/d*. The P-V Process Map based on these simulations can be seen in Figure 36 below. In this figure the green, red, and blue curves represent curves of constant area at 0.064 in^2, 0.032 in^2, and 0.016 in^2, respectively. The purple, light blue, and orange curves represent curves of constant *L/d* ratio of 4, 6, and 8, respectively.

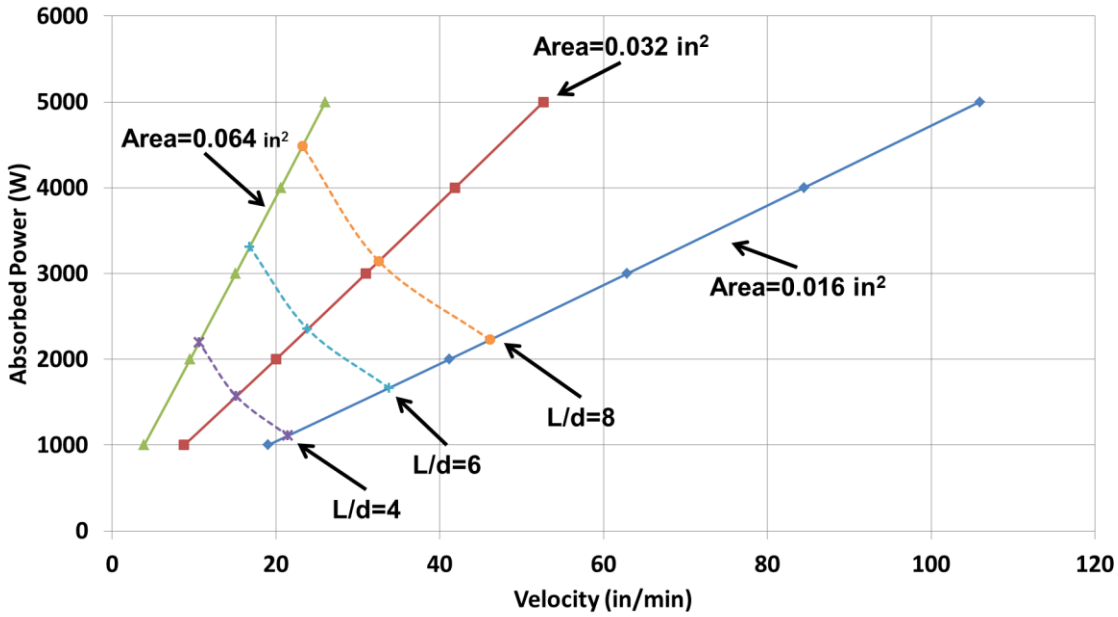

Figure 36. PV Process Map for 2D Thin Wall Finite Element Model.

3.1.3 Thin Wall Simulations

With the process maps for thin walls defined, step changes between curves of constant area are determined and presented in Figure 37. For these step changes, 2D finite element simulations were performed with the same setup as described before. It should be noted that the curves of constant area were defined with constant *t/D* ratios and therefore

varying wall thicknesses. However, during the transition, the wall thickness is held constant. To prevent scenarios where over-melting might occur, the larger of the two wall thicknesses is chosen for all transitions between two curves of constant melt pool area. For example, the Red curve of constant area is defined with a wall thickness of 0.25 in and the Blue curve of constant area is defined with a wall thickness of 0.18 in. Transitions between the Blue and Red curves of constant area use a wall thickness of 0.25 in, regardless of the direction of the transition.

In order to ensure that the wall thickness does not affect the steady state melt pool areas, new curves of constant area have been determined for an area of 0.032 in^2 with a wall thickness of 0.35 in and for an area of 0.016 in^2 with a wall thickness of 0.25in. These curves are denoted in Figure 37 as a red curve with triangular green points and a blue curve with square red points, respectively. Additionally, details for the analysis plan are presented in Table 10.

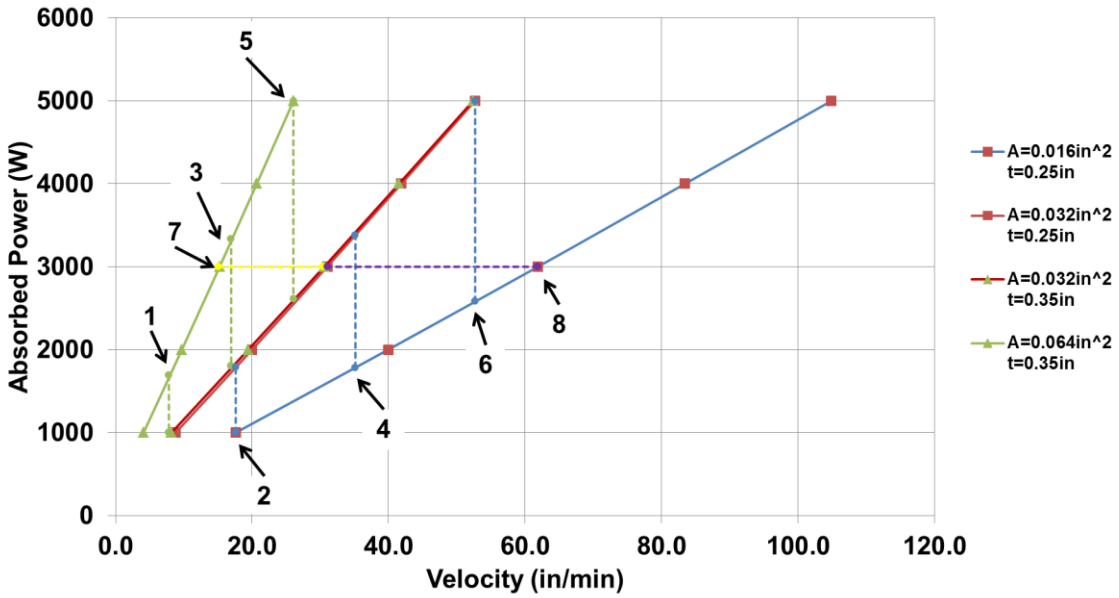

Figure 37. Analysis plan for the thin wall geometry.

Table 10. Analysis plan for the thin wall geometry.

Run #	Starting Power (W)	Final Power (W)	Starting Velocity (in/min)	Final Velocity (in/min)
1	1693.9	1000.0	7.8	7.8
2	1000.0	1786.0	17.6	17.6
3	3333.2	1802.1	16.9	16.9
4	1785.2	3377.9	35.1	35.1
5	5000.0	2611.1	26.0	26.0
6	2580.5	5000.0	52.7	52.7
7	3000.0	3000.0	15.1	30.4
8	3000.0	3000.0	61.9	31.0

Response times and distances are listed in Table 11. The response times are consistent with the single bead results, in that there is no clear trend in the values and the times are on the order of seconds. This would represent the limiting factor in a feedback control system as the response times are orders of magnitude longer than the time required for a control system to perform a change in process variables. Response distances, however, group together closely for step changes with matching initial and final steady state melt pool effective depths. Also, the response distances for the Blue to Red step changes are much shorter than the response distances for Green to Red step changes.

Table 11. Response times and distances for thin wall step changes.

	Run #	Initial Area (in^2)	Final Area (in^2)	Response Time (s)	Response Distance (in)
Green to Red	1	0.064	0.032	3.28	0.60
	3	0.064	0.032	1.60	0.57
	5	0.064	0.032	1.22	0.57
	7	0.064	0.032	1.16	0.55
Blue to Red	2	0.016	0.032	1.34	0.32
	4	0.016	0.032	0.79	0.29
	6	0.016	0.032	0.63	0.29
	8	0.016	0.032	0.88	0.31

The correlation seen in response distances can also be seen in Figure 38, which shows the melt pool depths as they transition from initial steady state to final steady state. The data presented in this figure are the maximum melt pool area achieved at each position along the build path. This is equivalent to sectioning an experiment plate perpendicular to the travel velocity to view the extent to which the wall was melted. It is clear that step changes with matching initial and final steady state melt pool areas respond similarly as they transition. As seen with the single bead response behaviors, the explanation for this is that the melt pool must move a certain *distance* after an abrupt change in beam power or beam velocity to achieve a new steady-state depth and that distance is largely governed by the initial and final melt pool sizes (melt pool depths or cross sectional areas), regardless of the initial and final power and velocity values.

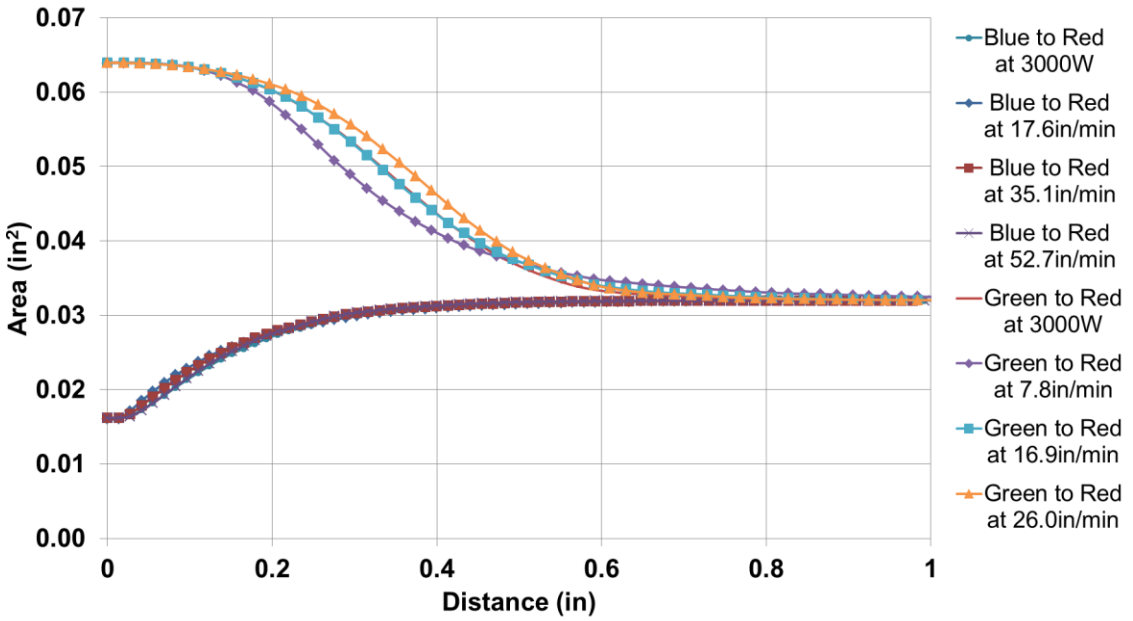

Figure 38. Response behavior for thin wall step changes.

In addition to the simulations presented in Figure 38, simulations for the reverse of these transitions (e.g. Red to Blue and Red to Green transitions) were also performed. A summary of these simulations and the ones from Figure 38 is presented in Figure 39 below. In this figure, the averages of all the step changes for a given transition are presented and the error bars represent the absolute deviation from the average at each location in the x-direction. As seen from the results, the reversed step changes behave well and confirm the hypothesis that the response behaviors will be similar regardless of position or path taken through the P-V process space; as long as the initial and final melt pool areas are the same, respectively.

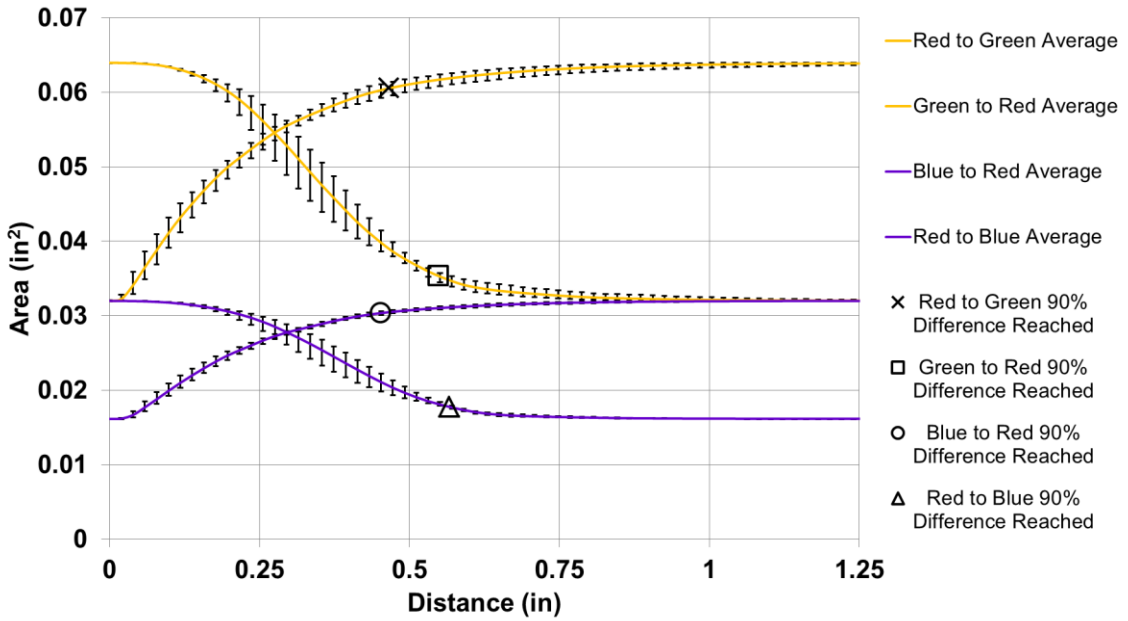

Figure 39. Response behavior averages with absolute deviation from averages.

Additionally, a comparison of the simulation results for thin walls to the single bead simulations is presented Figure 40. In this figure, the averages of the response behaviors are presented (comparing data from Figure 30 and Figure 39). Yellow and purple curves represent thin wall response behaviors, green and light blue curves represent single bead response behaviors. Solid lines represent increases in area, and dashed lines represent decreases in area for all step changes between two curves of constant area.

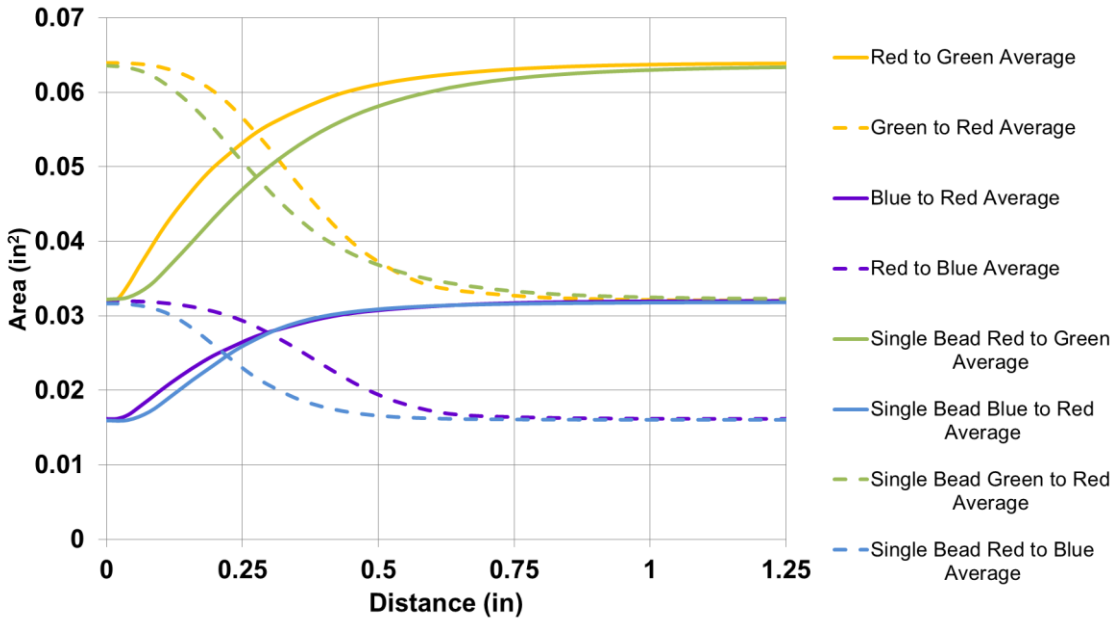

Figure 40. Comparison of Single Bead and Thin Wall Response Behavior.

It is shown from the figure that the step changes for increases in area for thin walls are very similar for Blue to Red transitions and slightly shorter for Red to Green transitions. For decreases in area the melt pool response for thin walls is longer than for single beads. This is because the response behavior for any geometry is a balance between the dissipation of the thermal field prior to the step change and the development of the thermal field after the step change. In the thin wall geometry, the pathways for heat to move away from the heat source through the substrate are restricted. Thus, for decreases in area, the dissipation of the thermal field prior to the step change has more of an influence in the thin wall geometry.

3.2 Thin Wall Experiments

Thin wall experiments were performed at the NASA Langley Research Center in their EBF^3 system. The experiment setup can be seen in Figure 41, below. In this setup, 0.25 in × 3 in × 12 in bars were placed on their side to replicate thin walls and allow the beam to

penetrate the 0.25 in side of the experiment plate and move down the 12 in direction. The bars were held in place with aluminum spacers and placed on top of an aluminum plate to protect the table.

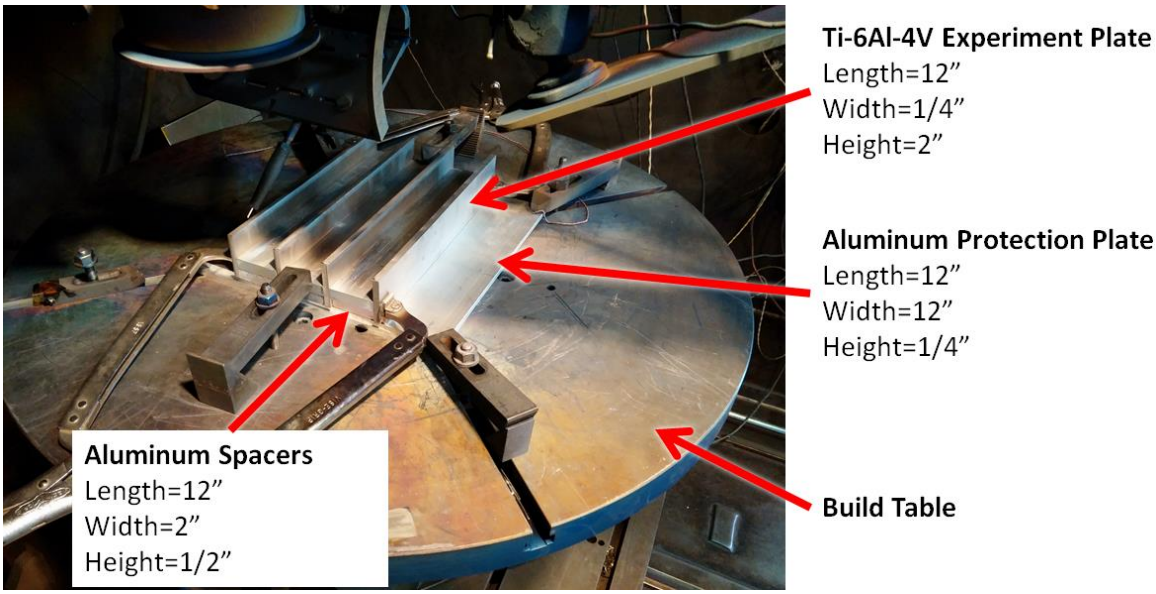

Figure 41. Thin wall experiment setup.

The analysis plan can be seen in Figure 42 and is detailed in Table 10. Due to the availability of materials when the experiments were performed, only step changes between the Red (0.032 in^2) and Blue (0.016 in^2) are included in the analysis plan. Powers listed in Table 10 are source powers assuming an absorptivity of 0.9, consistent with single bead experiments. Thus the powers listed match the absorbed power in Figure 27 divided by 0.9. Wire feed rates are calculated using a 0.063 in diameter wire.

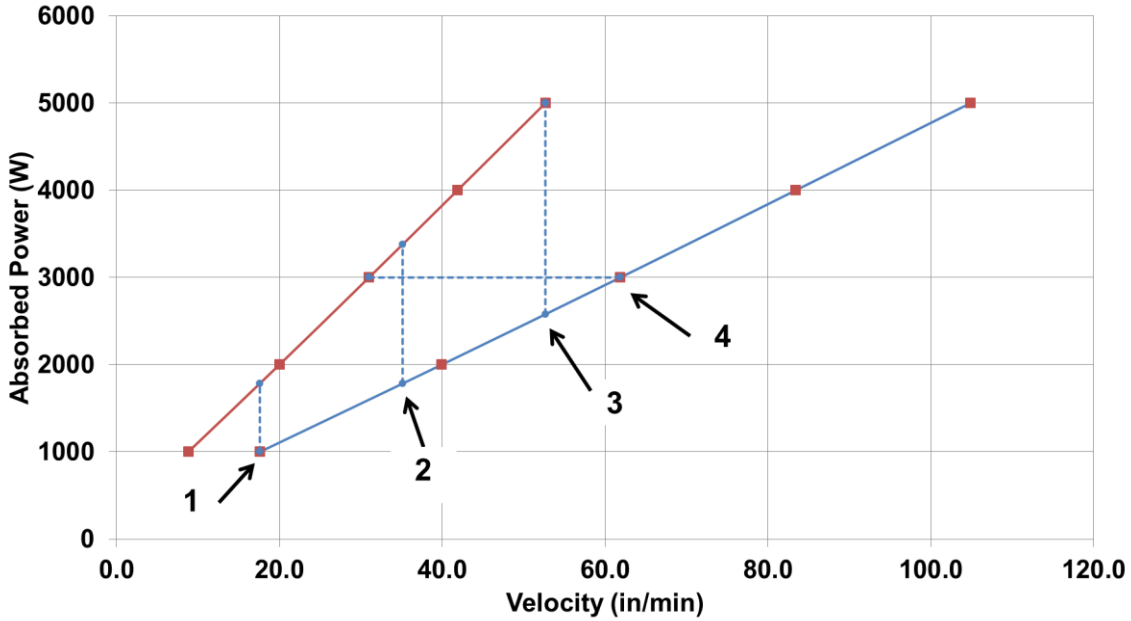

Figure 42. Analysis plan for thin wall experiments.

Table 12. Analysis plan for thin wall experiments.

Run #	Starting Source Power (W)	Final Source Power (W)	Starting Velocity (in/min)	Final Velocity (in/min)	Wire Feed Rate (in/min)
1	1111	1984	17.6	17.6	51.8
2	1984	3753	35.1	35.1	103.5
3	2867	5557	52.7	52.7	155.2
4	3333	3333	61.9	31.0	182.3
2R	3753	1984	35.1	35.1	103.5
4R	3333	3333	31	61.9	182.3

The experiments performed can be seen in Figure 43 and more closely in Figure 44. It is shown that qualitatively, the melt pools appear to be in general agreement with the simulation results. The range of response distances on the surface approximately 0.3 in to 0.7 in, while the simulations predicted 0.36 in to 0.52 in. However, while the setup used for experiments easily isolates the effect of geometry; it makes it difficult to ensure that the beam is perfectly centered on the wall. As such, it is difficult to get highly accurate

measurement or confirm that melt pools are responding as expected without sectioning the plate.

Figure 43. Example thin wall experiments post deposition.

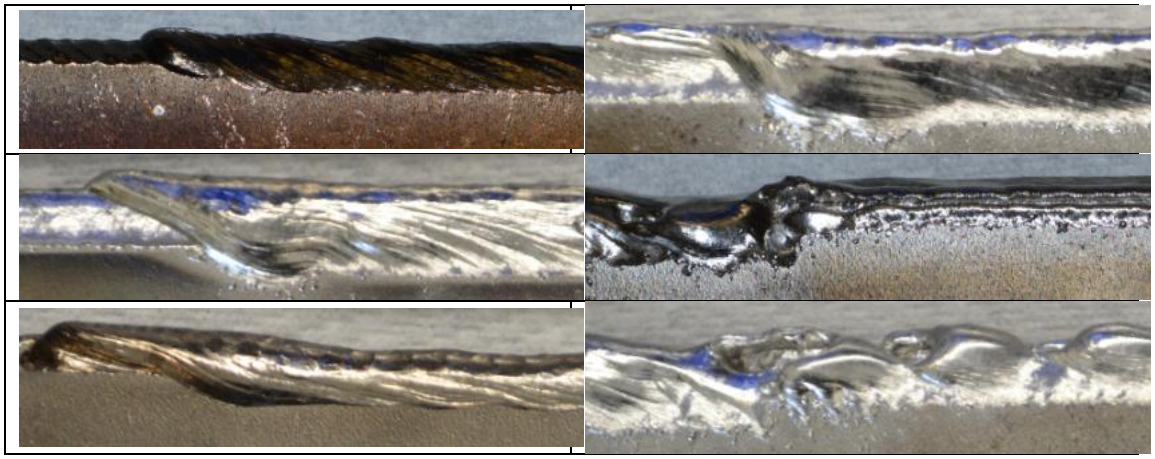

Figure 44. Close up of transitions in thin wall deposition. Left column from top to bottom: experiment 1, 2, 3. Right column from top to bottom: experiment 4, 2R, 4R. Travel velocity is from left to right.

An example of the polished sections of the experiment lines can be seen in Figure 45, below. Additionally, all images used in the analysis are included in Appendix B. Experiment lines were sectioned perpendicular to the travel direction, polished, and

etched to show the resulting microstructure. This allows the extent to which the wall was melted to be determined. As mentioned with the single bead experiments, the determination of the exact melt pool boundary can be difficult. This is because the beta transus temperature is much lower than the melting temperature and therefore microstructural transformation also occurring in the HAZ. The HAZ is the first guide for determining melt pool boundary, as it is the outer clear line seen in Figure 45. In addition to this, the point where the wall loses its straight edge can be used to help determine the melt pool boundary. From there a line is drawn that is qualitatively perpendicular to grain growth in order to determine the boundary of the melt pool.

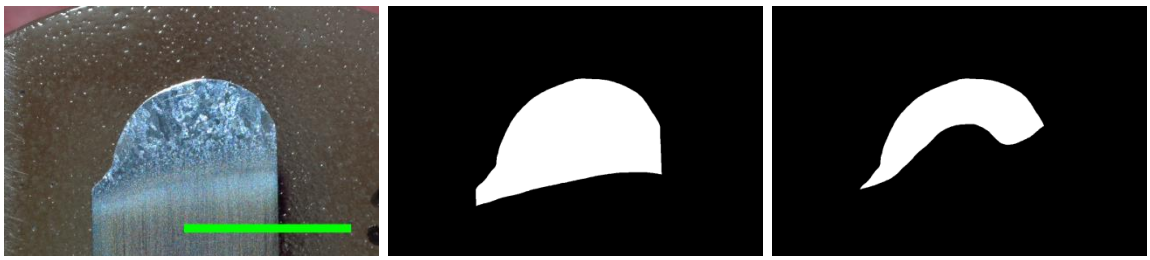

Figure 45. Polished cross-section (left) and the measurement of the heat affected zone (middle) and melted portion of the wall (right) for the initial steady state of experiment line 1. Green scale bar is 0.25 in.

Results of the measurements can be seen in Figure 46 and Figure 47 and show that there is a good correlation between the simulations and experiments. Some variability can be seen in the measurements and this can be due to several factors including waviness on the surface of the bead from movement of the molten material and inaccurate positioning of the beam on the thin wall. Regardless of the variability in the melt pool area measurements, however, the trend in the response behavior is quite clear and validates the results of the simulation work.

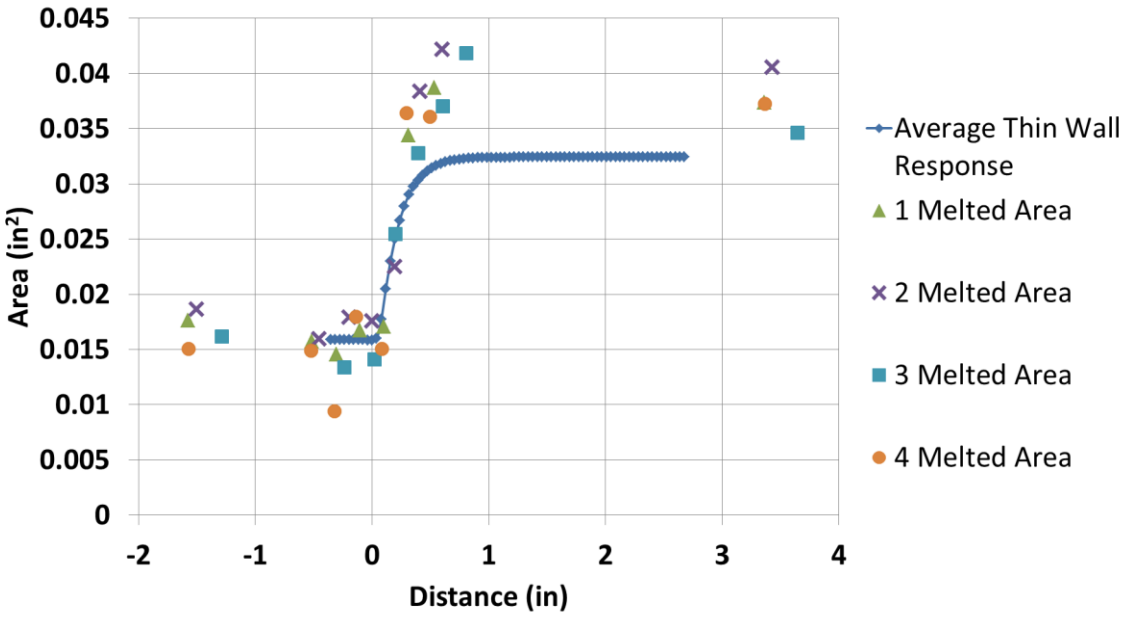

Figure 46. Comparison of thin wall experimental results and simulations for increases in area.

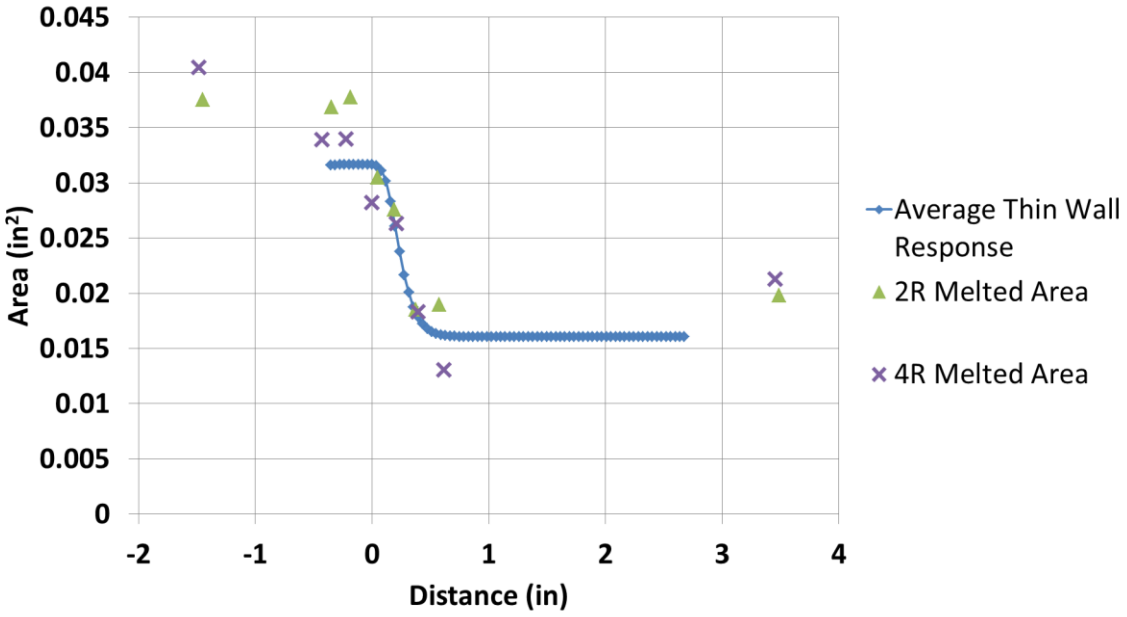

Figure 47. Comparison of thin wall experimental results and simulations for decreases in area.

3.3 Fitting of Transient Melt Pool Response for Thin Walls

3.3.1 Rule of Thumb Estimate

The previous chapter examined prediction of the melt pool behavior and compared the analysis to work completed by Aggarangsi [95]. Similar to the analysis presented in Chapter 2, rule of thumb generalizations can be determined based on the data presented in the previous section. For consistency with the previous chapter's rule of thumb estimates, effective depth is used for this analysis. While melt pools that are semi-circular are not expected in a thin wall geometry, the effective depth is a reflection of the melt pool area. This will keep the analysis consistent with the estimates for bulky parts and allow us to easily see the effect of geometry on response distance.

The comparison of this analysis to simulation data is summarized in Figure 48 and Table 13, below. It was found that decreases in area can be estimated by $2.9d_1$ and increases in area can be estimated by $2.3d_2$. Recall from the previous chapter that response distance can be estimated by $d_1 + 3d_2$ for decreases in area and $d_1 + 2d_2$ for increases in area in the single bead geometry. Therefore, the response distance for thin walls is dependent only on the larger of the two steady state areas (initial steady state for decreases in area and the final steady state for increases). This is different from the response distance for single beads, which is not only dependent on both steady state areas; it is more dependent on the final steady state for both increases and decreases. It should also be noted that the work by Aggarangsi in the laser powder stream system for stainless steel was not geometry dependent. That is, the equations for rule of thumb estimates presented were generalized to apply to both thin walls and bulky parts. For this

system and material, however, they are different for different geometries as well as increases in melt pool area versus decreases.

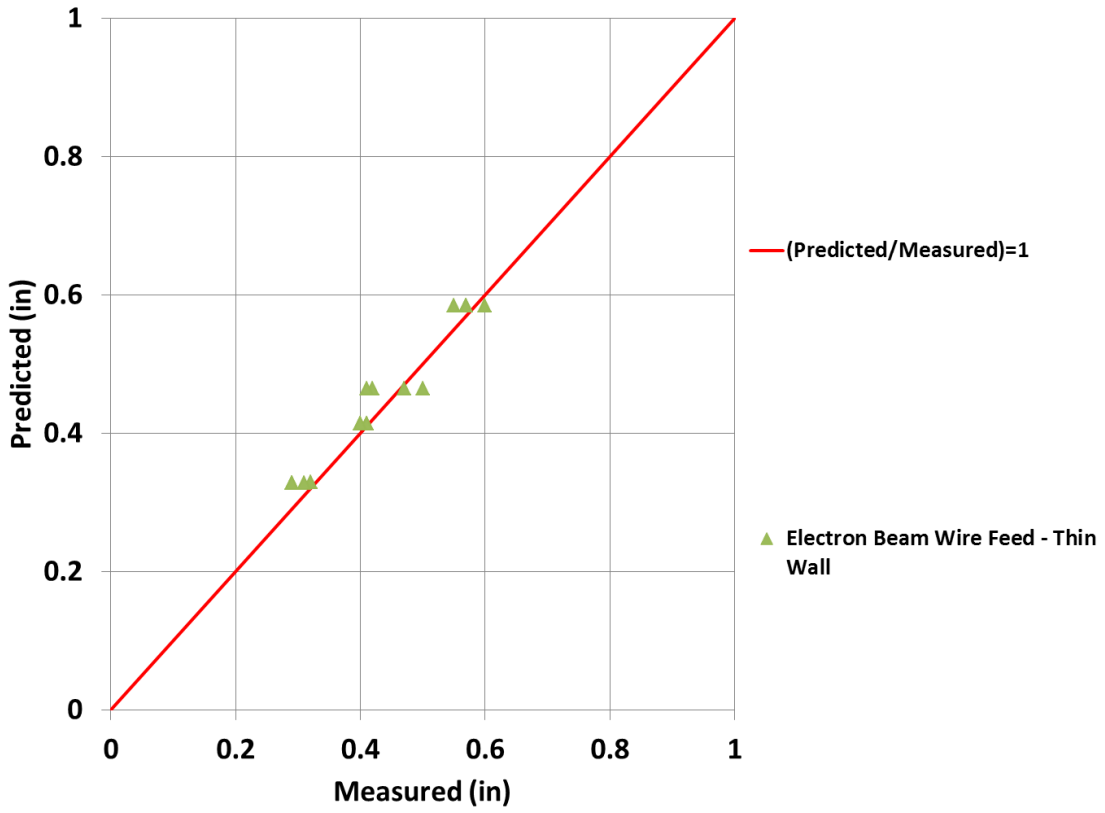

Figure 48. Predicted response distance versus measured response distance from simulation results.

Table 13. Comparison of Rule-of-Thumb estimates to simulation data.

	Simulation Details	Initial Effective Depth (in)	Final Effective Depth (in)	Response Distance (in)	Rule-of-Thumb Estimate (in)	Percent Error (%)
Decrease in Area	Green to Red @ 7.8 in/min	0.20	0.14	0.60	0.585	-3.1
	Green to Red @ 16.9 in/min	0.20	0.14	0.57	0.585	2.2
	Green to Red @ 26.0 in/min	0.20	0.14	0.57	0.585	2.4
	Green to Red @ 3000 W	0.20	0.14	0.55	0.585	7.3
	Red to Blue @ 17.6 in/min	0.14	0.10	0.41	0.414	0.3
	Red to Blue @ 35.1 in/min	0.14	0.10	0.40	0.414	2.2
	Red to Blue @ 52.7 in/min	0.14	0.10	0.41	0.414	0.5
	Red to Blue @ 3000 W	0.14	0.10	0.40	0.414	3.7
Increase in Area	Blue to Red @ 17.6 in/min	0.10	0.14	0.32	0.329	2.1
	Blue to Red @ 35.1 in/min	0.10	0.14	0.29	0.328	12.2
	Blue to Red @ 52.7 in/min	0.10	0.14	0.29	0.328	12.9
	Blue to Red @ 3000 W	0.10	0.14	0.31	0.328	5.0
	Red to Green @ 7.8 in/min	0.14	0.20	0.50	0.464	-7.8
	Red to Green @ 16.9 in/min	0.14	0.20	0.42	0.464	9.5
	Red to Green @ 26.0 in/min	0.14	0.20	0.41	0.464	12.8
	Red to Green @ 3000 W	0.14	0.20	0.47	0.464	-0.7

3.3.2 Fitting of Transient Response Behavior

With the rule of thumb estimate defined, formulas for the prediction of the behavior can be determined in the same manner as was done for single beads. Again, it was

important to capture the s-curve shape seen in the response behaviors. Thus as a starting point, the modified equation for a cumulative distribution function of a Gumbel distribution is used, as seen in (3) below.

(3) $$\mathbf{F(x) = Ae^{-e^{-(x-\mu)/\beta}} + C}$$

Where *C* is an offset used to increase the bounds of the s-curve and *A* is a multiplier used to increase the gap between the upper and lower bound. Excel's solver tool can be used to fit parameters in the function to the average data curves from Figure 39 by minimizing the squared difference between the function and the data. The resulting parameters from this fitting are listed in Table 14 and the predicted curves are compared to simulation results in Figure 49.

Table 14. Parameters for prediction of melt pool behavior.

	A	***μ***	***β***	***C***	**Initial Area (in^2)**	**Final Area (in^2)**	**Difference in Area (in^2)**
Red to Green	0.03216	0.13039	0.13218	0.03150	0.0320	0.0638	0.0319
Green to Red	-0.03186	0.29962	0.12198	0.06381	0.0640	0.0321	-0.0319
Blue to Red	0.01595	0.14347	0.12585	0.01597	0.0162	0.0320	0.0159
Red to Blue	-0.01577	0.33220	0.11926	0.03184	0.0320	0.0162	-0.0158

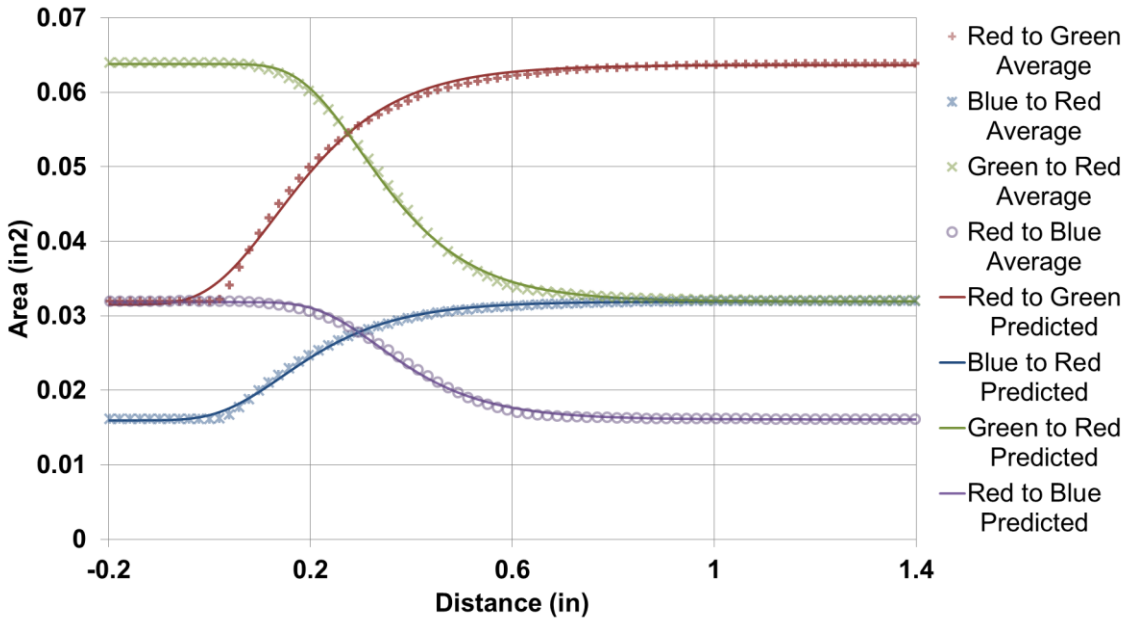

Figure 49. Comparison of predicted behavior to simulation results.

From Figure 49, it is apparent that the parameters for the selected equation accurately predict behaviors. The accuracy of the fit can also be confirmed by the coefficient of determination, R^2, which did not go below a value of 0.92 for any curve. Table 14 shows that the multiplier, A is approximately equal to the difference in area and the offset, C is approximately equal to the difference in area, however, appropriate correlations for μ and β have not yet been determined and more combinations of initial and final area simulations would be required to determine if a correlation exists for these variables.

3.3.3 Suggested Application to Feedback Control Systems

As with the analysis of single beads, it is important to understand the application of data presented on response distance in thin walls to feedback and feedforward control systems. Recall that because the start of the change in melt pool area does not necessarily correspond with the point at which the step change in process parameters is initiated the calculation of response time is not as simple as dividing the response distance by the

travel velocity. However, using the same methods as presented for single beads in Chapter 2, a rule of thumb can be developed based on the response distance plus some fraction of the final L' value minus some fraction of the initial L' value. The reason a fraction of the initial L' value is subtracted from the distance is to account for the fact that the melt pool area responds to the step change at a point in on the build path prior to where the step change is initiated.

Using this method and Excel's solver function to minimize the squared difference between the estimate and actual values, a rule of thumb was determined. The results of this analysis are presented in Figure 50 and Table 15, below. The equation used to determine the estimate was [Response Distance – (0.2 × Initial L') + (0.2 × Final L')] for increases in area and [Response Distance – (0.1 × Initial L') + (0.2 × Final L')] for decreases in area. From the data presented in Figure 50 and Table 15, it is clear that the predicted values for response time are in good agreement with the measured values (especially for increases in area).

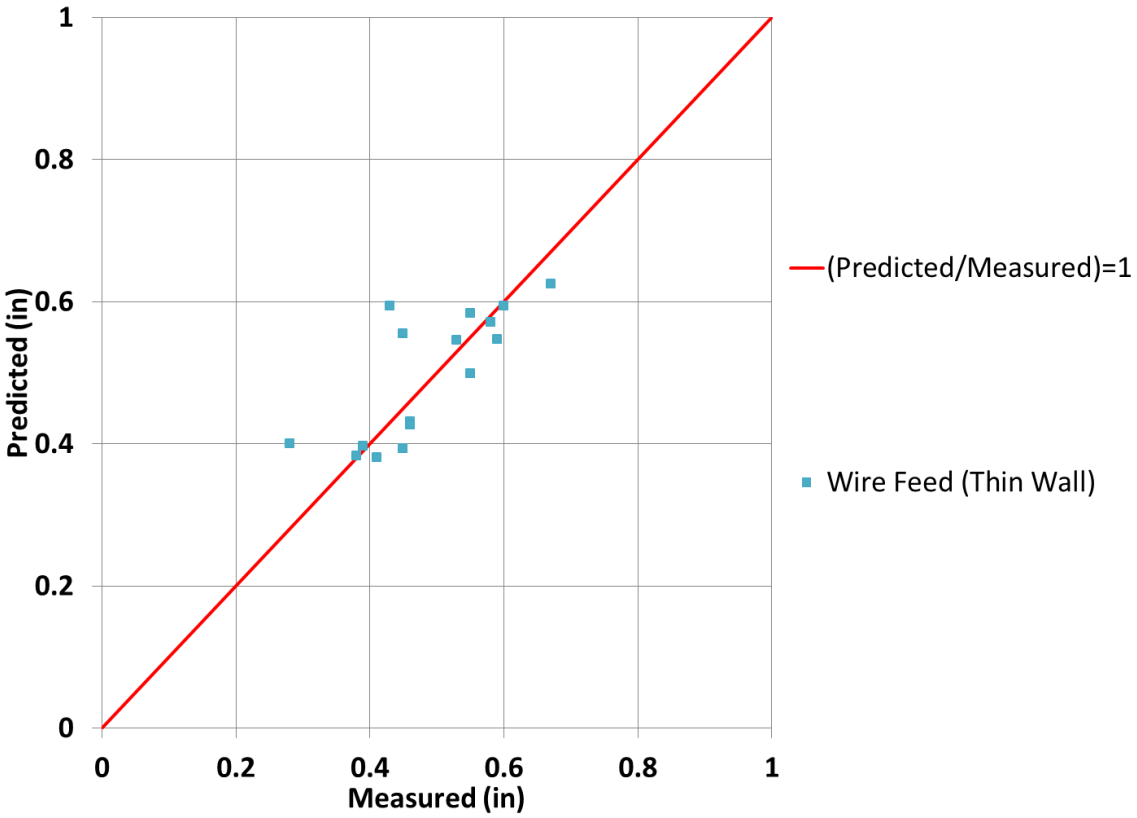

Figure 50. Predicted response time versus measured response time from simulation results.

Table 15. Comparison of response distance and response time via rule of thumb.

	Initial L' (in)	Final L' (in)	Response Time × Velocity (in)	Response Distance (in)	Estimated Response Time × Velocity (in)	Percent Error (%)
Blue to Red @ 16.4 in/min	0.05	0.20	0.39	0.32	0.397011	0.9
Blue to Red @ 30.4 in/min	0.10	0.37	0.46	0.29	0.431122	-5.6
Blue to Red @ 44.4 in/min	0.15	0.56	0.55	0.29	0.498787	-6.7
Blue to Red @ 3000 W	0.17	0.33	0.46	0.31	0.42713	-5.3
Red to Green @ 8 in/min	0.04	0.22	0.55	0.50	0.58414	5.0
Red to Green @ 15.5 in/min	0.09	0.39	0.58	0.42	0.571362	-1.6
Red to Green @ 23.1 in/min	0.13	0.56	0.67	0.41	0.624559	-4.8
Red to Green @ 3000 W	0.15	0.35	0.60	0.47	0.59421	-0.9
Red to Blue @ 16.4 in/min	0.20	0.05	0.43	0.60	0.594676	39.3
Red to Blue @ 30.4 in/min	0.37	0.10	0.45	0.57	0.555484	22.9
Red to Blue @ 44.4 in/min	0.56	0.15	0.53	0.57	0.545747	3.0
Red to Blue @ 3000 W	0.33	0.17	0.59	0.55	0.547521	-7.0
Green to Red @ 8 in/min	0.22	0.04	0.28	0.41	0.400149	40.9
Green to Red @ 15.5 in/min	0.39	0.09	0.38	0.40	0.383049	-0.4
Green to Red @ 23.1 in/min	0.56	0.13	0.41	0.41	0.381355	-7.5
Green to Red @ 3000 W	0.35	0.15	0.45	0.40	0.393761	-13.2

As with the single bead, the response distance can be used in feedback control systems, regardless of the ability to predict the response time for decreases in area. While the change in melt pool size will not be instantaneous, once the system senses the change

in melt pool, the distance to the new steady state is then known regardless of the change in L' or the point in which the step change is initiated.

3.4 Corner Geometry FEM

3.4.1 Corner Geometry Finite Element Analysis

Prior analysis in this dissertation has focused on steady state geometries or geometries such that if all parameters are held constant the size and shape of the melt pool remains constant as it moves through the geometry. In this section, focus is shifted to transient geometries or geometries that are the cause of a change in melt pool dimensions when all other parameters are held constant. Examples of transient geometries include internal/external corners, approaching/leaving a free edge, changes in beam direction at any angle, or changes in wall thickness; however, the focus of this analysis will be on an external corners. An example of an external corner can be seen in Figure 51 below.

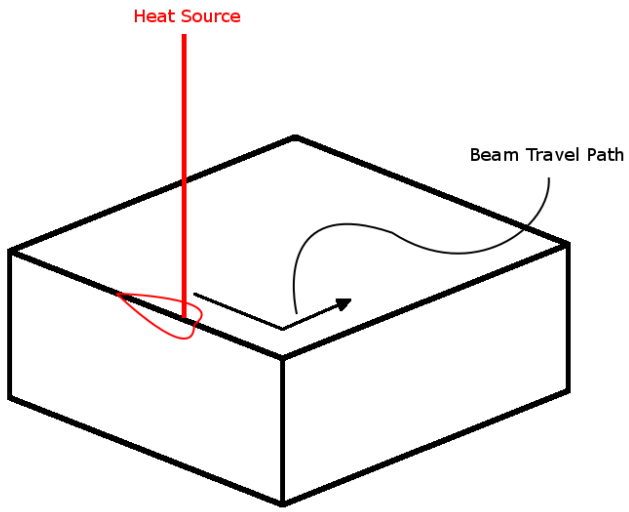

Figure 51. Example of an external corner geometry.

Prior work by Anvari and Beuth made use of 3D finite element models to investigate the change in melt pool depth through the corner geometry; reporting that the corner can

increase the melt pool depth by more than 50% [100]. For these results, concentrated heat flux at the edge of the substrate was used to replicate the heat source and all other parameters were similar to the single bead simulations presented in this dissertation. Initial results from this work can be seen in Figure 52 below. This figure depicts the maximum melt pool depth at points around the corner, regardless of where the heat source is located. This would be equivalent to sectioning an experiment sample and viewing the maximum depth at the edge after the experiment has been performed.

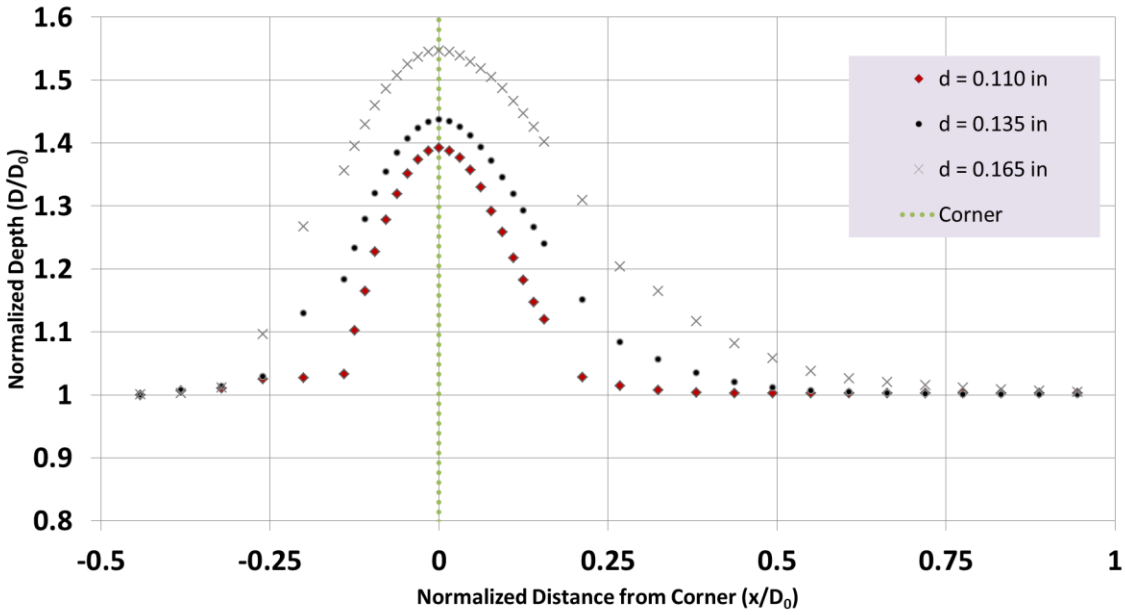

Figure 52. Melt pool depth through the corner.

To advance this work, new 3D finite element models were created to be run in the ABAQUS software package. An example of the geometry can be seen in Figure 53 below and additional settings for the simulations are the same as for single bead simulations presented in this dissertation.

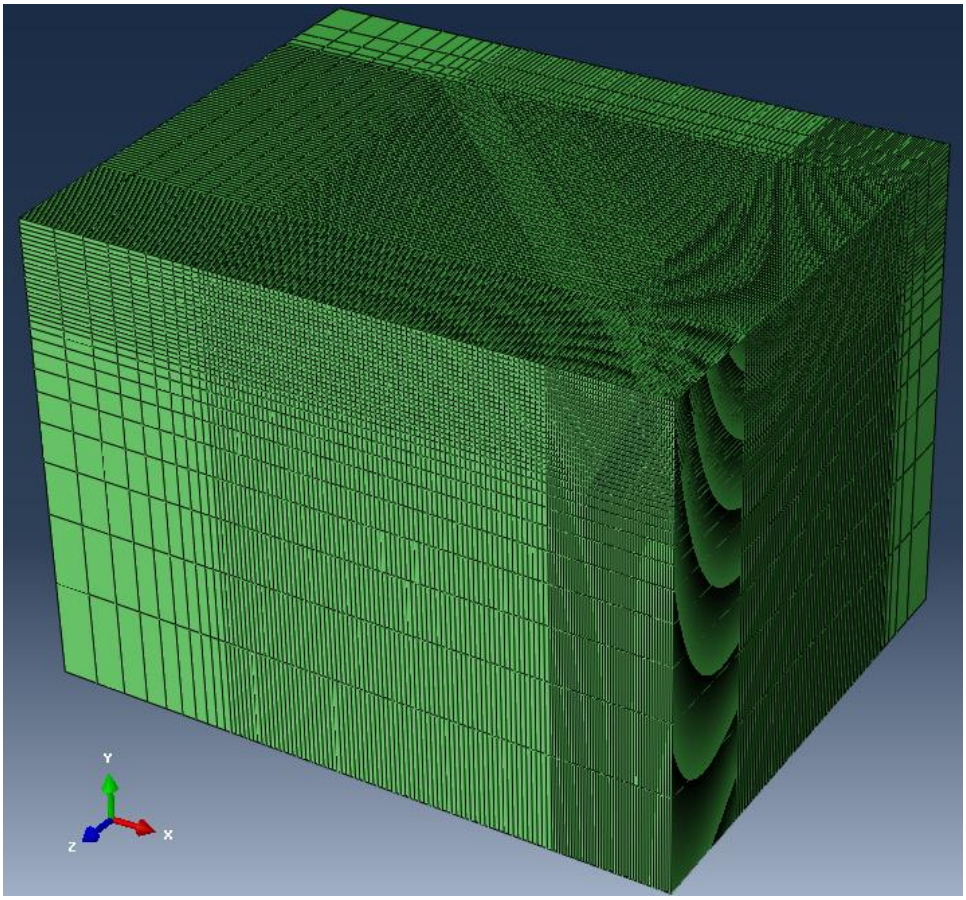

Figure 53. Example model for corner geometry.

The focus of this study will be to maintain melt pool depth through the transition. As a starting point, several simulations were run to determine the P-V Process Map for the maximum depth at the corner. This process map can be seen in Figure 54 below. The depth values for this figure are based on depth values for Green, Red, and Blue (0.064 in^2, 0.032 in^2, 0.016 in^2). So the purpose of Figure 54 is to determine power and velocity combinations (held constant through the entire simulation) that lead to maximum melt pool depths of 0.20 in^2, 0.14 in^2, and 0.10 in^2 respectively.

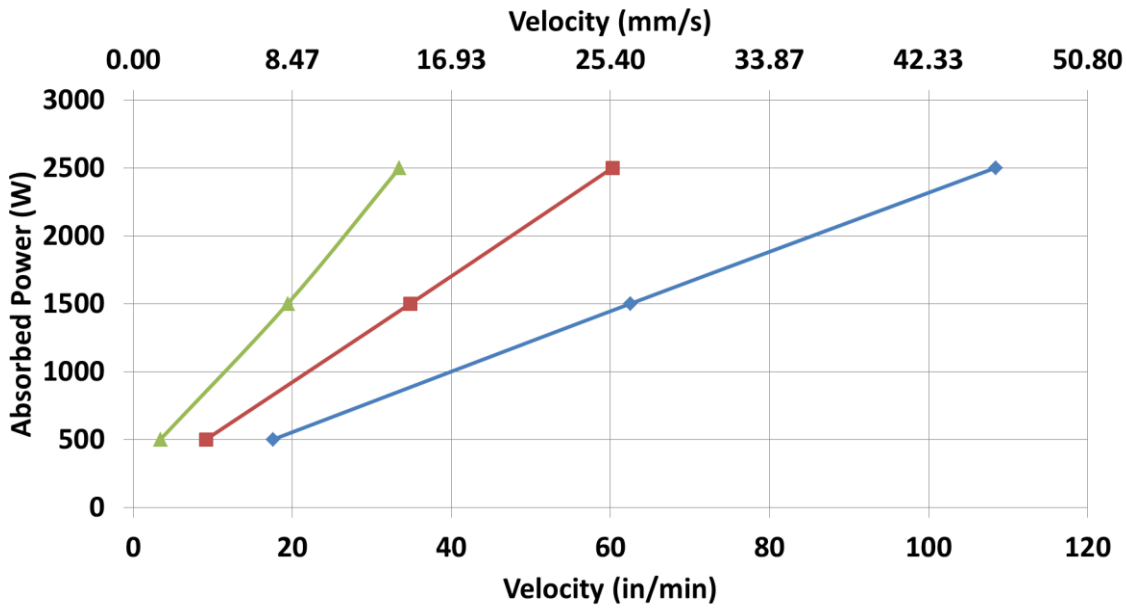

Figure 54. P-V Process Map for maximum depth in an external corner geometry.

This initial analysis was meant to determine a starting point for a priori melt pool control. The hypothesis is that if you know where in the process map the maximum depth occurs, then the user or designer of a control system can use knowledge of the transient response to develop feedforward control. The power-velocity combination of 1500 W and 25.5 in/min were chosen for the analysis as it is in the center of the free edge P-V Process Space. Initial attempts were to drop the power at the point where the melt pool depth began to change (Control Scheme 1). This is a common practice for control approaches to prevent over-melting. Additionally, control schemes that decrease the power a distance of three depths away from the corner (Control Scheme 2) and a distance of 4 depths before the corner (Control Scheme 3). To remove the effect of thermal energy coming from the heat source after it has gone around the corner, the power is held constant after the corner and schemes to control melt pool size in that section of the build can be determined after a scheme for controlling the maximum melt pool depth is determined. The power value

of 1135 W was chosen because this is the point in the maximum corner depth P-V Process Map (Figure 54) that has the desired maximum depth at 25.5 in/min.

As seen in Figure 55 below, this did not achieve the desired results, however, as these changes decreased the melt pool area too early and did not decrease the maximum value enough. The reason the maximum depth was not decreased enough was because the maximum depth process map was determined with constant power and velocity through the corner. Thus, it cannot be used to determine the amount of power decrease required as the larger melt pool on the edge as you approach the corner leads to more stored heat in the model and larger melt pools at the corner. The process map can, however, be used to determine how much the melt pool will increase as you go around the corner. End users can then use this knowledge to determine if that will still lead to an acceptable build or if it needs to be accounted for through control approaches.

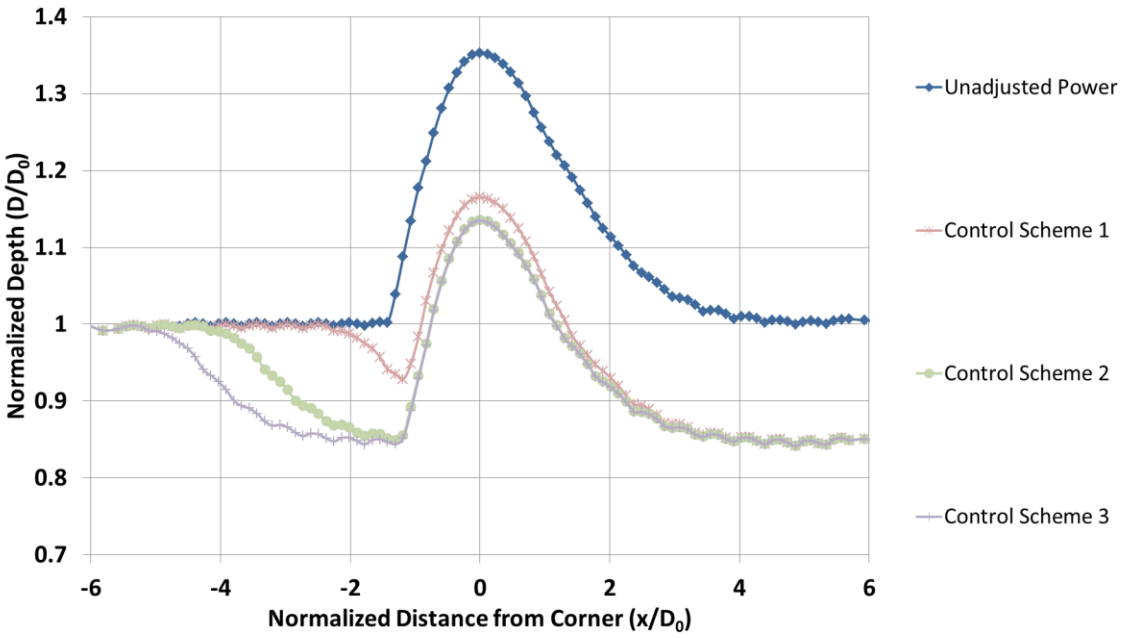

Figure 55. Normalized maximum melt pool depth from decreasing power as a control scheme.

The second attempt was to decrease beam power based on the increase in melt pool depth. This approach was similar to the one used in work by Aggarangsi et al. [96]. Several attempts were made and are detailed in Figure 56. This control approach was based on dividing the power (1500 W) by the normalized melt pool penetration depth (D/D_0). This was an iterative process, so once new melt pool depths were determined, those values were used to refine the power settings again. As seen in Figure 57, this did not have the same effect as Aggarangsi et al. [96] and, after the second iteration, the approach scheme began to diverge. Also, of the schemes listed in Figure 56, Control Scheme 5 performed the best. Thus, the same change in power was used but it was initiated prior to the point where the melt pool begins to change size, as this was successful in the work by Aggarangsi et al. [96]. The power values can be seen in Figure 56 and resulting melt pool depth can be seen in Figure 57.

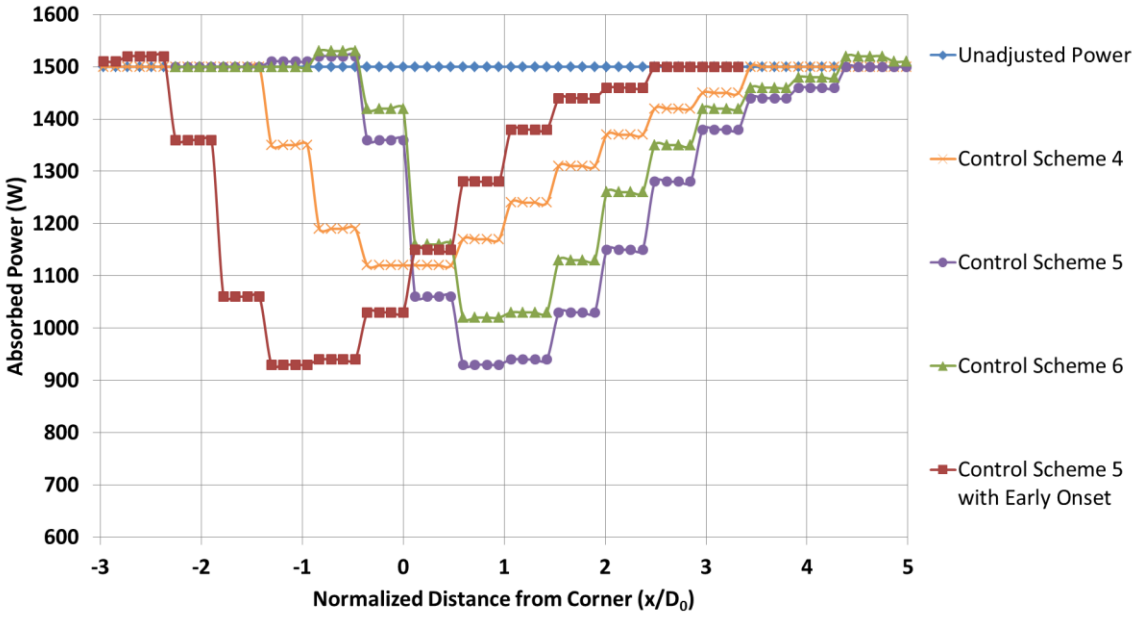

Figure 56. Control approaches based on increase in melt pool depth.

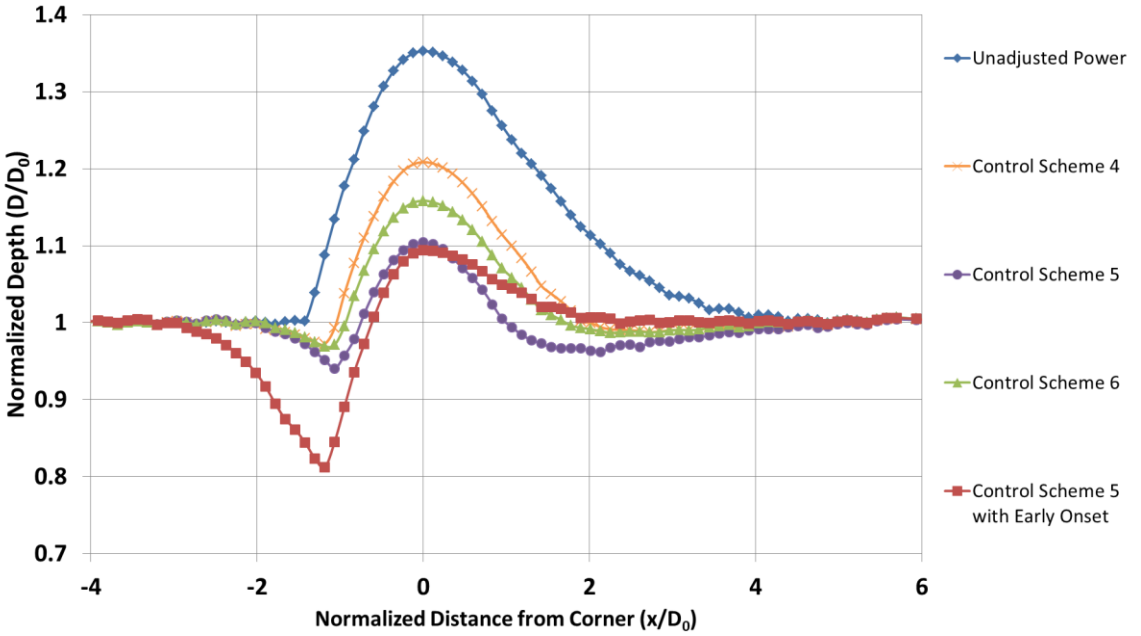

Figure 57. Normalized maximum melt pool depth based on control approaches from Figure 56.

With little success in these control approaches, the decision was made to take more of a "process mapping" approach to this control scheme. The primary goal was to keep the melt pool depth within ±5% of the desired value. Using the free edge process map, it was determined that a power decrease to 1370 W at constant velocity would keep the depth within the desired limit. Using the knowledge that the melt pool should require 3 or 4 melt pool depths to transition from 1500 W to a new steady state at 1370 W (from the single bead results), a step change in power was initiated approximately 4 melt pool depths before the corner (Control Scheme 7). To remove the effect of thermal energy coming from the heat source after it has gone around the corner, the power is held constant after the corner and schemes to control melt pool size in that section of the build can be determined after a scheme for controlling the maximum melt pool depth is determined. In addition to this, three simulations were run with the same drop to 1370 W and also a drop to 930 W two steps before the detected increase in melt pool depth (Control Scheme 8), at the step where the increase in melt pool depth is detected (Control

Scheme 9), one step before the corner (Control Scheme 10), and at the corner (Control Scheme 11). The beam power in these simulations continued at 930 W after turning the corner. The results of these simulations are presented in Figure 58 below.

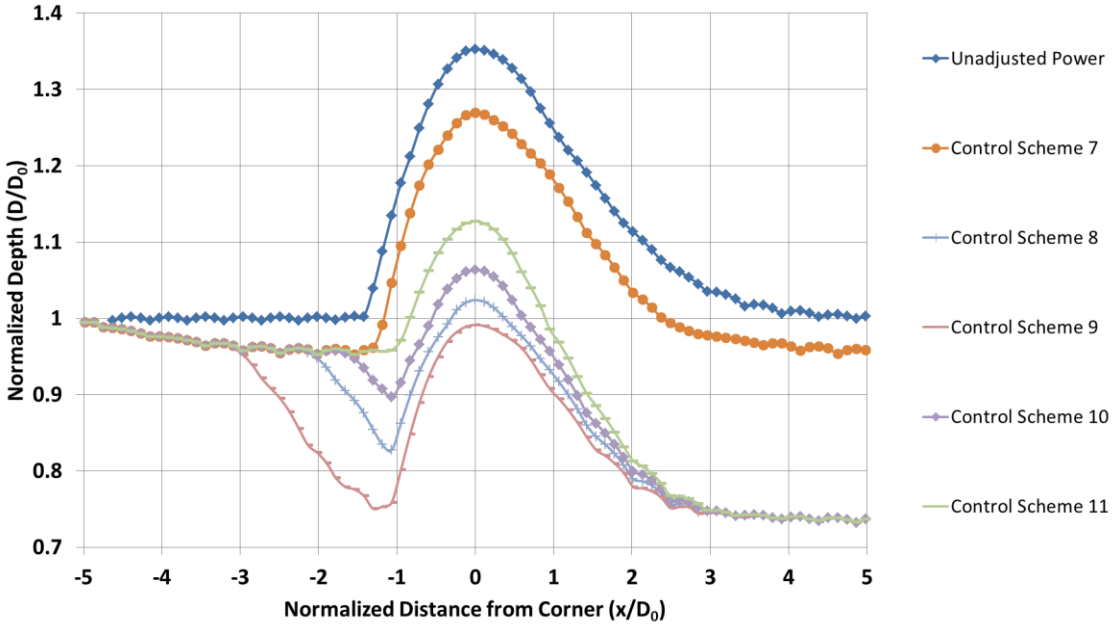

Figure 58. Normalized maximum melt pool depth for control approaches.

From this analysis, it was observed that the only simulation to not display a significant decrease in melt pool depth prior to reaching the corner was Control Scheme 11. This simulation did not decrease to 930 W until the heat source reached the corner. Thus, an attempt was made to only drop the power at the corner. These simulations stayed at 1500 W and then dropped to 730 W, 630 W, and 530 W (Control Scheme 12, 13, and 14, respectively) at the corner to determine the best value to use in later simulations. The result of these simulations can be seen in Figure 59 below.

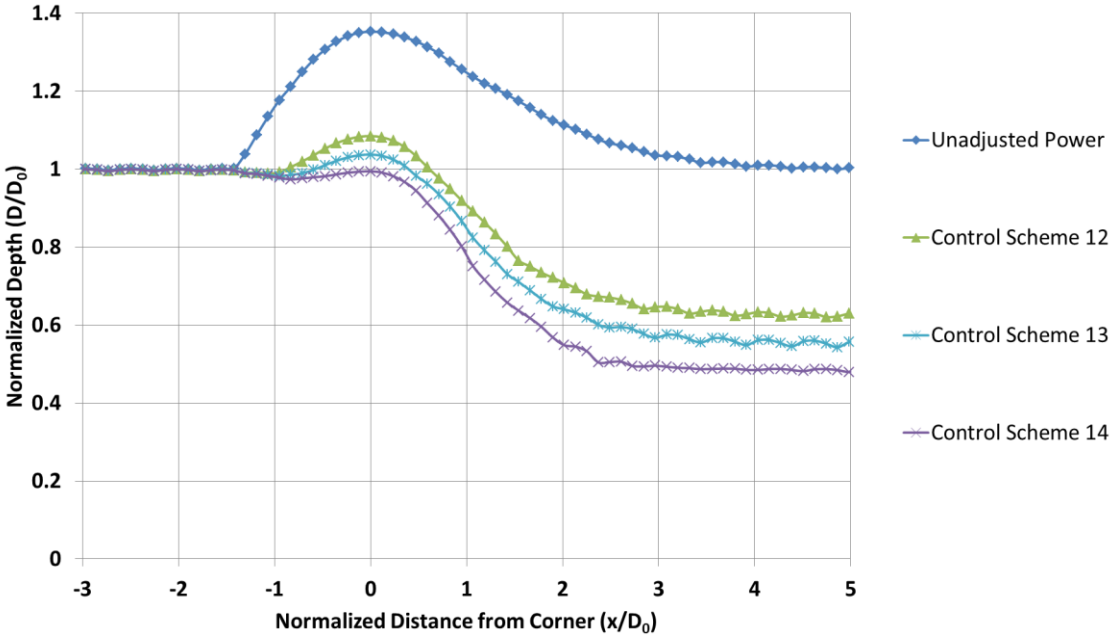

Figure 59. Normalized maximum melt pool depth for control approaches.

From these simulations it was determined that the control scheme should drop the beam power to 525 W and then increase it after the corner. These control schemes are detailed in Figure 60 and the results can be seen in Figure 61 below.

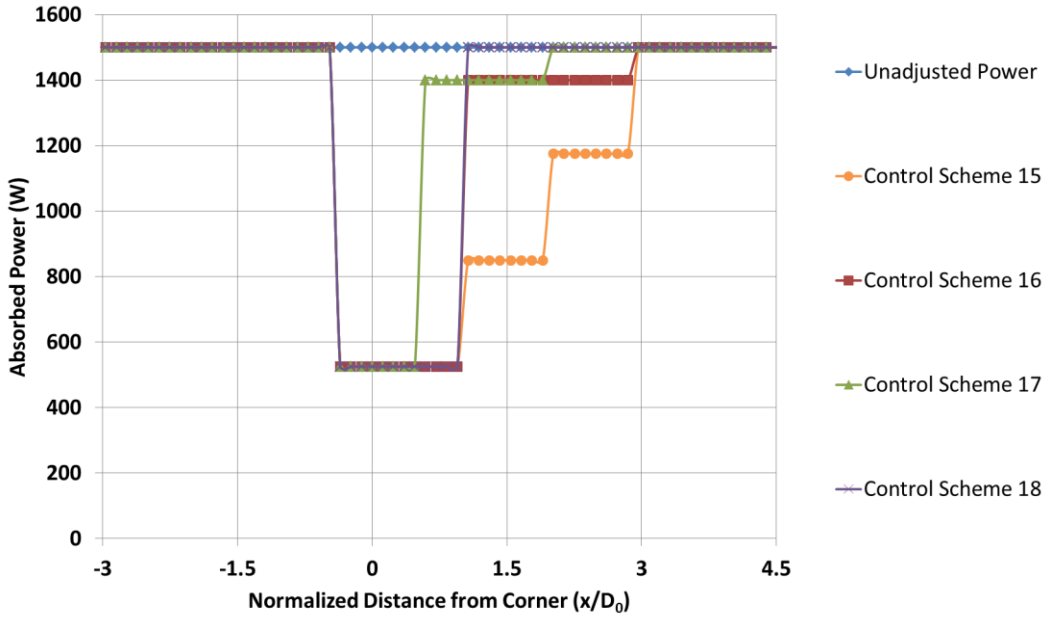

Figure 60. Control approaches for maintaining consistent melt pool depth in an exterior corner geometry.

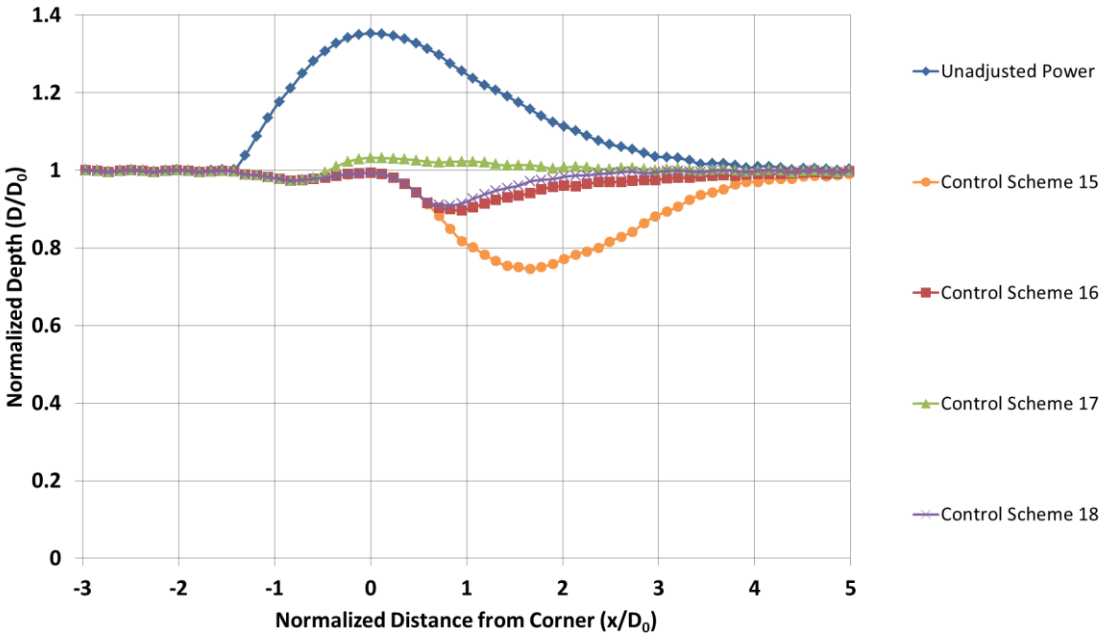

Figure 61. Results from control approaches in Figure 60.

From this approach, it is clear that keeping the maximum depth within ±3.5% of the original melt pool depth is possible by using Control Scheme 17.

3.4.2 Suggested Application to Feedback Control Systems

As with the thin wall and single bead geometries, it is important to discuss control approaches and how the information presented in this chapter can be leveraged toward their development. In the steady state geometries that have been studied in this dissertation, an important component of determining response time for the development of feedback control systems has been L'. This is because the location at which the melt pool begins to change size is often before the location where the step change in process parameters is initiated. In the corner geometry it was hoped that this could be advantageous for control schemes; however, if the approach relies on tracking the melt pool width or melt pool depth, the position of the beam is already past the corner by the time a change in either can be detected. Therefore feedback control may not be possible

in the corner geometry. However, feedforward control approaches have proven very successful; keeping the melt pool geometry within ±3.5% of the desired melt pool depth.

3.5 Discussion

In this chapter, the effect of geometry on melt pool response was explored and control approaches were applied to a transient geometry (an external corner). In the analysis of the thin wall geometry, two-dimensional finite element simulations were developed and run in the ABAQUS software package. Simulations were performed to develop a P-V Process Map for thin wall as well as analyze step changes between curves of constant area (analogous to methods used for analyzing single beads). Experiments were performed at the NASA Langley research center on their EBF^3 system, which validated the results of simulations.

As with the single bead analysis, potential sources of error in the simulations include the neglecting of physical phenomena through which heat can be removed from the system (such as melt pool convection and radiation); however, prior work has found this to be minimal when compared to conduction through the substrate. Additionally, the measurement of the melt pool area in the analysis of experiments is another source of error. As described in section 3.2, it can be very difficult to determine the exact boundary of the melt pool because of microstructural development occurring at temperatures below the melt temperature (in the HAZ). Regardless of these issues, the behavior seen in the experimental measurements closely matched the expected results, which validates the simulations presented.

Through this analysis, it was found that the response times are on the order of seconds and show little correlation, which is consistent with the results from the single bead analysis. As such, this would represent a limiting factor in the development of feedback control systems as the response time is orders of magnitude larger than the time required to initiate a change in beam power or travel velocity. Similar to single beads, it was found that response distances show a strong correlation and that the response distance and response behavior is the same regardless of path or position taken in the P-V Process Map when moving between the same curves of constant area. Response behavior was also compared to behavior seen in the single bead geometry and it was found that increases in area transitioned in a shorter distance and decreases transitioned in a longer distance for the thin walls. This was attributed to the restricted pathways for heat to conduct away from the heat source in the thin wall geometry.

Additionally, the prediction of response behavior, response distance, and response time was analyzed. Similar to the single bead work, response behavior can be predicted through a modified cumulative distribution of a Gumble distribution. While the behavior can be predicted very accurately, not enough information was available to derive physical meaning from several of the fitting parameters.

Prior work in the laser powder stream system for stainless steel found that prediction of response distance was not geometry dependent [95]. In this work, however, analysis found that the response distance for the wire feed electron beam system was geometry dependent. Also, it was found that the response distance was dependent only on the larger steady state effective depth, which was not the case for the single bead geometry or the laser powder stream system analyzed in prior work by Aggarangsi. Also, using response

distance in conjunction with the initial and final L' values associated with the steady state melt pool geometry led to an accurate prediction of the response time.

Response distance and response time are important parameters for the development of feedback and feedforward control systems. The work in this chapter of the dissertation gives a strong understanding of response behavior for a thin wall geometry in the wire feed electron beam system for Ti-6Al-4V and aids in the development of these control systems. As with the single bead work, it is apparent that step changes with matching initial and final steady state melt pool effective depths respond similarly as they transition. The explanation for this behavior is that the melt pool must move a certain *distance* after an abrupt change in beam power or beam velocity to achieve a new steady-state depth and that distance is largely governed by the initial and final melt pool sizes (melt pool depths or cross sectional areas), regardless of the initial and final power and velocity combinations.

Based on these findings, the response distance and response time can be ***predicted*** for a new system and/or material by fitting the multiples of key features of the steady state melt pool geometry (d_1, d_2, L'_1, and L'_2) to a small set of simulations (or even a single simulation) and extrapolating to cover the entire process space.

In the analysis of the corner geometry, the change in melt pool depth due to the presence of the corner was explored and held steady through the use of control schemes. In previous work, it was found that the melt pool depth can increase by over 50% as the melt pool passes through the corner geometry [100]. To account for this, several control schemes were explored. Traditional control schemes of simply decreasing power before

the corner or once a change in melt pool parameters is detected were not effective and melt pool depth deviated more than ±15%. Control approaches based on the detected change in melt pool depth were also found to be ineffective. That type of control scheme would be used in an iterative fashion where the part is built once and then rebuilt with adjusted power to control melt pool size during the subsequent builds. However, by changing the power the amount of heat stored in the system is also affected, making it difficult to accurately control melt pool size without multiple iterations. The best of these control schemes still suffers from a decrease in melt pool depth of 6.8% before the corner and an increase of 20.9% at the corner.

The next approach was to use knowledge of the process map to decrease power well before the corner and hold the melt pool at an acceptable lower limit (±5% of the desired depth value). Also, the distance before the corner a second decrease in power could be performed to prevent the melt pool from further decreasing in size was tested. It was determined that to prevent the melt pool depth from decreasing more than desired, the beam power could not be decreased prior to reaching the corner in the simulation. Thus, the power was held at 1500 W and adjusted only at and beyond the corner to determine the power drop necessary to prevent the melt pool area from increasing (525 W).

With the drop in power at the corner determined, the next step was to explore increases in beam power back to 1500 W after the corner while minimizing the effect on the size of the melt pool. Several attempts were made and it was determined that increasing to 1400 W approximately 60% of a depth out from the corner, and 1500 W approximately 200% of a depth out from the corner kept the melt pool depth within ±3.5% of the desired value. These findings have shown that feedback control approaches

may not be possible, but feedforward control can be used to maintain desired melt pool depth.

It is suspected that the control schemes that were successful in the work by Aggarangsi did not have the same result in this work because of the presence of L'. In the work by Aggarangsi, the velocities and powers are low enough that the melt pools approximate hemispheres and have L' values close to zero. Thus, a large quantity of heat moves ahead of the melt pool causing the dimensions to change before the heat source reaches the change in geometry and must be accounted for prior to any detectable change in the melt pool dimensions. In this system, there is a significant L' measurement in the melt pool dimensions. Thus, much less heat moves ahead of the heat source requiring the change in process parameters to occur at the corner to be effective (rather than requiring a change well before the change in geometry). However, the change in geometry still must be accounted for prior to any detectable change in the melt pool dimensions as seen by the control schemes presented. This is also due to the presence of L'. The distance between the heat source and the maximum melt pool area and the heat source (L') means that the melt pool depth at a given point is still developing well after the heat source has passed that point. Thus, feedback control is not feasible and feedforward control is required. This is likely the case for any system with a significant L' measurement in the melt pool. Future work should expand on the range of desired melt pool depths to determine the relationship between the size/shape of the melt pool and the changes in power required for the control scheme. It is expected that the magnitude of the decrease in power at the corner and the scheme for returning to the original power setting after the corner is dependent on the steady state melt pool geometry (for example, steady state

melt pool depth and/or L'). Additional testing would be required to confirm this hypothesis.

Finally, it is also suggested to monitor additional parameters, such as melt pool width and length to determine if similar control schemes can be used (alone or in conjunction with melt pool depth control) to maintain the consistency of these parameters through the corner geometry.

Chapter 4 Extension to Additional Systems

While results for the wire feed electron beam based system have been important, this system only represents a fraction of the AM technology available. In addition to this, it only represents a portion of the space for all AM (as seen in Figure 62, below). As such it is important to apply concepts from previous chapters to additional systems in AM. This chapter will explore transient response in the electron beam powder bed system with Ti-6Al-4V through finite element modeling and experimental analysis. In this system, due to the high beam travel velocities, it is expected that the melt pool response times no longer represent a limiting factor for feedback control systems (that is, they should be on the order of milliseconds) and the electron beam powder bed system is capable of resolutions on the order of the melt pool depth. However, the results presented in previous chapters have shown that the response distances can be on the order of several melt pool depths. Thus, an understanding of the transient response melt pool is required to maintain quality in the build.

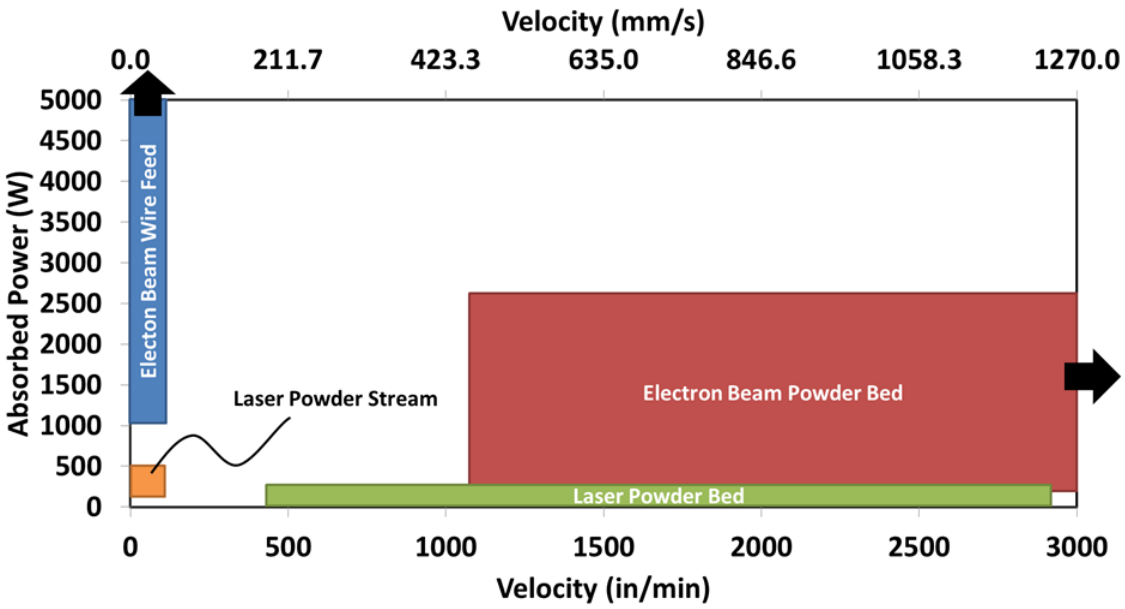

Figure 62. P-V process space for all Direct Metal AM.

4.1 Electron Beam Powder Bed Finite Element Analysis

For this analysis, 3D finite element simulations were developed and run in the ABAQUS software package. These simulations contain the same settings as the single bead electron beam wire feed simulations from Chapter 1 except for the following differences: The simulations in this chapter do not contain added material, the initial temperature of the model is set to 1023 K, the base of the model is held constant at 1023 K, and the size scale has been changed to accommodate the expected melt pool size of this system. The reason the simulations did not contain added material was to remove the complexity of modeling the powder particles and create an initial proof of concept for applying the concept from the electron beam wire feed system to this system. 1023K is used for the base and initial temperature in the system as this temperature is typically used as the preheat temperature in practice. An example of the model can be seen in Figure 63, below.

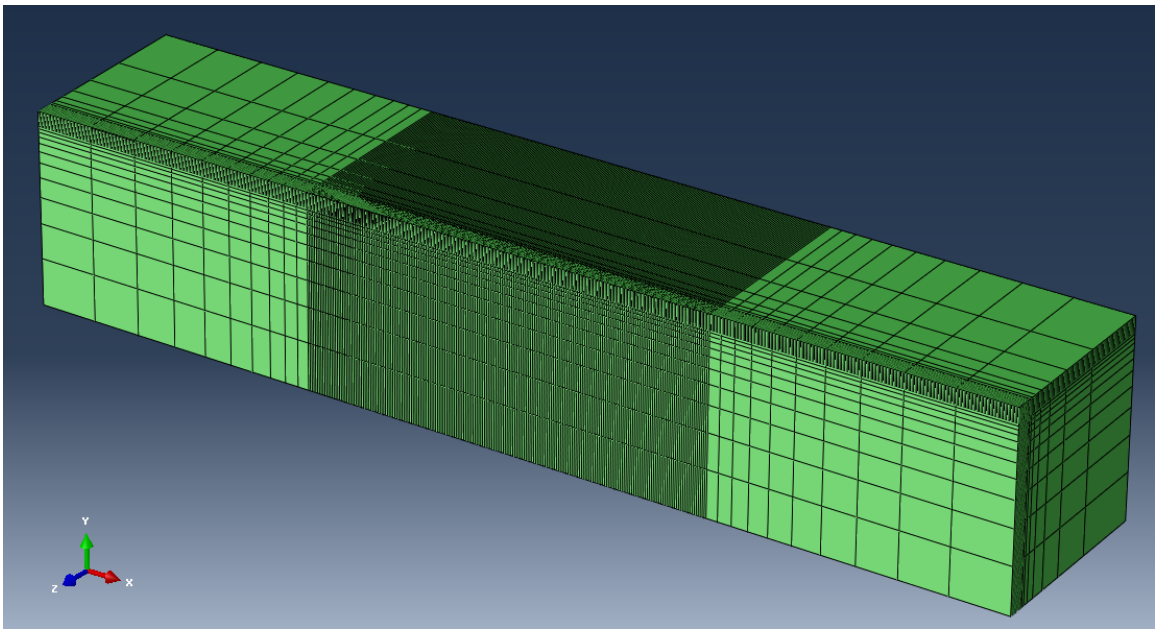

Figure 63. Example model for electron beam powder bed simulations.

Prior to this work, no P-V Process Map had been created for this system. Thus, simulations at several power and velocity combinations were run to determine the P-V Process Map for melt pool area and *L/d* seen in Figure 64, below. From this figure it is apparent that the melt pool areas are much smaller than in the electron beam wire feed system and the length to depth ratios are much larger, both as expected. Additionally, the trend in the curves is similar to the ones for the wire feed electron beam system. Curves of constant area are relatively straight and span diagonally across the process space from low power and low velocity to high power and high velocity. Curves of constant *L/d* intersect with, and have more curvature than, the curves of constant area.

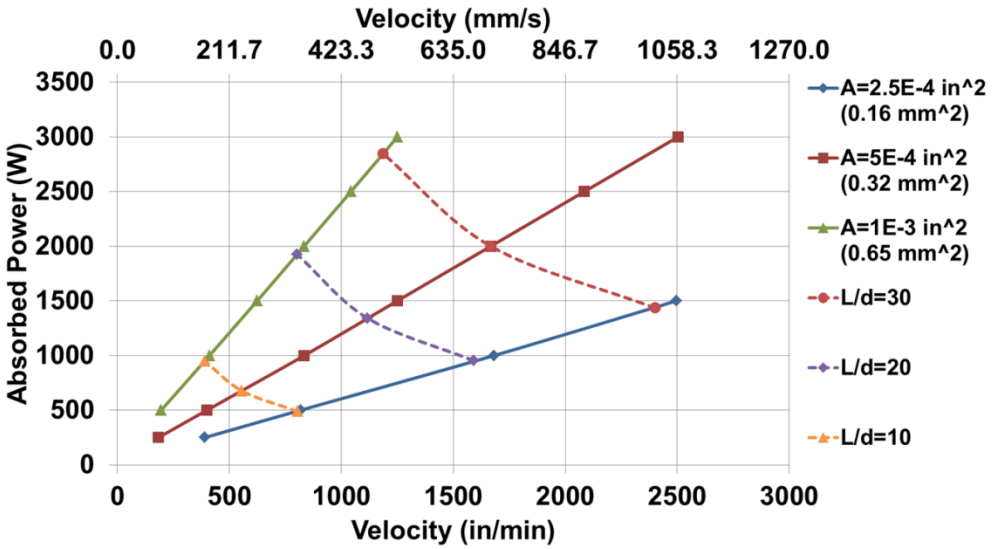

Figure 64. P-V Process Map for no material added electron beam powder bed (Ti-6Al-4V).

With the process space defined, step changes in power and velocity can be determined. The step changes for this analysis can be seen in Figure 65 and are detailed in Table 16. Curves of constant area for initial and final steady states were chosen based on previous experiments that determined power/velocity combinations that led to good bead stability and surface quality [101]. Simulations for both increases in area (Blue to Red transitions) and decreases in area (Red to Blue transitions) were performed.

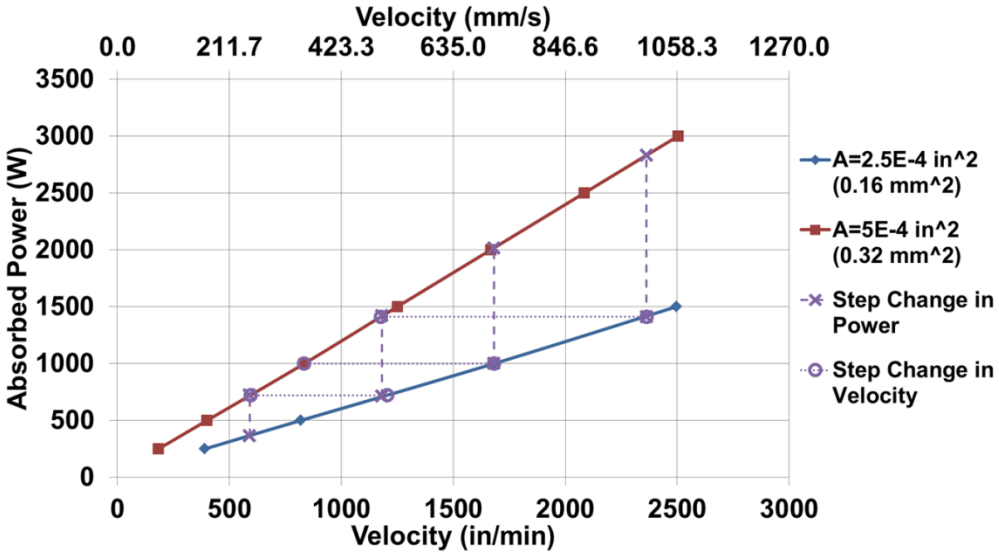

Figure 65. Analysis plan for electron beam powder bed system.

Table 16. Parameters for step changes in power plan for electron beam powder bed system.

	Blue Curve of Constant Area (2.5E-4 in^2)		Red Curve of Constant Area (5E-4 in^2)	
	Power (W)	**Velocity (in/min)**	**Power (W)**	**Velocity (in/min)**
Step Change in Power	364.2	591.0	721.1	591.0
	711.5	1181.0	1418.4	1181.0
	1000.0	1681.5	2014.5	1681.5
	1412.6	2362.0	2831.9	2362.0
Step Change in Velocity	721.1	1204.2	721.1	593.6
	1412.6	2362.0	1412.6	1176.1
	1000.0	1681.5	1000.0	834.0

Response times and response distances can be seen in Table 17. Response times, as expected, are on the order of milliseconds but show little correlation. Response distances, however, group closely for Red to Blue and Blue to Red transitions, respectively.

Table 17. Response times and response distances for step changes.

	Constant Power/Velocity Parameter	Time to 90% of Difference in SS Depth (s)		Distance to 90% of Difference in SS Depth (in)	
		Red to Blue	**Blue to Red**	**Red to Blue**	**Blue to Red**
Step Change in Power	591 in/min	6.3E-03	6.2E-03	4.9E-02	3.9E-02
	1181 in/min	4.7E-03	5.2E-03	4.8E-02	3.6E-02
	1681.5 in/min	4.3E-03	4.9E-03	4.7E-02	3.6E-02
	2362 in/min	4.0E-03	4.7E-03	4.7E-02	3.5E-02
Step Change in Velocity	721.1 W	4.7E-03	6.4E-03	4.9E-02	3.8E-02
	1000 W	4.3E-03	5.6E-03	4.8E-02	3.7E-02
	1412.6 W	4.0E-03	5.2E-03	4.7E-02	3.6E-02

In addition to response distance and response time, the behavior of the melt pool is observed. Melt pool response behavior can be seen in Figure 66, below. From this figure it is clear that response behaviors are similar for step changes between the same curves of constant area, regardless position or path taken through the P-V Process Map.

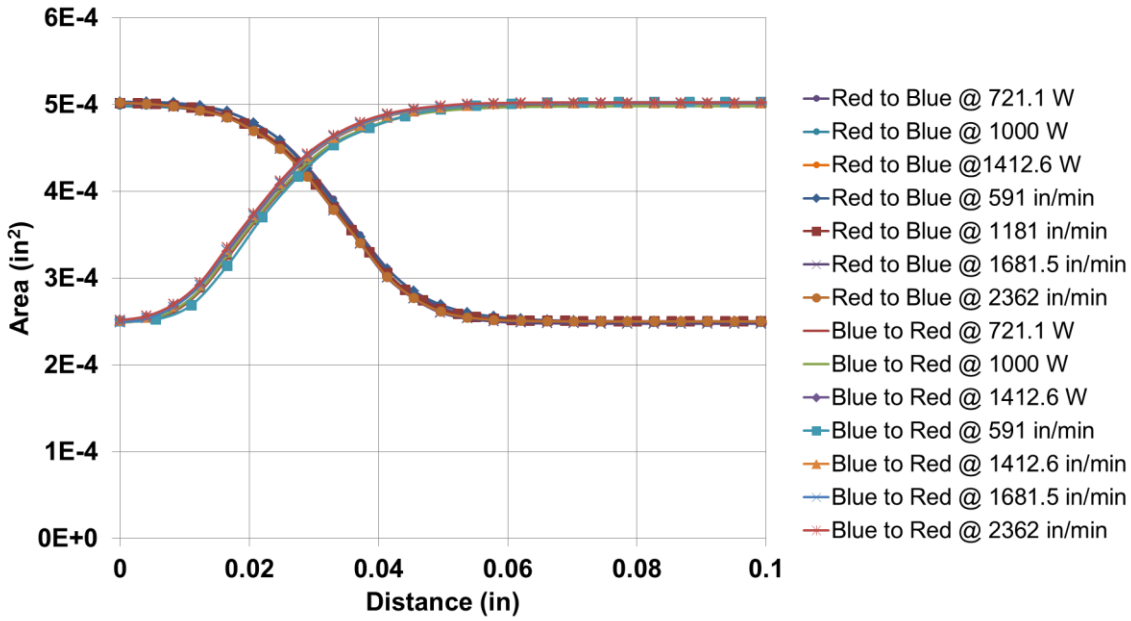

Figure 66. Response behavior for the electron beam powder bed system.

4.2 Fitting of Transient Response Behavior

4.2.1 Rule of Thumb Estimate

Similar to the single bead and thin wall geometries in the wire feed electron beam system, rule of thumb generalizations for determining the response distance can be determined based on the simulation data presented in the previous section. It is found that response distance is estimated for decreases in area by $\mathbf{2}\boldsymbol{d_1} + \boldsymbol{d_2}$ and by $\mathbf{1.5}\boldsymbol{d_1} + \boldsymbol{d_2}$ for increases in area, where d_1 and d_2 are the initial and final steady state melt pool effective depth respectively. This result has shown that there is more of a dependence on the initial steady state for both increases and decreases in area. This is in contrast to the wire feed electron beam results for single beads in Chapter 2, which was $\boldsymbol{d_1} + \mathbf{2}\boldsymbol{d_2}$ for increases in area and $\boldsymbol{d_1} + \mathbf{3}\boldsymbol{d_2}$ for decreases in area as well as the results for thin wall in Chapter 3, which was $\mathbf{2.3}\boldsymbol{d_2}$ for increases in area and $\mathbf{2.9}\boldsymbol{d_1}$ for decreases in area. The comparison of this generalization to the simulation data can be seen in Figure 67 and

Table 18, below. Consistent with the results for the wire feed electron beam system, the response distance in the powder bed electron beam system can accurately predict response distance in thin walls.

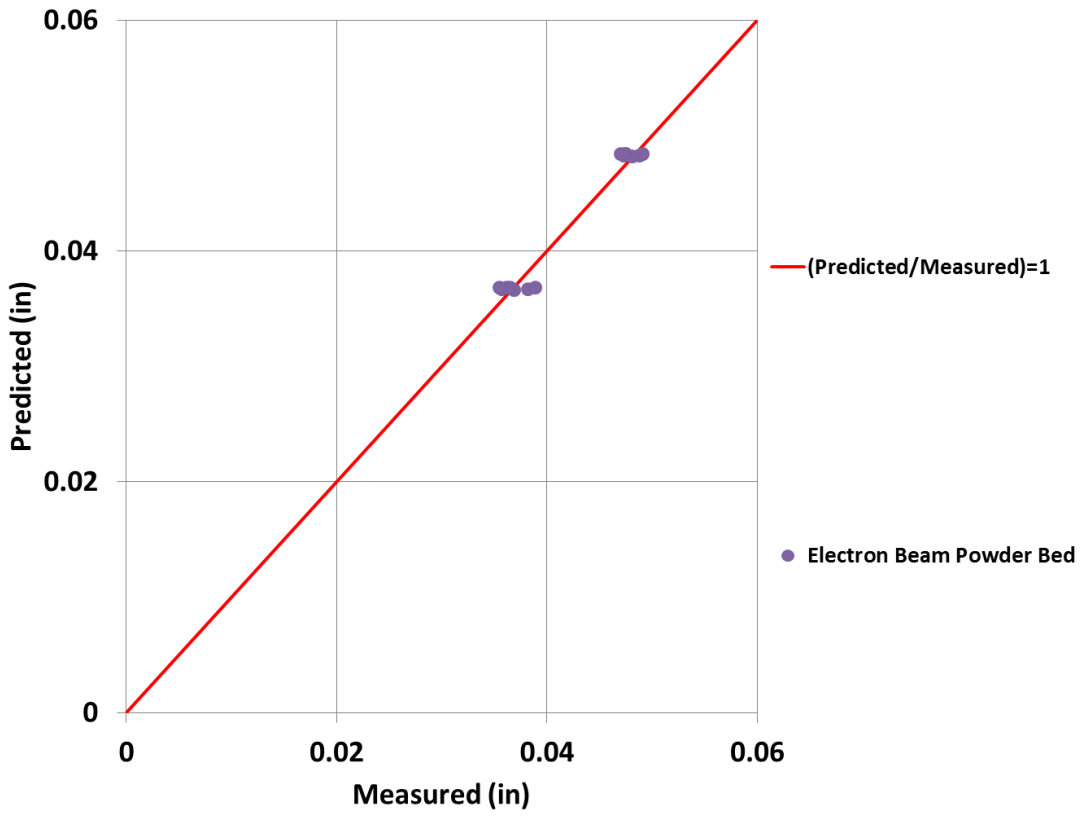

Figure 67. Predicted response distance versus measured response distance from simulation results.

Table 18. Comparison of rule of thumb estimates to simulation data.

	Simulation Details	Initial Effective Depth (in)	Final Effective Depth (in)	Response Distance (in)	Rule-of-Thumb Estimate (in)	Percent Error (%)
Decrease in Area	Red to Blue @ 721.1 W	1.79E-02	1.26E-02	4.88E-02	4.83E-02	-1.1
	Red to Blue @ 1000 W	1.78E-02	1.26E-02	4.81E-02	4.82E-02	0.3
	Red to Blue @ 1412.6 W	1.79E-02	1.26E-02	4.75E-02	4.84E-02	1.8
	Red to Blue @ 591 in/min	1.79E-02	1.26E-02	4.91E-02	4.84E-02	-1.5
	Red to Blue @ 1181 in/min	1.79E-02	1.26E-02	4.75E-02	4.84E-02	1.8
	Red to Blue @ 1681.5 in/min	1.79E-02	1.26E-02	4.73E-02	4.83E-02	2.1
	Red to Blue @ 2362 in/min	1.79E-02	1.26E-02	4.70E-02	4.84E-02	3.0
Increase in Area	Blue to Red @ 721.1 W	1.26E-02	1.79E-02	3.82E-02	3.67E-02	-3.8
	Blue to Red @ 1000 W	1.26E-02	1.78E-02	3.69E-02	3.66E-02	-0.6
	Blue to Red @ 1412.6 W	1.26E-02	1.79E-02	3.65E-02	3.68E-02	0.9
	Blue to Red @ 591 in/min	1.26E-02	1.79E-02	3.89E-02	3.68E-02	-5.3
	Blue to Red @ 1181 in/min	1.26E-02	1.79E-02	3.62E-02	3.68E-02	1.6
	Blue to Red @ 1681.5 in/min	1.26E-02	1.79E-02	3.57E-02	3.67E-02	2.8
	Blue to Red @ 2362 in/min	1.26E-02	1.79E-02	3.55E-02	3.68E-02	3.8

4.2.2 Fitting of Transient Response Behavior

In addition to the prediction of response distance, the formulas for the prediction of the behavior is determined in the same manner as the single beads and thin walls in the wire feed system. Again, it is important to capture the s-curve shape seen in the response

behaviors. Thus as a starting point, the modified equation for a cumulative distribution function of a Gumbel distribution is used, as seen in (4) below.

$$\mathbf{F(x) = Ae^{-e^{-(x-\mu)/\beta}} + C} \tag{4}$$

Where *C* is an offset to used increase the bounds of the s-curve and *A* is a multiplier used to increase the gap between the upper and lower bound. Excel's solver tool can be used to fit parameters in the function to the data curves from Figure 66 by minimizing the squared difference between the function and the data. The resulting parameters from this fitting are listed in Table 19 and the predicted curves are compared to simulation results in Figure 68. In this figure, the points represent the data from simulations and the solid lines represent the function predicted by the parameters in Table 19 applied to (4).

Table 19. Parameters for prediction of melt pool behavior.

	A	***μ***	***β***	***C***	**Initial Area (in^2)**	**Final Area (in^2)**	**Change in Area (in^2)**
Red to Blue	-2.52E-04	2.99E-02	8.68E-03	5.00E-04	5.01E-04	2.49E-04	-2.52E-04
Blue to Red	2.48E-04	1.77E-02	8.58E-03	2.49E-04	2.49E-04	5.01E-04	2.52E-04

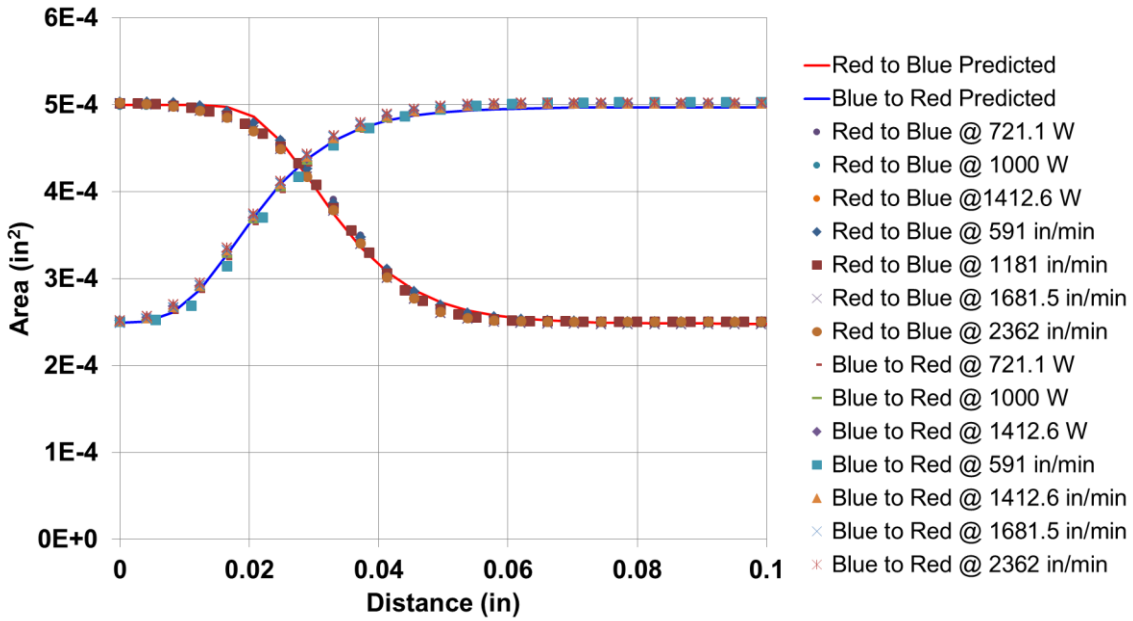

Figure 68. Comparison of predicted behavior to simulation results.

From Figure 68, it is clear that the parameters for the selected equation accurately predict behaviors. The accuracy of the fit can also be confirmed by the coefficient of determination, R^2, which did not go more than 8E-10 below a value of 1 for any curve. Table 19, shows that the multiplier (A) is approximately equal to the difference in area and the offset (C) is approximately equal to the difference in area, however, a correlation for μ and β has not yet been found and more combinations of initial and final area simulations would be required to determine if a correlation exists for these variables.

4.2.3 Suggested Application to Feedback Control Systems

In addition to prediction of response distance and behavior it is important to understand methods for application of the information presented in this section to feedback and feedforward control systems. While the response time is not a limiting factor in this system, it is important to have a strong understanding of it for the development of control systems. As with the analysis in previous chapters, the starting

point for determining response time is by taking the response distance, plus some fraction of the final L' value, and minus some fraction of the initial L' value. Using this method and Excel's solver function to minimize the squared difference between the estimate and actual values, a rule of thumb can be determined. The results of this analysis can be seen in Figure 69 and Table 20, below. The equation used to determine the estimate was [Response Distance – (0.1 x Initial L') + (0.6 x Final L')] for increases in area and [Response Distance – (0.1 x Initial L') + (1.1 x Final L')] for decreases in area. The data presented in Figure 69 and Table 20 verifies that this method estimates response time very accurately.

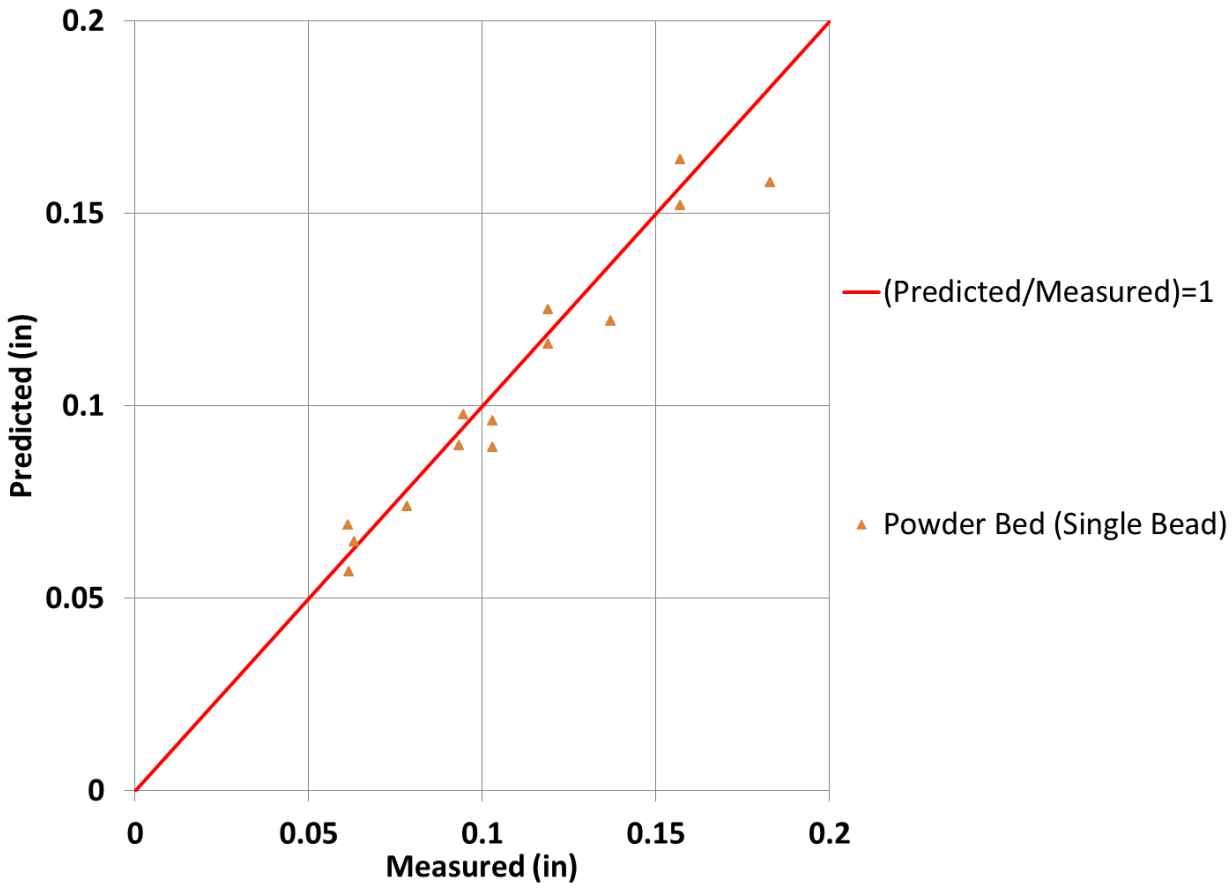

Figure 69. Predicted response time versus measured response time from simulation results.

Table 20. Comparison of response distance and response time via rule of thumb.

		Initial L' (in)	Final L' (in)	Response Time × Velocity (in)	Response Distance (in)	Estimated Response Time × Velocity (in)	Percent Error (%)
Red to Blue	721.1 W	5.22E-02	4.92E-02	9.47E-02	4.88E-02	9.78E-02	3.3
	1000 W	7.44E-02	7.70E-02	1.19E-01	4.81E-02	1.25E-01	4.9
	1412.6 W	1.07E-01	1.16E-01	1.57E-01	4.75E-02	1.64E-01	4.7
	591 in/min	5.22E-02	1.17E-02	6.16E-02	4.91E-02	5.68E-02	-7.8
	1181 in/min	1.08E-01	4.83E-02	9.34E-02	4.75E-02	8.98E-02	-3.9
	1681.5 in/min	1.56E-01	7.70E-02	1.19E-01	4.73E-02	1.16E-01	-2.5
	2362 in/min	2.23E-01	1.16E-01	1.57E-01	4.70E-02	1.52E-01	-3.0
Blue to Red	721.1 W	4.92E-02	5.22E-02	6.31E-02	3.82E-02	6.46E-02	2.3
	1000 W	7.70E-02	7.44E-02	7.84E-02	3.69E-02	7.38E-02	-5.8
	1412.6 W	1.16E-01	1.07E-01	1.03E-01	3.65E-02	8.93E-02	-13.0
	591 in/min	1.17E-02	5.22E-02	6.14E-02	3.89E-02	6.90E-02	12.5
	1181 in/min	4.83E-02	1.08E-01	1.03E-01	3.62E-02	9.61E-02	-6.3
	1681.5 in/min	7.70E-02	1.56E-01	1.37E-01	3.57E-02	1.22E-01	-11.0
	2362 in/min	1.16E-01	2.23E-01	1.83E-01	3.55E-02	1.58E-01	-13.9

While this shows that response times can be accurately predicted for use in feedback control systems, the response distance can be also used in feedback control algorithms, regardless of the prediction of response times. While the change in melt pool width will not be instantaneous, once the system senses the change in that metric, the distance to the

new steady state melt pool width is then known, regardless of the change in L' or the point in which the melt pool width begins to change.

4.3 Electron Beam Powder Bed Experiments

Experiments to validate simulations performed in the previous section were set up and run by Sneha Narra on the CMU lab's Arcam S12 system, which has been upgraded to have control software equivalent to the A2X, and the same step changes from the simulation work presented earlier were used. Experiments were performed on an 8.25 in × 8.25in × 0.25in Ti-6Al-4V plates with no powder added (beam on plate only). Parameters and numbering system for the analysis are listed in Table 21, below. Powers listed in the table are absorbed power and an absorptivity of 0.9 was assumed for the preparation of the machine settings. Two sets of experiments were run on separate plates. Moving forward, these experiments will be referred to by Plate # - Experiment Run #. For example, the number 1-4 will refer to the first experiment plate and run #4.

Table 21. Parameters for Arcam experiments.

Run #	Initial Absorbed Power (W)	Initial Velocity (in/min)	Final Absorbed Power (W)	Final Velocity (in/min)
1	364	591	721	591
2	721	591	364	591
3	712	1181	1418	1181
4	1418	1181	712	1181
5	1007	1680	2013	1680
6	2013	1680	1007	1680
7	1413	2362	2832	2362
8	2832	2362	1413	2362
9	721	1206	721	593
10	721	593	721	1206
11	1413	2362	1413	1190
12	1413	1190	1413	2362
13	1000	1682	1000	834
14	1000	834	1000	1682

An example experiment plate can be seen in Figure 70, below. In this image, experiments are in order from 1 to 14 going from bottom to top and the direction of travel velocity is from left to right. It should be noted that experiment lines 3 through 8 did not perform as expected in either set of experiments and had a pause between the initial and final beam settings. These were step changes in power at constant velocity, so it is assumed that system is not capable of performing power changes instantaneously once the power goes over 800W for one of the paired settings. Therefore, these experiment lines are not included in further analysis of the transient region.

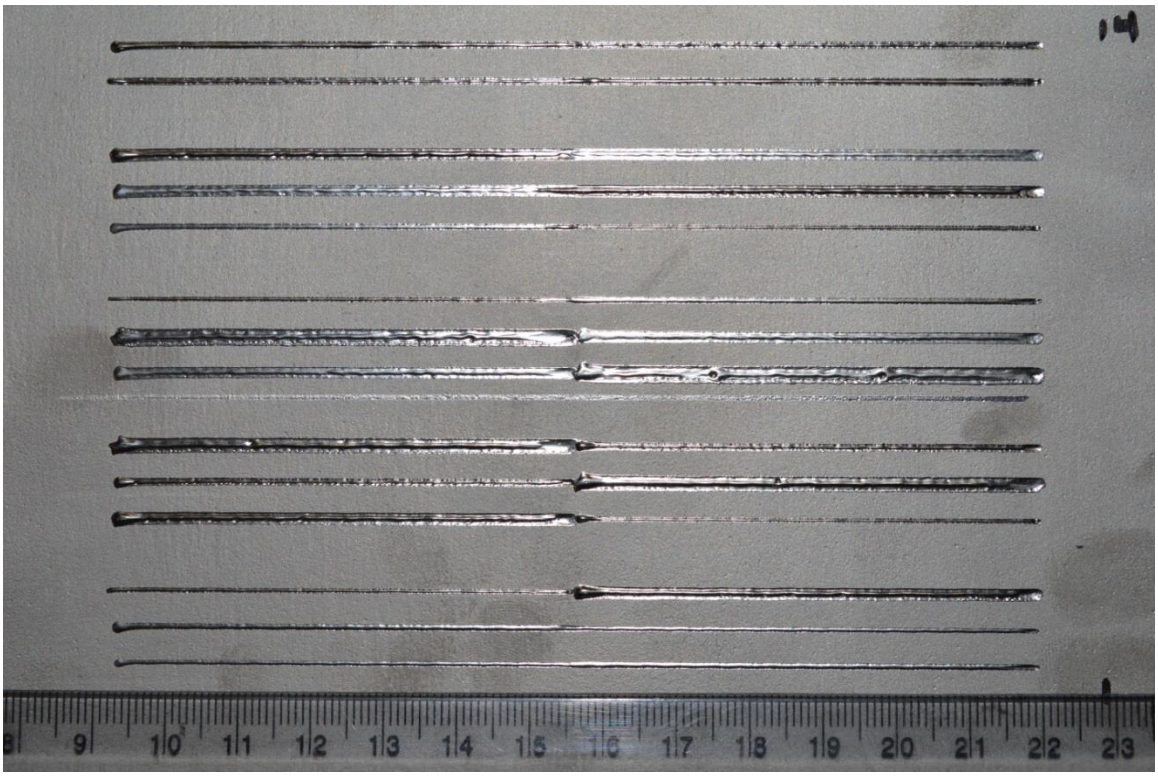

Figure 70. Example experiment plate.

More accurate images were taken via optical microscope for surface width measurements. An example image and measurement can be seen in Figure 71, below. In

this figure, experiment line 1-1 is presented (top) and beam travel direction is from left to right. The red lines of the surface width measurement (bottom) presents a trace of the edges of the melt pool. This was analyzed using Matlab to determine the distance between the red lines. Additional surface images and measurements can be seen in Appendix C.

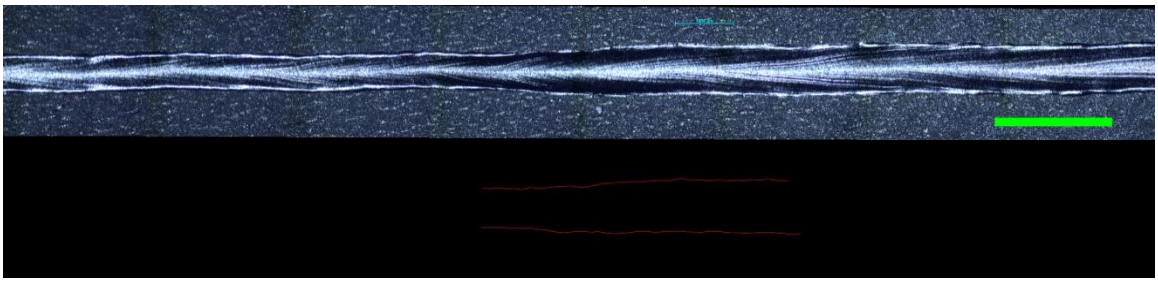

Figure 71. Example image of bead surface and surface width measurement (Experiment 1-1). Green scale bar is 2 mm (7.87E-2 in).

Results of the surface width measurements can be seen in Figure 72 through Figure 75. Measurements are presented as the (Surface Width)/2 and compared to the predicted effective depth from the previous section. The results show that several of the experiment lines performed as expected. Experiment lines 1, 2, 9, and 10 on both plates matched the expected width and response behavior quite well (Figure 72 and Figure 74). Some of the experiment lines, however, had melt pool widths that were much larger than expected (Figure 73 and Figure 75). In the case of experiment line 11 and 12 on both plates, there is still a significant agreement with the expected response distance. For experiment lines 13 and 14, however, there was little change in the width of the melt pool and so no transition could be seen from the surface. Regardless of these issues, there is strong evidence that the response behavior in the experiments match the predicted behavior.

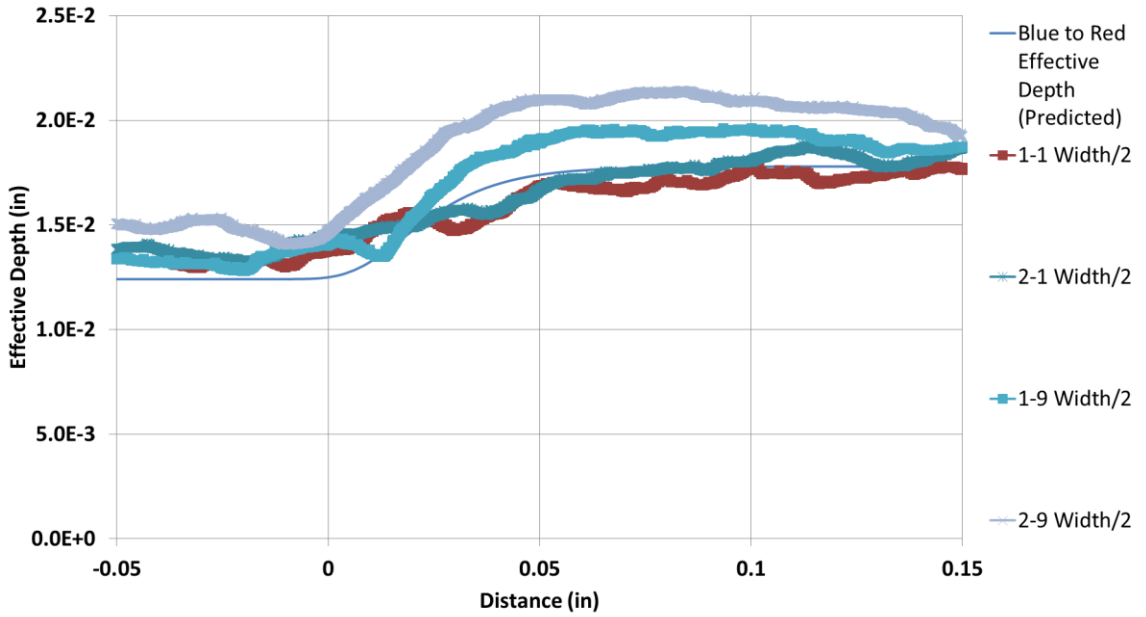

Figure 72. Surface width measurements for experiment lines 1-1, 2-1, 1-9, and 2-9.

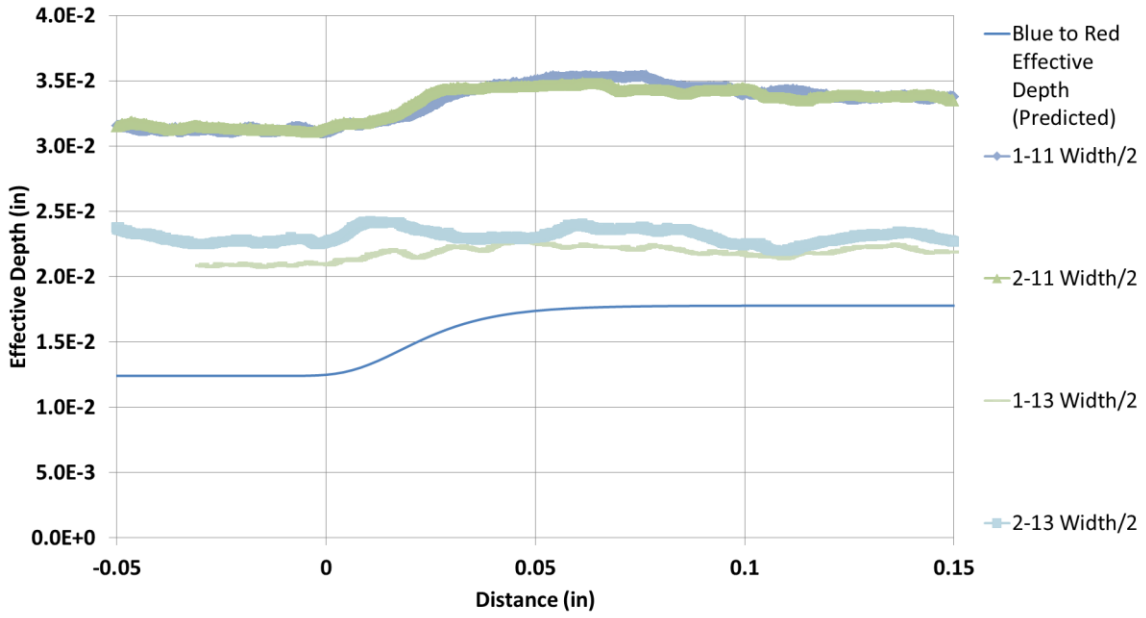

Figure 73. Surface width measurements for experiment lines 1-11, 2-11, 1-13, and 2-13.

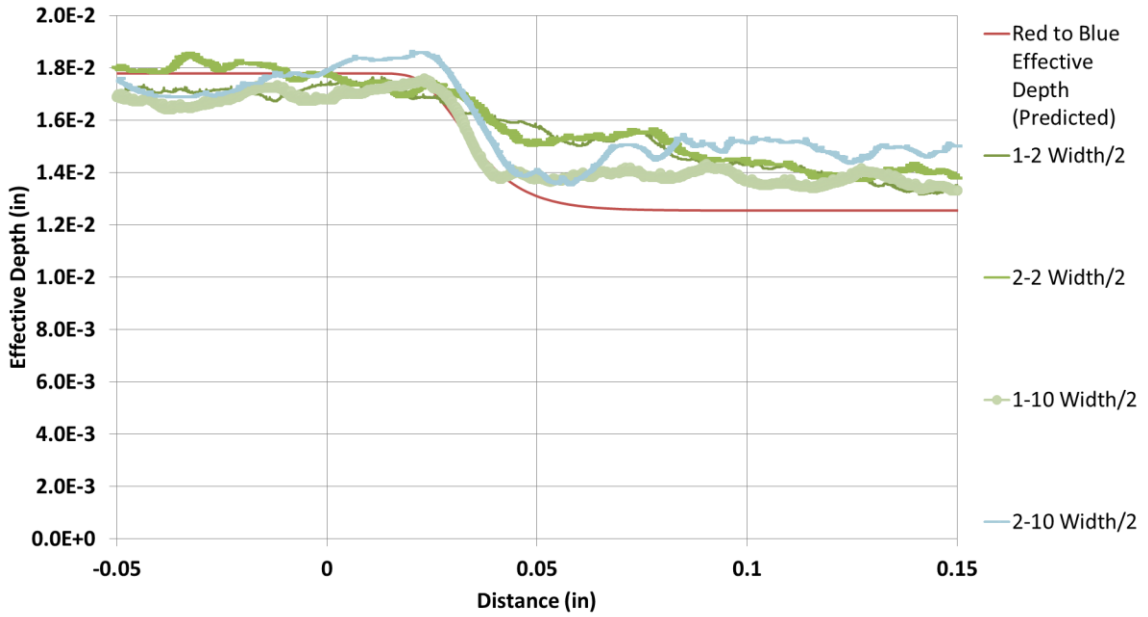

Figure 74. Surface width measurements for experiment lines 1-2, 2-2, 1-10, and 2-10.

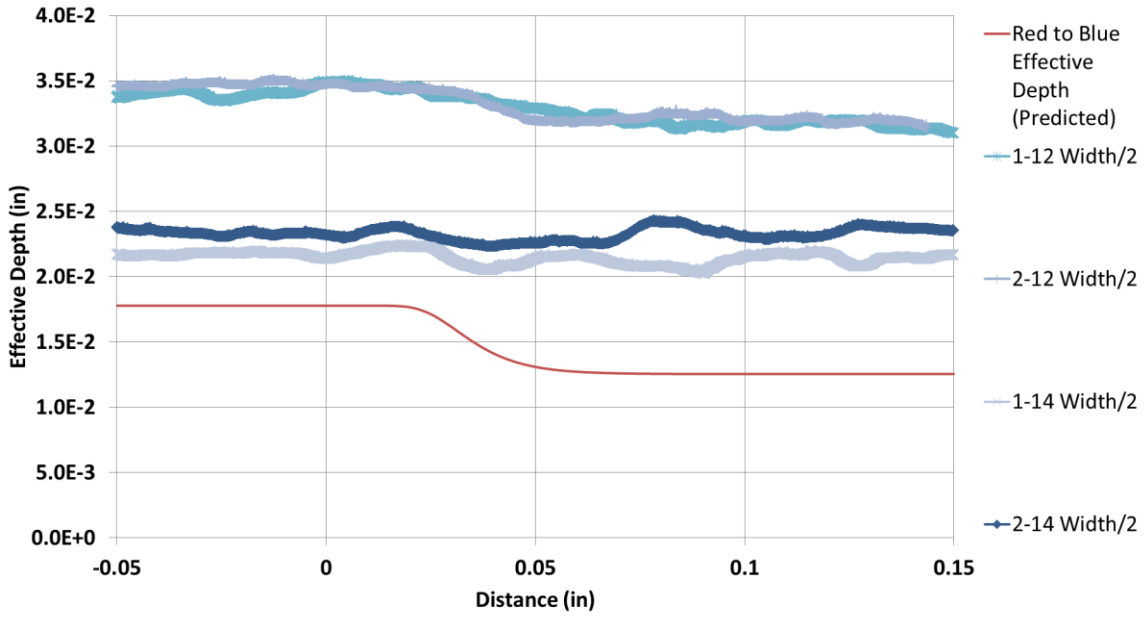

Figure 75. Surface width measurements for experiment lines 1-12, 2-12, 1-14, and 2-14.

In addition to surface width measurements, the experiment beads from the first plate were sectioned and polished to more accurately analyze the size of the melt pool. Sections were taken perpendicular to travel velocity and an example section can be seen in Figure 76, below. Images were taken using differential interference contrast to better

see the change in microstructure. DIC image can be seen on the left of the figure and measurement of the melt pool on the right. Additional images and measurements can be found in Appendix C.

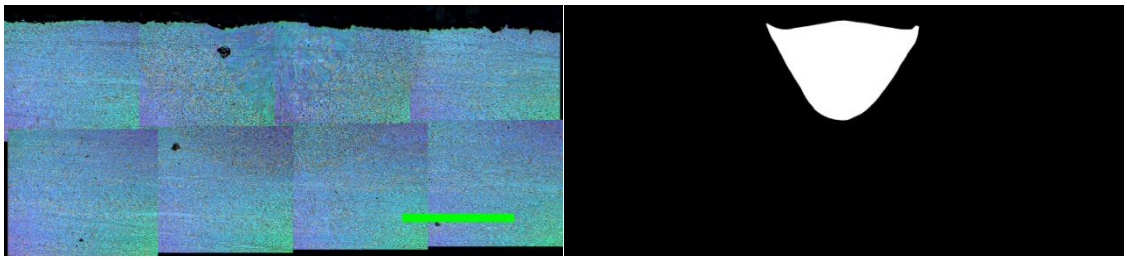

Figure 76. Measurement of melt pool area (experiment line 1 initial steady state). Green scale bar is 1 mm (3.94E-2 in).

Results of melt pool area measurements can be found in Table 22, below. Variability in measurements is most likely due to surface tension effects (seen in the surface width images in Appendix C). Additionally, discussions with the Arcam technician lead us to believe that the beam power can be off by as much as ±10%. Nonetheless, the results presented show that the melt pool area measurements are close to the expected values. This is important to note as melt pool width measurements for experiment lines 11 through 14 were much wider than expected. However, the analysis of the melt pool area has shown very wide and shallow melt pool for these cases. While reason for this departure from the other experiment lines is not known, the fact that the melt pool area measurements are still accurate suggest that melt pool areas that did not show transitions in melt pool width would still transition in area as expected.

Table 22. Melt pool area measurements.

Run #	Initial Area (in^2)	Expected Initial Area (in^2)	Final Area (in^2)	Expected Final Area (in^2)
1	2.94E-04	2.50E-04	6.10E-04	5.00E-04
2	6.72E-04	5.00E-04	2.89E-04	2.50E-04
9	3.06E-04	2.50E-04	6.48E-04	5.00E-04
10	6.00E-04	5.00E-04	2.93E-04	2.50E-04
11	2.62E-04	2.50E-04	5.39E-04	5.00E-04
12	5.18E-04	5.00E-04	2.46E-04	2.50E-04
13	2.93E-04	2.50E-04	5.50E-04	5.00E-04
14	5.62E-04	5.00E-04	2.52E-04	2.50E-04

To view the change in melt pool depth through the transition more accurately, transient sections of the experiment line would have to be polished and etched. This analysis is not included in the results for several reasons. The expected response distance is less than 5E-2 in so samples cannot be sectioned perpendicular to travel velocity at several points through the transition (as was done with the wire feed electron beam system). Thus, the samples would have to be sectioned parallel to travel velocity and polished until the center of the experiment line was exposed. This, however, is very difficult to accomplish due to several factors. The size of the melt pools means that to accurately be at the center of the melt pool, the sample would have to be polished to within ±1.5E-3 in of the desired location (or less). The mounting resin available was a cold mount resin that had a tendency to seep under edges of the sample, making it difficult to insure that the sample was perfectly level. The resin also did not cure with a flat back edge. While this can be fixed after the resin has set by sanding the excess away, it made it very difficult to keep the back of the sample level and added an addition source of error to the measurement of the sample height (and how much material is being removed at each step). Finally surface tension effects caused the melt pool to bead up and

be asymmetrical in several of the cases, which would lead to variability in the melt pool penetration depth measurements. However, even without this part of the analysis, it is clear that hypothesis regarding response time, response distance, and response behavior is accurate and the results presented can be applied to any of the direct metal AM processes.

4.4 Discussion

In this chapter, the analysis of transient response was extended to the electron beam powder bed system. Three dimensional finite element simulations have been developed and run in the ABAQUS software package. From these simulations, a P-V Process Map has been developed for no material added (beam on plate) at 1023K preheat. This process map was the basis for analyzing step changes in beam power or travel velocity between curves of constant area, analogous to the work on the wire feed electron beam based system. Experiments were also performed at Carnegie Mellon University on their Arcam S12 system, which verified the results of simulations.

As with the wire feed system, potential sources of error in this work include the neglecting of physical phenomena through which heat can be removed from the system (such as melt pool convection and radiation); however, prior work has found this to be minimal when compared to conduction through the substrate. Another source of error is the measurement of the melt pool area in the analysis of experiments. As described in section 4.3, it can be very difficult to determine the exact boundary of the melt pool because of microstructural development occurring at temperatures below the melt temperature (in the HAZ). Regardless of these issues, the steady state melt pool areas as well as the behavior seen in the experimental measurements closely matched the expected results, which validate the simulations presented.

As expected, the response times were on the order of milliseconds and showed little correlation. Response distances, however, grouped together well and can be predicted through a combination of initial and final melt pool effective depths in the same "rule of thumb" fashion as the wire feed electron beam based systems. In addition to this, response times can be predicted from response distances and knowledge of the initial and final steady state geometries of the transition (specifically L'). Response behaviors can also be predicted to a high degree of accuracy, but not enough information was available to derive physical meaning from the parameters and additional investigation would be required to do so. These are key findings as the ability to predict response time, distance and behavior will aid in the development of feedback and feedforward control systems.

Furthermore, response behaviors were similar regardless of path or position in the P-V Process Map when moving between the same curves of constant area. The explanation for this behavior is that the melt pool must move a certain ***distance*** after an abrupt change in beam power or beam velocity to achieve a new steady-state depth and that distance is largely governed by the initial and final melt pool sizes (melt pool depths or cross sectional areas), regardless of the initial and final power and velocity combinations. It is also important to note that while the parameters of the prediction equations may vary by system and geometry, they hold true for all of process space and therefore it is clear that response time, distance, and behavior can be predicted across all direct metal AM through an understanding of the P-V Process Map. Additionally, the response distance and response time can be ***predicted*** for a new system and/or material by fitting the multiples of key features of the steady state melt pool geometry (d_1, d_2, L'_1, and L'_2) to a

small set of simulations (or even a single simulation) and extrapolating to cover the entire process space.

Chapter 5 Effect of Modeling Parameters and Assumptions

5.1 Effect of Preheating in Thin Walls

The previous analysis of thin walls in Chapter 2 was performed with no preheat (293 K). However, as a wall is deposited, residual heat from previous layers will build up and increase the temperature of the wall. Thus, preheat temperatures of 373 K and 773 K were chosen to determine the effect preheat has on transient response in the thin wall geometry. 373 K was chosen to create a small amount of preheat and 773 K was chosen based on the work of Reeseewatt and Beuth to replicate the temperature of a wall that has been built through deposition of several layers [97].

For this analysis, two dimensional finite element simulations were developed and run in the ABAQUS software package. Conditions in the simulations were identical to the conditions described in the thin wall analysis in Chapter 2; aside from the change in preheat temperature. Several simulations were performed at each preheat temperature to determine a P-V Process Map for each. A comparison of the curves of constant area and curves of constant *L/d* are presented in Figure 77, below. As expected, as preheat increases, the curves of constant area shift to the right and curves of constant *L/d* shift toward the origin. This means that for higher levels of preheat, to maintain constant area, lower power or higher velocity is required. Also, for higher levels of preheat, melt pool lengths increase for the same melt pool areas. Thus, to maintain *L/d* at constant area for

increasing levels of preheat, power and velocity must move down the curve of constant area toward the origin.

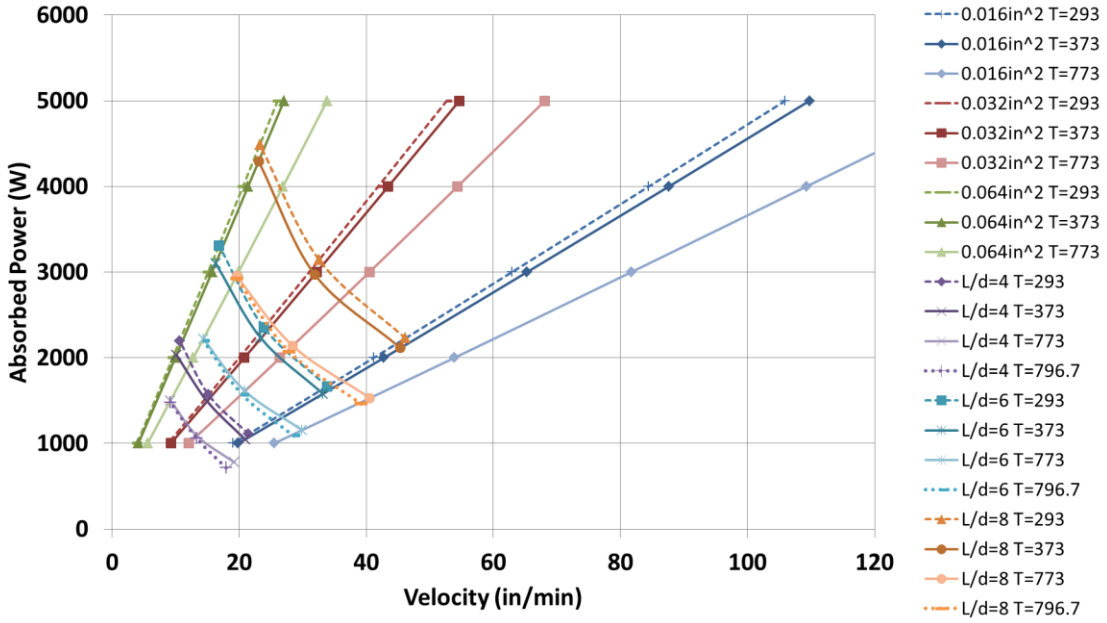

Figure 77. Comparisons of P-V Process Maps for different levels of preheat in a thin wall geometry.

Based on the changes to the P-V Process Map due to preheat temperature, step changes in power and velocity moving between the green and red curves of constant area and the blue and red curves of constant area, similar to the ones in Chapter 2 were performed. The details of the simulations can be found in Table 23 for step changes between the Red (0.032 in^2) and Green (0.064 in^2) curves of constant area and in Table 24 for step changes between the Blue (0.016 in^2) and Red (0.032 in^2) curves of constant area.

Table 23. Red and Green curve of constant area parameters for 373 K and 773 K preheat.

	Red Constant Area Parameters		Green Constant Area Parameters	
	Power (W)	**Velocity (in/min)**	**Power (W)**	**Velocity (in/min)**
373K Preheat	1000.0	8.2	1706.4	8.2
	1801.0	17.6	3339.5	17.6
	2609.2	27.0	5000.0	27.0
	3000.0	31.6	3000.0	15.7
773K Preheat	1000.0	11.1	1768.8	11.1
	1782.1	22.5	3367.7	22.5
	2570.9	33.8	5000.0	33.8
	3000.0	39.9	3000.0	19.9

Table 24. Blue and Red curve of constant area parameters for 373 K and 773 K preheat.

	Blue Constant Area Parameters		Red Constant Area Parameters	
	Power (W)	**Velocity (in/min)**	**Power (W)**	**Velocity (in/min)**
373K Preheat	1000.0	18.5	1800.2	18.5
	1775.0	36.6	3385.5	36.6
	2557.1	54.6	5000.0	54.6
	3000.0	64.8	3000.0	32.2
773K Preheat	1000.0	24.2	1848.8	24.2
	1761.7	46.2	3407.4	46.2
	2530.1	68.1	5000.0	68.1
	3000.0	81.4	3000.0	40.5

Step changes were performed using the parameter sets listed above for both levels of preheat. Response times and response distances can be seen for both levels of preheat in Table 25, below. As expected, response times are on the order of seconds and show little correlation for either level of preheat. Response distances, however, show the same correlations seen in previous chapters and group together closely for step changes with matching initial and final steady state melt pool areas.

Table 25. Response time and distance for a thin wall with 373K and 773K preheat.

		373K Preheat		773K Preheat	
		Response Time (s)	**Response Distance (in)**	**Response Time (s)**	**Response Distance (in)**
Green to Red	8.2 in/min	3.10	0.58	2.27	0.58
	17.6 in/min	1.60	0.57	1.42	0.56
	27.0 in/min	1.18	0.55	1.01	0.57
	3000 W	1.12	0.54	0.94	0.54
Blue to Red	18.5 in/min	1.36	0.35	1.08	0.33
	36.6 in/min	0.84	0.31	0.72	0.32
	54.6 in/min	0.68	0.34	0.62	0.31
	3000 W	0.93	0.33	0.79	0.31
Red to Green	8.2 in/min	4.02	0.51	3.00	0.47
	17.6 in/min	2.01	0.44	1.69	0.42
	27.0 in/min	1.50	0.41	1.33	0.41
	3000 W	2.31	0.48	1.92	0.45
Red to Blue	18.5 in/min	0.96	0.39	0.87	0.43
	36.6 in/min	0.61	0.39	0.51	0.45
	54.6 in/min	0.45	0.37	0.40	0.42
	3000 W	0.42	0.36	0.38	0.39

The correlation in response distances can also be seen in Figure 78 and Figure 79. These figures show the averages for all the step changes between the curves of constant area. Error bars represent the absolute deviation from the average. From this result, it is apparent that the response behaviors are similar regardless of the path or position of the step changes in the P-V Process Map when transitioning between the same curves of constant area. It is also clear that, while the addition of preheat changes the process map, it has a minimal effect on the response distance and the response behavior.

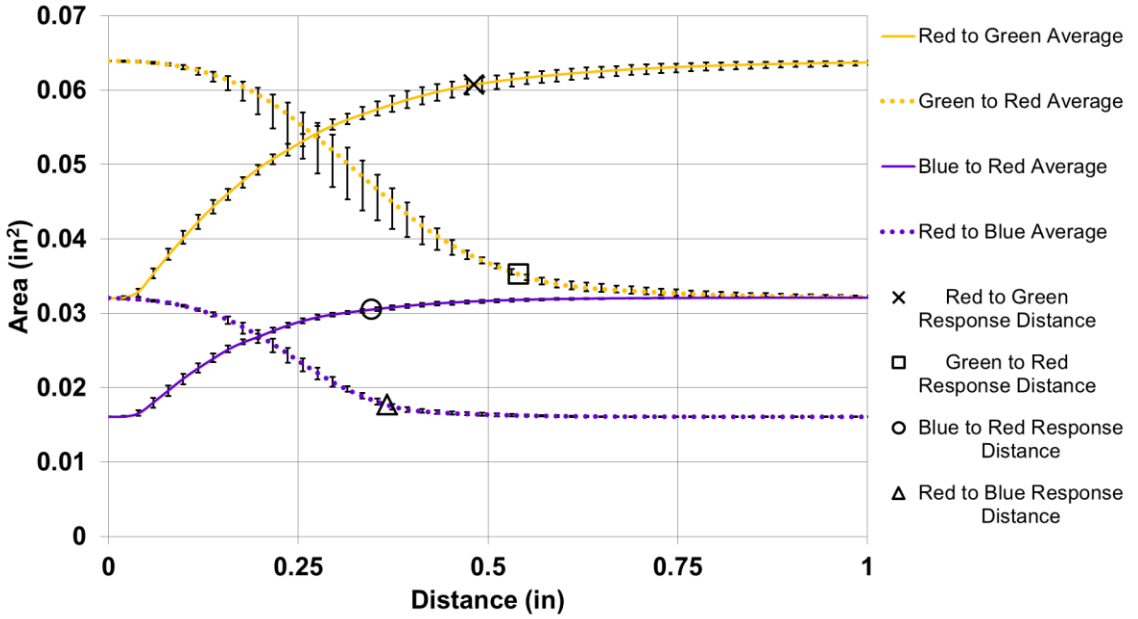

Figure 78. Response behaviors for a thin wall with 373 K preheat.

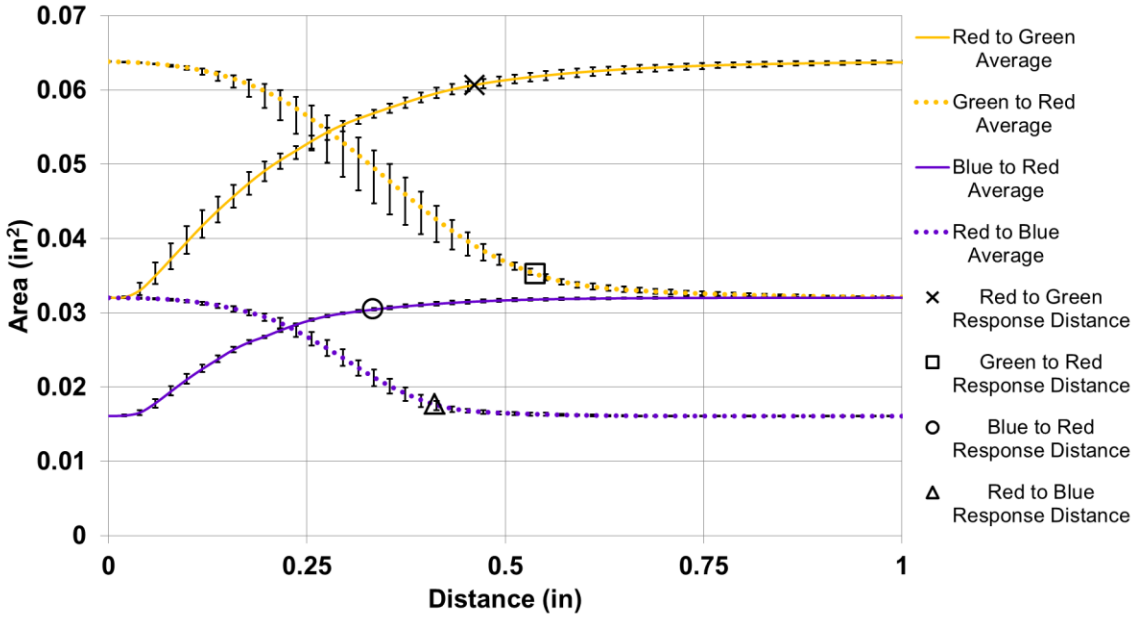

Figure 79. Response behaviors for a thin wall with 773 K preheat.

5.2 Effect of Preheating in Thin Walls on Melt Pool Response Prediction

5.2.1 Rule of Thumb Estimate

As with the previous work, rule of thumb estimates for predicting the response distance can be determined. Using Excel's solver, it was determined that the following equations could be used to estimate response distance. For a preheat of 373K, the equations are $2.3d_2$ for increases in area and $2.8d_1$ for decreases in area. For a preheat of 773K, the equations are $2.2d_2$ for increases in area and $2.9d_1$ for decreases in area. As seen in Chapter 3, this is slightly different from the single bead rule of thumb estimates as they are only dependent on the larger of the two steady state areas. The results from this analysis are presented in Table 26, below. From the percent error listed in the table, it is apparent that the equations for the rule of thumb estimate accurately predict the response distance.

Table 26. Rule of thumb estimate for response distance in thin walls (373K and 773K preheat).

		373K Preheat			773K Preheat		
		Response Distance (in)	**Rule of Thumb Estimate (in)**	**Percent Error (%)**	**Response Distance (in)**	**Rule of Thumb Estimate (in)**	**Percent Error (%)**
Green to Red	8.2 in/min	0.58	0.56	-2.5	0.58	0.58	1.2
	17.6 in/min	0.57	0.57	-0.6	0.56	0.58	3.7
	27.0 in/min	0.55	0.57	2.8	0.57	0.59	2.3
	3000 W	0.54	0.57	4.2	0.54	0.58	8.2
Blue to Red	18.5 in/min	0.35	0.33	-6.3	0.33	0.31	-3.6
	36.6 in/min	0.31	0.33	5.4	0.32	0.31	-0.4
	54.6 in/min	0.34	0.33	-2.2	0.31	0.31	2.3
	3000 W	0.33	0.33	-0.7	0.31	0.31	0.5
Red to Green	8.2 in/min	0.51	0.46	-9.6	0.47	0.44	-5.2
	17.6 in/min	0.44	0.46	5.4	0.42	0.44	6.3
	27.0 in/min	0.41	0.46	13.4	0.41	0.44	7.2
	3000 W	0.48	0.46	-3.8	0.45	0.44	-2.1
Red to Blue	18.5 in/min	0.39	0.40	2.2	0.43	0.41	-3.9
	36.6 in/min	0.39	0.40	3.9	0.45	0.41	-8.2
	54.6 in/min	0.37	0.40	9.0	0.42	0.41	-1.0
	3000 W	0.36	0.40	10.2	0.39	0.41	5.8

5.2.1 Suggested Application to Feedback Control Systems

The response distance prediction calculated using the rule of thumb determined in the previous section can be used in the development of feedforward controls systems as it provides the developer with a strong understanding of the distance required for changes in beam power and travel velocity to translate into changes in the melt pool size. Furthermore, it can be used to aid in the development of feedback control systems. If the point where the melt pool begins to change is detected, then the feedback control system can predict the point where the melt pool will reach the new steady state.

In addition to this, it is important to understand the prediction of response time and how this information can be applied to feedback control. As with previous sections, response distance is determined based on the point at which the melt pool area deviates

from the initial steady state and this may or may not be at the point where the beam is located when the step change occurs. Additionally, the distance behind the beam position where the maximum melt pool area occurs is also variable along and between curves of constant area. As such, prediction of response time is determined by an estimated distance divided by the final velocity. The estimated distance based on the rule of thumb value determined in the previous section and the initial and final values of L' (the distance between the point of maximum area and the heat source).

Using this as the starting point, coefficients for the initial and final L' values were then determined using Excel's solver tool to minimize the difference between the estimate and actual values. For a preheat of 373K, the equation was [(Response Distance) - 0.1(Initial L') +0.4(Final L')] for increases in area and [(Response Distance) - 0.3(Initial L') +1.2(Final L')] for decreases in area. For a preheat of 773K, the equation was [(Response Distance) - 0.1(Initial L') +0.5(Final L')] for increases in area and [(Response Distance) - 0.3(Initial L') +1.1(Final L')] for decreases in area. The results of this analysis can be seen in Table 27 for a 373 K preheat and Table 28 for a 773 K preheat. From these tables it is shown that there are a few outliers for the prediction of response time (Green to Red at 8.2 in/min for both preheats and Red to Blue at 18.5 in/min773K preheat), but aside from those simulations it is clear that response time can be accurately predicted by a strong understanding of the P-V Process Map.

Table 27. Determination of response time via response distance and L' for 373 K preheat.

		Response Time × Velocity (in)	Initial L' (in)	Final L' (in)	Estimated Response Time × Velocity (in)	Percent Error (%)
Green to Red	8.2 in/min	0.43	0.20	0.04	0.55	29.8
	17.6 in/min	0.47	0.39	0.08	0.54	14.9
	27.0 in/min	0.53	0.57	0.14	0.56	5.5
	3000 W	0.59	0.35	0.16	0.65	10.0
Blue to Red	18.5 in/min	0.42	0.04	0.20	0.40	-3.8
	36.6 in/min	0.51	0.08	0.37	0.47	-7.7
	54.6 in/min	0.62	0.12	0.57	0.55	-12.3
	3000 W	0.50	0.16	0.33	0.45	-10.1
Red to Green	8.2 in/min	0.55	0.04	0.20	0.54	-2.3
	17.6 in/min	0.59	0.08	0.39	0.61	4.1
	27.0 in/min	0.68	0.14	0.57	0.68	0.3
	3000 W	0.60	0.16	0.35	0.59	-2.4
Red to Blue	18.5 in/min	0.29	0.20	0.04	0.39	31.8
	36.6 in/min	0.37	0.37	0.08	0.38	2.7
	54.6 in/min	0.41	0.57	0.12	0.37	-9.9
	3000 W	0.45	0.33	0.16	0.49	8.4

Table 28. Determination of response time via response distance and L' for 773 K preheat.

		Response Time × Velocity (in)	Initial L' (in)	Final L' (in)	Estimated Response Time × Velocity (in)	Percent Error (%)
Green to Red	8.2 in/min	0.42	0.30	0.06	0.56	33.24
	17.6 in/min	0.53	0.49	0.12	0.57	7.00
	27.0 in/min	0.57	0.73	0.16	0.54	-5.11
	3000 W	0.63	0.45	0.20	0.67	5.89
Blue to Red	18.5 in/min	0.44	0.04	0.26	0.44	0.67
	36.6 in/min	0.55	0.10	0.49	0.55	-0.72
	54.6 in/min	0.70	0.16	0.73	0.66	-5.96
	3000 W	0.53	0.20	0.41	0.50	-5.86
Red to Green	8.2 in/min	0.56	0.06	0.30	0.59	5.39
	17.6 in/min	0.63	0.12	0.49	0.68	6.90
	27.0 in/min	0.75	0.16	0.73	0.79	6.03
	3000 W	0.64	0.20	0.45	0.65	2.19
Red to Blue	18.5 in/min	0.35	0.26	0.04	0.38	7.89
	36.6 in/min	0.39	0.49	0.10	0.37	-4.47
	54.6 in/min	0.45	0.73	0.16	0.37	-18.10
	3000 W	0.51	0.41	0.20	0.51	-0.68

5.3 Additional Parameters and Their Effect on Modeling

5.3.1 Square Bead Assumption

The assumption of a fixed square bead geometry used in this work is sometimes criticized. While this is not something that is expected in experiments, the comparison of simulations to experiments in the previous chapter has shown that there is little effect from the shape of the bead. Regardless, an analysis has been performed to determine if this assumption could be a source of error in the results.

To accomplish this, three dimensional finite element simulations have been set up and run in the ABAQUS software package. These simulations are identical to the ones presented in Chapter 2, except for the fact that the added material is a round bead instead of a square bead. Note that while the shape of the added material has changed, the size of the added material remains the same. To create the round bead, triangular prism shaped elements were used at the edge of the bead to simulate a round shape and rectangular prism elements were used everywhere else in the simulation. An example of the bead shape can be seen in Figure 80, below.

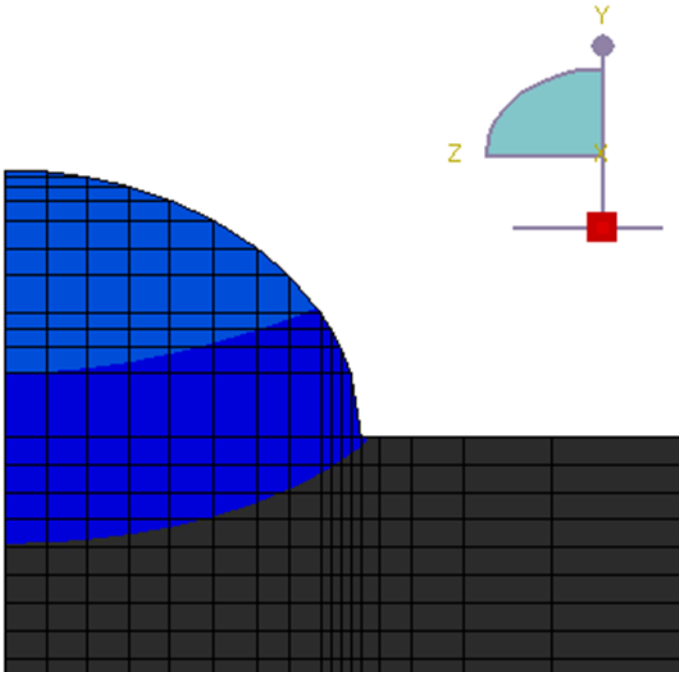

Figure 80. Example of a round bead used in simulations.

Results from three round bead simulations (one for each added material size in the P-V Process Map) were compared to the results from square bead simulations for accuracy and are presented in Table 29, below. It can be seen from these results that the shape of the bead has little impact on the simulation predictions. Based on this and the comparison of square bead simulation results to experiments in previous chapters, it is clear that the shape of the bead has little bearing on the simulation results presented in this dissertation.

Table 29. Comparison of round bead to square bead simulations.

			Square Bead		Round Bead			
Added Material Size	**Power (W)**	**Velocity (in/min)**	**Area (in^2)**	**Length (in)**	**Area (in^2)**	**Length (in)**	**Area Percent Error (%)**	**Length Percent Error (%)**
Green	3000	16.35	0.061	0.998	0.061	0.947	0.2	-5.1
Red	3000	25.76	0.034	0.876	0.033	0.847	-2.8	-3.3
Blue	3000	53.13	0.016	0.846	0.016	0.810	-0.4	-4.3

5.3.2 2D vs 3D for Thin Walls

In this dissertation, 2D finite element simulations were used for the analysis of thin walls. While the experimental results from Chapter 3 confirm the accuracy of the 2D simulations, it was important to review the assumption of a 2D thin wall by running 3D simulations that contain a thin wall attached to a bulky substrate (see Figure 81). To do this, 3D finite element simulations were developed and run in the ABAQUS software package. The simulations contained a large bulky substrate with a thin wall that is 12 beads high, meaning that 12 passes of added material would need to be deposited in order to achieve the simulation wall height. The wall height and thickness were chosen to replicate the experiments performed in Chapter 3.

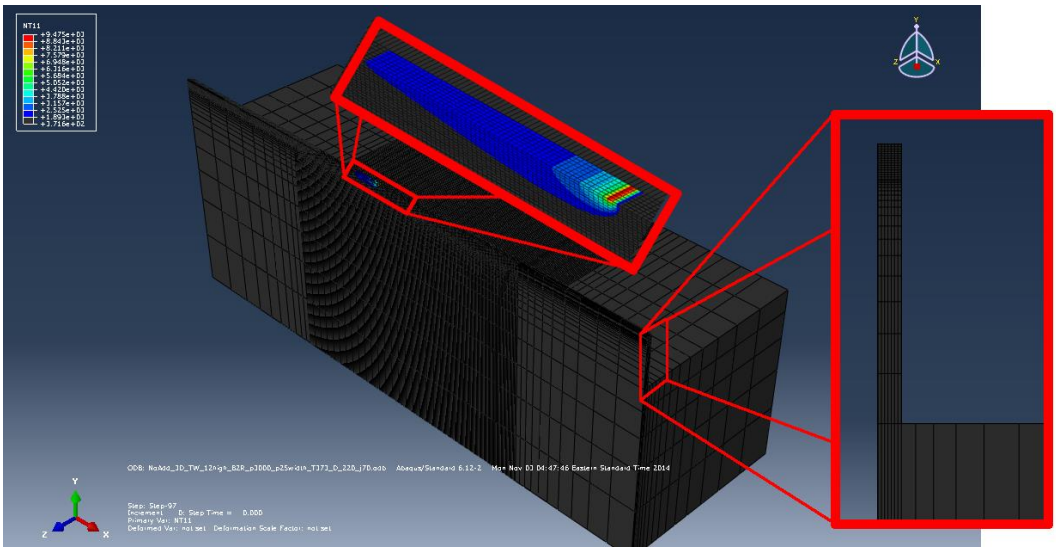

Figure 81. 3D Thin Wall Finite Element Model.

For this comparison, parameters for the step changes in the 2D thin wall with 373 K preheat were run in the 3D thin wall simulation with the same preheat. The results of the 3D simulations are presented in Figure 82, below. When compared to the 2D results in Figure 78, the error bars presented show that there is less variability in the response behavior in the 3D simulations. Additionally, a comparison of response distance is

presented in Table 30. It is evident from these results that the 2D and 3D simulation show little difference in initial and final steady state areas, as well as the response distance.

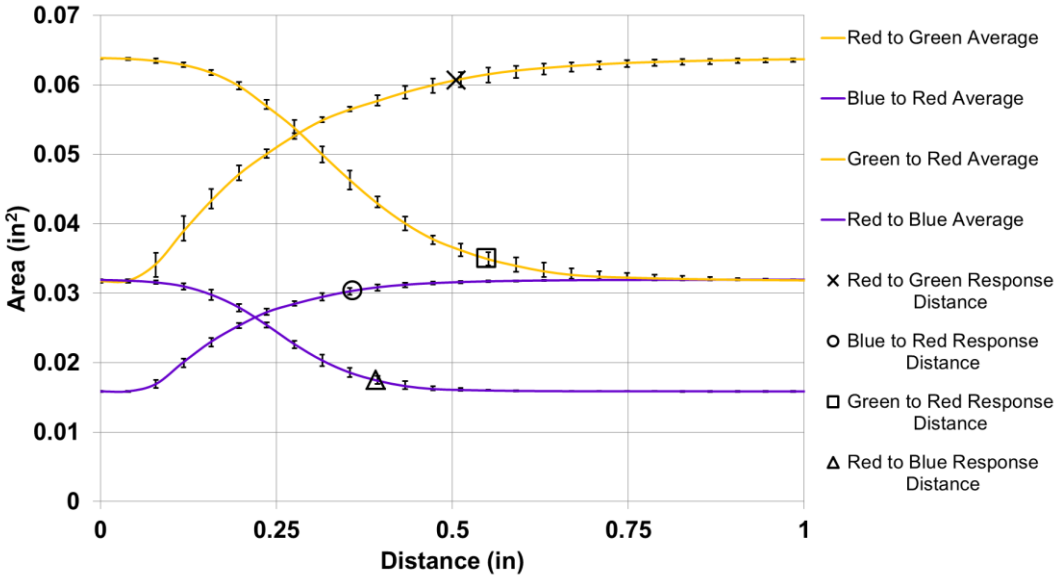

Figure 82. Response behaviors for 3D thin wall simulations with 373 K preheat.

Table 30. Comparison of 2D and 3D thin wall simulation results.

		2D			3D		
		Initial Area (in^2)	**Final Area (in^2)**	**Response Distance (in)**	**Initial Area (in^2)**	**Final Area (in^2)**	**Response Distance (in)**
Green to Red	8.2 in/min	0.064	0.032	0.58	0.064	0.032	0.64
	17.6 in/min	0.064	0.032	0.57	0.064	0.032	0.58
	27.0 in/min	0.064	0.032	0.55	0.064	0.032	0.54
	3000 W	0.064	0.032	0.54	0.064	0.032	0.54
Blue to Red	18.5 in/min	0.016	0.032	0.35	0.016	0.032	0.38
	36.6 in/min	0.016	0.032	0.31	0.016	0.032	0.33
	54.6 in/min	0.016	0.032	0.34	0.016	0.032	0.32
	3000 W	0.016	0.032	0.33	0.016	0.032	0.35
Red to Green	8.2 in/min	0.032	0.064	0.51	0.032	0.064	0.54
	17.6 in/min	0.032	0.064	0.44	0.032	0.064	0.48
	27.0 in/min	0.032	0.064	0.41	0.032	0.064	0.44
	3000 W	0.032	0.064	0.48	0.032	0.064	0.48
Red to Blue	18.5 in/min	0.032	0.016	0.39	0.032	0.016	0.44
	36.6 in/min	0.032	0.016	0.39	0.032	0.016	0.44
	54.6 in/min	0.032	0.016	0.37	0.032	0.016	0.42
	3000 W	0.032	0.016	0.36	0.032	0.016	0.39

5.3.3 Melt Pool Convection and Surface Radiation

Another assumption that was made for this analysis was neglecting radiation from the surface and convection within the melt pool. Prior work has found these to be minor effects when compared to the conduction of heat through the substrate [17]. To verify this assumption, simulations have been run comparing the effect of both the surface radiation and the melt pool convection. For melt pool convection, it is difficult to simulate the melting and solidification of material in ABAQUS. Thus, to simulate the melt pool convection, an effective thermal conductivity is used for temperatures above 1893 K (the melting temperature). The effective thermal conductivity is increased by factors of 1.5, 5, and 10 based on prior work by Fachinotti et al. [36]. While values of 10 conductivity are much higher than expected for the effective thermal conductivity in the melt pool, it provides an upper limit for the effect increased conductivity will have on the melt pool [37]. For the radiation, emissivity values of 0.5, 0.7, and 0.9 were tested and an ambient temperature of 1023 K was assumed.

For the analysis, a no material added simulation from the powder bed electron beam system was used for comparison. Absorbed power and velocity values of 500 W and 385.16 in/min were used in all the simulations for this comparison. Aside from changes to conductivity or emissivity, simulations were identical to the ones presented in Chapter 4. The results of the analysis can be seen in Table 31, below. As seen in the results, both the increase in conductivity and radiation from the surface affect the size and shape of the melt pool. Increases in conductivity lead to an increase in the melt pool area and decrease in length. The addition of surface radiation decreases the melt pool area, as expected, but also increases the length. The reason for the increase in length is because the melt pool

length is determined from the point of maximum area. While the distance from the point of maximum area to the tail end of the melt pool increases, the overall length of the melt pool decreases. When both phenomena are present in the simulations, the increase in conductivity dominates the change in the melt pool, as seen by the increase in area in the results below.

Table 31. Review of melt pool convection and surface radiation.

	Area (in^2)	Length (in)	Percent Change in Area (%)	Percent Change in Length (%)
No Surface Radiation or Change to Conductivity	5.26E-04	0.130	--	--
Increase Conduction by 1.5x	5.75E-04	0.120	9.3	-7.7
Increase Conduction by 5x	6.59E-04	0.095	25.3	-26.9
Increase Conduction by 10x	6.84E-04	0.079	30.2	-39.4
Add Emissivity of 0.5	4.48E-04	0.135	-14.9	3.6
Add Emissivity of 0.7	4.32E-04	0.138	-17.9	6.1
Add Emissivity of 0.9	4.18E-04	0.138	-20.4	5.8
Increase Conduction by 10x and Add Emissivity of 0.5	6.83E-04	0.076	29.9	-41.4
Increase Conduction by 10x and Add Emissivity of 0.7	6.82E-04	0.076	29.8	-41.7
Increase Conduction by 10x and Add Emissivity of 0.9	6.82E-04	0.076	29.7	-41.9

While most of the experimental measurements confirm the accuracy of response behavior, the variations seen in this analysis could provide an explanation for the

increased melt pool areas seen in some of the tests. Also, since predictions of response times from the simulations are dependent on melt pool length (through the value of L'), further analysis of these phenomena could provide a way to improve the accuracy of response time prediction and help explain the variability of response time seen in the simulation work.

5.4 Discussion

In this chapter, an analysis of the effect of preheat in thin walls as well as a review of modeling assumptions made in previous chapters is presented. In the review of the effect of preheat, 2D finite element simulations were set up and run in the ABAQUS software package. In these simulations, initial temperatures of 373 K and 773 K were chosen to compare to the 293 K analysis presented in Chapter 3. While the difference in preheat causes a shift in the curves of constant area and *L/d*, little change is found in the prediction of response distance.

The review of modeling assumptions made throughout the dissertation include the square bead of added material, use of 2D finite element simulations to model a thin wall geometry, neglecting convection within the melt pool, and neglecting surface radiation. Experimental results in each of the chapters validate the accuracy of the simulations presented and the effect of these assumptions is minor; however, it is important to determine if these assumptions are the cause of any of the variability seen in the experimental measurements.

To review the assumption of the square bead, simulations with a round bead of added material were run for comparison. Both the melt pool area and melt pool length in the

round bead simulations were very similar to the expected values from the square bead simulations. Therefore, the square bead assumption has negligible effect on the simulation results.

Accuracy of 2D finite element simulations for modeling the thin wall geometry was compared to 3D simulations with a thin wall on a bulky substrate. This analysis found negligible difference between the simulations and, as such, was not a source of error in the analysis.

Melt pool convection and surface radiation, however, was found to have a minor effect on simulation results. Melt pool convection was analyzed using an effective thermal conductivity in the temperatures above 1893 K in the material, consistent with similar work in the field [36,37]. It was found that the melt pool convection increased the area and decreased the length of the melt pool. Therefore, it is a possible explanation for the increase in melt pool area seen in several of the experiments, but proved not to be a significant source of error in the calculation of response distance or response behavior.

Chapter 6 Conclusions and Future Work

6.1 Conclusions

In order to maintain process stability in AM, control of the melt pool dimensions is imperative. This can be achieved via feedback or feedforward control approaches; however, a strong understanding of the transient response of the melt pool is required. The work presented in this dissertation investigates the transient response of the melt pool for multiple geometries and for multiple systems. To aid in the analysis of transient response, P-V Process Maps for melt pool dimensions were developed. For the wire feed electron beam system, the existing P-V Process Map for single bead deposition was updated and a map for a tall, thin wall geometry was developed. For the powder bed electron beam system, a P-V Process Map for no added material was developed. These systems/geometries were investigated to determine the transient response of the melt pool and control schemes were applied to a corner geometry in the wire feed electron beam system.

In the corner geometry investigated in Chapter 3, feedback control was found to not be possible because the position of the heat source is already past the corner once the change in melt pool width or depth is detected. Iterative control approaches, where the beam power is adjusted based on the change in melt pool depth were also found to be ineffective as it was not able to hold the melt pool depth to acceptable limits before diverging. Feedforward control, on the other hand, proved highly effective as the maximum melt pool depth was held to within ±3.5% of the desired value; validating that control approaches can be used to maintain consistent melt pool depth through a transient geometry.

In the wire feed and powder bed systems, step changes in power and velocity between curves of constant area have shown that response times can be very long (on the order of seconds for the wire feed system), show little correlation, and can limit feedback capabilities. Response distances, however, can be predicted through an understanding of the initial and final melt pool geometry. The distance between the point of maximum melt pool area and the heat source (L') was also defined and has provided a method for determining response time, which prior to this work showed little correlation. Finally, response behaviors were found to be similar for step changes with matching initial and final steady state areas and not the position or path taken in the P-V Process Map and this result is true for all systems and geometries studied in this dissertation.

6.2 Implications of the Research

While prior investigations into control systems for AM have been accomplished, little research on the transient response of the melt pool had been completed. This research has provided significant insight into the development of feedback and feedforward control schemes and the contributions of the research are as follows:

- Importance of response distance across processing space: Prior work has shown that response distance is the key metric to consider for understanding response behavior in the laser powder bed system (a small portion of the P-V process space for AM). This work has shown that this relationship extends to a wide range of process variables that span all of the P-V process space for AM. These relationships hold for the single bead as well as the thin wall geometries. Additionally, this work has shown a dependence on geometry and AM system, which was not seen in the previous work.

- Expansion of P-V Process Maps to new systems, geometries, and materials: This work has presented P-V process maps for the deposition of Ti-6Al-4V for a single bead on a bulky substrate and a thin wall in the electron beam wire feed system and for a single bead on a bulky substrate for the electron beam powder bed system, which were not previously available.
- Definition of L' and equations for determination of response time: Prior to this work, no accurate method for predicting melt pool response time has been presented. This work has discovered that the distance between the heat source and the maximum area of the melt pool (L') is a key parameter to determine response time and is the missing link for aligning the response time with response distance.
- Importance of feedforward control for a corner geometry: In this work, it was found that feedback control is not feasible for a corner geometry. Feedforward control, however, was able to maintain melt pool depth to within ±3.5% of the desired value.
- Ability to understand a new system or material with limited testing: A major impact of this work is that the response distance and response time can be ***predicted*** for a new system and/or material by fitting the multiples of key features of the steady state melt pool geometry (d_1, d_2, L'_1, and L'_2) to a small set of simulations (or even a single simulation) and extrapolating to cover the entire process space for that material and system.

6.3 Future Work

The work presented in this dissertation relates the transient response of the melt pool to the initial and final melt pool geometry. The breakthrough of this research is the ability to determine melt pool response distance and response time through minimal experimental testing or simulation work, providing a basis for feedback and feedforward control. While considerable progress has been made in this research, there are several potential areas for future work:

- Additional materials: The analysis in this dissertation was for one material (Ti-6Al-4V), however, several materials are used in AM. Melt pool geometry and transient response are dependent on the thermal properties of the material being deposited. As such it is important to determine how transient response differs between materials. The findings presented in this dissertation show that the response distance and response time can be ***predicted*** for a new material by fitting the multiples of key features of the steady state melt pool geometry (d_1, d_2, L'_1, and L'_2) to a small set of simulations (or even a single simulation) and extrapolating to cover the entire process space for that material and system.
- Detailed analysis of the corner geometry (and other transient geometries): A method for controlling melt pool depth in a corner geometry has been presented. It was found that feedback control was not feasible and that feedforward control is required. More importantly, it was found that the presence of a non-zero L' required the control scheme to decrease power at the corner (not before the corner) to maintain a desired melt pool depth. It is

suspected that the magnitude of the decrease in power required is related to the steady state melt pool geometry but additional testing is required to confirm this hypothesis. Additionally, the analysis can be extended to include other transient geometries.

- Expansion to additional steady state geometries: In this work, single bead and thin wall geometries are explored. However, there are additional geometries that can be studied to further develop an understanding of the effect geometry plays on the transient response of the melt pool. Again, the findings presented in this thesis show that response distance and response time can be predicted for a new geometry through a small set of simulations (or even a single simulation) and extrapolating to the full process space of that geometry in the given system.
- Application to feedback control systems: Based on the analysis presented, feedback and feedforward control systems can be developed. While access to thermal imaging systems was not available at the time of this research, advancements in the use of thermal imaging in AM make it possible to put the knowledge gained through this dissertation into practice.

References

[1] Taminger, K. M., and Hafley, R. A., 2006, "Electron beam freeform fabrication for cost effective near-net shape manufacturing," NATO/RTO AVT-139 Specialists' Meeting on Cost Effective Manufacture via Net Shape Processing, Amsterdam, The Netherlands, pp. 9–25.

[2] Taminger, K. M., and Hafley, R. A., 2013, "Electron beam freeform fabrication: a rapid metal deposition process," Proceedings of the 3rd Annual Automotive Composites Conference, Society of Plastics Engineers, Troy, MI.

[3] Soylemez, E., Beuth, J. L., and Taminger, K., 2010, "Controlling Melt Pool Dimensions Over a Wide Range of Material Deposition Rates in Electron Beam Additive Manufacturing," Solid Freeform Fabrication Proceedings, Austin, TX, pp. 571–582.

[4] Taminger, K. M., Hafley, R. A., and Dicus, D. L., 2002, "Solid Freeform Fabrication: An Enabling Technology for Future Space Missions," Proceedings of the 2002 International Conference on Metal Powder Deposition for Rapid Prototyping, San Antonio, TX.

[5] Gibson, I., Rosen, D., and Stucker, B., 2015, Additive Manufacturing Technologies, Springer New York, New York, NY.

[6] Horn, T. J., Harrysson, O. L., Little, J. P., West II, H. A., and Marcellin-Little, D. J., "DESIGN AND MANUFACTURING OF BONE ANALOG MODELS FOR THE MECHANICAL EVALUATION OF CUSTOM MEDICAL IMPLANTS."

[7] Horn, T. J., and Harrysson, O. L. A., 2012, "Overview of current additive manufacturing technologies and selected applications," Science Progress, **95**(3), pp. 255–282. DOI: 10.3184/003685012X13420984463047.

[8] Harrysson, O. L. A., Cansizoglu, O., Marcellin-Little, D. J., Cormier, D. R., and West II, H. A., 2008, "Direct metal fabrication of titanium implants with tailored materials and mechanical properties using electron beam melting technology," Materials Science and Engineering: C, **28**(3), pp. 366–373. DOI: 10.1016/j.msec.2007.04.022.

[9] Beuth, J., Fox, J., Gockel, J., Montgomery, C., Yang, R., Qiao, H., Soylemez, E., Reeseewatt, P., Anvari, A., and Narra, S., 2013, "Process Mapping for Qualification Across Multiple Direct Metal Additive Manufacturing Processes," Solid Freeform Fabrication Proceedings, Austin, TX, pp. 655–665.

[10] Aggarangsi, P., Beuth, J. L., and Gill, D. D., 2004, "Transient Changes in Melt Pool Size in Laser Additive Manufacturing Processes," Solid Freeform Fabrication Proceedings, pp. 163–174.

[11] Thompson, J. R., 2014, "RELATING MICROSTRUCTURE TO PROCESS VARIABLES IN BEAM-BASED ADDITIVE MANUFACTURING OF INCONEL 718," Wright State University.

[12] Montgomery, C., Beuth, J., and Moylan, S., 2014, "Process Mapping of Melt Pool Geometry in the Laser Powder Bed Additive Manufacturing of Inconel 625."

[13] Narra, S., 2015, Internal Report, "Process Mapping of Aluminum Alloys", Carnegie Mellon University.

[14] Beuth, J., 2013, "Process Mapping of Melt Pool Geometry." PCT/US2012/048658. Issued February 7, 2013.

[15] Beuth, J. L., Klingbeil, N. W., and Gockel, J., 2013, "Process Mapping of Cooling Rates and Thermal Gradient." PCT/US2013/055422. Filed August 16, 2013.
[16] Rosenthal, D., 1946, "The Theory of Moving Sources of Heat and its Application to Metal Treatments," Transactions of the ASME, **68**, pp. 849–866.
[17] Dobranich, D., and Dykhuizen, R., 1998, "Scoping Thermal Calculation of the LENS Process," Sandia National Laboratories Internal Report.
[18] Siegle, R., and Goldstein, M., 1970, "Analytical Method for Steady State Heat Transfer in Two-Dimensional Porous Media." National Aeronautics and Space Administration. Lewis Research Center. Cleveland, Ohio.
[19] Goldak, J., Chakravarti, A., and Bibby, M., 1984, "A new finite element model for welding heat sources," Metallurgical transactions B, **15**(2), pp. 299–305.
[20] Goldak, J., Bibby, M., Moore, J., House, R., and Patel, B., 1986, "Computer modeling of heat flow in welds," MTB, **17**(3), pp. 587–600. DOI: 10.1007/BF02670226.
[21] Mundra, K., DebRoy, T., and Kelkar, K. M., 1996, "NUMERICAL PREDICTION OF FLUID FLOW AND HEAT TRANSFER IN WELDING WITH A MOVING HEAT SOURCE," Numerical Heat Transfer, Part A: Applications, **29**(2), pp. 115–129. DOI: 10.1080/10407789608913782.
[22] Westerberg, K. W., Merier, T. C., McClelland, M. A., Braun, D. G., Berzins, L. V., Anklam, T. M., and Storer, J., 1998, Analysis of the E-Beam Evaporation of Titanium and Ti-6al-4v, Lawrence Livermore National Lab., CA (United States).
[23] Barclay, R. C., 2013, "Parameter optimization for controlling aluminum loss when laser depositing Ti-6Al-4V." Missouri University of Science and Technology.
[24] Nguyen, N. T., Ohta, A., Matsuoka, K., Suzuki, N., and Maeda, Y., 1999, "Analytical solutions for transient temperature of semi-infinite body subjected to 3-D moving heat sources," WELDING JOURNAL-NEW YORK-, **78**, p. 265–s.
[25] Lee, Y. S., Nordin, M., Babu, S. S., and Farson, F., 2014, "Influence-of-Fluid-Convection-on-Weld-Pool-Formation-in-Laser-Cladding.pdf," Welding Journal, **93**, pp. 292–300.
[26] Rai, R., Elmer, J. W., Palmer, T. A., and DebRoy, T., 2007, "Heat transfer and fluid flow during keyhole mode laser welding of tantalum, Ti–6Al–4V, 304L stainless steel and vanadium," J. Phys. D: Appl. Phys., **40**(18), p. 5753. DOI: 10.1088/0022-3727/40/18/037.
[27] Rai, R., Burgardt, P., Milewski, J. O., Lienert, T. J., and DebRoy, T., 2009, "Heat transfer and fluid flow during electron beam welding of 21Cr–6Ni–9Mn steel and Ti–6Al–4V alloy," J. Phys. D: Appl. Phys., **42**(2), p. 025503. DOI: 10.1088/0022-3727/42/2/025503.
[28] Mahrle, A., and Schmidt, J., 2002, "The influence of fluid flow phenomena on the laser beam welding process," International Journal of Heat and Fluid Flow, **23**(3), pp. 288–297. DOI: 10.1016/S0142-727X(02)00176-5.
[29] Zacharia, T., Vitek, J. M., Goldak, J. A., DebRoy, T. A., Rappaz, M., and Bhadeshia, H. K. D. H., 1995, "Modeling of fundamental phenomena in welds," Modelling Simul. Mater. Sci. Eng., **3**(2), p. 265. DOI: 10.1088/0965-0393/3/2/009.
[30] Lindgren, L.-E., 2006, "Numerical modelling of welding," Computer Methods in Applied Mechanics and Engineering, **195**(48–49), pp. 6710–6736. DOI: 10.1016/j.cma.2005.08.018.

[31] Han, L., Liou, F. W., and Musti, S., 2005, "Thermal Behavior and Geometry Model of Melt Pool in Laser Material Process," J. Heat Transfer, **127**(9), pp. 1005–1014. DOI: 10.1115/1.2005275.

[32] Neela, V., and De, A., 2009, "Three-dimensional heat transfer analysis of LENSTM process using finite element method," Int J Adv Manuf Technol, **45**(9-10), pp. 935–943. DOI: 10.1007/s00170-009-2024-9.

[33] Roberts, I. A., Wang, C. J., Esterlein, R., Stanford, M., and Mynors, D. J., 2009, "A three-dimensional finite element analysis of the temperature field during laser melting of metal powders in additive layer manufacturing," International Journal of Machine Tools and Manufacture, **49**(12-13), pp. 916–923. DOI: 10.1016/j.ijmachtools.2009.07.004.

[34] Shen, N., and Chou, K., 2012, "NUMERICAL THERMAL ANALYSIS IN ELECTRON BEAM ADDITIVE MANUFACTURING WITH PREHEATING EFFECTS."

[35] Shen, N., and Chou, K., 2012, "Thermal Modeling of Electron Beam Additive Manufacturing Process–Powder Sintering Effects," Proceedings of the ASME 2012 International Manufacturing Science and Engineering Conference MSEC2012-7253, pp. 1–9.

[36] Fachinotti, V. D., Cardona, A., Baufeld, B., and Van der Biest, O., 2012, "Finite-element modelling of heat transfer in shaped metal deposition and experimental validation," Acta Materialia, **60**(19), pp. 6621–6630. DOI: 10.1016/j.actamat.2012.08.031.

[37] Raghavan, A., Wei, H. L., Palmer, T. A., and DebRoy, T., 2013, "Heat transfer and fluid flow in additive manufacturing," Journal of Laser Applications, **25**(5), p. 052006. DOI: 10.2351/1.4817788.

[38] Hodge, N. E., Ferencz, R. M., and Solberg, J. M., 2014, "Implementation of a thermomechanical model for the simulation of selective laser melting," Comput Mech, pp. 1–19. DOI: 10.1007/s00466-014-1024-2.

[39] Martukanitz, R., Michaleris, P., Palmer, T., DebRoy, T., Liu, Z.-K., Otis, R., Heo, T. W., and Chen, L.-Q., 2014, "Toward an integrated computational system for describing the additive manufacturing process for metallic materials," Additive Manufacturing, **1–4**, pp. 52–63. DOI: 10.1016/j.addma.2014.09.002.

[40] Manvatkar, V., De, A., and DebRoy, T., 2014, "Spatial variation of melt pool geometry, peak temperature and solidification parameters during laser assisted additive manufacturing process," Mater. Sci. Technol., p. 1743284714Y.0000000701. DOI: 10.1179/1743284714Y.0000000701.

[41] Manvatkar, V., De, A., and DebRoy, T., 2014, "Heat transfer and material flow during laser assisted multi-layer additive manufacturing," Journal of Applied Physics, **116**(12), p. 124905. DOI: 10.1063/1.4896751.

[42] Vasinonta, A., Beuth, J. L., and Griffith, M. L., 1999, "Process Maps for Laser Deposition of Thin-Walled Structures," Solid Freeform Fabrication Proceedings, Austin, TX, pp. 383–391.

[43] Vasinonta, A., Beuth, J. L., and Griffith, M. L., 2000, "Process maps for controlling residual stress and melt pool size in laser-based SFF processes," Solid Freeform Fabrication Proceedings, Austin, TX, pp. 200–208.

[44] Vasinonta, A., Beuth, J. L., and Ong, R., 2001, "Melt pool size control in thin-walled and bulky parts via process maps," Solid Freeform Fabrication Proceedings, Austin, TX, pp. 432–440.
[45] Beuth, J., and Klingbeil, N., 2001, "The Role of Process Variables in Laser-Based Direct Metal Solid Freeform Fabrication," JOM, **53**(9), pp. 36–39. DOI: 10.1007/s11837-001-0067-y.
[46] Vasinonta, A., 2002, Process maps for melt pool size and residual stress in Laser-based solid freeform fabrication, UMI.
[47] Klingbeil, N. W., Zinn, J. W., and Beuth, J. L., 1997, "Measurement of Residual Stresses in Parts Created by Shape Deposition Manufacturing," Solid Freeform Fabrication Proceedings, Austin, TX, pp. 125–132.
[48] Klingbeil, N. W., Beuth, J. L., Chin, R. K., and Amon, C. H., 1998, "Measurement and Modeling of Residual Stress-Induced Warping in Direct Metal Deposition Processes," Solid Freeform Fabrication Proceedings, Austin, TX, pp. 367–374.
[49] Klingbeil, N. W., Beuth, J. L., Chin, R. K., and Amon, C. H., 2002, "Residual Stress-Induced Warping in Direct Metal Solid Freeform Fabrication," International Journal of Mechanical Sciences, **44**(1), pp. 57–77. DOI: 10.1016/S0020-7403(01)00084-4.
[50] Ong, R., Beuth, J. L., and Weiss, L. E., 2000, "Residual Stress Control Issues for Thermal Deposition of Polymers in SFF Processes," Solid Freeform Fabrication Proceedings, Austin, TX, pp. 209–218.
[51] Mercelis, P., and Kruth, J.-P., 2006, "Residual Stresses in Selective Laser Sintering and Selective Laser Melting," Rapid Prototyping Journal, **12**(5), pp. 254–265. DOI: 10.1108/13552540610707013.
[52] Van Belle, L., Vansteenkiste, G., and Boyer, J. C., 2013, "Investigation of Residual Stresses Induced during the Selective Laser Melting Process," Key Engineering Materials, **554-557**, pp. 1828–1834. DOI: 10.4028/www.scientific.net/KEM.554-557.1828.
[53] Miller, R. S., Cao, G., and Grujicic, M., 2001, "Monte Carlo Simulation of Three-Dimensional Nonisothermal Grain-Microstructure Evolution: Application to LENS Rapid Fabrication," Journal of materials synthesis and processing, **9**(6), pp. 329–345.
[54] Mishra, S., and DebRoy, T., 2004, "Measurements and Monte Carlo simulation of grain growth in the heat-affected zone of Ti–6Al–4V welds," Acta Materialia, **52**(5), pp. 1183–1192. DOI: 10.1016/j.actamat.2003.11.003.
[55] Kobryn, P. A., and Semiatin, S. L., 2001, "The Laser Additive Manufacture of Ti-6Al-4V," JOM, **53**(9), pp. 40–42. DOI: 10.1007/s11837-001-0068-x.
[56] Kelly, S. M., and Kampe, S. L., 2004, "Microstructural Evolution in Laser-Deposited Multilayer Ti-6Al-4V Builds: Part I. Microstructural Characterization," Metallurgical and Materials Transactions A, **35**(6), pp. 1861–1867. DOI: 10.1007/s11661-004-0094-8.
[57] Zheng, B., Zhou, Y., Smugeresky, J. E., Schoenung, J. M., and Lavernia, E. J., 2008, "Thermal Behavior and Microstructural Evolution during Laser Deposition with Laser-Engineered Net Shaping: Part I. Numerical Calculations," Metallurgical

and Materials Transactions A, **39**(9), pp. 2228–2236. DOI: 10.1007/s11661-008-9557-7.

[58] Hrabe, N., and Quinn, T., 2013, "Effects of Processing on Microstructure and Mechanical Properties of a Titanium Alloy (Ti–6Al–4V) Fabricated Using Electron Beam Melting (EBM), Part 1: Distance From Build Plate and Part Size," Materials Science and Engineering: A, **573**, pp. 264–270. DOI: 10.1016/j.msea.2013.02.064.

[59] Hrabe, N., and Quinn, T., 2013, "Effects of Processing on Microstructure and Mechanical Properties of a Titanium Alloy (Ti–6Al–4V) Fabricated Using Electron Beam Melting (EBM), Part 2: Energy Input, Orientation, and Location," Materials Science and Engineering: A, **573**, pp. 271–277. DOI: 10.1016/j.msea.2013.02.065.

[60] Brandl, E., and Greitemeier, D., 2012, "Microstructure of Additive Layer Manufactured Ti–6Al–4V After Exceptional Post Heat Treatments," Materials Letters, **81**, pp. 84–87. DOI: 10.1016/j.matlet.2012.04.116.

[61] Vrancken, B., Thijs, L., Kruth, J.-P., and Van Humbeeck, J., 2012, "Heat treatment of Ti6Al4V produced by Selective Laser Melting: Microstructure and mechanical properties," Journal of Alloys and Compounds, **541**, pp. 177–185. DOI: 10.1016/j.jallcom.2012.07.022.

[62] Alphons ANTONYSAMY, 2012, "Microstructure, Texture and Mechanical Property Evolution during Additive Manufacturing of Ti6Al4V Alloy for Aerospace Applications," University of Manchester.

[63] Bontha, S., and Klingbeil, N. W., 2003, "Thermal process maps for controlling microstructure in laser-based solid freeform fabrication," Solid Freeform Fabrication Proceedings, Austin, TX, pp. 219–226.

[64] Bontha, S., Klingbeil, N. W., Kobryn, P. A., and Fraser, H. L., 2009, "Effects of process variables and size-scale on solidification microstructure in beam-based fabrication of bulky 3D structures," Materials Science and Engineering: A, **513-514**, pp. 311–318. DOI: 10.1016/j.msea.2009.02.019.

[65] Klingbeil, N. W., Bontha, S., Brown, C. J., Gaddam, D. R., Kobryn, P. A., Fraser, H. L., and Sears, J. W., 2004, "Effects of process variables and size scale on solidification microstructure in laser-based solid freeform fabrication of Ti-6Al-4V," Solid Freeform Fabrication Proceedings, Austin, TX, pp. 92–103.

[66] Davis, J. E., Klingbeil, N. W., and Bontha, S., 2010, "Effect of Free-Edges on Melt Pool Geometry and Solidification of Microstructure in Beam-Based Fabrication of Bulky 3-D Structures," Solid Freeform Fabrication Proceedings, Austin, TX, pp. 230–241.

[67] Doak, H. N., 2013, "EFFECT OF PROCESS VARIABLES ON SUB-MELT THERMAL BEHAVIOR AND SOLID-STATE PHASE TRANSFORMATIONS IN BEAM-BASED ADDITIVE MANUFACTURING OF TI-6AL-4V," Wright State University.

[68] Gockel, J., and Beuth, J. L., 2013, "Understanding Ti-6Al-4V Microstructure Control in Additive Manufacturing via Process Maps," Solid Freeform Fabrication Proceedings, Austin, TX, pp. 666–674.

[69] Gockel, J., Fox, J., Beuth, J., and Hafley, R., 2014, "Integrated melt pool and microstructure control for Ti–6Al–4V thin wall additive manufacturing," Mater. Sci. Technol., p. 1743284714Y.0000000704. DOI: 10.1179/1743284714Y.0000000704.

[70] Gockel, J., 2014, "Integrated Control of Solidification Microstructure and Melt Pool Dimensions In Additive Manufacturing of Ti - 6Al - 4V," Dissertations.

[71] Wang, L., Felicelli, S., Gooroochurn, Y., Wang, P. T., and Horstemeyer, M. F., 2008, "Optimization of the LENS® Process for Steady Molten Pool Size," Materials Science and Engineering: A, **474**(1-2), pp. 148–156. DOI: 10.1016/j.msea.2007.04.119.

[72] Chokkalingham, S., Chandrasekhar, N., and Vasudevan, M., 2011, "Predicting the depth of penetration and weld bead width from the infra red thermal image of the weld pool using artificial neural network modeling," J Intell Manuf, **23**(5), pp. 1995–2001. DOI: 10.1007/s10845-011-0526-4.

[73] Sibillano, T., Ancona, A., Rizzi, D., Mezzapesa, F., Konuk, A. R., Aarts, R., Huis in 't Veld, B., and Lugarà, P. M., 2012, "Spectroscopic closed loop control of penetration depth in laser beam welding process," p. 82390S–82390S–8. DOI: 10.1117/12.906778.

[74] Lucas, W., Bertaso, D., Melton, G., Smith, J., and Balfour, C., 2012, "Real-time vision-based control of weld pool size," Welding International, **26**(4), pp. 243–250. DOI: 10.1080/09507116.2011.581336.

[75] Wang, Z., Zhang, Y., and Wu, L., 2012, "Adaptive interval model control of weld pool surface in pulsed gas metal arc welding," Automatica, **48**(1), pp. 233–238. DOI: 10.1016/j.automatica.2011.09.052.

[76] Huang, W., and Kovacevic, R., 2012, "Development of a real-time laser-based machine vision system to monitor and control welding processes," Int J Adv Manuf Technol, **63**(1-4), pp. 235–248. DOI: 10.1007/s00170-012-3902-0.

[77] Kristiansen, M., Kristiansen, E., Jensen, C. H., and Christensen, R. S., 2014, "Vision of the Arc for Quality Documentation and for Closed Loop Control of the Welding Process," Journal of Automation and Control Engineering Vol, **2**(4).

[78] Benda, J., 1994, "Temperature controlled selective laser sintering," Proceedings of the Solid Freeform Fabrication Symposium, pp. 277–84.

[79] Hu, D., and Kovacevic, R., 2003, "Modelling and measuring the thermal behaviour of the molten pool in closed-loop controlled laser-based additive manufacturing," Proceedings of the Institution of Mechanical Engineers, Part B: Journal of Engineering Manufacture, **217**(4), pp. 441–452. DOI: 10.1243/095440503321628125.

[80] Hu, D., and Kovacevic, R., 2003, "Sensing, modeling and control for laser-based additive manufacturing," International Journal of Machine Tools and Manufacture, **43**(1), pp. 51–60. DOI: 10.1016/S0890-6955(02)00163-3.

[81] Hu, D., Mei, H., and Kovacevic, R., 2002, "Improving solid freeform fabrication by laser-based additive manufacturing," Proceedings of the Institution of Mechanical Engineers, Part B: Journal of Engineering Manufacture, **216**(9), pp. 1253–1264. DOI: 10.1243/095440502760291808.

[82] Wang, L., Felicelli, S., and Craig, J., 2007, "Thermal modeling and experimental validation in the LENSTM process," 18th Solid Freeform Fabrication Symposium. Austin, TX, pp. 100–111.

[83] Kruth, J.-P., Mercelis, P., Van Vaerenbergh, J., and Craeghs, T., 2007, "Feedback control of selective laser melting," pp. 521–527.

[84] Tang, L., Sparks, T. E., Ruan, J., Landers, R. G., and Liou, F. W., 2009, "ONLINE MELT POOL TEMPERATURE CONTROL FOR LASER METAL DEPOSITION PROCESSES."

[85] Song, L., and Mazumder, J., 2011, "Feedback Control of Melt Pool Temperature During Laser Cladding Process," IEEE Transactions on Control Systems Technology, **19**(6), pp. 1349–1356. DOI: 10.1109/TCST.2010.2093901.

[86] Song, L., Bagavath-Singh, V., Dutta, B., and Mazumder, J., 2012, "Control of Melt Pool Temperature and Deposition Height During Direct Metal Deposition Process," Int J Adv Manuf Technol, **58**(1-4), pp. 247–256. DOI: 10.1007/s00170-011-3395-2.

[87] Rodriguez, E., Medina, F., Espalin, D., Terrazas, C., Muse, D., Henry, C., and Wicker, R. B., 2012, "Integration of a Thermal Imaging Feedback Control System in Electron Beam Melting," WM Keck Center for 3D Innovation, University of Texas at El Paso.

[88] Craeghs, T., Clijsters, S., Kruth, J.-P., Bechmann, F., and Ebert, M.-C., 2012, "Detection of Process Failures in Layerwise Laser Melting with Optical Process Monitoring," Physics Procedia, **39**, pp. 753–759. DOI: 10.1016/j.phpro.2012.10.097.

[89] RIEDER, H., DILLHÖFER, A., SPIES, M., BAMBERG, J., and HESS, T., 2014, "Online Monitoring of Additive Manufacturing Processes Using Ultrasound."

[90] Zalameda, J. N., Burke, E. R., Hafley, R. A., Taminger, K. M., Domack, C. S., Brewer, A., and Martin, R. E., 2013, "Thermal imaging for assessment of electron-beam freeform fabrication (EBF3) additive manufacturing deposits," Proc. SPIE 8705, p. 87050M–87050M–8. DOI: 10.1117/12.2018233.

[91] Dinwiddie, R. B., Dehoff, R. R., Lloyd, P. D., Lowe, L. E., and Ulrich, J. B., 2013, Thermographic In-Situ Process Monitoring of the Electron Beam Melting Technology used in Additive Manufacturing, Oak Ridge National Laboratory (ORNL).

[92] Krauss, H., Eschey, C., and Zaeh, M. F., "Thermography for Monitoring the Selective Laser Melting Process."

[93] Moylan, S., Whitenton, E., Lane, B., and Slotwinski, J., 2014, "Infrared thermography for laser-based powder bed fusion additive manufacturing processes," AIP Conference Proceedings, AIP Publishing, pp. 1191–1196. DOI: 10.1063/1.4864956.

[94] Birnbaum, A., Aggarangsi, P., and Beuth, J., 2003, "Process Scaling and Transient Melt Pool Size Control in Laser-Based Additive Manufacturing Processes," Solid Freeform Fabrication Proceedings, Austin, TX, pp. 328–339.

[95] Aggarangsi, P., 2006, "Transient melt pool size and stress control in additive manufacturing processes," Dissertation Abstracts International, **67**(12).

[96] Aggarangsi, P., Beuth, J. L., and Griffith, M. L., 2003, "Melt pool size and stress control for laser-based deposition near a free edge," Solid Freeform Fabrication Proceedings, pp. 196–207.

[97] Reeseewatt, P., and Beuth, J. L., 2012, "Control of Melt Pool Dimensions in the Building of Thin-Walled Structures by Electron Beam Direct Digital Manufacturing," Carnegie Mellon University Bennett Conference.

[98] Beuth, J. L., and Fox, J., "Process mapping of transient thermal response due to value changes in a process variable." PCT/US2014/029096. Filed March 14, 2014.

[99] Qiao, H., and Beuth, J., 2013, "Deposition Near a Free Edge in Direct Metal Additive Manufacturing," Pittsburgh, PA.
[100] Anvari, A., and Beuth, J., 2013, "Analysis of Melt Pool Dimensions in a Corner Geometry", Carnegie Mellon University, Pittsburgh, PA.
[101] Gockel, J., Christiansen, D., and Fox, J., 2014, "Arcam Single Pass Experiment Summary", Carnegie Mellon University, Pittsburgh, PA.

Appendix A Measurement of Single Bead Samples

No Added Material

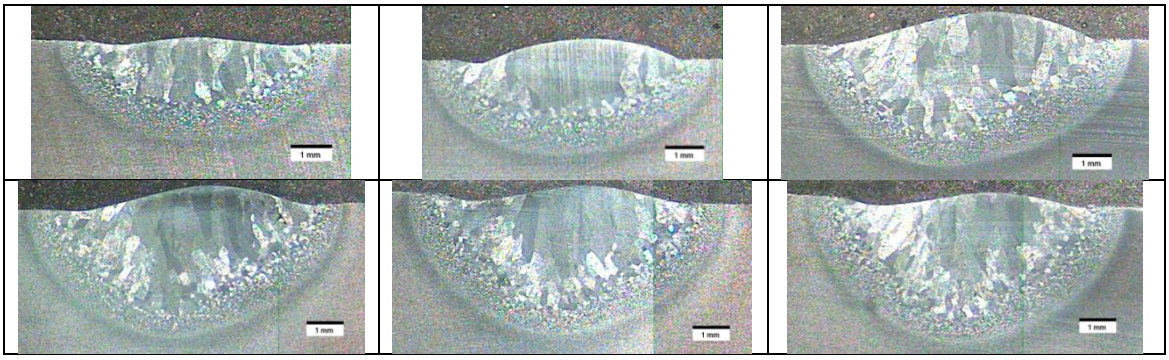

Figure 83. Sectioned and polished images of Cool Down experiment run 2. Black / white scale bars are 1 mm (3.94E-2 in).

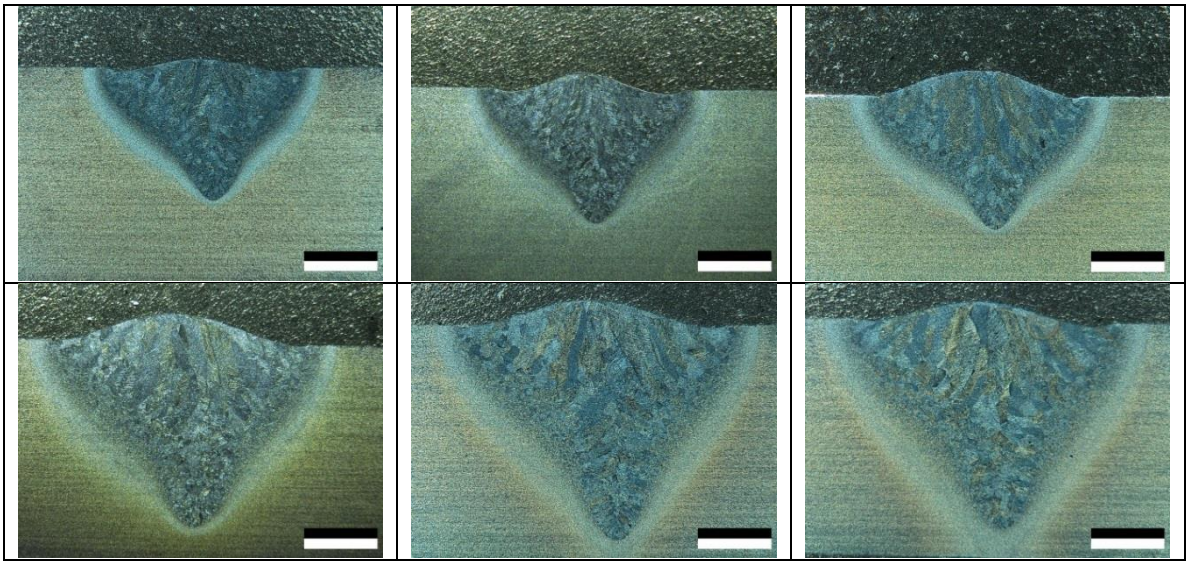

Figure 84. Sectioned and polished images of Cool Down experiment run 8. Black/white scale bar measures 7.87E-2 in (2 mm).

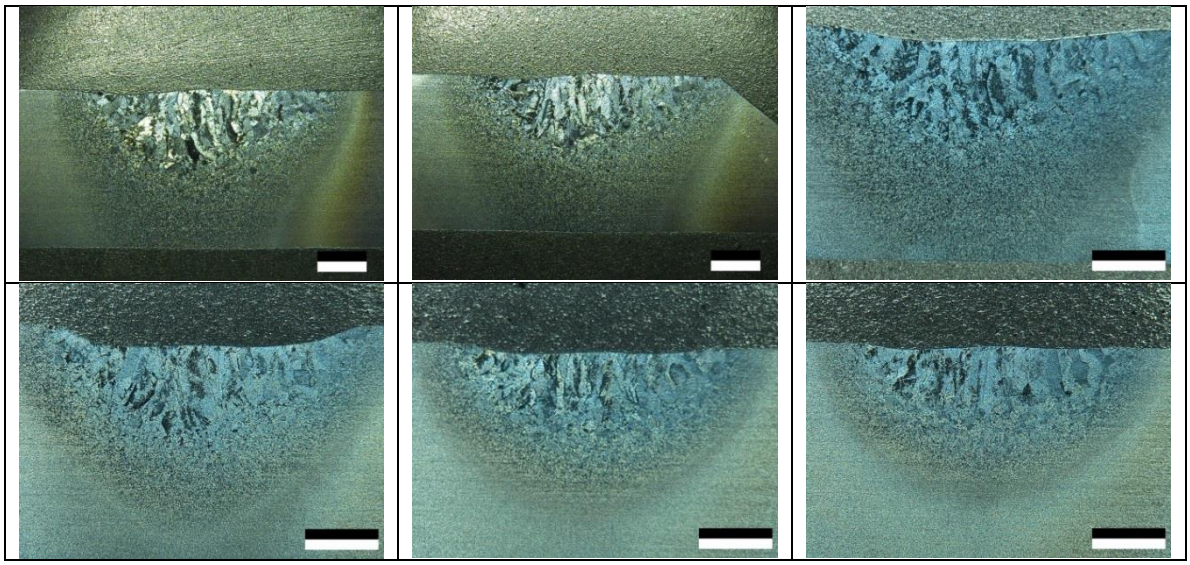

Figure 85. Sectioned and polished images of Rapid experiment run 1. Black/white scale bar measures 7.87E-2 in (2 mm).

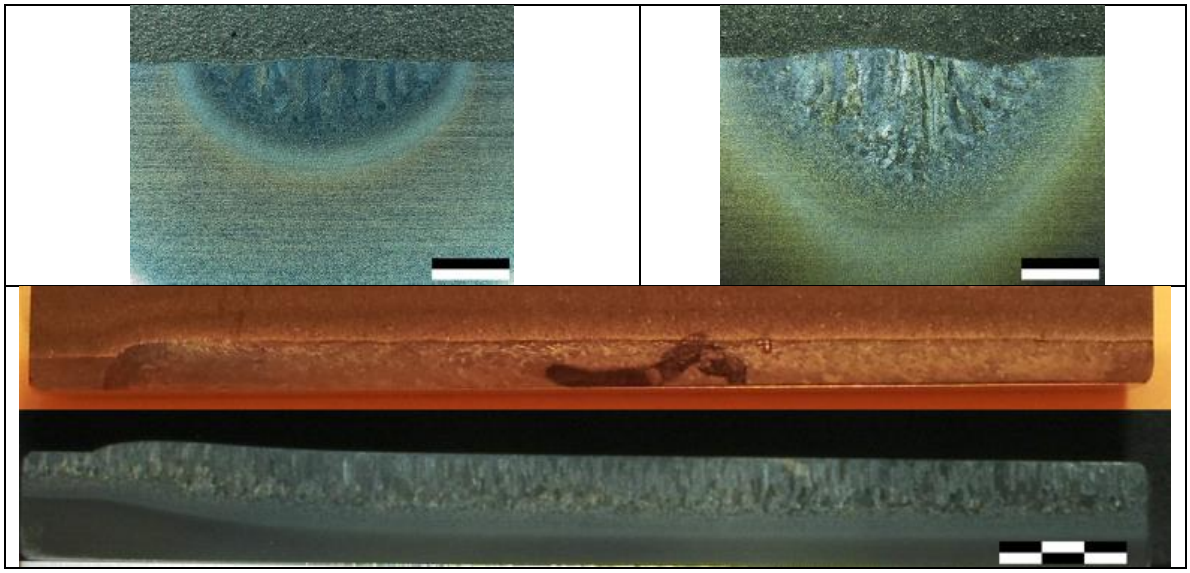

Figure 86. Sectioned and polished images from Rapid experiment run 2: initial steady state (top left), final steady state (top right), transient region (bottom). Each black/white scale bar section measures 7.87E-2 in (2 mm).

Added Material

Polished samples for single bead of added material experiments in the wire feed electron beam system are presented in this appendix. For samples cut perpendicular to travel velocity (similar to Figure 87) the polished sample, measurement of the head affected zone, and measurement of the melted area are presented on the left, middle, and right of each figure, respectively. For samples cut parallel to travel velocity (similar to Figure 88), the polished sample is presented with three red lines for measuring distances. The top line is the top of the bead, the middle line is the melted depth, and the bottom line is the heat affected zone. Green scale bars are 0.25 in.

Experiment Line 1

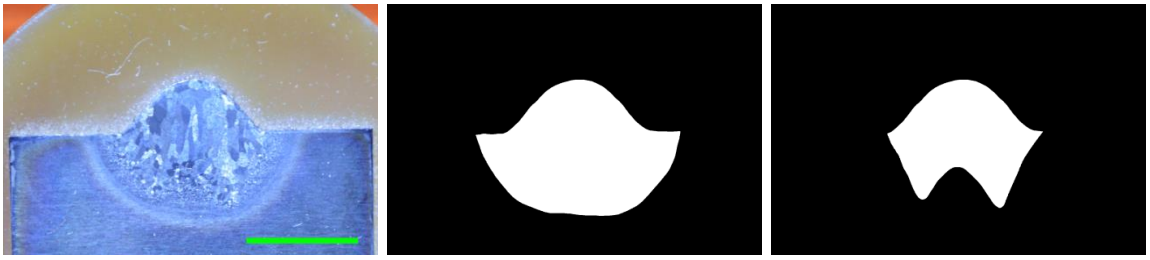

Figure 87. Sample 1A. Experiment line 1, initial steady state.

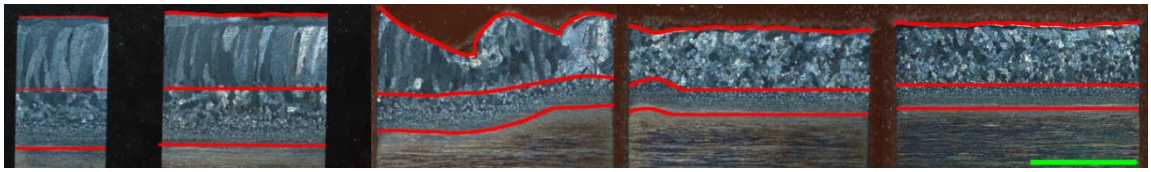

Figure 88. Example cross section to view melt pool depth (Experiment 1, Transient Section).

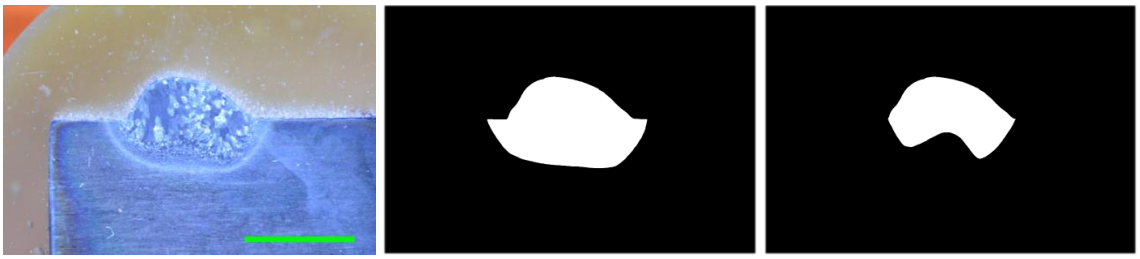

Figure 89. Sample 1B. Experiment line 1, final steady state.

Experiment Line 2

Figure 90. Sample 2A. Experiment line 2, initial steady state.

Figure 91. Sample 2-1. Experiment line 2, first section in transient region.

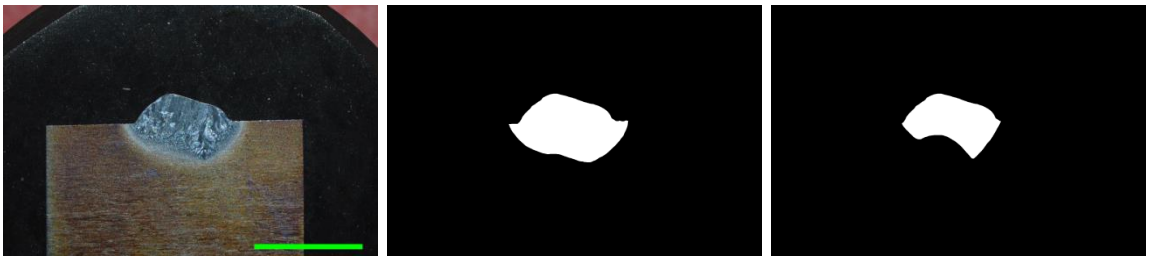

Figure 92. Sample 2-2. Experiment line 2, second section in transient region.

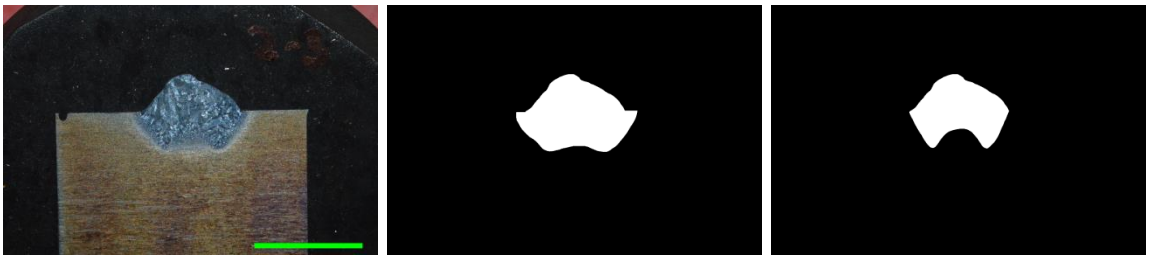

Figure 93. Sample 2-3. Experiment line 2, third section in transient region.

Figure 94. Sample 2-4. Experiment line 2, fourth section in transient region.

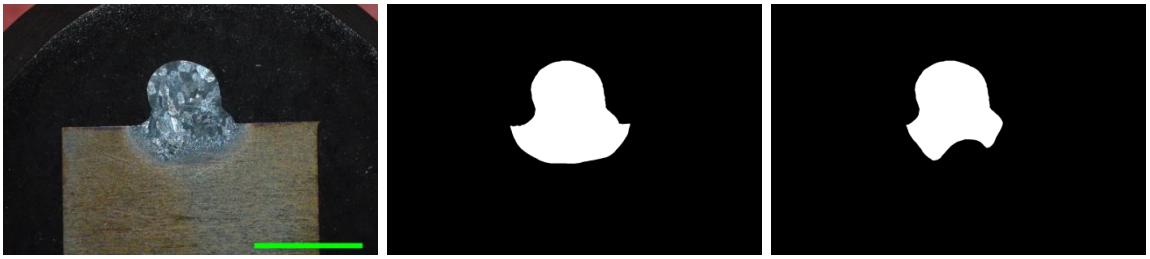

Figure 95. Sample 2-5. Experiment line 2, fifth section in transient region.

Figure 96. Sample 2-6. Experiment line 2, sixth section in transient region.

Figure 97. Sample 2-7. Experiment line 2, seventh section in transient region.

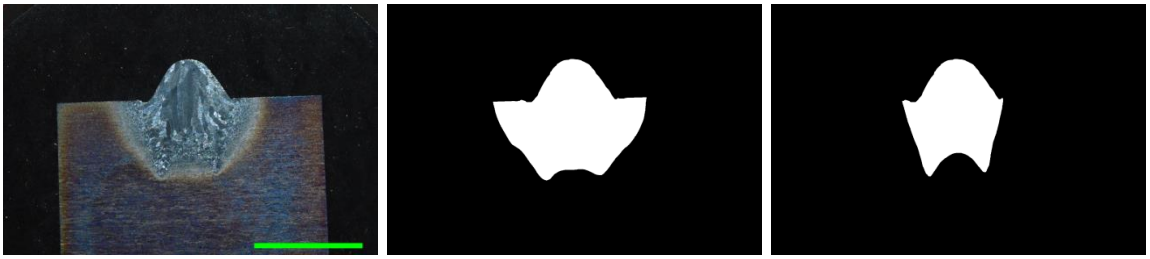

Figure 98. Sample 2-8. Experiment line 2, eighth section in transient region.

Figure 99. Sample 2-9. Experiment line 2, ninth section in transient region.

Figure 100. Sample 2-10. Experiment line 2, tenth section in transient region.

Figure 101. Sample 2B. Experiment line 2, final steady state.

Experiment Line 3

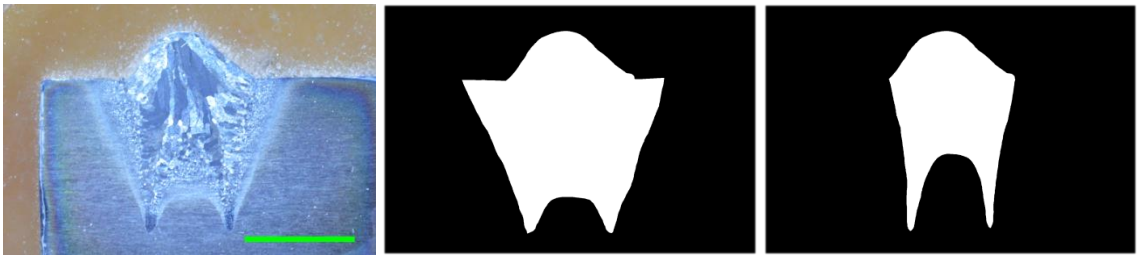

Figure 102. Sample 3A. Experiment line 3, initial steady state.

Figure 103. Sample 3-1. Experiment line 3, first section in transient region.

Figure 104. Sample 3-2. Experiment line 3, second section in transient region.

Figure 105. Sample 3-3. Experiment line 3, third section in transient region.

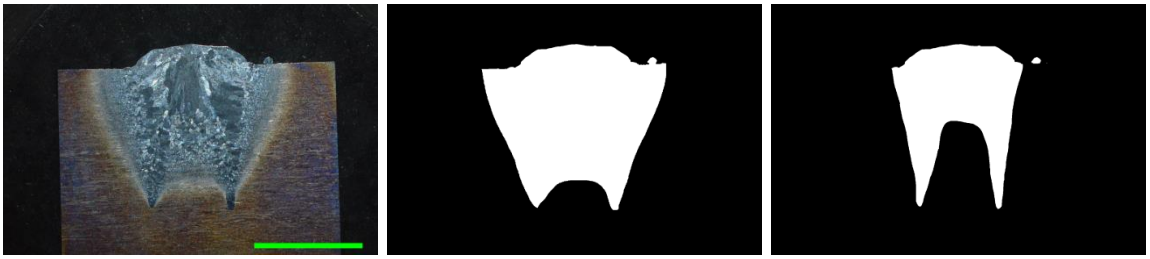

Figure 106. Sample 3-4. Experiment line 3, fourth section in transient region.

Figure 107. Sample 3-5. Experiment line 3, fifth section in transient region.

Figure 108. Sample 3-6. Experiment line 3, sixth section in transient region.

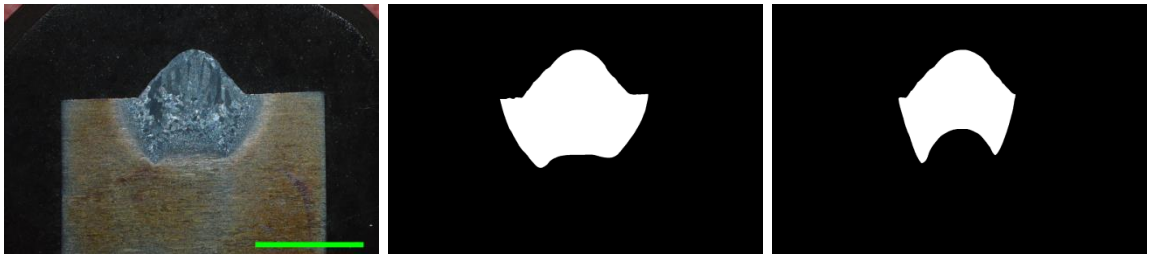

Figure 109. Sample 3-7. Experiment line 3, seventh section in transient region.

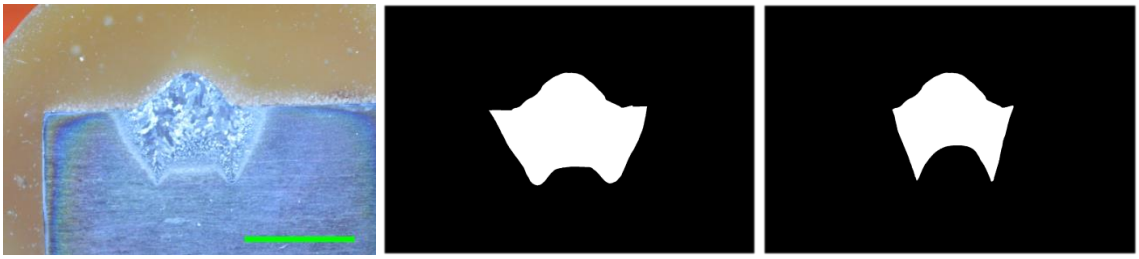

Figure 110. Sample 3B. Experiment line 3, final steady state.

Experiment Line 4

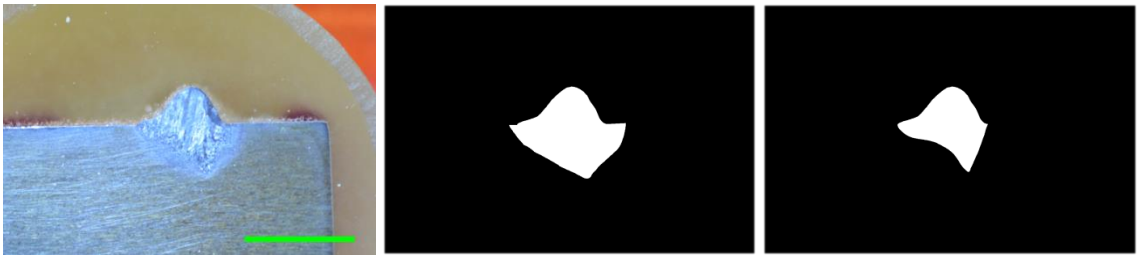

Figure 111. Sample 4A. Experiment line 4, initial steady state.

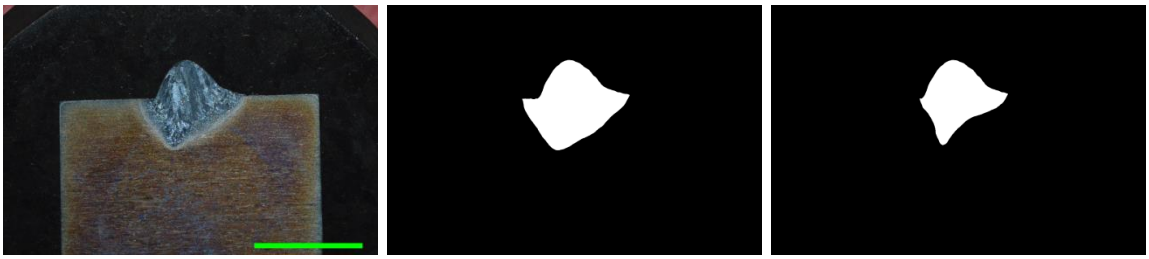

Figure 112. Sample 4-2. Experiment line 4, second section in transient region.

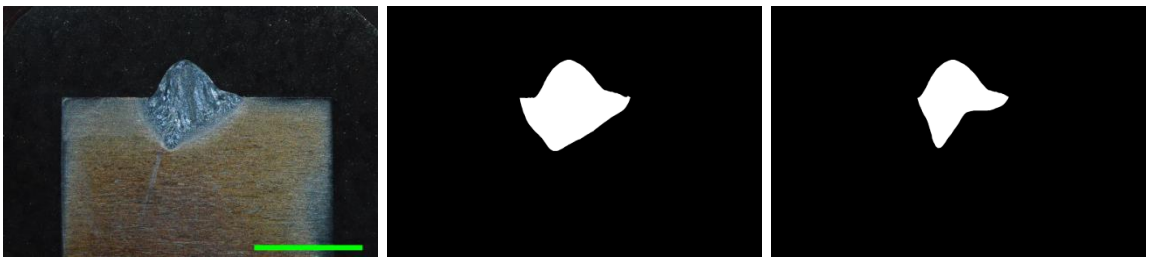

Figure 113. Sample 4-3. Experiment line 4, third section in transient region.

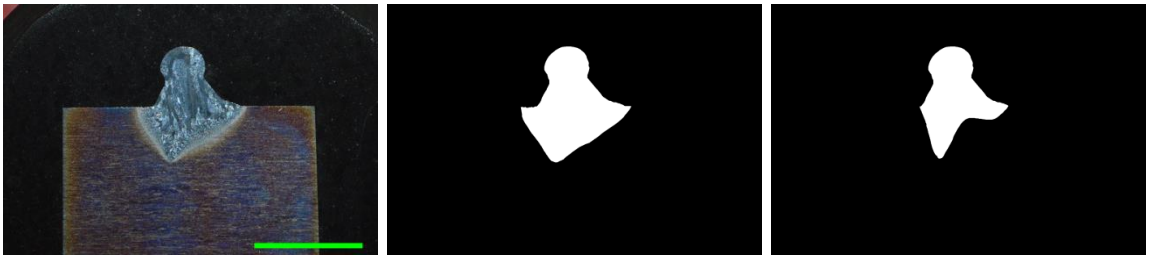

Figure 114. Sample 4-4. Experiment line 4, fourth section in transient region.

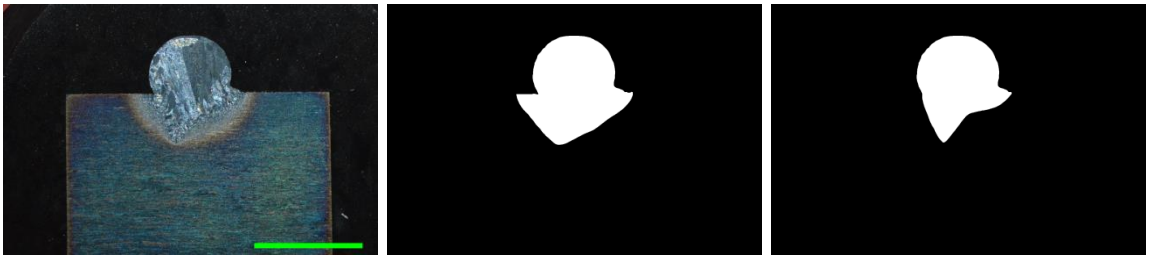

Figure 115. Sample 4-5. Experiment line 4, fifth section in transient region.

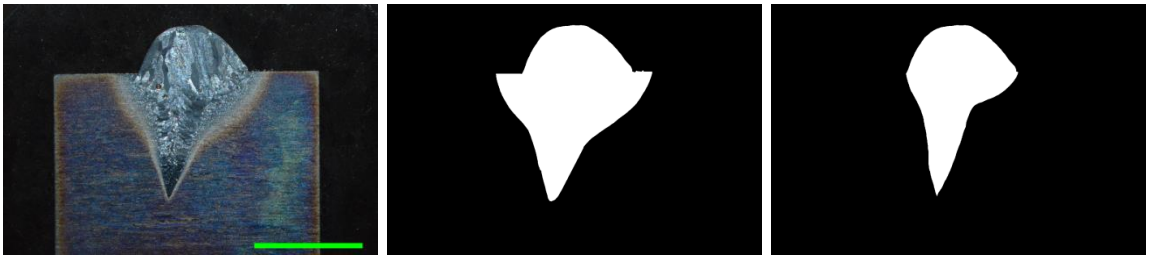

Figure 116. Sample 4-6. Experiment line 4, sixth section in transient region.

Figure 117. Sample 4-7. Experiment line 4, seventh section in transient region.

Figure 118. Sample 4-8. Experiment line 4, eighth section in transient region.

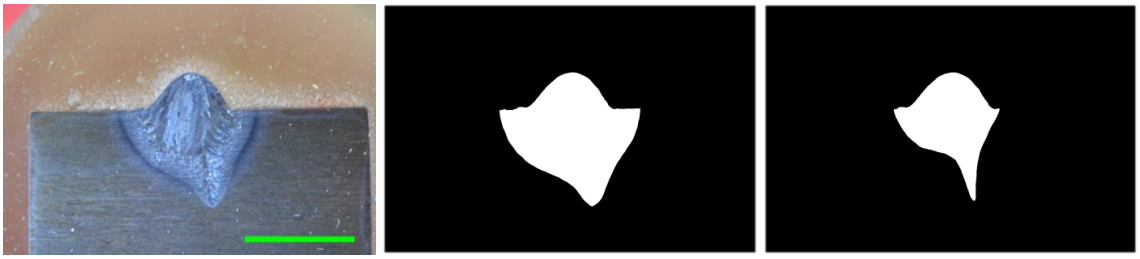

Figure 119. Sample 4B. Experiment line 4, final steady state.

Experiment Line 5

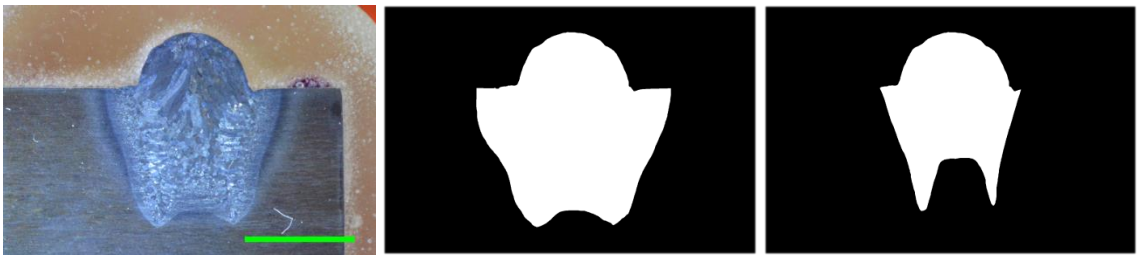

Figure 120. Sample 5A. Experiment line 5, initial steady state.

Figure 121. Sample 5-1. Experiment line 5, first section in transient region.

Figure 122. Sample 5-2. Experiment line 5, second section in transient region.

Figure 123. Sample 5-3. Experiment line 5, third section in transient region.

Figure 124. Sample 5-4. Experiment line 5, fourth section in transient region.

Figure 125. Sample 5-5. Experiment line 5, fifth section in transient region.

Figure 126. Sample 5-6. Experiment line 5, sixth section in transient region.

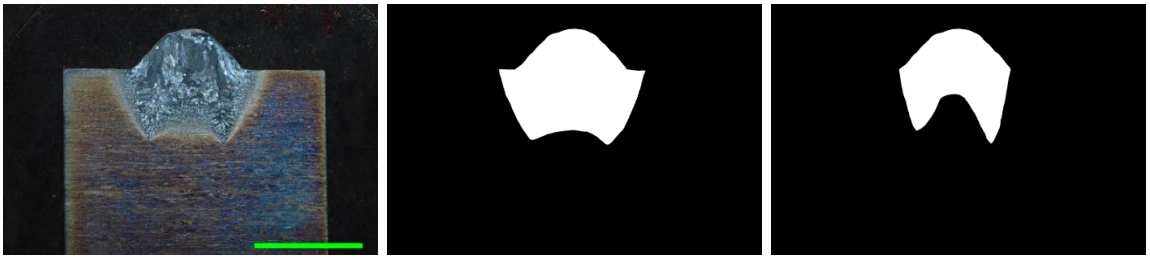

Figure 127. Sample 5-7. Experiment line 5, seventh section in transient region.

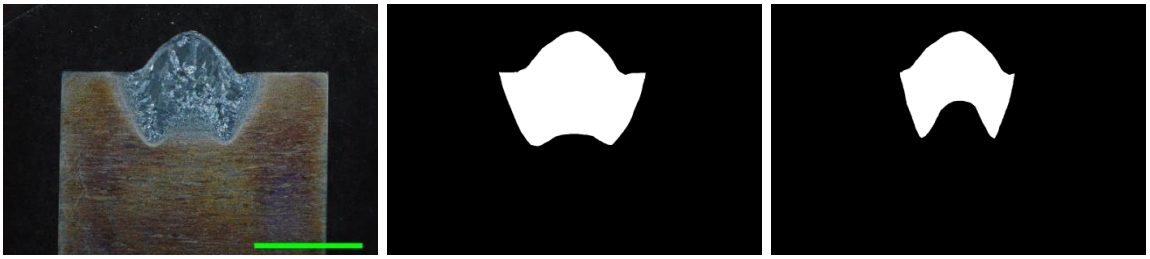

Figure 128. Sample 5-8. Experiment line 5, eighth section in transient region.

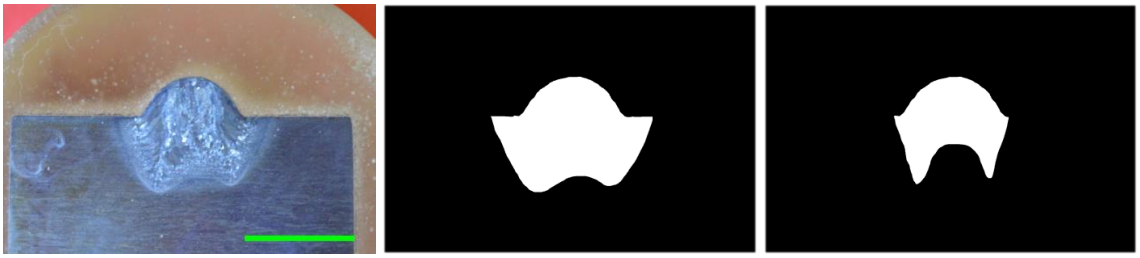

Figure 129. Sample 5B. Experiment line 5, final steady state.

Experiment Line 6

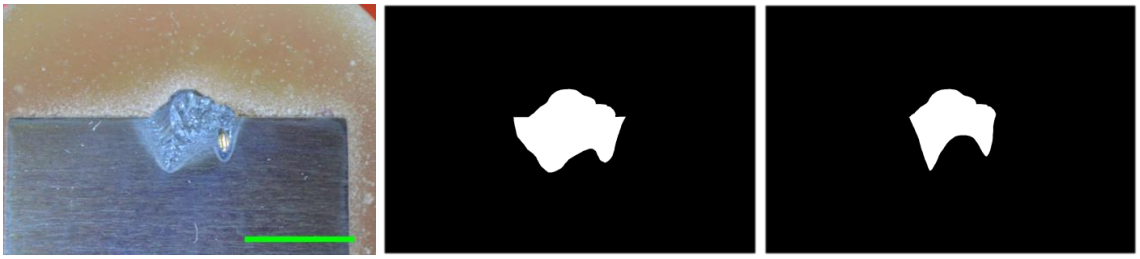

Figure 130. Sample 6A. Experiment line 6, initial steady state.

Figure 131. Sample 6-2. Experiment line 6, second section in transient region.

Figure 132. Sample 6-3. Experiment line 6, third section in transient region.

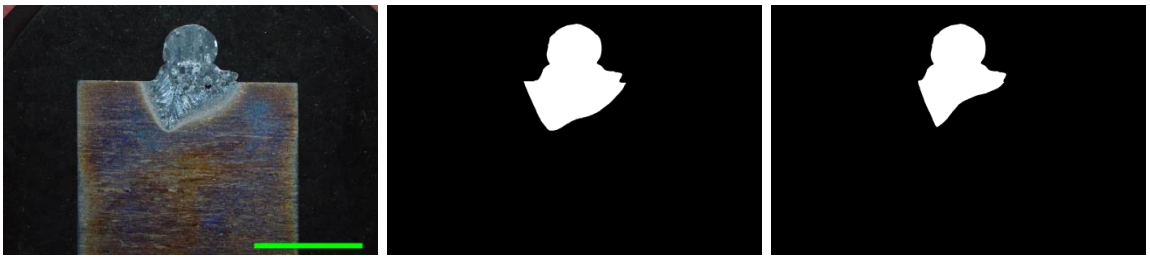

Figure 133. Sample 6-4. Experiment line 6, fourth section in transient region.

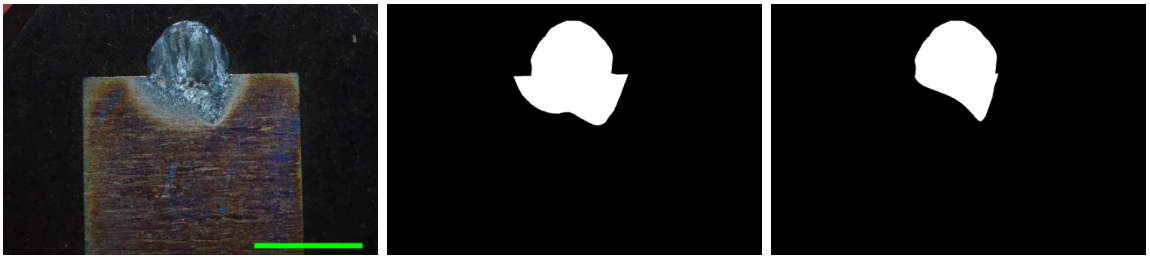

Figure 134. Sample 6-5. Experiment line 6, fifth section in transient region.

Figure 135. Sample 6-6. Experiment line 6, sixth section in transient region.

Figure 136. Sample 6-7. Experiment line 6, seventh section in transient region.

Figure 137. Sample 6-8. Experiment line 6, eighth section in transient region.

Figure 138. Sample 6B. Experiment line 6, final steady state.

Experiment Line 7

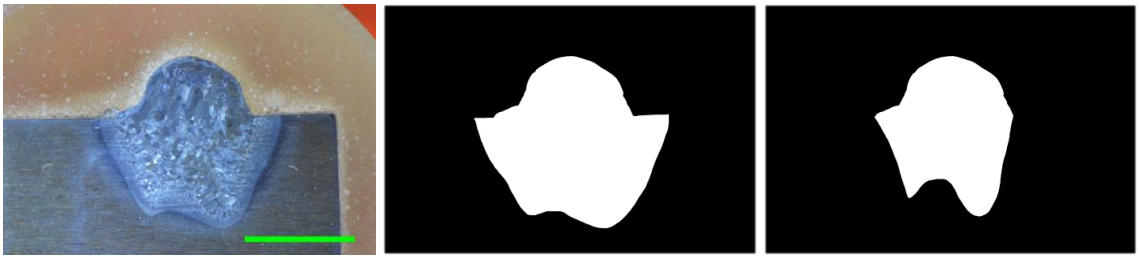

Figure 139. Sample 7A. Experiment line 7, initial steady state.

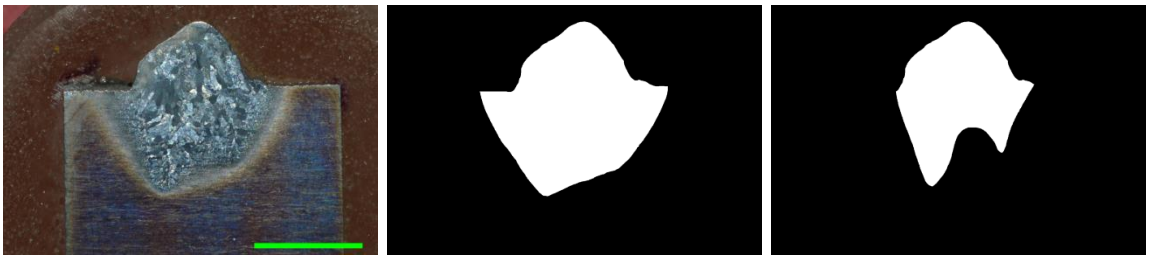

Figure 140. Sample 7-1. Experiment line 7, first section in transient region.

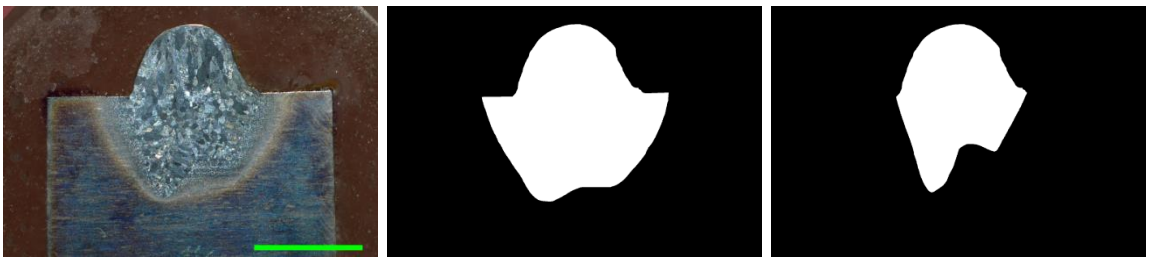

Figure 141. Sample 7-2. Experiment line 7, second section in transient region.

Figure 142. Sample 7-3. Experiment line 7, third section in transient region.

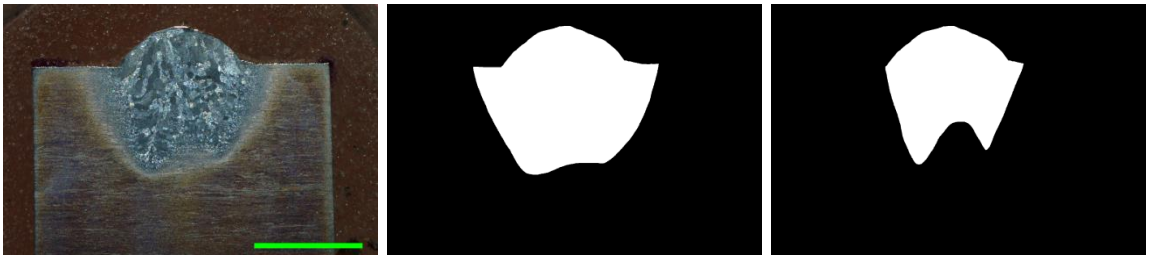

Figure 143. Sample 7-4. Experiment line 7, fourth section in transient region.

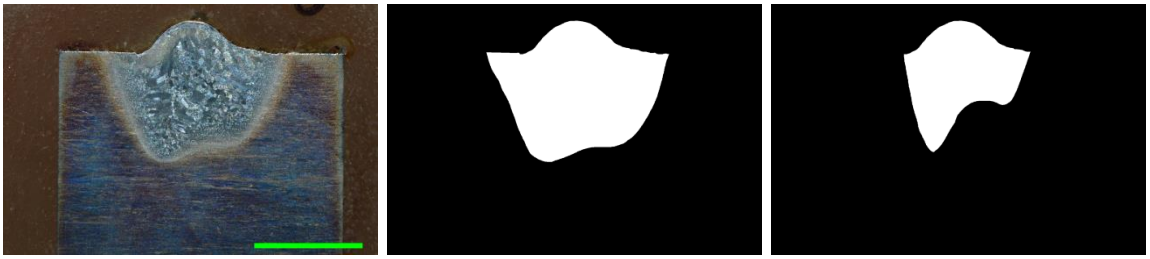

Figure 144. Sample 7-5. Experiment line 7, fifth section in transient region.

Figure 145. Sample 7-6. Experiment line 7, sixth section in transient region.

Figure 146. Sample 7-7. Experiment line 7, seventh section in transient region.

Figure 147. Sample 7-8. Experiment line 7, eighth section in transient region.

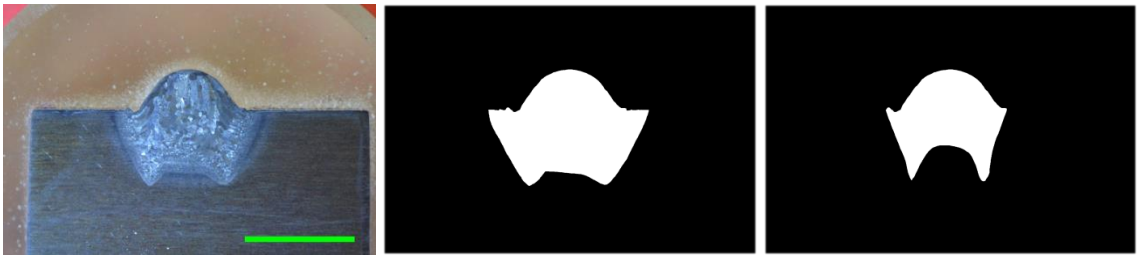

Figure 148. Sample 7B. Experiment line 7, final steady state.

Experiment Line 8

Figure 149. Sample 8A. Experiment line 8, initial steady state.

Figure 150. Sample 8-3. Experiment line 8, third section in transient region.

Figure 151. Sample 8-4. Experiment line 8, fourth section in transient region.

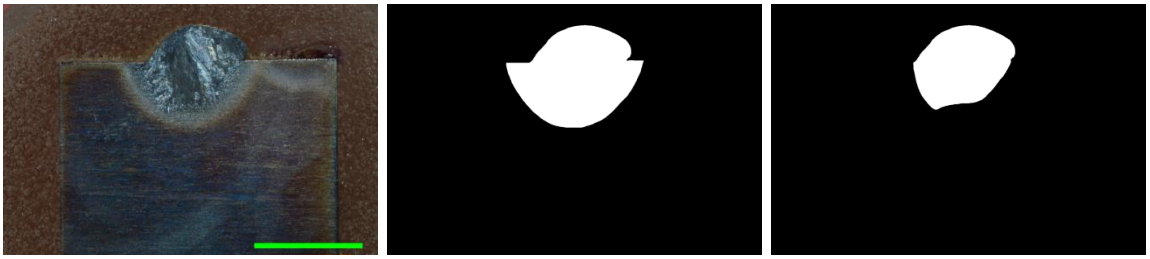

Figure 152. Sample 8-5. Experiment line 8, fifth section in transient region.

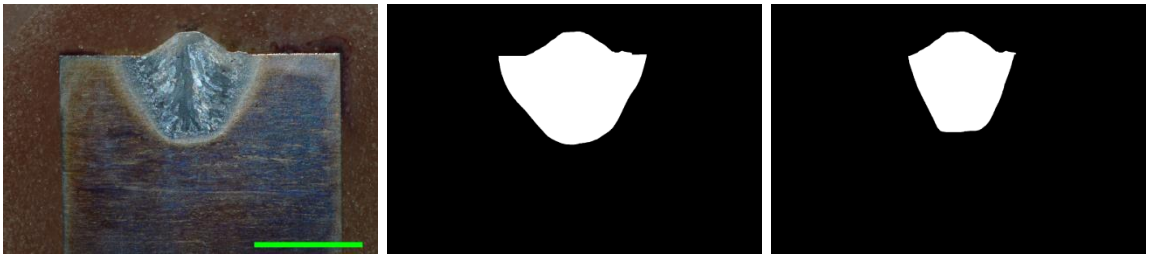

Figure 153. Sample 8-6. Experiment line 8, sixth section in transient region.

Figure 154. Sample 8-7. Experiment line 8, seventh section in transient region.

Figure 155. Sample 8-8. Experiment line 8, eighth section in transient region.

Figure 156. Sample 8-9. Experiment line 8, ninth section in transient region.

Figure 157. Sample 8-10. Experiment line 8, tenth section in transient region.

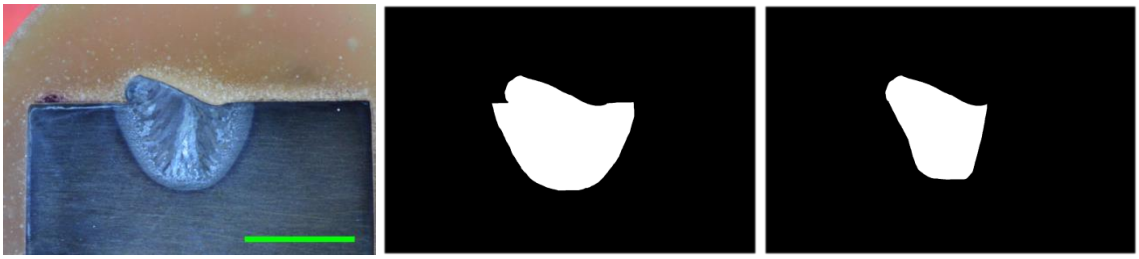

Figure 158. Sample 8B. Experiment line 8, final steady state.

Experiment Line 9

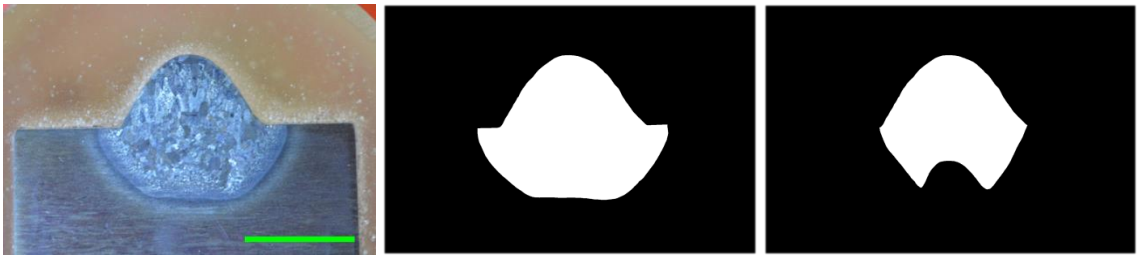

Figure 159. Sample 9A. Experiment line 9, initial steady state.

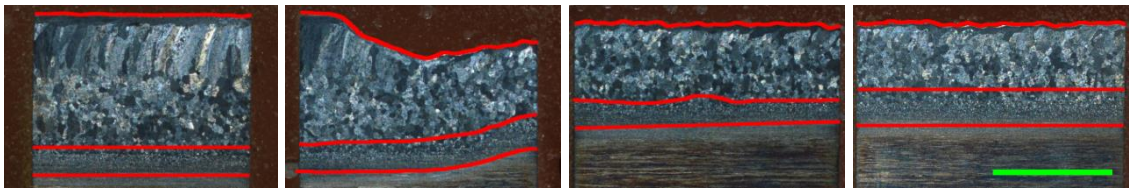

Figure 160. Experiment line 9, transient section.

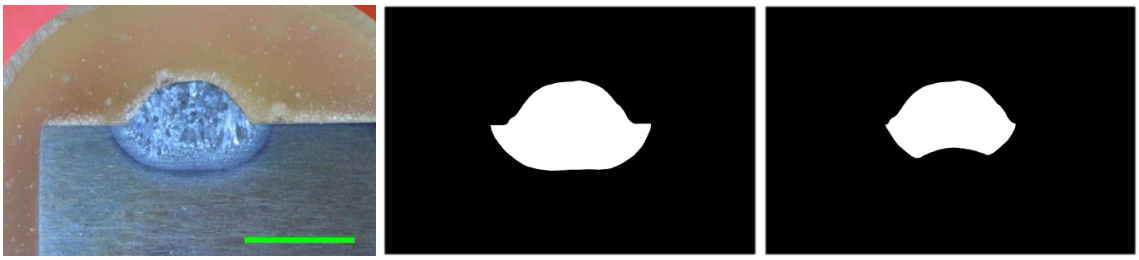

Figure 161. Sample 9B. Experiment line 9, final steady state.

Experiment Line 10

Figure 162. Sample 10A. Experiment line 10, initial steady state.

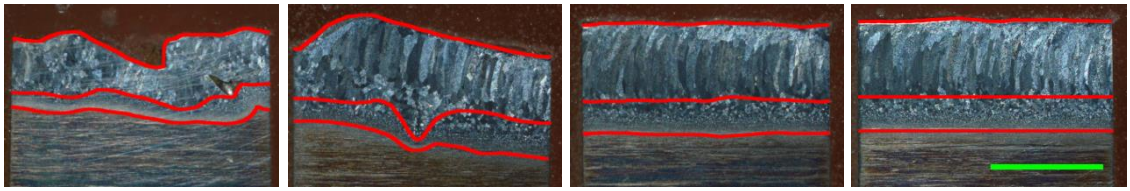

Figure 163. Experiment line 10, transient section.

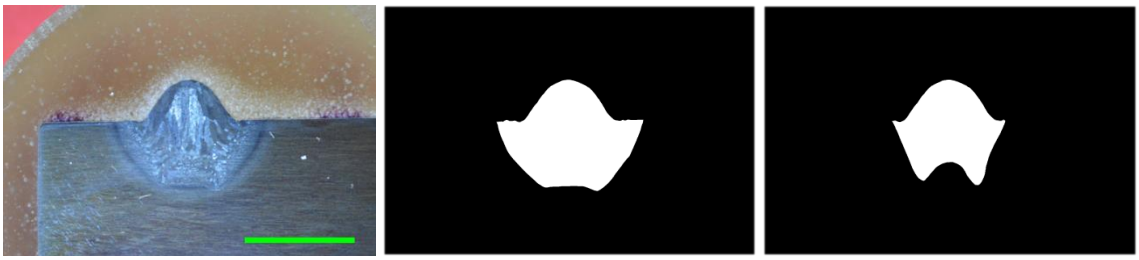

Figure 164. Sample 10B. Experiment line 10, final steady state.

Experiment Line 11

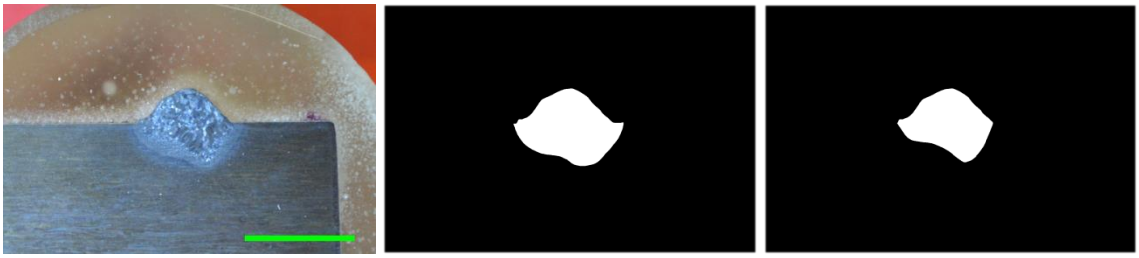

Figure 165. Sample 11A. Experiment line 11, initial steady state.

Figure 166. Sample 11-2. Experiment line 11, second section in transient region.

Figure 167. Sample 11-3. Experiment line 11, third section in transient region.

Figure 168. Sample 11-4. Experiment line 11, fourth section in transient region.

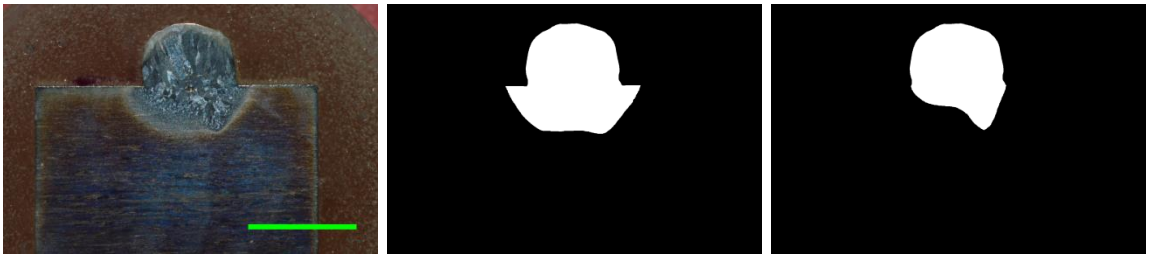

Figure 169. Sample 11-5. Experiment line 11, fifth section in transient region.

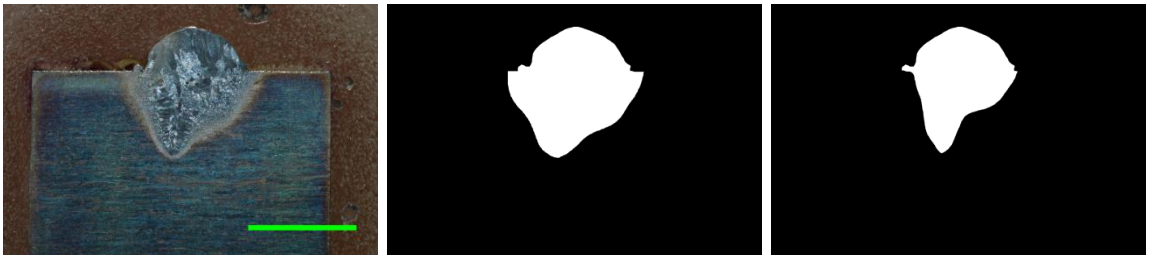

Figure 170. Sample 11-6. Experiment line 11, sixth section in transient region.

Figure 171. Sample 11-7. Experiment line 11, seventh section in transient region.

Figure 172. Sample 11-8. Experiment line 11, eighth section in transient region.

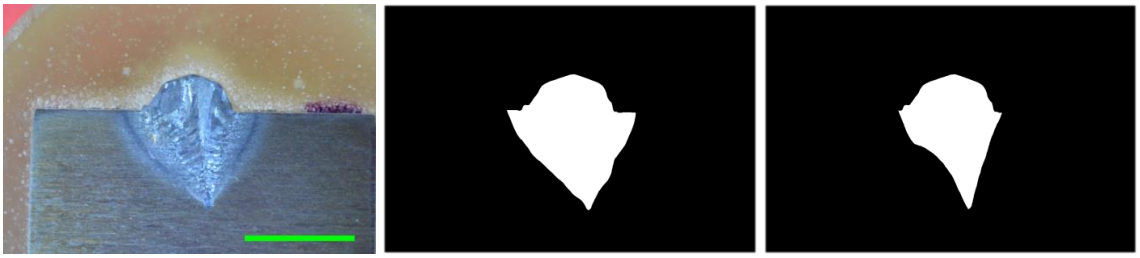

Figure 173. Sample 11B. Experiment line 11, final steady state.

Experiment Line 12

Figure 174. Sample 12A. Experiment line 12, initial steady state.

Figure 175. Sample 12B. Experiment line 12, final steady state.

Appendix B Measurement of Thin Wall Samples

This appendix contains the images from polished thin wall samples. All figures contain the polished surface (left) and black and white photos of the measured heat affected zone (middle) and melt zone (right). Heat affected zone is determined by the change in color observed in the wall. Melted zone is determined by determining an approximate line of constant grain size/morphology in the sample. Green scale bars are 0.25 in.

Experiment Line 1

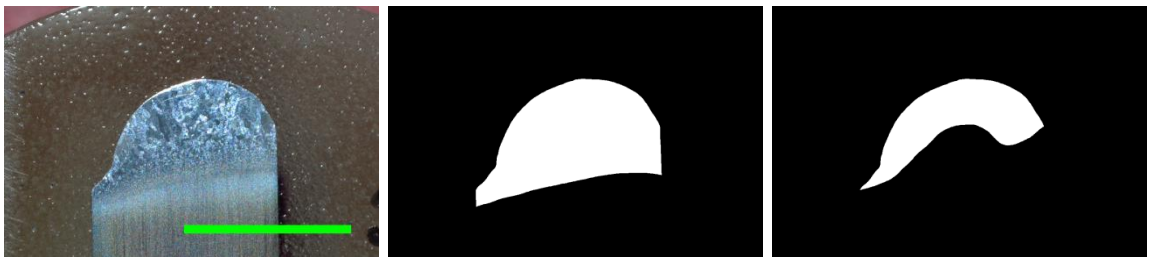

Figure 176. Sample 1A. Experiment line 1, initial steady state.

Figure 177. Sample 1-1. Experiment line 1, first section in transient region

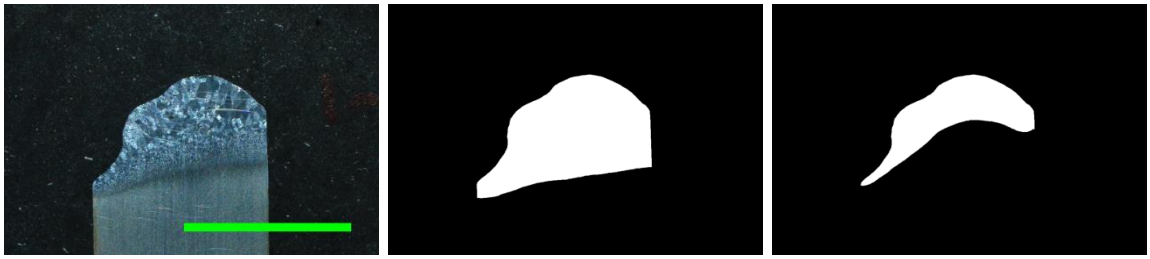

Figure 178. Sample 1-2. Experiment line 1, second section in transient region

Figure 179. Sample 1-3. Experiment line 1, third section in transient region.

Figure 180. Sample 1-4. Experiment line 1, fourth section in transient region.

Figure 181. Sample 1-5. Experiment line 1, fifth section in transient region.

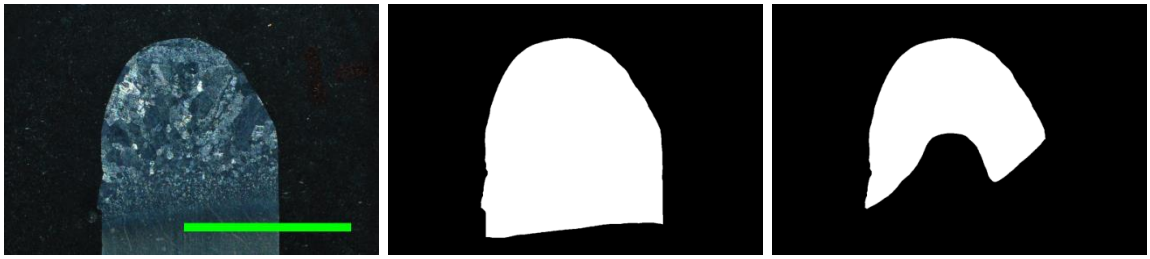

Figure 182. Sample 1-6. Experiment line 1, sixth section in transient region.

Figure 183. Sample 1B. Experiment line 1, final steady state.

Experiment Line 2

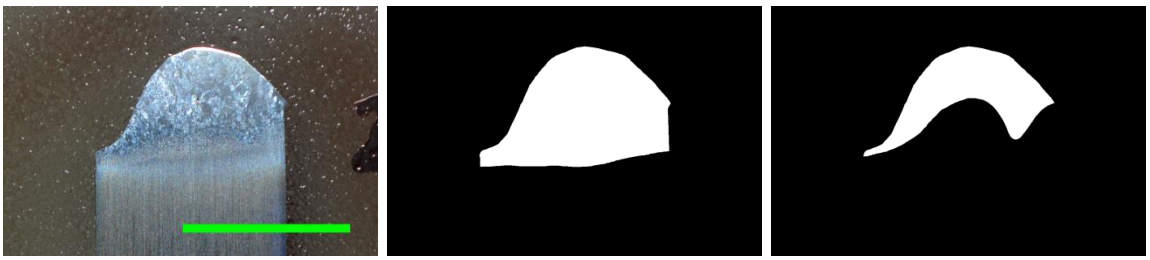

Figure 184. Sample 2A. Experiment line 2, initial steady state.

Figure 185. Sample 2-1. Experiment line 2, first section in transient region.

Figure 186. Sample 2-2. Experiment line 2, second section in transient region.

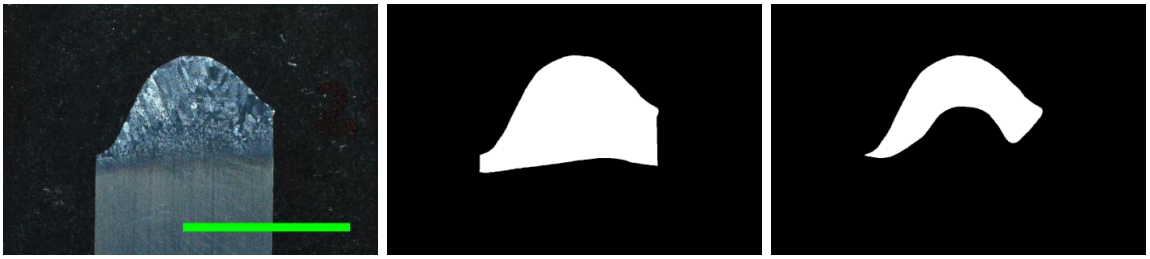

Figure 187. Sample 2-3. Experiment line 2, third section in transient region.

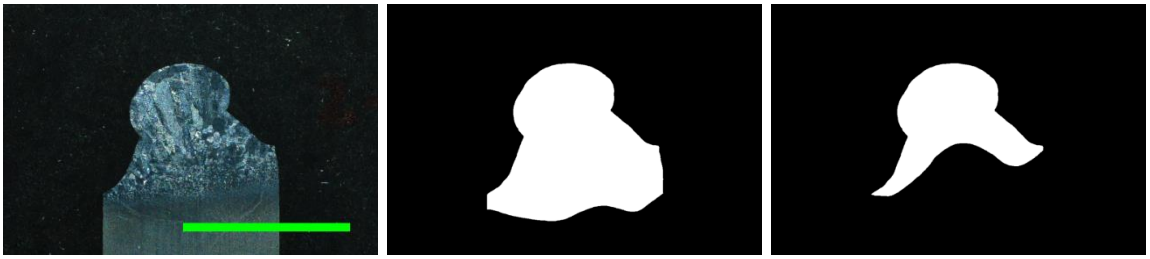

Figure 188. Sample 2-4. Experiment line 2, fourth section in transient region.

Figure 189. Sample 2-5. Experiment line 2, fifth section in transient region.

Figure 190. Sample 2-6. Experiment line 2, sixth section in transient region.

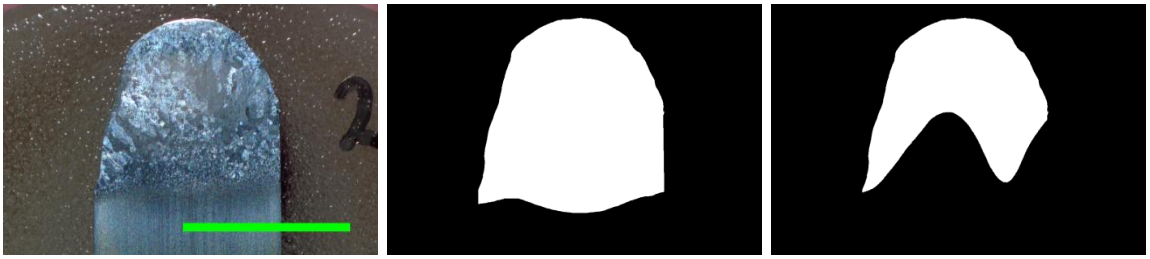

Figure 191. Sample 2B. Experiment line 2, final steady state.

Experiment Line 3

Figure 192. Sample 3A. Experiment line 3, initial steady state.

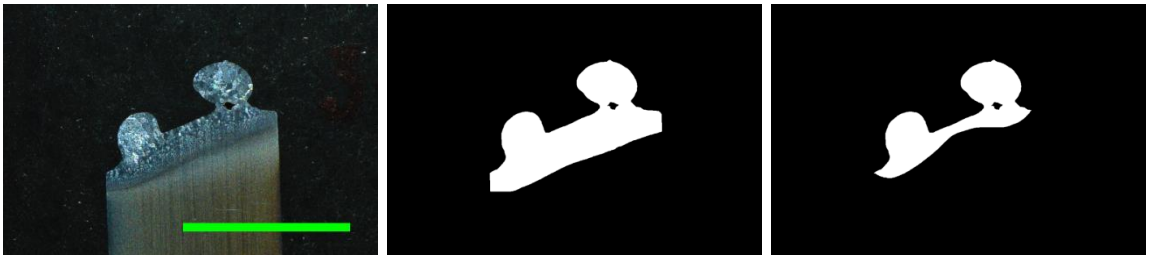

Figure 193. Sample 3-1. Experiment line 3, first section in transient region.

Figure 194. Sample 3-2. Experiment line 3, second section in transient region.

Figure 195. Sample 3-3. Experiment line 3, third section in transient region.

Figure 196. Sample 3-4. Experiment line 3, fourth section in transient region.

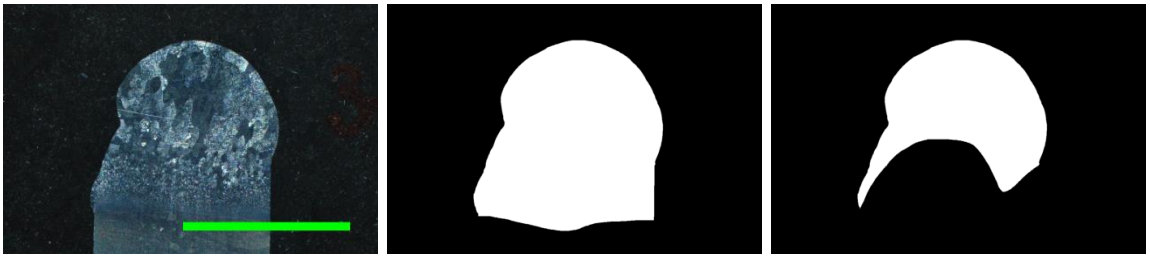

Figure 197. Sample 3-5. Experiment line 3, fifth section in transient region.

Figure 198. Sample 3-6. Experiment line 3, sixth section in transient region.

Figure 199. Sample 3A. Experiment line 3, final steady state.

Experiment Line 4

Figure 200. Sample 4A. Experiment line 4, initial steady state.

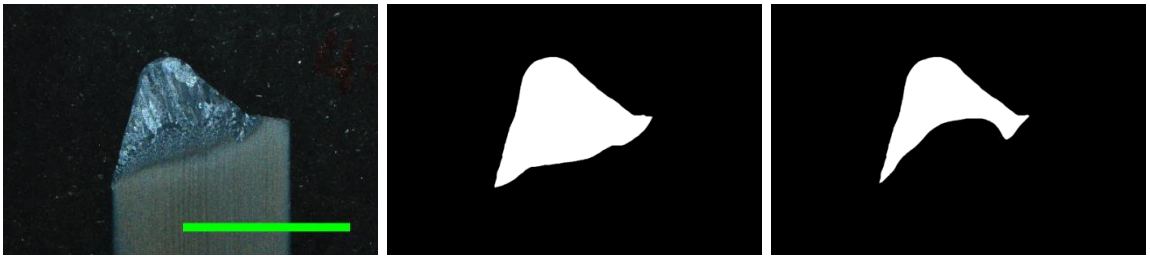

Figure 201. Sample 4-1. Experiment line 4, first section in transient region.

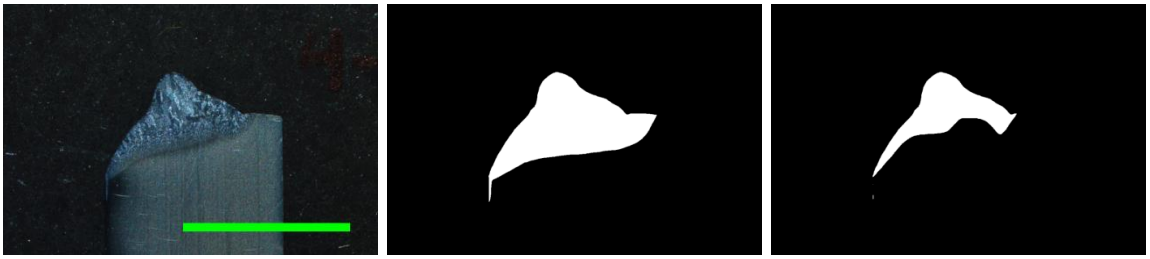

Figure 202. Sample 4-2. Experiment line 4, second section in transient region.

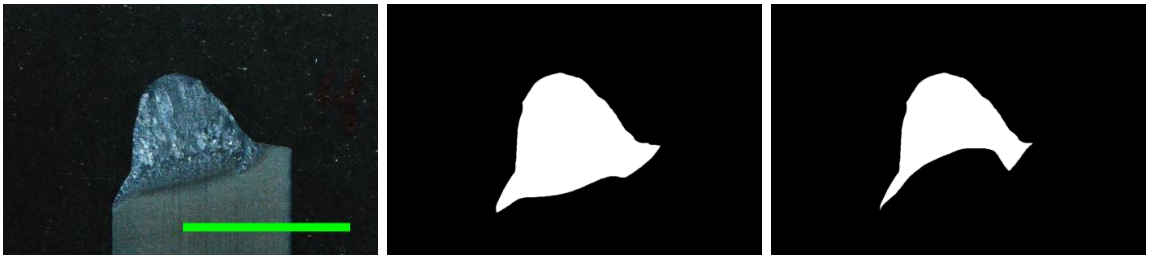

Figure 203. Sample 4-3. Experiment line 4, third section in transient region.

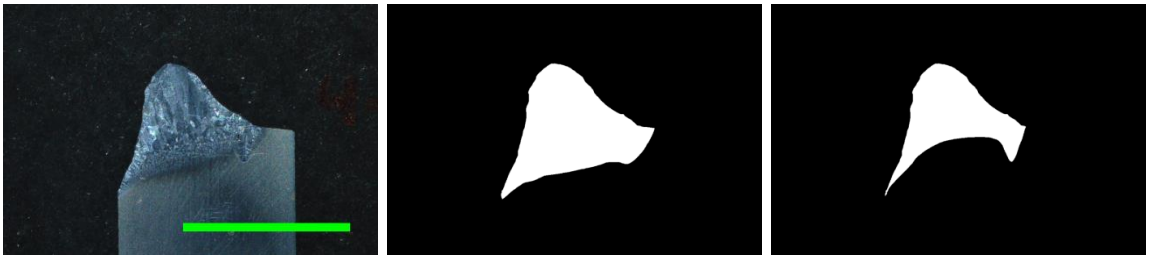

Figure 204. Sample 4-4. Experiment line 4, fourth section in transient region.

Figure 205. Sample 4-5. Experiment line 4, fifth section in transient region.

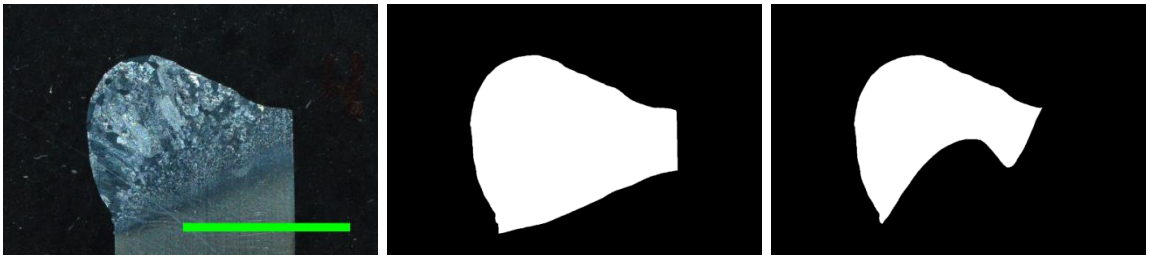

Figure 206. Sample 4-6. Experiment line 4, sixth section in transient region.

Figure 207. Sample 4B. Experiment line 4, final steady state.

Experiment Line 2R

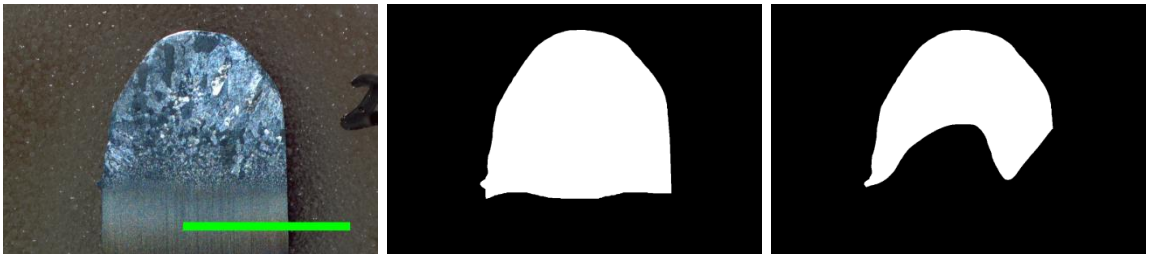

Figure 208. Sample 2RA. Experiment line 2R, initial steady state.

Figure 209. Sample 2R-1. Experiment line 2R, first section in transient region.

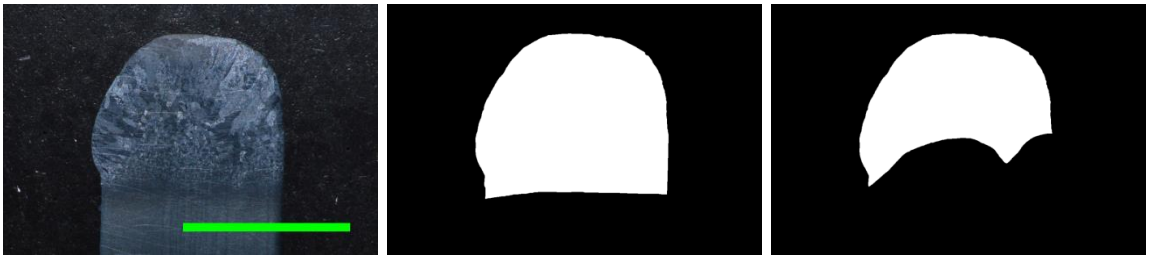

Figure 210. Sample 2R-2. Experiment line 2R, second section in transient region.

Figure 211. Sample 2R-3. Experiment line 2R, third section in transient region.

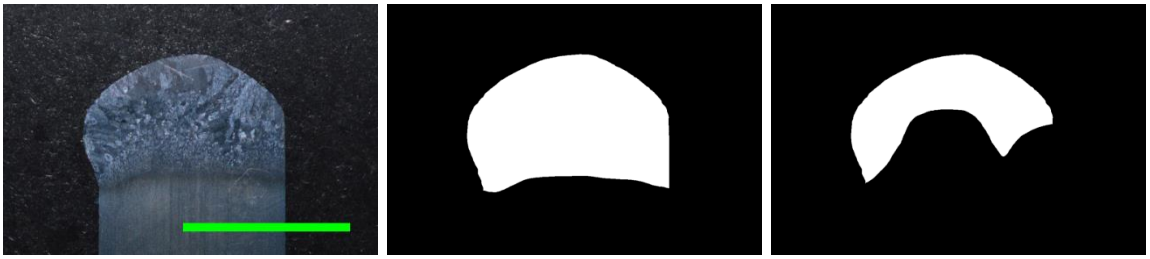

Figure 212. Sample 2R-4. Experiment line 2R, fourth section in transient region.

Figure 213. Sample 2R-5. Experiment line 2R, fifth section in transient region.

Figure 214. Sample 2R-6. Experiment line 2R, sixth section in transient region.

Figure 215. Sample 2RB. Experiment line 2R, final steady state.

Experiment Line 4R

Figure 216. Sample 4RA. Experiment line 4R, initial steady state.

Figure 217. Sample 4R-1. Experiment line 4R, first section in transient region.

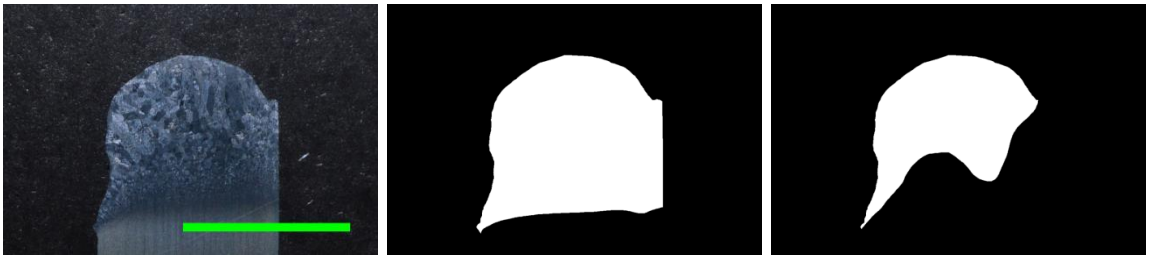

Figure 218. Sample 4R-2. Experiment line 4R, second section in transient region.

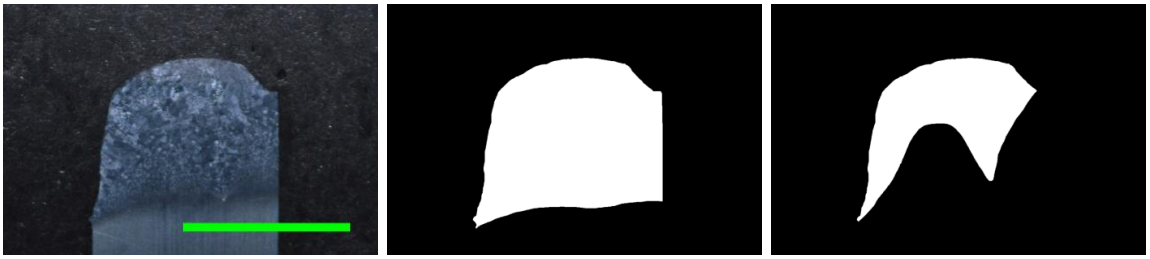

Figure 219. Sample 4R-3. Experiment line 4R, third section in transient region.

Figure 220. Sample 4R-4. Experiment line 4R, fourth section in transient region.

Figure 221. Sample 4R-5. Experiment line 4R, fifth section in transient region.

Figure 222. Sample 4R-6. Experiment line 4R, sixth section in transient region.

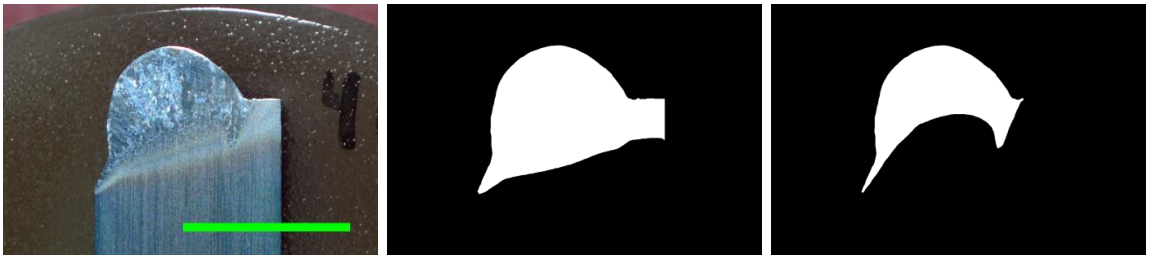

Figure 223. Sample 4RB. Experiment line 4R, final steady state.

Appendix C Measurement of Single Bead Electron Beam Powder Bed Samples

Surface Width Measurements

Green scale bars are 2 mm (7.87E-2 in).

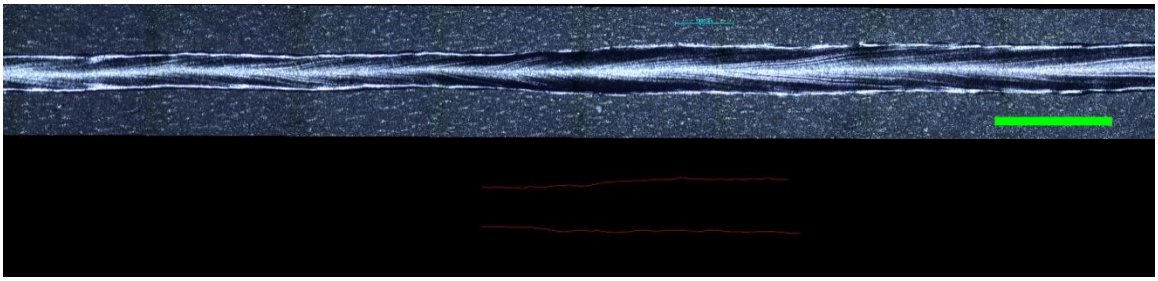

Figure 224. Experiment 1-1. Surface width measurement of line 1 on plate 1.

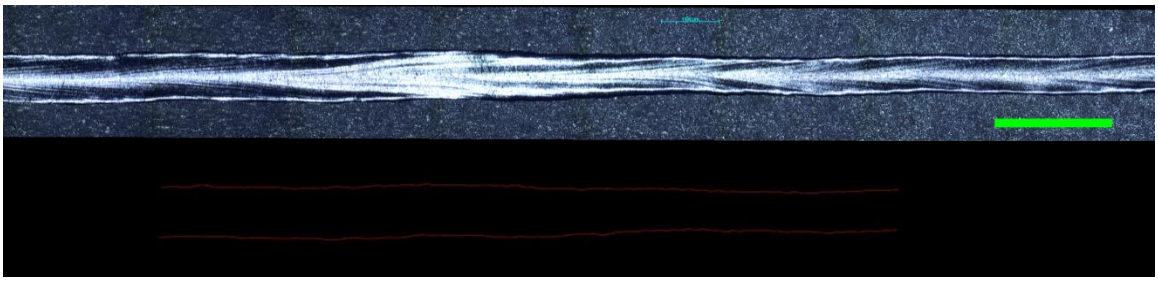

Figure 225. Experiment 1-2. Surface width measurement of line 1 on plate 1.

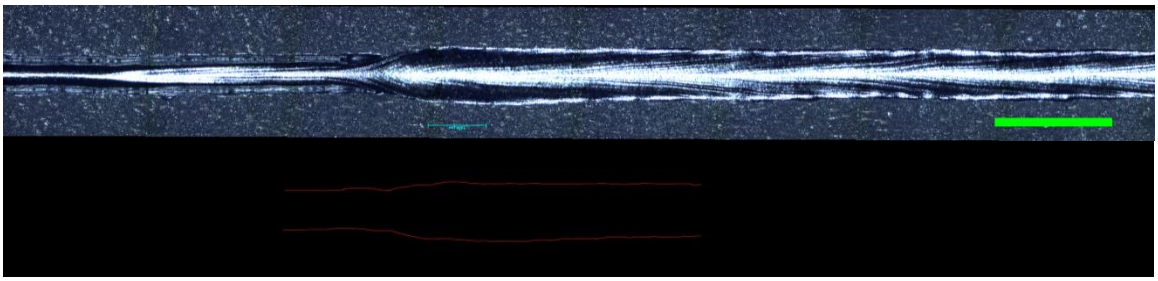

Figure 226. Experiment 1-9. Surface width measurement of line 9 on plate 1.

Figure 227. Experiment 1-10. Surface width measurement of line 10 on plate 1.

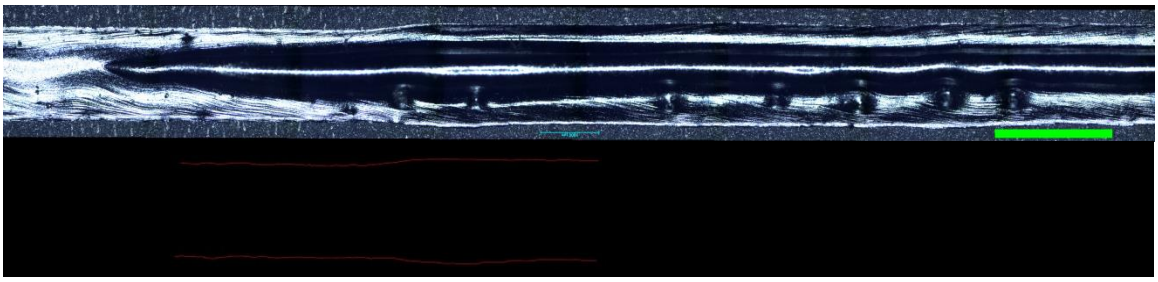

Figure 228. Experiment 1-11. Surface width measurement of line 11 on plate 1.

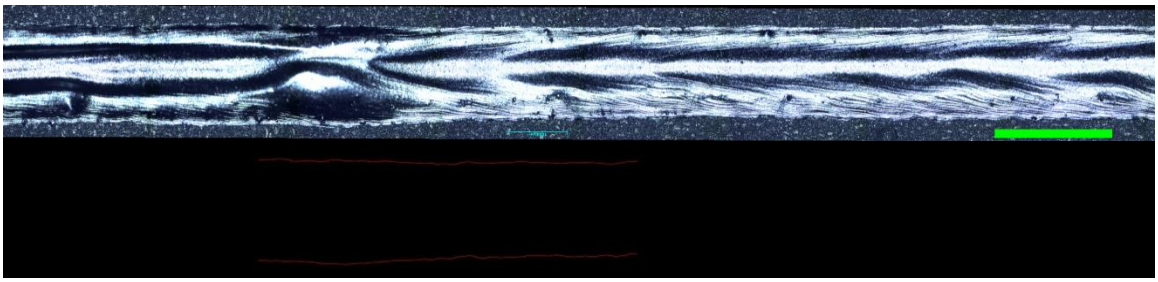

Figure 229. Experiment 1-12. Surface width measurement of line 12 on plate 1.

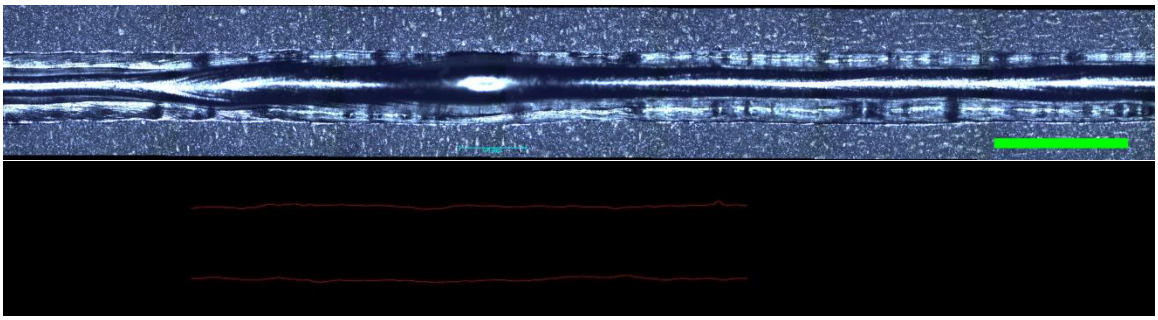

Figure 230. Experiment 1-13. Surface width measurement of line 13 on plate 1.

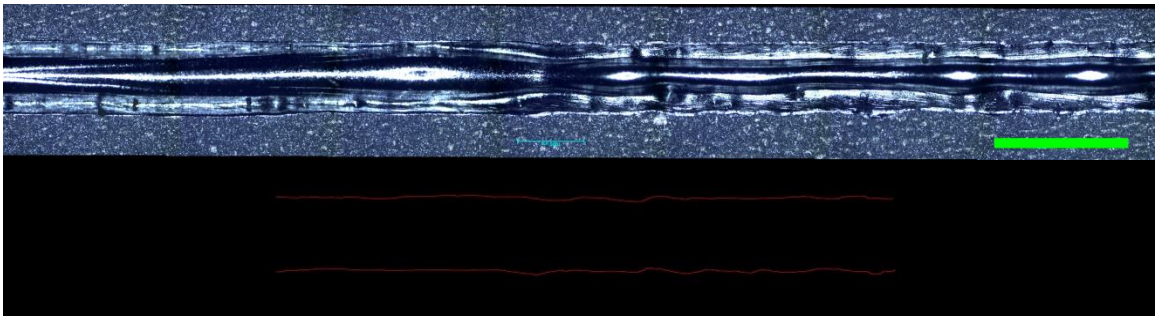

Figure 231. Experiment 1-14. Surface width measurement of line 14 on plate 1.

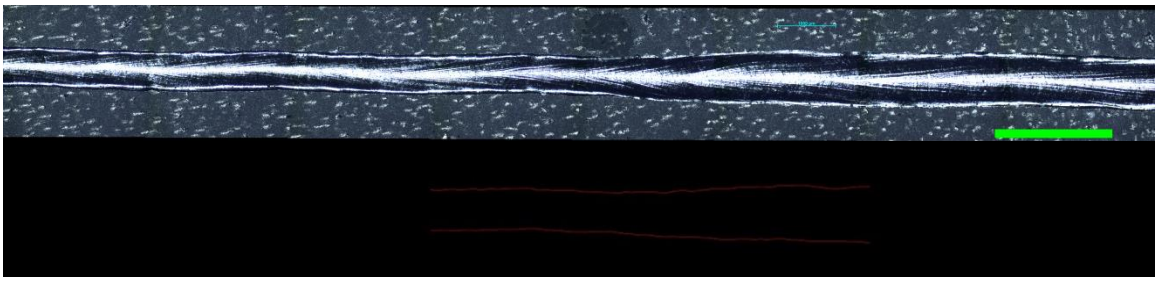

Figure 232. Experiment 2-1. Surface width measurement of line 1 on plate 2.

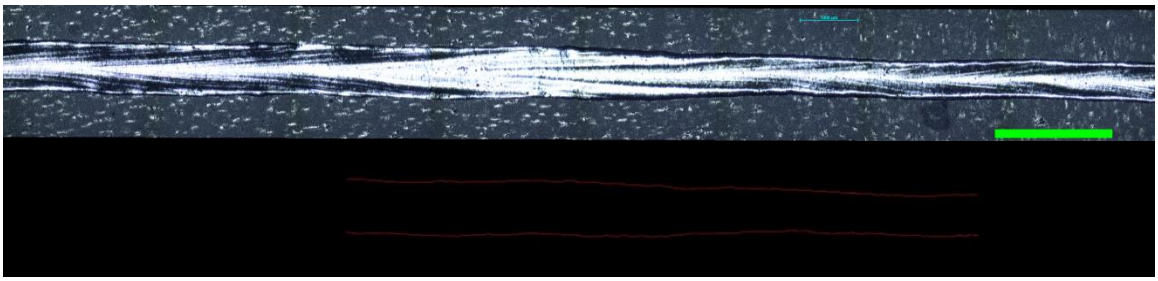

Figure 233. Experiment 2-2. Surface width measurement of line 1 on plate 2.

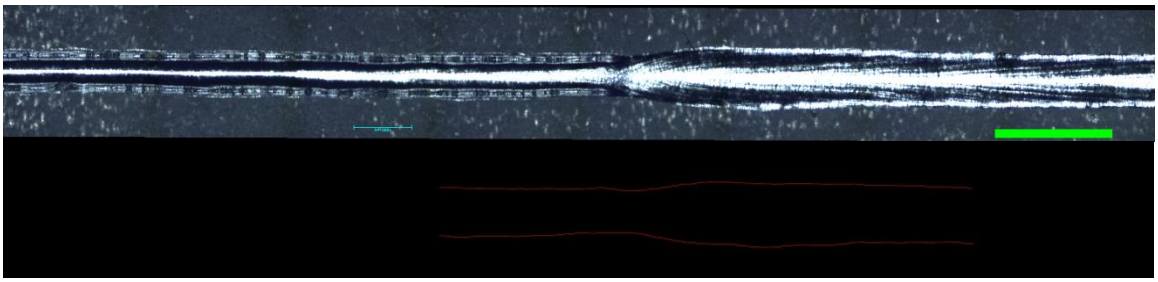

Figure 234. Experiment 2-9. Surface width measurement of line 9 on plate 2.

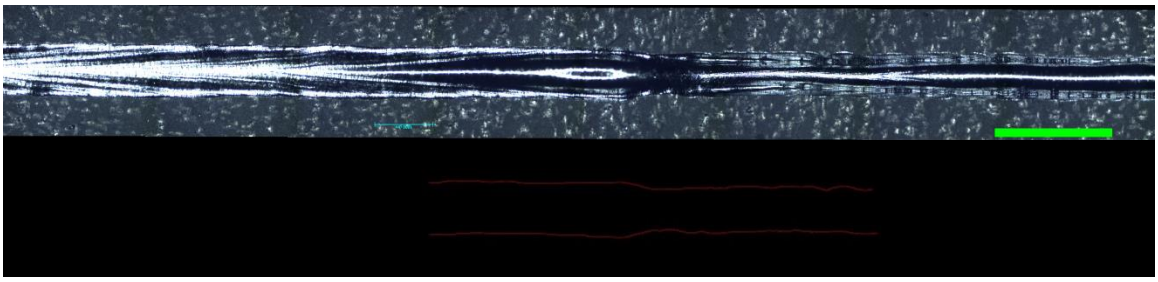

Figure 235. Experiment 2-10. Surface width measurement of line 10 on plate 2.

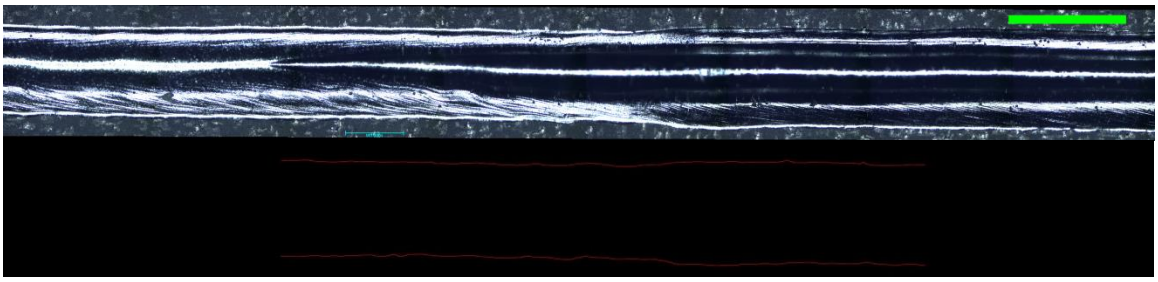

Figure 236. Experiment 2-11. Surface width measurement of line 11 on plate 2.

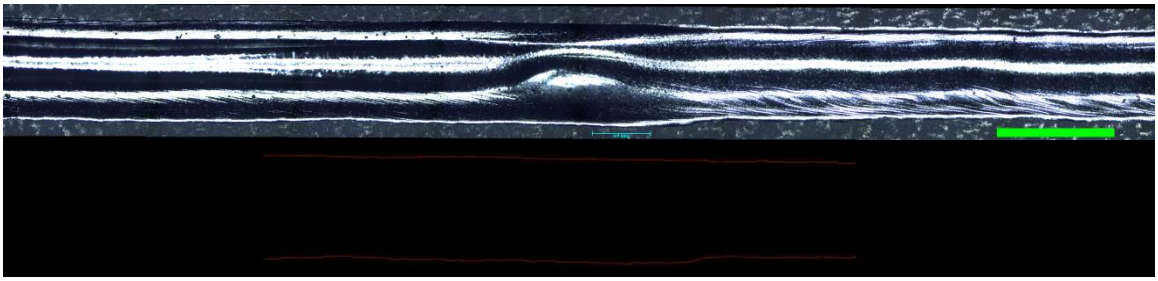

Figure 237. Experiment 2-12. Surface width measurement of line 12 on plate 2.

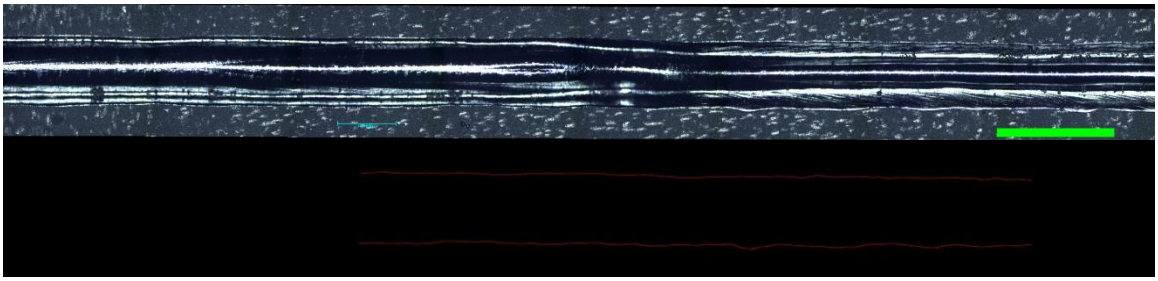

Figure 238. Experiment 2-13. Surface width measurement of line 13 on plate 2.

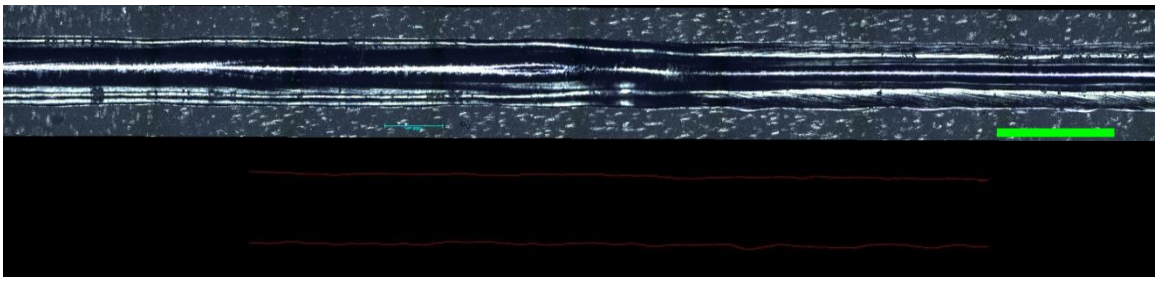

Figure 239. Experiment 2-14. Surface width measurement of line 14 on plate 2.

Area Measurements

Green scale bars are 1 mm (3.94E-2 in).

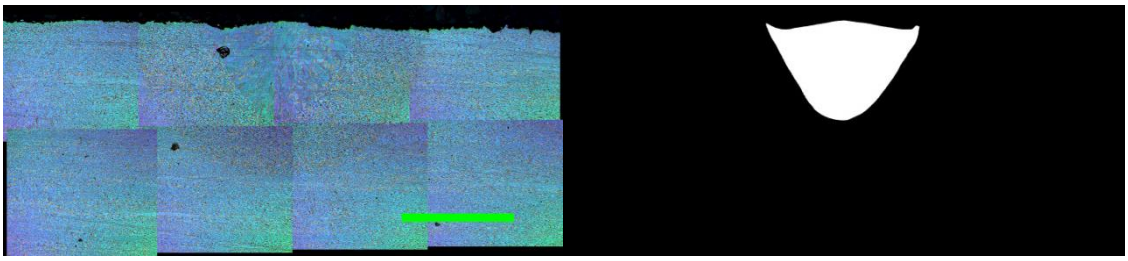

Figure 240. Sample 1-1A. Melt pool area measurement of plate 1, experiment line 1, initial steady state.

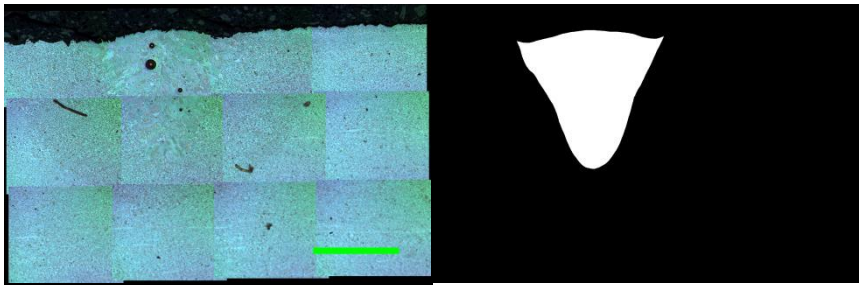

Figure 241. Sample 1-1B. Melt pool area measurement of plate 1, experiment line 1, final steady state.

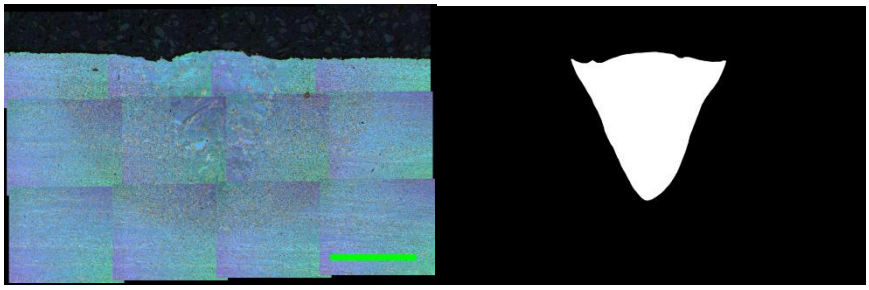

Figure 242. Sample 1-2A. Melt pool area measurement of plate 1, experiment line 2, initial steady state.

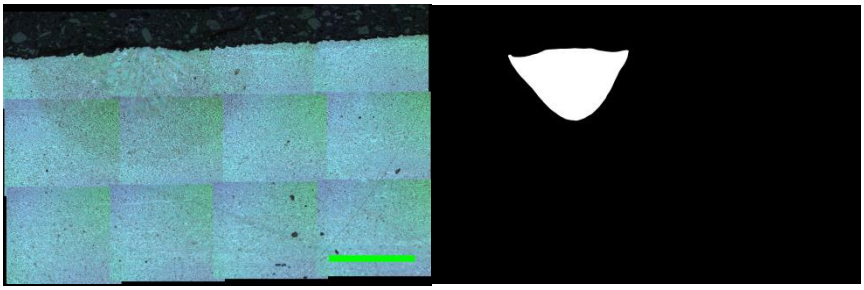

Figure 243. Sample 1-2B. Melt pool area measurement of plate 1, experiment line 2, final steady state.

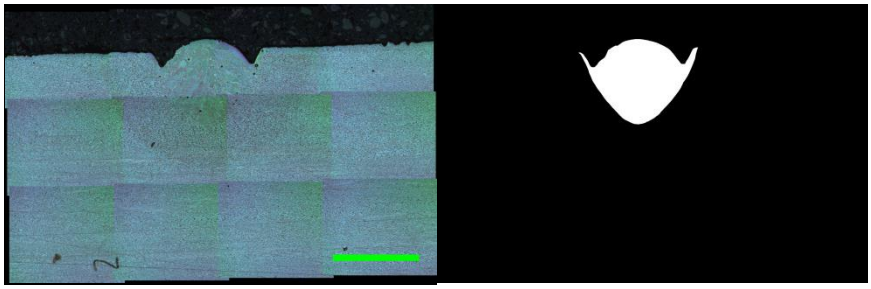

Figure 244. Sample 1-9A. Melt pool area measurement of plate 1, experiment line 9, initial steady state.

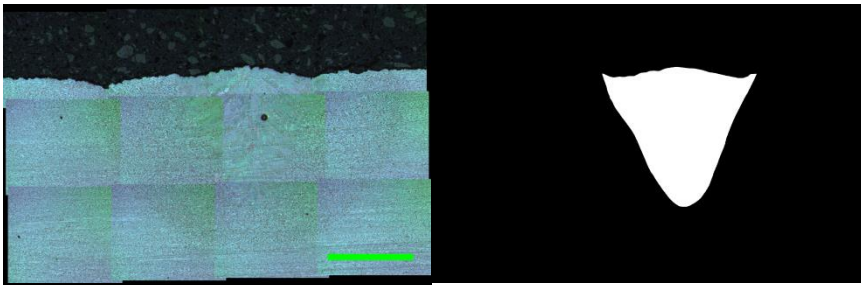

Figure 245. Sample 1-9B. Melt pool area measurement of plate 1, experiment line 9, final steady state.

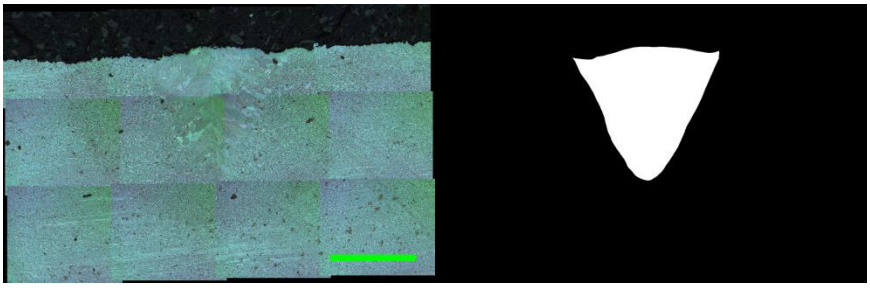

Figure 246. Sample 1-10A. Melt pool area measurement of plate 1, experiment line 10, initial steady state.

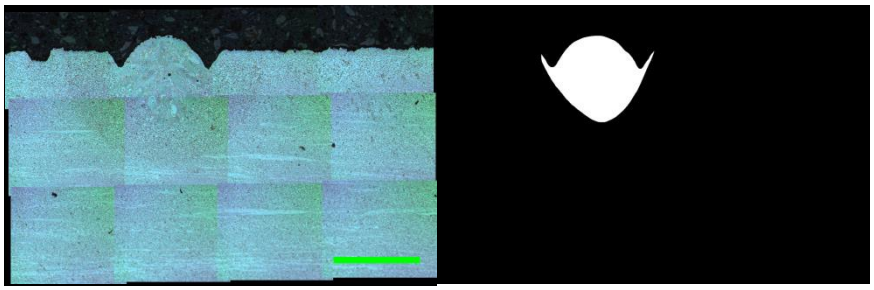

Figure 247. Sample 1-10B. Melt pool area measurement of plate 1, experiment line 10, final steady state.

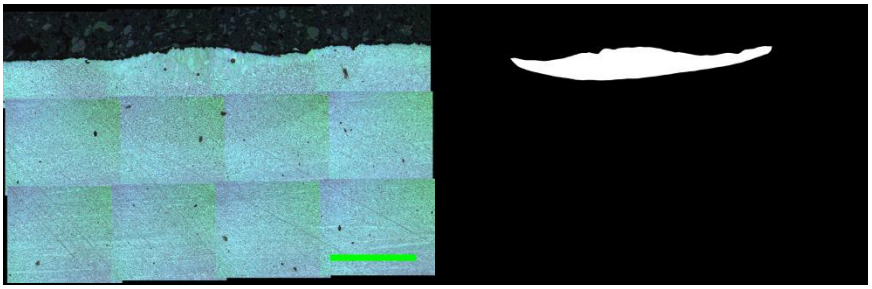

Figure 248. Sample 1-11A. Melt pool area measurement of plate 1, experiment line 11, initial steady state.

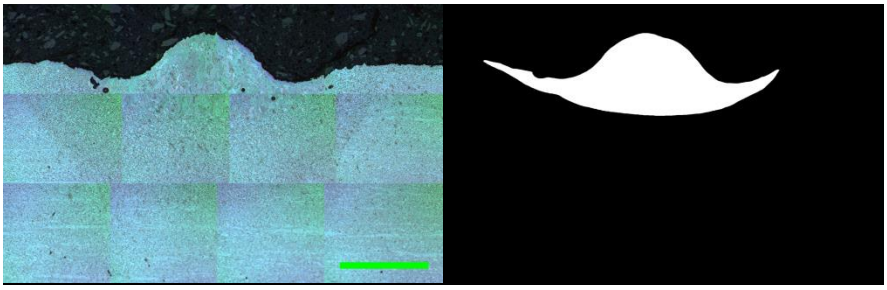

Figure 249. Sample 1-11B. Melt pool area measurement of plate 1, experiment line 11, final steady state.

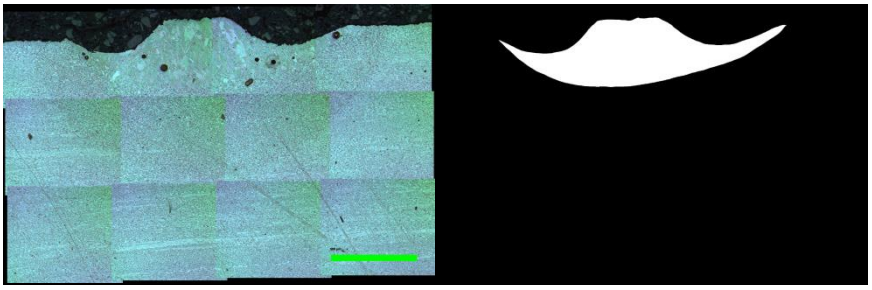

Figure 250. Sample 1-12A. Melt pool area measurement of plate 1, experiment line 12, initial steady state.

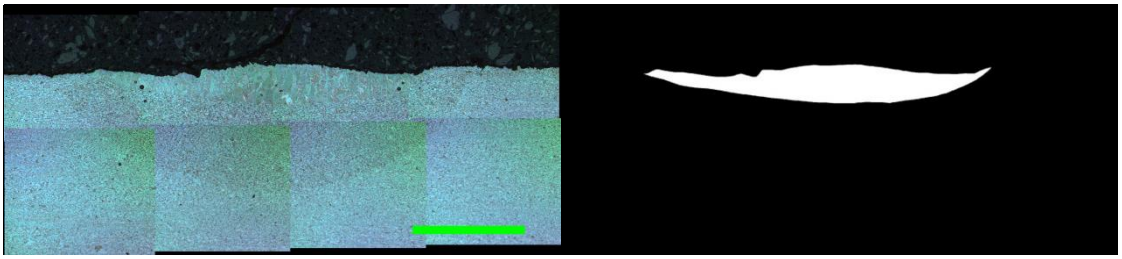

Figure 251. Sample 1-12B. Melt pool area measurement of plate 1, experiment line 12, final steady state.

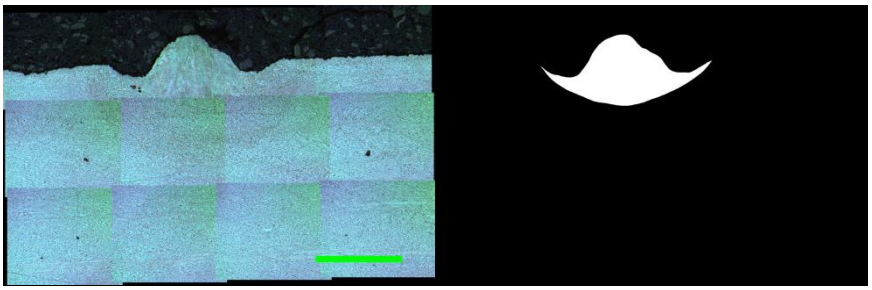

Figure 252. Sample 1-13A. Melt pool area measurement of plate 1, experiment line 13, initial steady state.

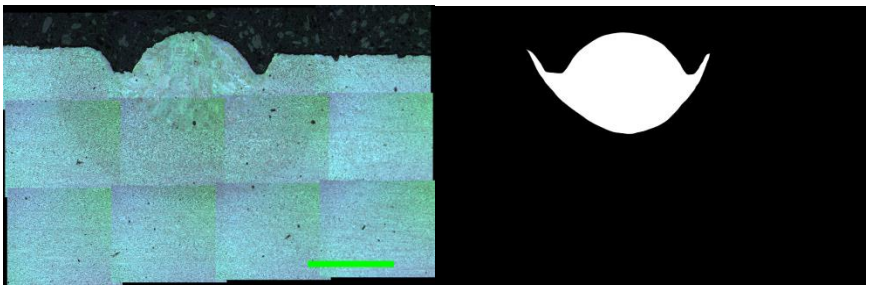

Figure 253. Sample 1-13B. Melt pool area measurement of plate 1, experiment line 13, final steady state.

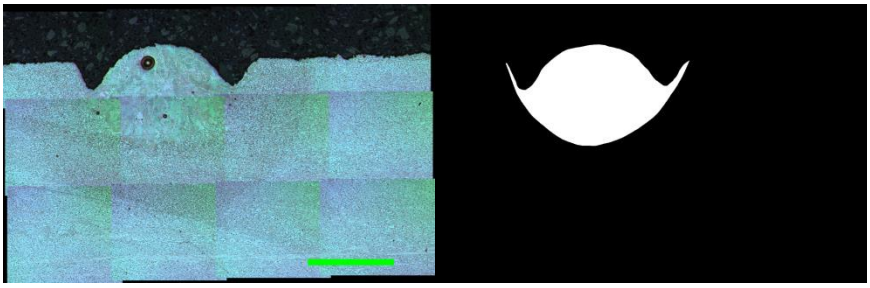

Figure 254. Sample 1-14A. Melt pool area measurement of plate 1, experiment line 14, initial steady state.

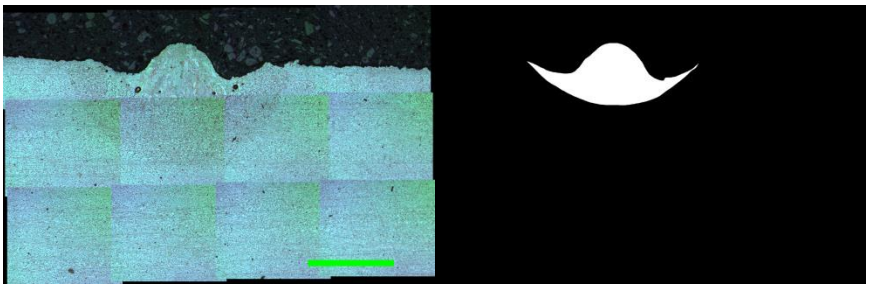

Figure 255. Sample 1-14B. Melt pool area measurement of plate 1, experiment line 14, final steady state.